Nanophotonic antennas for enhanced single-molecule fluorescence detection and nanospectroscopy in living cell membranes

Raju Regmi

Nanophotonic antennas for enhanced single-molecule fluorescence detection and nanospectroscopy in living cell membranes

Raju Regmi

under the supervision of

Jérôme Wenger

and

María F. García-Parajo

submitted this thesis in partial fulfillment
of the requirements for the degree of

DOCTOR
by

Aix-Marseille Université, France
and
Universitat Politècnica de Catalunya, Espagne

November 2017

PhD Thesis as part of the doctoral school

PHYSICS AND SCIENCES OF MATTER: ED 352

with specialization in: OPTICS, PHOTONICS AND IMAGE PROCESSING

defended publicly by

Raju Regmi

on the 10^{th} of November, 2017

Nanophotonic antennas for enhanced single-molecule fluorescence detection and nanospectroscopy in living cell membranes

Members of the thesis committee

President	Didier Marguet	Centre d'Immunologie de Marseille, France
Reviewer	Peter Zijlstra	TU Eindhoven, The Netherlands
Reviewer	Guillermo Acuna	TU Braunschweig, Germany
Examiner	Niek F. van Hulst	ICFO-Institut de Ciències Fotòniques, Spain
Invited	Hervé Rigneault	Institut Fresnel, CNRS, France
Advisor	Jérôme Wenger	Institut Fresnel, CNRS, France
Co-advisor	María F. García-Parajo	ICFO-Institut de Ciències Fotòniques, Spain

Abstract

Single-molecule fluorescence spectroscopy has revolutionized the field of biophysical sciences by enabling visualization of dynamic molecular interactions and nanoscopic features with high spatiotemporal resolution. Monitoring enzymatic reactions and studying diffusion dynamics of individual molecules (such as lipids and proteins) help us understand how these nanoscopic entities influence and control various biochemical processes. Nanophotonic antennas can efficiently localize electromagnetic radiation into nanoscale spatial dimensions comparable to single bio-molecules (<10 nm). These ultra-confined illumination hotspots thereby offer the opportunity to follow single-molecule events at physiological expression levels.

In this thesis, we explore various photonic nanoantenna platforms (double nanohole apertures, dimer nanogap antennas and planar "antenna-in-box") and demonstrate their application in enhanced single-molecule fluorescence detection. Using fluorescence burst analysis, fluorescence correlation spectroscopy (FCS), time-correlated TCSPC measurements, and near field simulations, we quantify nanoantenna detection volumes, fluorescence enhancement factors and discuss the fluorescence photodynamic accelerations mediated by optical nanoantennas. An alternative to plasmonic structures, all-dielectric nanoantenna based on silicon nanogap is also demonstrated to enhance the fluorescence detection of single molecules diffusing in concentrated solutions.

Further, using resonant planar "antenna-in-box" devices we investigate the diffusion dynamics of phosphoethanolamine and sphingomyelin on the plasma membrane of living cells and discuss the results in the context of *lipid rafts*. Together with cholesterol depletion experiments, we provide evidence of cholesterol-induced nanodomain partitioning within less than 10 nm diameters and characteristic times being $\sim$100 μs.

Keywords: optical nanoantennas, fluorescence correlation spectroscopy (FCS), single-molecule detection, living cells

Résumé en français

La spectroscopic de fluorescence de molécule individuelle a révolutionné le domaine des sciences biophysiques, en permettant la visualisation des interactions moléculaires dynamiques et des caractéristiques nanoscopiques avec une haute résolution spatio-temporelle. Le contrôle des réactions enzymatiques et l'étude de la dynamique de diffusion de molécules individuelles (à titre d'exemple, des lipides et protéines) permet de comprendre l'influence et le contrôle de ces entités nanoscopiques sur plusieurs processus biophysiques, en incluant l'adhésion cellulaire, la transduction du signal et l'immunologie.

La nanophotonique basée sur la plasmoniques offre des nouvelles opportunités de suivi d'évènements à molécule unique, puisque il est possible de confiner des champs électroma-g nétiques dans les hotspots à nano échelle, à dimensions spatiales comparables à une molécule unique (<10 nm).

Dans ce projet de thèse, nous explorons plusieurs plateformes de nano antennas photoniques (notamment des nano ouvertures doubles, des nanogap-antennas et des "antenna-in-box" planaires) avec des hotspots ultra-confinés, et nous avons démontré les applications dans l'amélioration de la spectroscopic de fluorescence de molécule individuelle. En utilisant la *fluorescence burst analysis*, l'analyse de fluctuations temporelle de fluorescence, *time-correlated measurements* et des simulations de champ proche, nous quantifions les facteurs d'amélioration de fluorescence, les volumes de détection de nanoantennas; ainsi, nous discutons l'accélération de fluorescence photo dynamique. En alternative aux structures plasmoniques, des antennes diélectriques basées sur les dimères en silicone sont aussi démontrées d'améliorer la détection de fluorescence à molécule unique, pour des concentrations micro molaires physiologiquement pertinentes.

En outre, nous explorons des systèmes planaires "antenna-in-box" pour l'investigation de la dynamique de diffusion de la phosphoéthanolamine et de la sphingomyéline dans les membranes des cellules vivantes. Avec des expériences de déplétion de cholestérol, nous démonstrons le cloisonnement des membranes plasmatiques induits par cholestérol, et nous discutons les résultats dans le contexte des radeaux lipidiques.

Mots clés: nanoantennas optiques, spectroscopicde corrélation de fluorescence, détection de molécule unique, cellules vivantes

Resumen en español

La espectroscopía de fluorescencia de una sola molécula ha revolucionado el campo de las ciencias biofísicas, permitiendo la visulización de interacciones moleculares dinámicas y características nanoscópicas con alta resolución espaciotemporal. La monitorización de las reacciones enzimáticas y el análisis de la dinámica de difusión de moléculas individuales (como lípidos y proteínas) nos ayudan a comprender cómo estas entidades nanoscópicas influyen y controlan diversos procesos bioquímicos.

Las antenas nanofotónicas pueden localizar eficientemente la radiación electromagnética en dimensiones espaciales en nanoescala, comparables a biomoléculas únicas (<10 nm). Estos "hotspots" de iluminación ultra configurados ofrecen de este modo la oportunidad de monitorizar eventos de molécula única a niveles de expresión fisiológica.

En esta tesis, exploramos varias plataformas fotónicas de nanoantenas (*double nanohole aperture*, dímero *nanogap* antenas y "antenna-in-box" planares) y demostramos su aplicación en la mejora de la detección una sola molécula de fluorescencia. Utilizando el análisis por explosión de fluorescencia, espectroscopia de correlación de fluorescencia (FCS), medidas TCSPC correlacionadas en el tiempo y simulaciones de campo cercano, cuantificamos volúmenes de detección de nanoantenas, factores de mejora de fluorescencia y discutimos las aceleraciones fotodinámicas de fluorescencia mediada por nanoantennas ópticas. Las nanoantennas dieléctricas basadas en "nanogaps" de silico se han propuesto como una alternativa en el realce de la detectión de fluorescencia de difusión de moléculas únicas en soluciones concentradas.

Además, utilizando dispositivos resonantes planares de "antenna-in-box", investigamos la dinámica de difusión de la fosfoetanolamina y la esfingomielina en la membrana plasmática de las células vivas y discutimos los resultados en el contexto de las balsas lipídicas. Junto con experimentos de disminción de colesterol, proporcionamos pruebas de división inducida por colesterol en el nanodominio dentro de diámetros menors de 10 nm y con tiempos característicos de ∼100 microsegundos.

Palabras clave: nanoantennas ópticas, espectroscopía de correlación de fluorescencia (FCS), detección de moléculas únicas, células vivas

Contents

List of Figures

List of Tables

Abbreviations

Acronym	What (it) Stands For
ACF	Auto correlation function
CHO	Chinese hamster ovary
CV	Crystal Violet
DNA	Deoxyribonucleic acid
DNH	Double nanohole
DOPC	1,2-dioleoyl-sn-glycerol-3-phosphocholine
FCS	Fluorescence correlation spectroscopy
FDTD	Finite difference time domain
FIB	Focused ion beam
GPI	Glycosylphosphatidylinositol
LDOS	Local density of optical states
MCD	Methyl-β-cyclodextrin
MV	Methylviologen
NSOM	Near field scanning optical microscopy
PE	Phosphoethanolamine
SEM	Scanning electron microscopy
SM	Shingomyelin
SNR	Signal-to-noise ratio
SPR	Surface plasmon resonance
STED	Stimulated emission depletion microscopy
TCSPC	Time correlated single photon counting
TIRF	Total internal reflection fluorescence microscopy
ZMW	Zero mode waveguides

Introduction

Single-molecule detection techniques have revolutionized biophysical sciences by enabling the study of dynamic processes on living systems at the molecular level [1]. Understanding how bio-molecules interact with each other at the single molecule level helps us understand their influence in various biological processes such as signaling and immunology [2]. After the first optical detection of single-molecules by Moerner [3] and Orrit [4, 5] in the early 90's, the field has seen tremendous development with major readout approach being the fluorescence signal. However, the size mismatch between a single molecule (below 5 nm) and wavelength of the visible light (400-800 nm), has been a major limiting factor for efficient detection of single molecules. The fundamental phenomenon of diffraction [6], limits the interaction between the propagating optical field and an individual emitter, resulting in low fluorescence signal and large statistical noise.

Transient interactions between proteins, nucleic acids and enzymes typically occur at micromolar concentrations [7, 8]. However, diffraction-limited confocal techniques are restricted to concentrations in the pico to nanomolar range in order to isolate a single-molecule within the femtoliter confocal detection volumes [9]. To observe a large class of enzymes and proteins interactions with single-molecule resolution at physiologically relevant conditions, the optical detection volume must be reduced by more than three orders of magnitude as compared to the confocal configuration [10].

Photonic nanoantennas realize a new paradigm to localize electromagnetic energy into nanoscale spatial dimensions [11, 12], enhance the luminescence of quantum emitters [13] and even trap single proteins [14]. To overcome the diffraction limit, nanoantenna designs take advantage of sharp curvature radii, nanoscale gaps and plasmonic resonances, using metal nanoparticles [15, 16], nanorods [17, 18], bowtie antennas [19] or dimer gap antennas [20, 21, 22]. The enhanced electric field in the nanoscale probe areas yield a high signal to noise ratio ultimately making it possible to follow single-molecule events at physiological expression levels. The enhanced detection of single fluorescent molecules in concentrated solutions is a major and emerging field of application for optical nanoantennas [8, 23].

This dissertation has two major goals: (i) design and optimization of photonics nanoantenna platforms for enhanced single-molecule fluorescence detection at biologically relevant micromolar concentrations, and (ii) application of these ultra-confined electromagnetic hotspots to investigate the nanoscopic organization of lipids in the plasma

membrane of living cells.

The thesis starts with a summary on the recent advances in the nanoantenna based single-molecule fluorescence techniques in Chapter 1. The experimental methods, fluorescence correlation spectroscopy and time-correlated single-photon counting technique are detailed in Chapter 2. In addition, this thesis has four other main chapters and are organized as following:

Chapter 3

In this chapter, we explore the double nanohole (DNH) design for enhanced single-molecule fluorescence detection by exploiting the localized electric fields within the nanoscale apex region. Using FCS and TCSPC, we quantify the fluorescence enhancement factors, nanoscale detection volumes and discuss the photokinetics decay mechanism of the molecules diffusing through the DNH apex. A relatively simple antenna geometry: two connected circular nanoapertures with a apex region, DNH is fabricated by FIB milling. Using a 25 nm nominal apex size DNH, we report fluorescence enhancement factors above 100-fold, steaming from confined detection volumes ($\sim$70 zL), together with 30-fold LDOS enhancement and single-molecule sensitivity at concentrations exceeding 20 μM.

Chapter 4

All-dielectric optical nanoantennas are presented as a potential alternative to their plasmonic counterparts. Arrays of all-silicon nanogap antennas with 20 nm nominal gap separations are fabricated on a glass substrate. Using burst analysis, fluorescence correlation spectroscopy and TCSPC measurements, we report fluorescence enhancement up to 270-fold within a 140 zL detection volume, together with 15-fold LDOS enhancement for single molecules diffusion through the nanogap region. Detailed comparison with the gold dimer nanoantenna in similar experimental conditions is also presented.

Chapter 5

This chapter focuses on planar nanoantenna optimized for full hotspot accessibility and extremely planar surface topology. Combining electron beam lithography with planarization, etch back and template stripping, we present a large set of flat gold nanoantenna arrays, featuring sharp edges and direct surface accessibility of the electromagnetic hotspots. Using 10 nm nominal gap antenna, we quantify giant fluorescence enhancement factors (above 15,000-fold) within confined detection volumes in the 20 zL range, together with 100-fold LDOS enhancement when compared to diffraction-limited confocal scheme.

Chapter 6

In this chapter, we exploit the planarity of in-plane "antenna-in-box" devices to assess the dynamic nanoscale organization of the plasma membranes in living Chinese hamster ovary cells. Using the planar nanoantenna design, we investigate diffusion dynamics in membrane regions as small as 10 nm with sub-ms temporal resolution. Our results show the existence of dynamic nanodomains on the plasma membranes of living cells with characteristic domain sizes less than 10 nm diameter and transient trapping times as short as 100 μs.

This PhD dissertation has been completed within the framework of Europhotonics doctorate program funded by the European Union (Grant 159224-1-2009-1-FR-ERA MUNDUS-EMJD). All research activites were carried out within the Institut Fresnel (Marseille, France) and ICFO (Barcelona, Spain) under an international co-tutelle agreement constituting to a dual doctorate award: Doctor of Science in Physics from the AMU, Marseille, France and Doctorate in Photonics Engineering, Nanophotonics and Biophotonics from the UPC, Barcelona, Spain. All external collaborations are mentioned in the appropriate Chapters to follow.

Chapter 1

Optical nanoantennas for sub-diffraction photonics

1.1 Single-molecule fluorescence spectroscopy

Dynamic bio-molecular interactions such as, protein folding or polymerization and enzymatic interactions are best studied at the single-molecule level. The development of modern optics and the selectivity offered by the fluorescence probes have significantly advanced the biological sciences with applications ranging from super-resolution optical microscopy to monitoring real-time DNA sequencing [24, 25]. Single-molecule fluorescence spectroscopy offers a powerful platform to observe how single molecules work and interact in a physiological environment. This eventually helps to understand the mechanisms that drive and control the functions (such as cell adhesion, signaling pathways and immunology) of living systems at the molecular level [10].

Over the last two decades, enormous progress has been made in the optical detection of single molecules. However, efficient detection of single molecules still remains a major challenge. The main bottleneck being the minimum attainable spatial resolution due to the fundamental phenomenon of light diffraction [6]. In diffraction-limited optics, the size mismatch between a single molecule (usually below 5 nm) and typically few hundreds of nm for visible light spectrum, limits the efficient interaction between the propagating light field and an individual emitter. Thereby, the direct consequences being low fluorescence signals and ensemble averaging [26].

Moreover, diffraction limited optical microscopes generate detection volumes on the order of $\sim$0.5 fL which impose nanomolar concentrations of the molecular species in order to isolate a single molecule within the detection volume. However, the low molecular

density condition does not meet the requirement of a large majority of enzymes and proteins which call for concentrations in the micromolar range to reach relevant reaction kinetics and biochemical stability. Figure 1.1 displays the histogram of Michaelis constant (the substrate concentration such that the reaction rate is half the maximum achievable rate) for 118,000 enzymes taken from the Brenda database and shows that the biological binding constants are usually in the micro to millimolar range [7, 27].

As we progress into this dissertation, we will demonstrate different nanophotonics approaches to achieve extreme light confinement and discuss the concentration limit allowed in each case for single-molecule resolution. The enhanced electric field in the nanoscale probe area yields a sub-diffraction spatial resolution ultimately making it possible to follow the single molecule events at very high fluorophore concentrations.

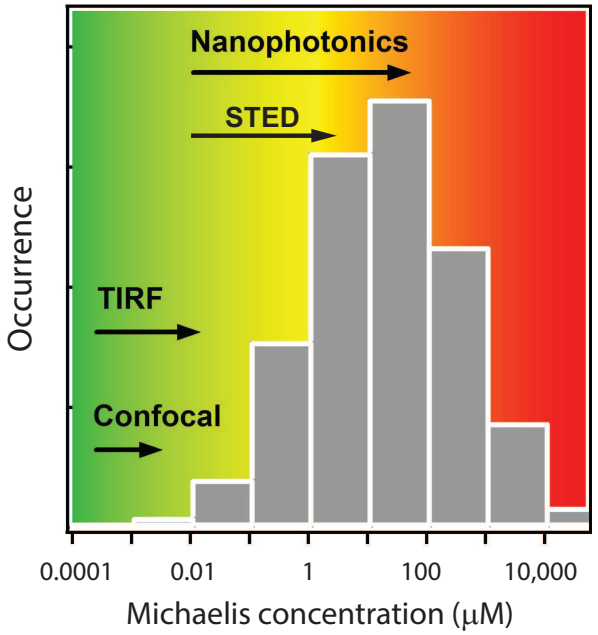

FIGURE 1.1: **Histogram of Michaelis constant.** Histogram of Michaelis constant for 118,000 enzymes taken from the Brenda database (http://www.brenda-enzymes.org/). The arrows indicate the concentration regime reached by different techniques. TIRF stands for total internal reflection fluorescence microscopy, and STED stands for stimulated emission depletion microscopy.

1.2 Advances in single-molecule detection techniques

Single-molecule techniques are designed either by optically shaping the excitation beam profile (as in STED and SPIM) or by exploiting the plasmon resonance of metallic nanoparticles to locally tailor the excitation/emission profiles of the nearby molecule.

We start with a brief summary of well established single-molecule fluorescence techniques and then will focus discussion on nanoantenna enhanced florescence detection.

Near field scanning optical microscope (NSOM)

After Moerner demonstrated the detection of single molecules in solid phase at the cryogenic temperatures [3], Betzig in 1992 obtained the first super-resolution image of a biological sample (at room temperature) using the near field scanning optical microscopy (NSOM) [28, 29]. This technique is based on sub-wavelength apertures which are scanned across the sample surface at a distance of few nanometers to acquire super-resolution mapping. Usually a nanoaperture at the apex of a metallic tip is used to constrain the light in both lateral and axial dimensions and the resolution in NSOM relies mainly on the physical size of the aperture (rather than the illumination wavelength itself) and the tip-sample separation distance. The main application of NSOM has been to investigate the nanoscale organization of membrane proteins in living intact cells [30]. In addition, NSOM has been successfully demonstrated to monitor rotational and translational diffusion of single molecules [10, 31].

In recent years, improved illuminations schemes based on monopole nanoantennas engineered on bowtie nanoaperture at the apex NSOM probe have been demonstrated for simultaneous dual-color single-molecule imaging with spatial resolution down to 20 nm. This design provides extreme confinement of light along with high photon counts per molecule proving background-free nanolight source for live cell research at biologically-relevant high concentrations [32].

Total internal reflection fluorescence microscopy (TIRF)

TIRF is another class of near field microscope which restricts the excitation and detection of fluorophores within immediate interface between the sample and the substrate. TIRF microscopes circumvent the diffraction barrier by exploiting the properties of evanescent fields created by internally reflecting light at the interface between two media with different refractive indices [33]. TIRF inherently selects the surface-bound molecules, and thus is capable of resolving features as close as 100 nm near the surface. Together with FCS, TIRF microscopes have been used to investigate membrane dynamics with high temporal and spatial resolution. In particular, TIRF-FCS has been demonstrated to investigate the binding and release of single molecules with enhanced counts per molecule and a high signal-to-background ratio as compared to conventional confocal microscopes [34].

Stimulated emission depletion microscopy (STED)

STED microscopy is a powerful far-field optical technique with spatial resolution down to ∼40 nm. The resolution enhancement in STED is based on switching off the fluorophores in the outer periphery of the diffraction-limited excitation spot by stimulated emission using intense laser source [35]. The STED microscope has a pair of synchronized laser pulses: first pulse to excite the fluorescence dye with an ordinary diffraction-limited focus; and second (also called depletion pulse) is immediately followed after the excitation pulse. The depletion pulse is red-shifted in frequency compared to the emission spectrum of the fluorophore molecule and thereby quenches the fluorescence from molecules at the periphery of the excitation focal point *via* stimulated emission [36].

Further improvement in the STED resolution has been achieved by time gating the detected signals (gated-STED). Together with FCS, dynamic observation of complex molecular interaction have been realized with STED and importantly at near-physiological conditions. Apart from STED microscopy, techniques such as PALM and STORM, have also demonstrated nanoscopy spatial resolution. But the limited temporal resolution in such localization based techniques have restricted applications in studying single-molecule dynamics. In addition, selective plane illumination microscopy (SPIM) has also been widely used for high-throughput fluorescence imaging. As the illumination is restricted to a single plane within the sample, this technique significantly reduces the background signal enabling high-resolution and high-throughput imaging [37]. Together with FCS, light-sheet microscopy based SPIM-FCS has been used as a quantitative bio-imaging tool to study the dynamics of bio-molecular interactions in living cells [38, 39].

Figure 1.2 summarizes the different methods of achieving spatial confinement in optical microscopy. As shown in Figure 1.2a, single-molecule fluorescence microscopy techniques are improved by confining light at the nanoscale. This confinement of excitation light will eventually lead to significant reduction in the background fluorescence. The light confinement is mainly achieved either by shaping the illumination beam profiles as in STED (b), and light sheet microscopy (b), or by physical confinement as in wide-field techniques (d) to study micron-size bacterial cells. Additionally, surface bound-illumination confinement as in TIRF (e), and the extreme field confinement through plasmonic interactions at the nanoscale (f) have been widely used in fluorescence microscopy to study molecular dynamics much below the diffraction limit of light.

Although all of these techniques have been successful in direct visualization of molecular interactions in very diluted sample concentrations or in fixed cells, the live cell

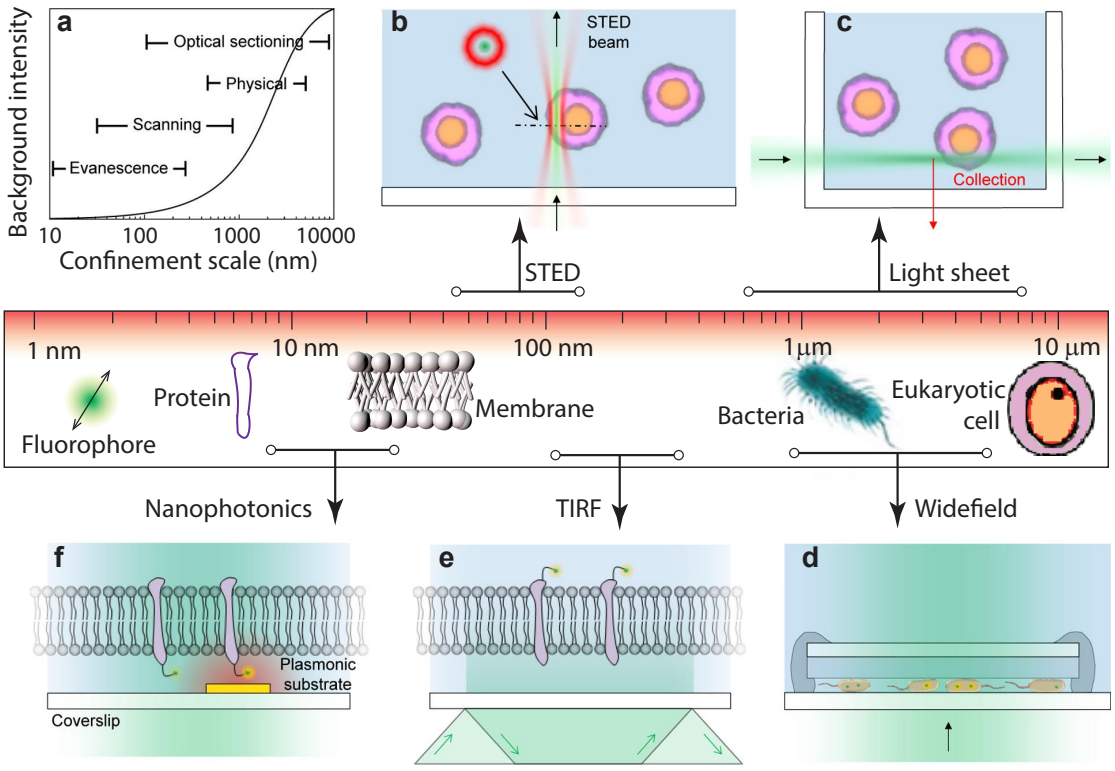

FIGURE 1.2: **Bridging optical microscopy and sub-cellular biophysics by various confinement methods.** (a) Relative reduction in background signal for a high numerical aperture objective lens as a function of axial confinement. (b-f) Various modes of confinement and their relative scales. The main strategies for volume confinement in fluorescence microscopy being: excitation confinement by laser illumination with beam shaping; physical confinement by micron-scale geometries; and nanoscale confinement by nanophotonics. Figure adapted from [26].

research has been always a major concern. Nanophotonics provides a rather straightforward, yet powerful platform for enhanced single-molecule fluorescence detection and nanospectroscopy in living cells.

1.3 Controlling light with optical nanoantennas

As discussed in earlier Section 1.2, to observe a large class of enzymes and proteins at physiologically relevant conditions with single-molecule resolution, the optical detection volume must be reduced by more than three orders of magnitude as compared to the confocal volumes. This can be achieved by exploiting the unique optical properties of metallic nanostructures that support local surface plasmon modes, and has led to the concept of optical nanoantenna.

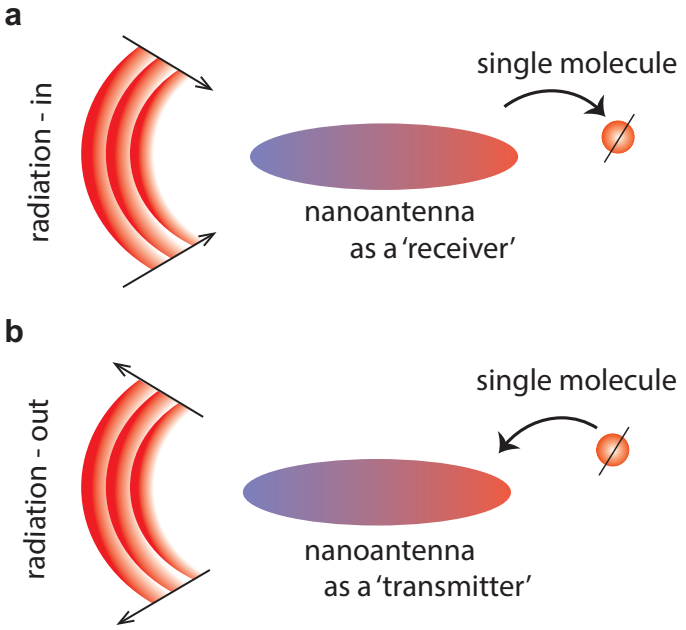

FIGURE 1.3: **Optical nanoantenna: Controlling light at the nanoscale.** Photonic nanoantennas reversibly convert freely propagating optical radiations into localized energy and tailor light-matter interaction at the nanoscale. An atom or a molecule interacts with optical radiation *via* an optical nanoantenna: (a) receiving and (b) transmitting nanoantenna configurations. Arrows indicate the direction of energy flow. In spectroscopy and microscopy, the two antenna concepts are combined; *i.e.*, the nanoantenna is used both as a receiver and as a transmitter. Figure adapted from [11].

Optical nanoantennas, like their radio and microwave counterparts, convert propagating radiation into localized energy and enable interactions between light and single quantum emitters. However, the translation of the radio and microwave antenna concept into the optical frequency regime is not straightforward, primarily because of the nanometric spatial scales required (and the fabrication challenges) in order to cover the visible spectrum of the light (400-800 nm). Due to the fundamental phenomenon of diffraction of light, the minimum confinement (of the propagating optical fields) possible with tradition optics is limited roughly to half a wavelength. In recent years, the significant advancement in the field of nanotechnology providing control and manipulation of materials at the nanometric scales has resulted in significant research interest in optical nanoantenna with achievable spatial dimensions being well below the diffraction limit of light. As optical nanoantennas can efficiently confine electromagnetic radiations into localized hotspots, they have been widely used to improve the spatial resolution in optical microscopy and spectroscopy. These confined volumes are much smaller than those achieved with conventional focusing or objective lenses [11]. However, before being able to comment/interpret the photo-physical properties and dynamics of single molecule in nanoantenna-enhanced experiments at high molecular concentrations (usually micromolar regime), quantifying

the fluorescence enhancement factors and understanding the mechanism behind it is crucial. Hereafter we briefly discuss the origin of fluorescence enhancement in the vicinity of the nanostructures and the photo kinetics decay mechanisms involved.

Figure 1.3 illustrates the general concept of optical nanoantenna, in which a local source (usually a molecule or an atom) interacts with the optical radiation *via* either a receiving (a) or a transmitting (b) nanoantenna. The nanoscale interactions between the single emitter and the optical radiation field take advantage of the plasmonic properties of metallic nanostrucures leading to particular surface plasmon resonances modes. In general, optical nanoantennas take form of sharp edges on metallic particles and nanometric gaps between the particles, and their properties being strongly dependent upon the shapes, sizes and the material compositions. The near field coupling between an emitter and the optical radiation in the presence of an optical nanoantenna is mainly influenced by (i) the near field enhancement, and (ii) the accelerated decay rates.

In addition to the surface plasmon resonance effect, the local electric field around the emitter is also modified *via* lightning rod effect. The sharp curvatures (or tips) of metal surface leads to an increase in surface charge density. As the near field is directly proportional to the surface charge density, this ultimately results in enhanced local electric fields. Further, a nanoantenna can locally enhance the electric field by increasing the absorption rate at the emitter's position. Thus, the strength of the near field enhancement mainly depends upon the emitter's position, orientation with respect to the nanoantenna dipole and also on the resonance mode of the nanoantenna. These effects combined result in amplified photon counts rates for a fluorescent emitter placed in the vicinity of the nanoantenna.

To characterize the fluorescence photokinetics enhancement induced by the nanoantenna, let us model the electronic states involved in the fluorescence emission with a simple three-level system as shown in Figure 1.4. S_0 and S_1 are the ground state and the first excited electronic states respectively. If we denote the excitation intensity by I_{exc}, and the excitation cross section by σ, then the excitation rate is given by $\Gamma_{\text{exc}} = \sigma I_{\text{exc}}$. Following the absorption of incident photons, the electrons are promoted to an excited state (higher energy level S_1 or higher) from the ground state S_0. The excited states gets depopulated via radiative or non radiative emission to the stable ground state.

The rate constants for all possible pathways as: radiative emission (Γ_{rad}), and non radiative de-excitation pathways such as internal conversion (Γ_{ic}), intersystem crossing (Γ_{isc}) and triplet state de-excitation (Γ_{ph}) are shown in Figure 1.4. The total de-excitation rate from the excited singlet state S_1 to the ground state S_0 is $\tau = \frac{1}{\Gamma_{rad} + \sum \Gamma_{nr}} = \frac{1}{\Gamma_{\text{tot}}}$, where τ is called the excited state lifetime.

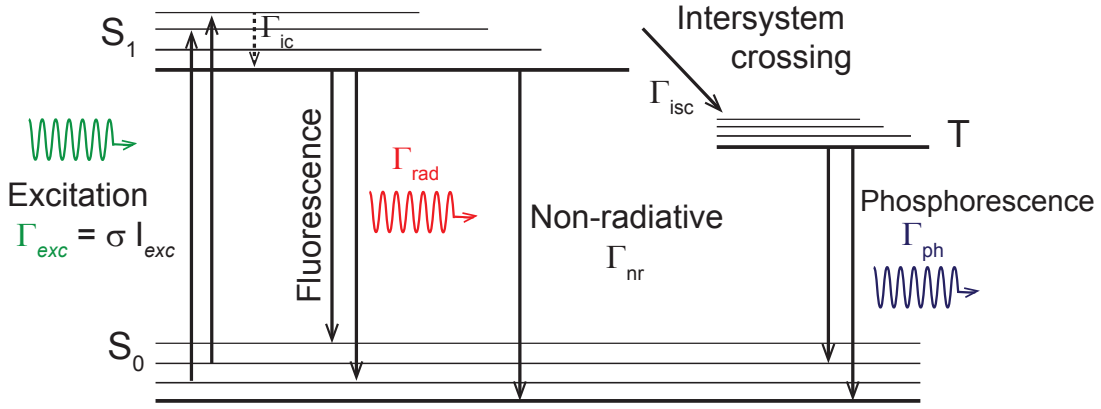

FIGURE 1.4: **Jablonski diagram describing the molecular transition rates.** The excited states gets depopulated *via* radiative or non radiative emission. Fluorescence lifetime is the average time a fluorophore remains in the excited state following the excitation.

The local environment around an emitter largely influences the spontaneous emission rate, and therefore modifies the lifetime of the excited state transition to the ground state. The change in this lifetime is critically influenced by the radiative decay routes (causing a photon emission), and by the non-radiative decay mechanism (such as energy dissipation into the local environment) [40].

The intrinsic quantum yield of an emitter in homogenous medium is defined as: $\phi = \frac{\Gamma_{rad}}{\Gamma_{rad}+\Gamma_{nr}}$, where Γ_{rad} is the radiative decay rate and Γ_{nr} is the non-radiative rate.

The presence of a nanostructure modifies the quantum yield as: $\phi^* = \frac{\Gamma^*_{rad}}{\Gamma^*_{tot}} = \frac{\Gamma^*_{rad}}{\Gamma^*_{rad}+\Gamma_{nr}+\Gamma^*_{loss}}$. In addition to the modified radiative rate, the presence of nanostructure introduces an extra decay route, *i.e* Γ^*_{loss} due to the metallic losses .

Following the Fermi's Golden rule, the transition probability (also called decay probability) per unit time from the initial state $|i\rangle$ to a set of final states $|f\rangle$ is given by [41]:

$$\Gamma_{i\to f} = \frac{2\pi}{\hbar} |M_{\text{if}}|^2 \rho(\omega)$$

where M_{if} is the transition matrix element between the molecular states, and $\rho(\omega)$ denotes the local density of optical states (LDOS). In absence of an incident field, and without any preferred dipole orientation, the transition matrix element in free space (averaged over all direction) is given by: $|M_{\text{if}}|^2 = |\text{p}|^2 \hbar\omega/6\epsilon_o$, where $\text{p} = \text{-}\ e\langle i|r|f\rangle$ represents the dipole moment associated with the electronic transition. Local density of optical states (LDOS) in free space is given by: $\rho(\omega) = \omega^2/\pi^2 c^3$

As we discussed, the presence of a nanostructure significantly modifies the LDOS by changing the radiative rate and by adding an extra route of de-excitation *via* losses. If the plasmon resonance of the nanoantenna has significant spectral overlap with the emission frequency of the emitter, the LDOS depends upon the excitation probability of the plasmonic resonance (λ_{res}), and thus the ratio of radiative rate of the emitter in the presence of nanoantenna (Γ^*_{rad}) and the same without a nanoantenna (Γ_{rad}) takes the form of [42]:

$$\frac{\Gamma^*_{rad}}{\Gamma_{rad}} = \frac{3}{4\pi^2}\left[\frac{\lambda_{\text{res}}\, L}{n^3\, V}\right]$$

where L represent the quality factor, V being the mode volume and n is the refractive index of the medium. Moreover, in order to achieve strong modification in the spontaneous emission rate with minimum perturbation in the non radiative rates, the following criterion must be met while designing the nanoantenna:

- tailored antenna geometry to have plasmon resonance in the region where dissipation losses are minimum and ensuring higher order plasmon modes are separated from the dipolar one,
- elongated plasmonic structures (such as rod-geometry) are preferred over spherical particles in-order to benefit from strong near field enhancement at the sharp tips,
- adjusting the orientation of the emitter with respect to the electric dipole moment of the nanoantenna, and
- choosing the antenna's mode volume such that the radiation is stronger than the absorption.

Further, if k be the light collection efficiency of the system and $\phi = \frac{\Gamma_{rad}}{\Gamma_{rad}+\sum\Gamma_{nr}} = \frac{\Gamma_{rad}}{\Gamma_{\text{tot}}}$ describes the quantum yield of the dye, then under steady state excitation, the detected count rate per molecule is given by [43]:

$$Q = \frac{k\phi\sigma I_{\text{exc}}}{1 + I_{\text{exc}}/I_{\text{sat}}} \tag{1.1}$$

where, I_{sat} denotes the saturation intensity and is given by $\frac{\Gamma_{\text{tot}}}{\sigma\left(1+\Gamma_{\text{isc}}/\Gamma_{\text{ph}}\right)}$

At low excitation regime, the detected count rate is proportional to the collection efficiency and the quantum yield and has linear dependence with the excitation intensity. Thus the Equation 1.1 further simplifies to:

$$\text{Q} = k\phi\sigma I_{\text{exc}} \qquad [I_{\text{exc}} << I_{\text{sat}}]$$

However, at excitation power exceeding the saturation intensity, the fluorescence count rate does not scale linearly with the excitation intensity, but depends only on the radiative rate and the collection efficiency, which is represented as:

$$\mathrm{Q} = k\phi\sigma I_{\mathrm{sat}} \qquad [I_{\mathrm{exc}} >> I_{\mathrm{sat}}]$$

Higher excitation intensity is not favored in the field of fluorescence microscopy and spectroscopy as bio-molecules, cells and tissues are extremely sensitive to the environment we expose them to. Throughout this thesis, we work in the regime where excitation intensity is well below the saturation level of the dyes. As the experiments are performed with molecules diffusing in solution, it is safe to assume that the fluorophore's absorption cross section is unchanged with the presence of nanoantennas.

Finally, the fluorescence enhancement factor is estimated as:

$$\begin{aligned}\text{fluorescence enhancement } (\eta_{\mathrm{F}}) &= \frac{\text{brightness per molecule with nanoantenna } (Q^*)}{\text{brightness per molecule in open solution } (Q_{\mathrm{conf}})} \\ &= \frac{k^*}{k}\frac{\phi^*}{\phi}\frac{I^*_{\mathrm{exc}}}{I_{\mathrm{exc}}} \\ &= \eta_k\,\eta_\phi\,\eta_{I_{\mathrm{exc}}}\end{aligned}$$

Thus in the regime below saturation, the gain in fluorescence signal in proximity of the nanoantenna is mainly due to the:

- highly directive emission which increases the collection efficiency of the system,
- increased quantum yield of the emitter, and
- enhanced local field contributing to the high excitation efficiency.

All these three factors can be independently or collectively tuned by proper choice of nanoantenna structure or fluorescent dye. And an increase in any of these quantities will contribute to an enhanced fluorescence count rate. For optimal enhancement in fluorescence signal, along with the local excitation enhancement, it is also necessary to have enhancement in the quantum yield of the dye. Therefore, high enhancement factors can be expected with dyes having low quantum yields. Designing a nanoantenna whose resonance overlaps both the excitation and emission wavelength results in very high photon count rates.

1.4 Emerging nanostructures and biophotonic applications

After the discussion on optical nanoatenna concept and design rule optimization, in this section we summarize various nanophotonics strategies designed to isolate a single-molecule from a crowded background molecules present within the diffraction-limited detection volume. Various nanoantenna geometries and their applications in the context of enhanced florescence spectroscopy will be discussed.

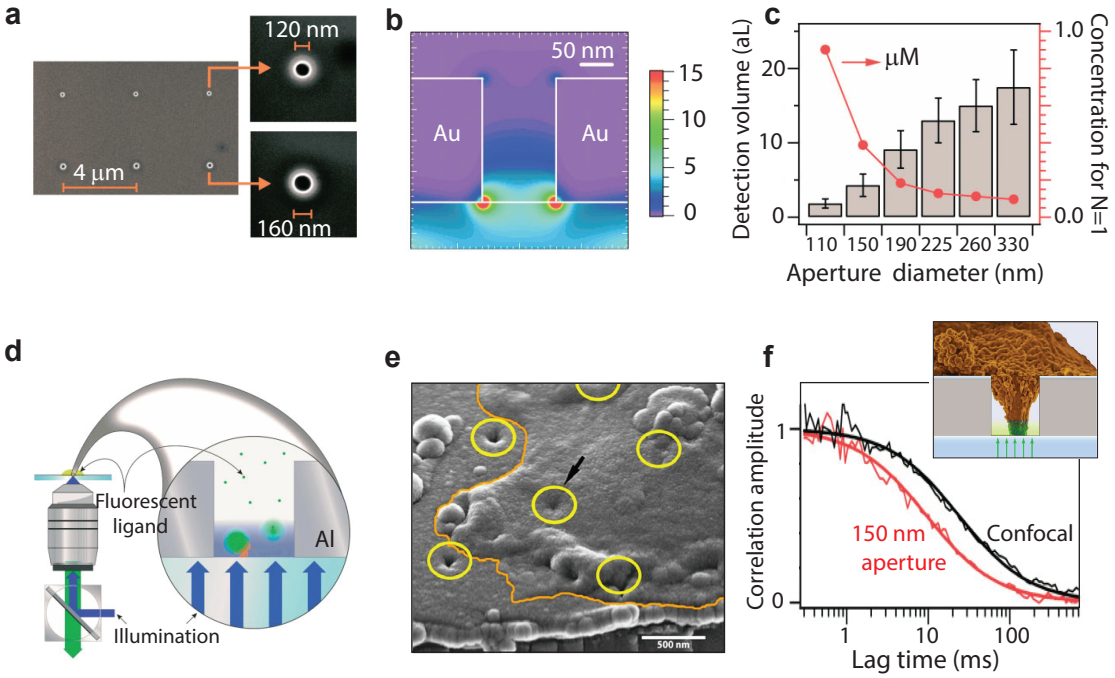

FIGURE 1.5: **Zero-mode waveguides for enhanced fluorescence detection.** (a) Scanning electron microscope image of circular nanoapertures milled in gold films. (b) Near field intensity distribution on a 120 nm diameter gold aperture with 633 nm excitation wavelength [48]. (c) Observation volume measured as the function of aperture diameter. The right axis shows the concentration required for single-molecule sensitivity [50]. (d) Nanoaperture enhanced single-molecule enzymology [47]. (e) Scanning electron microscope image (tilted view) of cross-sectional cuts of the nanoapertures. Cell membranes are outlined by the orange line and aperture locations have been circled in yellow. Cell membrane spanning a nanoaperture dips down (black arrow), indicating membrane invagination [52]. (f) Normalized correlation functions obtained for the FL-GM1 ganglioside lipid analog, demonstrating a significant reduction of the diffusion time within the 150 nm nanoaperture [52, 53]. The inset cartoon depicts the cell invaginating into a subwavelength aperture.

The efficient control, visualization and manipulation of optical fields at the nanoscale provides various opportunities with board applications ranging from biosensing, photovoltaics to single-molecule spectroscopy, and investigating membrane dynamics in living cells [44, 45, 46]. The scientific field of nanophotonic enhanced fluorescence was pioneered in 2003 by the groups of Harold Craighead and Watt Webb by using a single nanometric

aperture milled in an opaque metallic film to confine light below the diffraction limit [47]. These nanometric apertures can be easily fabricated in Au- or Al-films using FIB, which uses a focused beam of ions (usually gallium ion) to create desired nanoscale features by etching/ablating surfaces. Figure 1.5a shows SEM image displaying arrays of nanoholes milled in gold films with increasing diameters. As the aperture diameter is below half of the optical wavelength, the light does not propagate though the aperture and evanescently decays within a few tens of nanometer inside the nanoaperture (see near field simulation in Figure 1.5b), which are therefore called as zero-mode waveguides (ZMW). The near field intensity distribution shown in (b) considers a 120 nm water-filled gold aperture illuminated at 633 nm [48]. The nanoaperture acts as pinhole in the sample plane as thus provides detection volume in the attoliter (10^{-18} L) range which is around three-orders of magnitude smaller than the diffraction-limited confocal detection volume [50, 51]. This confined detection volume allows molecular concentration in $\sim$1 μM range for single-molecule isolation (see Figure 1.5c).

Levene *et al* have demonstrated arrays of ZMW with single molecule sensitivity at micromolar concentration for enhanced single-molecule enzymology application (see sketch in Figure 1.5d). Using nanoapertures with 43 nm diameters, DNA polymerase was monitored at 10 μM concentration [47]. These simple-to-fabricate apertures have also been demonstrated to monitor real-time single molecule DNA sequencing [25], and to investigate sub-diffraction membrane dynamics in living cells [52, 53]. Figure 1.5e shows cell membrane spanning over arrays of nanoaperture. The dip down (black arrow) indicates membrane invagination into the nanoapertures. The reduced illumination area with ZMW was then used to study the diffusion dynamics of membrane lipids (Figure 1.5f). The inset in f shows the cell invaginating into a subwavelength aperture as seen in SEM image in Figure 1.5e.

However, the fluorescence enhancement factors in ZMW's remain weak due to the lack of intense field localization and also the fluorescence quenching becomes dominant for aperture with diameters less then 100 nm, resulting to near unity signal-to-noise ratio [54, 55]. Plasmonic nanostructures with sharp tips sustain high local electromagnetic intensities stemming from a combination of lightning rod effect, local surface plasmon resonance and coupling between single emitters.

Figure 1.6 summarizes the applications of gold-nanorod structure for achieving higher field localization along with high signal-to-noise ratio [13, 18, 56, 57]. Using these simple nanorod structures (length $\sim$50 nm and width $\sim$25 nm), enhancement factors over 1000-fold were reported for an emitter with low quantum yield (CV molecules with 2 % quantum yield). Figure 1.6a shows representative fluorescence time trace for CV molecules diffusing in solution and recorded with a gold nanorod (green) having SPR at

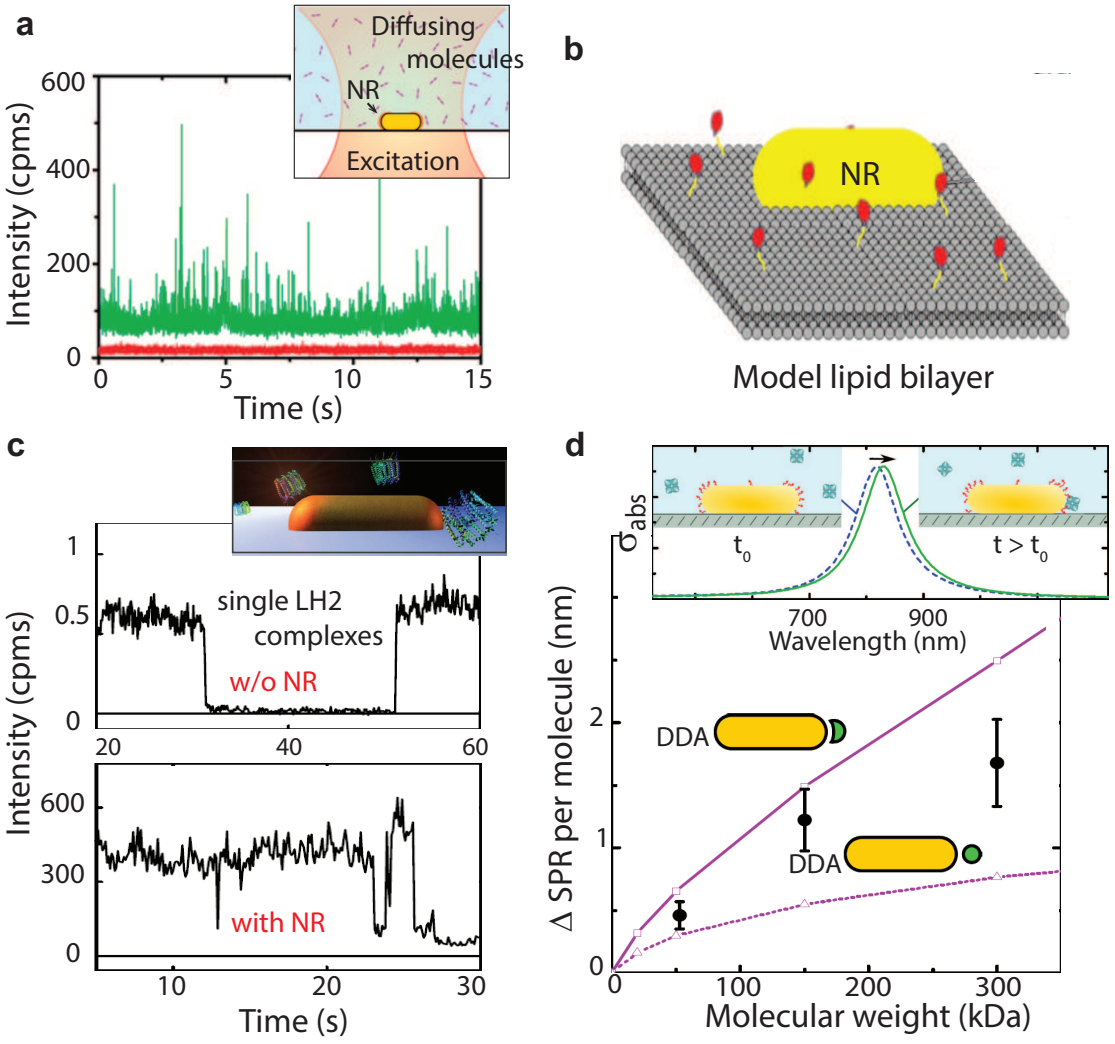

FIGURE 1.6: **Gold nanorods for fluorescence enhancement and single-molecule detection.** (a) Typical fluorescence time trace of CV molecules diffusing in a glycerol solution recorded with a gold nanorod (green) and the background fluorescence with no nanorod present (red) [18]. (b) Strategy for protein anchoring onto the model lipid bilayer for gold nanorod enhanced fluorescence experiments [56]. (c) A single gold nanorod interacting with a single light-harvesting complex yields strong fluorescence enhancement. The enhanced fluorescence brightness per molecule is then exploited to recorded the first photon antibunching of a single light-harvesting complex under ambient conditions [13]. (d) Gold nanorod for optical detection of single non-absorbing molecules. A single gold nanorod is functionalized with biotin and is introduced to an environment with the protein of interest. Binding of the analyte molecules to the receptors induces a redshift of the longitudinal SPR and is monitored at a single frequency using photothermal microscopy. The graph displays the magnitude of SPR change as a function of molecular weight of the protein. The solid lines represents the DDA calculations of the SPR red shift for purely refractive proteins, calculated for two different protein conformations on the surface of the gold nanorod [57].

629 nm and excited at 633 nm. The background signal without the nanorods (displayed in red) is flat around the zero intensity [18]. These nanorods were also demonstrated to enhanced FCS experiments with high quantum yield dyes in model lipid bilayers (sketched in Figure 1.6b). The enhanced FCS curves were computed after filtering the single-molecule burst events on the basis of their shortened lifetime in the presence of the nanorod. This strategy was shown to enhance the correlation contrast in FCS experiments by more than an order of magnitude [56].

Further, tuning the nanorod length in resonance with single light-harvesting complex 2 (LH2 with λ_{exc} = 800 nm; and λ_{exc} = 870 nm), Wientjes *et al* have recorded the first photon antibunching of a single light-harvesting complex under ambient conditions. Figure 1.6c shows the fluorescence time trace from single unenhanced LH2 complex (top), and the same from an enhanced LH2 complex (bottom). The on-off blinking to a near-zero background level confirms that the emission stems from a single complex. Fluorescence enhancement factors over 500-fold were reported using LH2 complex having ∼10 % intrinsic fluorescence quantum efficiency [13].

Apart from enhanced fluorescence experiments, gold nanorods have shown their potentials in detecting non-absorbing molecules based on the local changes in the refractive index producing a resonance shift. Figure 1.6d shows the experimental strategy with a single gold nanorod functionalized with biotin which is then introduced into an environment with the protein of interest. Binding of the analyte molecules to the receptors results a redshift of the longitudinal SPR which is monitored at a single frequency using photothermal microscopy [57]. Black dots in Figure 1.6d shows the magnitude of the biggest two steps in photothermal time traces (showing single-molecule binding events) as a function of molecular weight of the protein. Calculations based on Discrete-dipole approximation (DDA) of the SPR red shift for purely refractive proteins, calculated for two different protein conformations on the surface of the nanorod are displayed in solid lines. Gold nanorods can easily be mass produced using wet chemistry synthesis, and thus hold promise for many biologically-inspired experiments where analyte concentration can not be arbitrarily diluted.

In order to extend the applications of plasmonic nanoantennas, tuning the plasmon resonance of the nanostructure while simultaneously preserving the localized and enhanced near field is crucial. To this extent, nanoscale patch antenna concept has been put forward [58, 59]. Figure 1.7a shows the schematic of the plasmonic nanopatch antenna, consisting of a silver nanocube (colloidally synthesized with diameter 65-95 nm) dispersed over a 50 nm gold film and separated by a fluorophore-coated spacer layer with varying thickness from 5-15 nm. This sandwich configuration produces the sub-10 nm gaps and have been demonstrated to achieve high Purcell factors in plasmonic

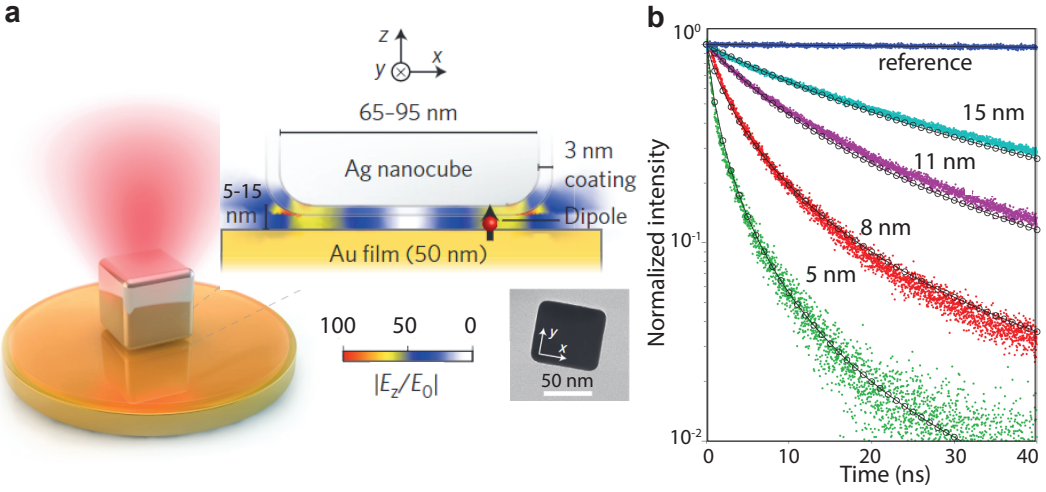

FIGURE 1.7: **Plasmonic nanopatch antenna for large Purcell enhancements.** (a) Schematic of a plasmonic nanopatch antenna: silver nanocube situated on a gold film separated by a 5-15 nm spacer layer containing a fluorescent material. Schematic cross-section of a film-coupled silver nanocube showing the simulated fundamental plasmonic gap mode showing that dominant component of the gap electric field is in the vertical (z) direction and is largest near the corners of the nanocube. Transmission electron microscopy image of a representative single silver nanocube is shown in bottom left of (a). The scale bar is 50 nm. (b) Measured and simulated time-resolved Ru dye emission for four gap thicknesses demonstrating the gap thickness dependence of spontaneous emission rates [58].

nanoantennas. Figure 1.7b shows the measured (colored dots) and simulated (black circles) time-resolved Ru dye emission for different gap thicknesses (nominal being 5 nm). This nanoscale patch antenna geometry have been shown to have large emission rate enhancement, high radiative efficiency, and directionality of emission. These properties have been further exploited in the context of enhanced fluorescence [59] and enhanced Raman scattering experiments [60].

Figure 1.8a shows the bowtie nanoantenna to enhance single-molecule fluorescence from dyes diffusing within the nanogap. Large scale fabrication of bowtie nanoantenna was achieved by e-beam lithography. This technique uses a focused electron beam to pattern custom shapes with nanometric features on an electron-sensitive resist (such as PMMA over a silicon wafer). The e-beam exposed resist is then developed by immersing into a solvent that allows selective removal of either the exposed or non-exposed regions of the resist. This eventually creates small structures in the resist which are subsequently transferred to any substrate. Gold bowtie nanoantenna with 10 nm nominal gap size were reported to produce over 1000-fold fluorescence enhancement using an emitter with intrinsically low, ~2.5% quantum yield (TPQDI molecules indicated by black arrows, doped in PMMA layer in light blue). In addition, emission decay times as short as 10 ps were observed for molecules diffusing through the nanogap region [19]. As a

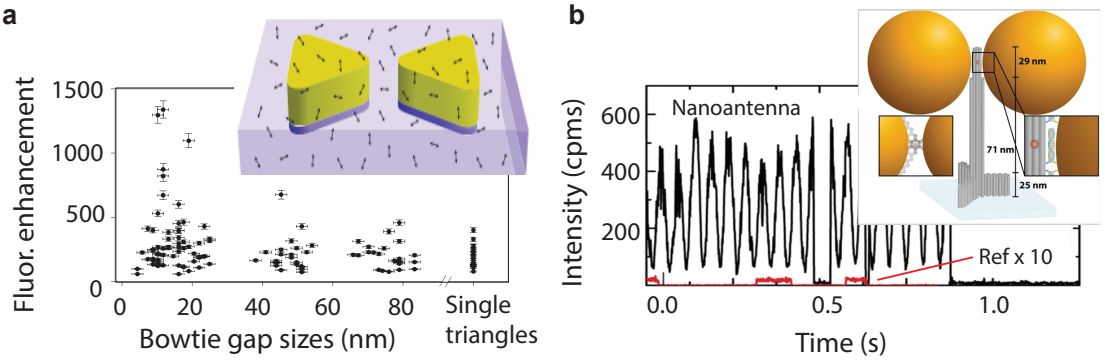

FIGURE 1.8: **Bowtie nanoantenna and DNA origami for large single-molecule fluorescence enhancements.** (a) Scatter plot of single-molecule fluorescence brightness enhancement for 129 nanoantenna as a function of bowtie gap size. Inset shows the schematic of bowtie nanoantenna (gold) coated with TPQDI molecules (indicated by the balck arrows) in PMMA (light blue) on a transparent substrate [19]. (b) Single-molecule fluorescence trajectory for a DNA origami based dimer nanoantenna (black line) and for a DNA origami structure without nanoparticles (red line) obtained using 10× more excitation intensity. The inset shows a sketch of the DNA origami optical nanoantenna with two 100 nm Au nanoparticles with an overall interparticle distance being 12 to 17 nm [61].

powerful alternative, the DNA origami method is used to achieve exquisite nanofabrication control for both the self-assembly of nanoparticles into complex antenna design to localize the desired target molecule in the antenna hotspot [20]. Figure 1.8b shows a representative single-molecule fluorescence time trace for Atto647N molecules recorded with a DNA origami with ∼12 nm nominal gap size (black traces). The same acquired with 10× excitation power but without the gold dimers is also displayed in red for direct comparison. Experiments performed $NiCl_2$ as the chemical quencher have been reported with fluorescence enhancement factors over 5000-fold, and single-molecule sensitivity at 25 μM fluorophore concentrations [61].

A specific requirement for the detection of fluorescent molecules in solution at high concentration is the rejection from the background signal from molecules a few tens of nanometer away from the plasmonic antenna, yet within the confocal detection volume. At the targeted concentrations of several micromolar, the number of non-enhanced molecules in the confocal volume can reach several thousands, and their collective fluorescence signal can severely outshine the signal from an individual molecule enhanced by the plasmonic hotspot. Current approaches mostly exploit the low quantum yield of the emitters diffusing through the hotspot to increase the contrast between the detected molecule and the background. More recently, innovative nanoantenna design termed "antenna-in-box" combining a central nanogap antenna together with a metal cladding layer has shown great potential, enabling single molecule operation at concentrations

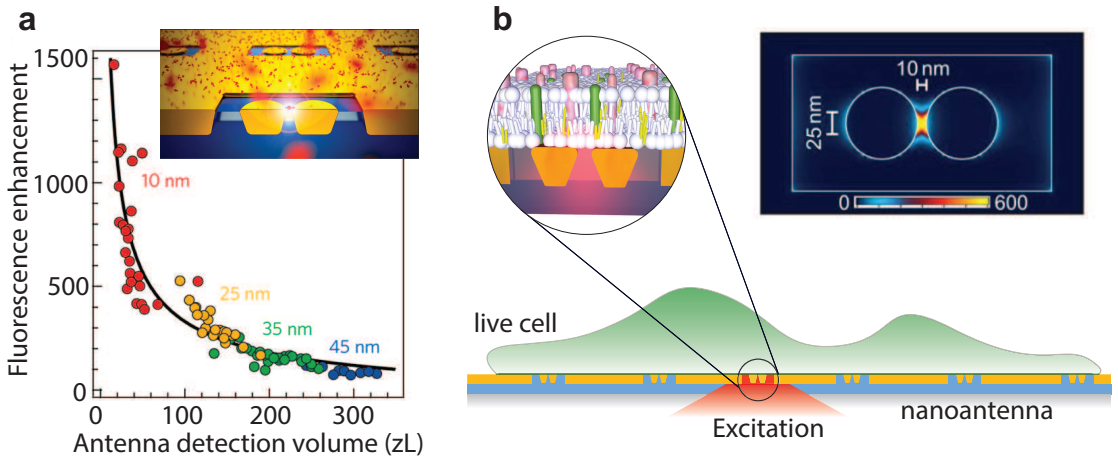

FIGURE 1.9: **Planar "antenna-in-box" platforms with single-molecule sensitivity at physiological expression levels.** Planar optical nanoantennas yield giant single-molecule fluorescence enhancements for molecules diffusing in solution (a) and for investigating lipid diffusion dynamics in the plasma membrane of living cells (b) [62, 64]. The ultra confined volumes (in 20 zL range) are brought to the surface of the nanostructure with an innovative nanofabrication technique that applies planarization, etch back and template stripping to expose the excitation hotspot at the surface. The inset in b shows the FDTD simulations of the electric field intensity profile within a 10 nm gap "antenna-in-box" illuminated at 633 nm. The colorscale indicates the enhancement of the local excitation intensity.

above 25 μM. The central nanogap provides the extreme localization of the incident electromagnetic fields, while the surrounding box-aperture screens the fluorescence signal preventing the excitation of background molecules diffusing away from the nanogap. This structure was investigated during the course of this PhD project, and as we progress into the thesis we will discuss in detail in Chapter 5 and Chapter 6. Figure 1.9a summarizes the fluorescence enhancement factors achieved with FCS on planar optical nanoantenna for molecules diffusing in solution [62]. We further exploited these planar nanoantenna platforms to investigate model lipid membranes and plasma membranes in living cells with high spatial and temporal resolution [63, 64]. Figure 1.9b displays the planar antenna-in-box concept for live cell nanospectroscopy and we will discuss this project in Chapter 6.

In general, the nanoantenna or nanoapertures based single-molecule approach is realized: (i) by limiting the light-exposed sample region as in the case of zero-mode waveguides where nanometric circular apertures with diameters slightly smaller then 100 nm are used to achieve reduction in detection volumes, or (ii) by enhancing the local excitation intensity in extremely localized hotspots through resonant plasmonic interaction which yields both volume reduction and very high fluorescence count rates. Importantly, the

"antenna-in-box" design benefits from both of these features and thus ideal for single-molecule experiments at near-physiological expression levels.

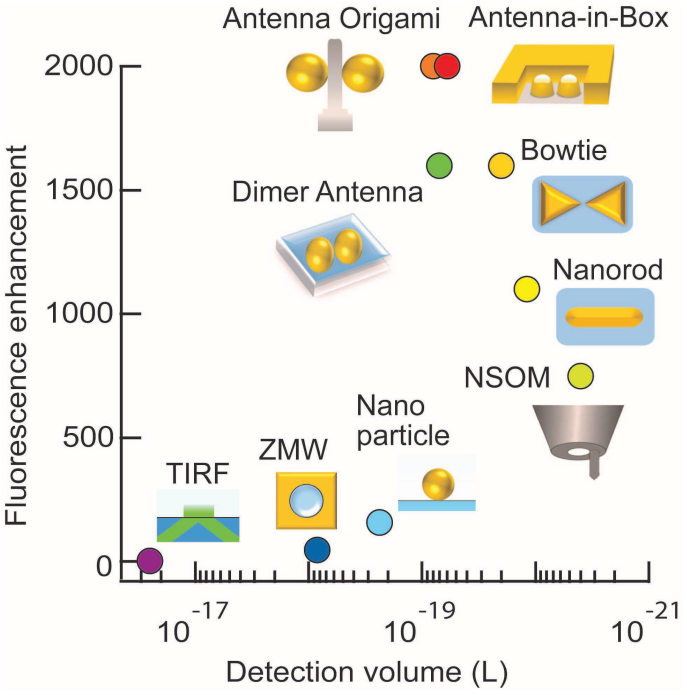

FIGURE 1.10: **Fluorescence enhancement factors summarized for different nanophotonics approach.** Comparison between different approaches to confine light and enhance fluorescence. The fluorescence enhancement factors are estimated for an emitter with 2% quantum yield. The upper threshold in both the axis accommodates the results published until the start of this PhD project (see Roadmap article [7]). As we will see in the upcoming Chapters, higher figure of merits have been achieved.

Figure 1.10 summarizes various nanophotonics approaches for enhanced single-molecule fluorescence detection. Various structures such as single aperture, aperture arrays, bowtie structures, double nanoholes structures have been widely used for enhanced single-molecule fluorescence detection [7, 48, 49, 50, 51, 65, 66]. While specific design must be found for the plasmonic antennas (as per desired experiments), their integration into microscope apparatus, the nanofabrication itself is another great challenge.

Classical top-down techniques like electron-beam lithography or focused ion beam milling have made decisive contributions in the development of nanophotonics, yet they are both expensive to run and slow in throughput. Bottom-up self-assembly or stencil nanolithography offer alternative strategies to overcome these limitations. Nanostructures such as spherical gold nanoparticles, nanorods, or dimer geometries (such as DNA origami) provides nanofabrication control with relatively simple designs [22, 44, 67].

While metals provide nanoscale localization of intense light fields, resistive heating losses in metals can simultaneously severely limit the performance of plasmonic antennas due to

non-radiative energy transfer from the molecule to the metal. This fluorescence quenching phenomenon critically depends on the molecular distance from the metal as well as the fluorescence emission spectra position respective to the nanoantenna mode resonances. Therefore, a balance must be found to maximize the net fluorescence enhancement. In Chapter 4, we will demonstrate a powerful alternative dielectric nanogap antenna for enhanced single-molecule fluorescence detection [68].

1.5 Summary

The recent achievements of plasmonics and nanophotonics enable to overcome the diffraction limit and confine the light towards dimensions similar to the size of a single molecule. These promising new techniques pave the way to bring single-molecule microscopy into a new dimension of molecular concentration reaching physiological conditions close to the native environment of the living cell. A huge number of proteins and enzymes which were only monitored using ensemble measurements can now be investigated with single molecule resolution to reveal sample heterogeneity, sub populations and dynamic disorder. Applying plasmonics and nanophotonics to single-molecule detection at high concentrations holds great promises to reveal new insights on biological functions and dynamics.

Chapter 2

Fluorescence correlation spectroscopy and time correlated techniques

This chapter starts with the discussion on the principle and theoretical background of confocal FCS and time-correlated single-photon counting technique. Further, the experimental setup used during the course of this PhD will be detailed. And finally a short summary on nanoantenna mediated FCS and the decay mechanism will be presented.

2.1 Fluorescence correlation spectroscopy (FCS)

FCS is a powerful solution-based single-molecule technique widely adopted for studying dynamics and bio-molecular interactions [43, 69]. Monitoring the fluorescence fluctuation of the molecules continuously moving in-and-out of the illumination spot, gives us the information about the dynamic molecular properties at a single molecule level which are otherwise hidden in ensemble averaging. As FCS relies on the intensity fluctuation of molecules freely diffusing in solution, this technique is less prone to photophysical damages introduced by the excitation source when compared to the single molecule experiments performed with fixed dyes. Although being first purposed in 1972 by Madge, Elson and Webb [70], until recently the applications were restricted to solutions with ultra low sub nanomolar analyte concentration [43, 69, 71]. As we progress into this thesis, we will demonstrate that using nanoantenna (or nanoapertures), it is now possible to follow single-molecule dynamics at high physiological concentrations with very high SNR.

As shown in Figure 2.1a, FCS uses the information about the fluctuation of the fluorescence signal form the molecules diffusing in-and-out of the confocal volume to compute the temporal auto-correlation function (Figure 2.1b). The continuous diffusion is governed by random Brownian motion and so apart from yielding a direct measure of the molecular interactions at cellular level, it also contains the information about the dynamics of single molecules such as diffusion behaviors, chemical reaction rates, hydrodynamic radii and so on. All phenomenon affecting the fluorescence intensity with time should be detectable using FCS.

Relationship between fluorescence fluctuation and average particle number:

The number of randomly diffusing molecules in the confocal volume at any time is governed by Poisson distribution, thus the property of randomly distributed process yields the sample variance as:

$$\langle \delta N \rangle^2 = \langle N \rangle \tag{2.1}$$

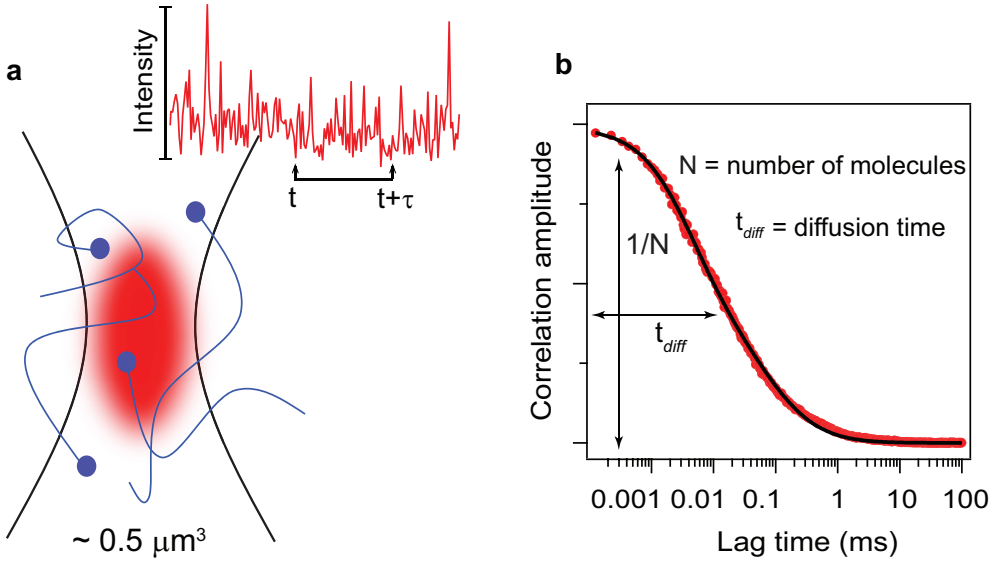

FIGURE 2.1: **Principle of fluorescence correlation spectroscopy.** (a) The excitation beam is focused in a solution containing fluorescence molecules diffusing in-and-out of the confocal illumination spot (typical volume 0.5 μm^3) governed by the Brownian motion. The fluorescence intensity fluctuations are recorded with time and the temporal auto correlation of intensity at time t is computed with the same after a certain time delay (t+τ). (b) The resulting correlation amplitude indicates the average number of molecules present within the illumination volume and the roll off time in the correlation curve indicates the mean translation diffusion time.

As the fluorescence intensity (not fluctuations but the mean intensity) is directly proportional to the number of molecules, defining α as a proportionality constant we can

write:

$$\begin{aligned} \langle F \rangle &= \alpha \langle N \rangle \\ \text{And, } \left\langle (\delta F)^2 \right\rangle &= \alpha^2 \langle \delta N \rangle^2 \\ &= \alpha^2 \langle N \rangle \quad \text{[Using Equation 2.1]} \end{aligned}$$

Thus, normalization of the above equations:

$$\frac{\left\langle (\delta F)^2 \right\rangle}{\langle F \rangle^2} = \frac{1}{\langle N \rangle}$$

It is worth noting that apart from fluorescence intensity (F), another physical parameter, *i.e.* concentration (C) is also directly proportional to the number of particles (N) and follows the same relation:

$$\frac{\left\langle (\delta F)^2 \right\rangle}{\langle F \rangle^2} = \frac{\left\langle (\delta C)^2 \right\rangle}{\langle C \rangle^2} = \frac{\left\langle (\delta N)^2 \right\rangle}{\langle N \rangle^2} = \frac{1}{\langle N \rangle} \tag{2.2}$$

The above equation describes relationship between intensity fluctuations and average number of particles by incorporating the average intensity value, $\langle F \rangle$ which can be easily measured.

Deriving the correlation amplitude:

Under constant excitation power, the fluorescence fluctuations can be defined as the deviation from the temporal average of the signal,

$$\delta F(t) = F(t) - \langle F(t) \rangle$$

where the temporal average of signal over time T is given by:

$$\langle F(t) \rangle = \frac{1}{T} \int_0^T F(t)\, \mathrm{d}t$$

Considering a system in equilibrium, let us now describe the dynamics of the fluorescence dye in single-molecule level by $\delta\big(\sigma\, q\, C(\vec{r}, t)\big)$ that includes the fluctuation in molecular absorption cross-section ($\delta\sigma$), quantum yield (δq) and the same in the local particle concentration $\delta C(\vec{r}, t)$. Owing to the fact that the fluctuations arise only form the change in local concentration within the focal volume, the variation in fluorescence signal can

be written as:

$$\delta F(t) = \kappa \int_V I_{exc}(\vec{r})\; S(\vec{r})\; \delta\big(\sigma\, q\, C(\vec{r},t)\big)\, \mathrm{d}V \tag{2.3}$$

where κ denotes the detection efficiency, $S(\vec{r})$ is the optical transfer function, and $I_{exc}(\vec{r})$ describes the spatial distribution of the excitation energy with I_0 maximum.

The above equation can be simplified by defining a new convolution function: $W(\vec{r}) = I_{exc}(\vec{r})/I_0 \; * \; S(\vec{r})$, that incorporates the two dimensionless spatial optical transfer functions. $W(\vec{r})$ describes the spatial distribution of the emitted light which is usually approximated by three-dimensional Gaussian function, that decays to $1/e^2$ at r_0 in lateral direction and at z = z_0 in axial direction. Mathematically this is represented as:

$$W(\vec{r}) = e^{-2\frac{(x^2+y^2)}{r_0^2}}\; e^{-2\frac{z^2}{z_0^2}}$$

Further introducing a parameter $\eta = I_0\, \kappa\, \sigma\, q$ that describes the photon count rate per molecule per unit time, the Equation 2.3 can be now rewritten as:

$$\delta F(t) = \int_V W(\vec{r})\, \delta\big(\eta\, C(\vec{r},t)\big)\, \mathrm{d}V \tag{2.4}$$

The temporal auto correlation of the fluctuation in signal with a certain lag time (τ) is defined as:

$$\begin{aligned} g(\tau) &= \frac{\langle \delta F(t)\, \delta F(t+\tau)\rangle}{\langle F(t)\rangle^2} \\ &= \frac{\iint W(\vec{r}) W(\vec{r}')\, \big\langle \delta\big(\eta\, C(\vec{r},t)\big)\delta\big(\eta\, C(\vec{r}',t+\tau)\big)\big\rangle\, \mathrm{d}V \mathrm{d}V'}{\big(\int W(\vec{r})\, \big\langle \delta\big(\eta\, C(\vec{r},t)\big)\big\rangle\, \mathrm{d}V\big)^2} \end{aligned}$$

[Using Equation 2.4]

Further, the fluctuation term can be separated as:

$$\delta\big(\eta\, C(\vec{r},t)\big) = C\delta\eta + \eta\delta C$$

Under the condition that the fluorophore property is not changing within the measurement time (*i.e.* $\delta\eta = 0$), the auto correlation equation simplifies to:

$$g(\tau) = \frac{\iint W(\vec{r}) W(\vec{r}')\, \big\langle \delta C(\vec{r},0)\delta C(\vec{r}',\tau)\big\rangle\, \mathrm{d}V \mathrm{d}V'}{\big(\langle C\rangle \int W(\vec{r})\, \mathrm{d}V\big)^2}$$

If we consider only the particle freely diffusing in 3D with diffusion constant (D), then the number density auto correlation term in the above equation *i.e.* $\big\langle \delta C(\vec{r},0)\; \delta C(\vec{r}',\tau)\big\rangle$

can be replaced by $\langle C \rangle \ \frac{1}{(4\pi D\tau)^{-3/2}} \ e^{-\frac{(\vec{r}-\vec{r}')^2}{4D\tau}}$

Thus $g(\tau)$ reduces to:

$$\begin{aligned} g(\tau) &= \frac{\iint W(\vec{r})W(\vec{r}')\,\langle C \rangle \ \frac{1}{(4\pi D\tau)^{-3/2}} \ e^{-\frac{(\vec{r}-\vec{r}')^2}{4D\tau}}\,\mathrm{d}V\mathrm{d}V'}{\left(\langle C \rangle \int W(\vec{r})\,\mathrm{d}V\right)^2} \\ &= \frac{1}{\langle C \rangle} \ \frac{1}{(4\pi \mathrm{D}\tau)^{-3/2}} \ \frac{\iint W(\vec{r})W(\vec{r}') \ e^{-\frac{(\vec{r}-\vec{r}')^2}{4D\tau}}\,\mathrm{d}V\mathrm{d}V'}{\left(\int W(\vec{r})\,\mathrm{d}V\right)^2} \end{aligned} \tag{2.5}$$

τ_{D} is the lateral diffusion time which represents the time period a molecule spends in the illumination confocal volume, and is related with the diffusion constant as:

$$\tau_{\mathrm{D}} = \frac{r_0^2}{4\,\mathrm{D}}$$

And the effective confocal volume (V_{eff}) is defined as:

$$V_{\mathrm{eff}} = \frac{\left(\int W(\vec{r})\,\mathrm{d}V\right)^2}{\int W^2(\vec{r})\,\mathrm{d}V} = \pi^{\frac{3}{2}} \ r_0^2 \ z_0$$

Replacing these values of τ_{D} and V_{eff} in Equation 2.5, we get the auto correlation function for freely diffusing molecules as:

$$\begin{aligned} g(\tau) &= \frac{1}{\langle C \rangle \, V_{\mathrm{eff}}} \frac{1}{1 + (\tau/\tau_{\mathrm{D}})} \frac{1}{\sqrt{1 + (r_0/z_z)^2(\tau/\tau_{\mathrm{D}})}} \\ &= \frac{1}{\langle N \rangle} \frac{1}{1 + (\tau/\tau_{\mathrm{D}})} \frac{1}{\sqrt{1 + s^2(\tau/\tau_{\mathrm{D}})}} \end{aligned}$$

where $\langle N \rangle = \langle C \rangle \, V_{\mathrm{eff}}$ is the average number of molecules within the confocal volume and $s = r_0/z_z$ denotes the ratio of transverse to axial dimension of the detection volume. Thus, as the values of r_0 and z_0 can be deduced from the calibration measurements, the amplitude of correlation at zero lag time gives us information about the particle concentration: $g(0) = \frac{1}{\langle N \rangle}$

Finally, similar to the correlation coefficient between the fluctuations, the definition of the correlation coefficient of the intensity at time t and the intensity at some time

interval τ later follows the same definition:

$$G(\tau) = \frac{\langle F(t)\, F(t+\tau)\rangle}{\langle F(t)\rangle^2} = 1 + \frac{\langle \delta F(t)\, \delta F(t+\tau)\rangle}{\langle F(t)\rangle^2}$$
$$= 1 + \frac{1}{\langle N\rangle} \frac{1}{1+(\tau/\tau_{\mathrm{D}})} \frac{1}{\sqrt{1+s^2(\tau/\tau_{\mathrm{D}})}} \tag{2.6}$$

It is important to recall that the equation derived was based on the assumption that the molecule's fluorescence properties are not changing while it crosses the illumination focus (*i.e.* $\delta\eta = 0$). However for most of the fluorescence experiments (usually at high fluorophore concentrations and for high excitation power), the dye tends to have transition to first excited triplet state appearing to be in dark state before finally going to ground state, eventually interrupting the fluorescence emission. Describing the triplet transition by a simple exponential decay, and defining $\langle B\rangle$ as the background noise, n_{T} the amplitude of dark state population, and τ_{b_T} as the blinking time of the dark state, we can now rewrite the correlation amplitude as:

$$G(\tau) = 1 + \frac{1}{\langle N\rangle} \left(1 - \frac{\langle B\rangle}{\langle F\rangle}\right)^2 \left[1 + n_{\mathrm{T}}\, e^{-\frac{\tau}{\tau_{b_T}}}\right] \frac{1}{1+(\tau/\tau_{\mathrm{D}})} \frac{1}{\sqrt{1+s^2(\tau/\tau_{\mathrm{D}})}}$$
[3D random diffusion] (2.7)

The last term in the above equation is know as the motility-term and is strictly for a case of three dimensional Brownian motion. However the mobility of particles in case of lipid bilayers (model membranes or in plasma membranes of living cells) is more accurately described by a 2D Brownian diffusion model and thus the correlation amplitude takes the form of:

$$G(\tau) = 1 + \frac{1}{\langle N\rangle} \left(1 - \frac{\langle B\rangle}{\langle F\rangle}\right)^2 \left[1 + n_{\mathrm{T}}\, e^{-\frac{\tau}{\tau_{b_T}}}\right] \frac{1}{1+(\tau/\tau_{\mathrm{D}})}$$
[2D membrane diffusion] (2.8)

Using these equations (Equation 2.7 and Equation 2.8), various investigations such as diffusion analysis, concentration measurements, studying conformational changes and molecular interactions can be readily carried out with FCS technique [72, 73]. The confocal illumination volume (∼0.5 fL) is larger than the dimension of single molecules ∼5 nm, thereby restricting FCS in early days to solutions with ultra low analyte concentrations as reliable fluctuation could only be observed in presence of fewer molecules. When the focal spot contains a large population of molecules, then those leaving and entering the illumination volume do not have significant fluctuation in the intensity time

trace, making it difficult to analyze and interpret it. Further details on nanoantenna mediated FCS will be detailed at the end of this chapter. And in following chapters, we will demonstrate how engineering nanostructures with different shapes and sizes, single-molecule resolution at very high fluorophore concentrations is readily achievable with FCS. Apart from single molecule sensitivity, nanoantenna-FCS has an additional advantage of high temporal and spatial resolution (with confined electromagnetic hotspots), which will be further exploited to explore the plasma membrane architecture in living cells.

2.2 Time correlated single-photon counting (TCSPC)

TCSPC is a time domain technique based on the detection of single photons. This technique is capable of recording low level light with extremely high temporal (usually few ps) resolution. The immediate applications are in fluorescence lifetime measurements, fluorescence resonance energy transfer (FRET) experiments and fluorescence lifetime imaging (FLIM) [74, 75, 76].

The technique requires a pulsed excitation source with high repetition rate. After each pulse of excitation, the excited state electrons decay back to the ground state with a certain rate that incorporates all possible decay pathways either radiative (Γ_r) or non radiative way (Γ_{nr}). Fluorescence and phosphorescence are radiative pathways while transition like inter-system crossing and internal conversion are non radiative decay mechanism. The rate of de-excitation of the electrons ultimately depends upon the nature of excited state. Fluorescence lifetime is the average time a fluorophore remains in the excited state following the excitation. Mathematically, fluorescence lifetime (τ) is defined as:

$$\tau = \frac{1}{\Gamma_r + \sum \Gamma_{nr}} = \frac{1}{\Gamma_{\text{tot}}}$$

As the arrival times of single photons at the detector follows a Poisson distribution, fitting the number of detected photons *vs* gives the excited state or fluorescence lifetime information. Since fluorescence lifetime of molecules near nanoapertures can be as short as few ps, the sampling time has to be at least 10× faster than the expected decay time to be measured. TCSPC instruments make it possible having ps time resolution otherwise it is impossible to get such resolution with any analog photon counters. The data acquisition is extended over multiple cycles with the pulsed excitation, and from the data collected over many cycles, a single decay profile (exponential fit) is constructed.

Ideally, the exponential decay governed by $S(t) = A.exp(-t/\tau)$ gives the information about molecular fluorescence decay dynamics.

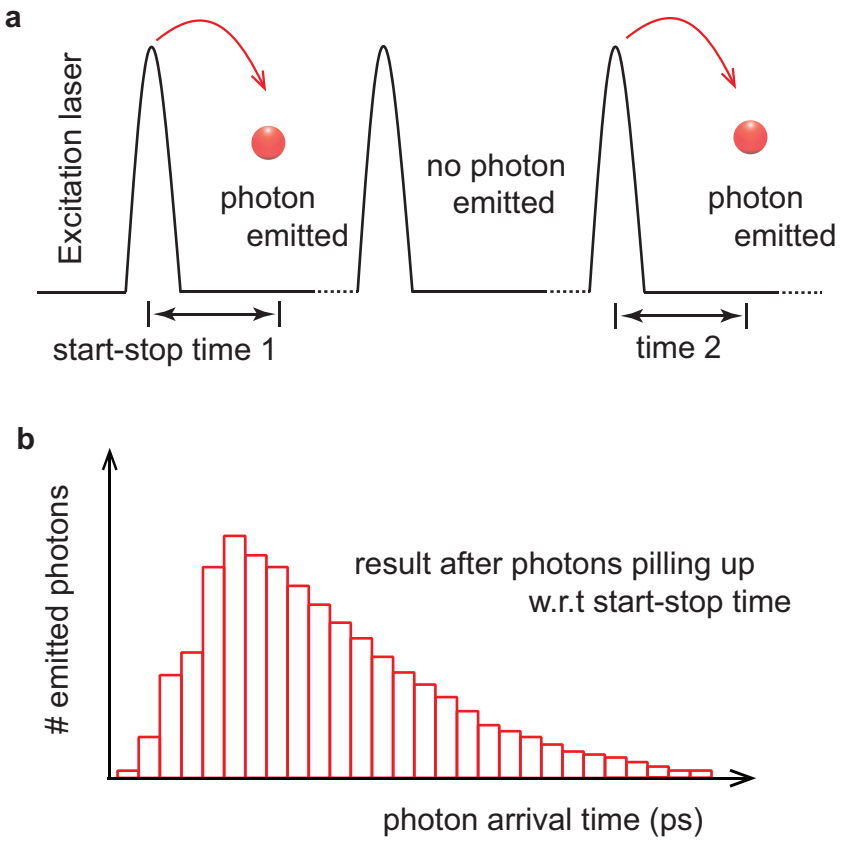

FIGURE 2.2: **TCSPC technique for fluorescence lifetime analysis.** (a) TCSPC technique is a fast stopwatch with two inputs. The reference pulse starts the clock, and is stopped by the signal pulse originating from sample. (b) The time measured for one such start-stop measurement is then stored by an increase of count in a histogram. The measurement is carried out over a large number of such cycles and the final signal waveform/histogram is efficiently reconstructed by determining the arrival times of the photons, and counting them in several time bins with respect to the excitation pulses.

The high repetition rate (assured by pulsed excitation) and low level signal intensity is required to make sure that the probability of detecting more than one photon in one signal period is negligible. Based upon the photon arrival time relative to a reference pulse (Figure 2.2a), a corresponding histogram is build up. As depicted in Figure 2.2b, the final histogram is actually a distribution of the photon arrival probability. As the condition of single photon probability is ensured, the collective set of registered photons over multiple cycles essentially represents the decay profile one would have obtained from a single shot time-resolved analog measurement.

2.3 Experimental setup: FCS and TCSPC

Institut Fresnel, Marseille

The fluorescence experiments are carried upon an inverted confocal microscope. The schematic diagram of the experimental system (FCS and TCSPC) is shown in Figure 2.3. And the optical setup can be broadly divided into two main subsystem as:

- Excitation path with microscope and sample stage, and
- Detection subsystem with correlator and TCSPC electronics.

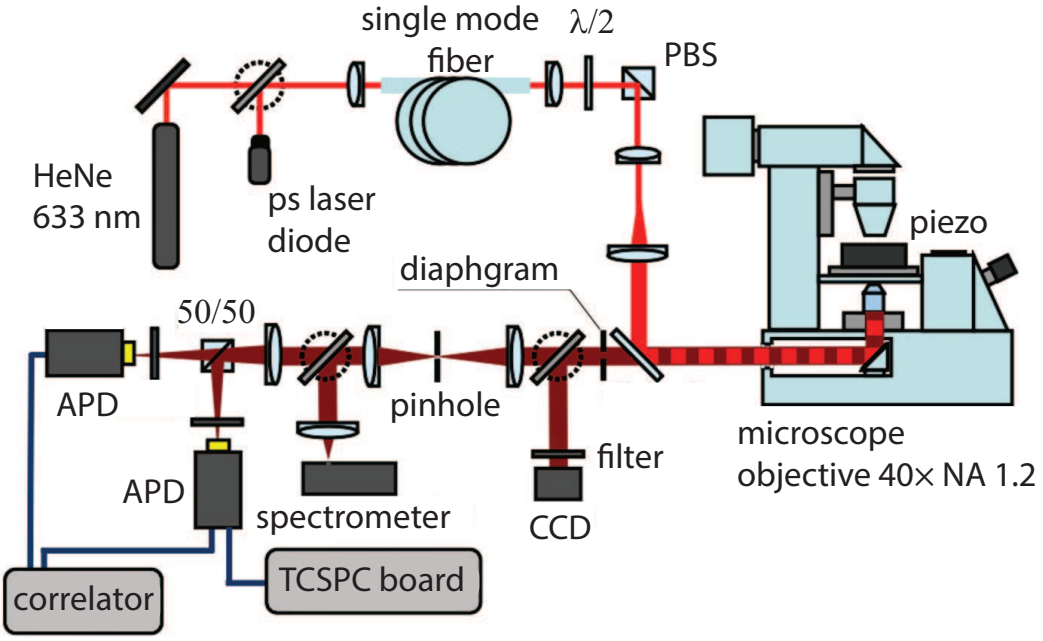

FIGURE 2.3: **Schematic of the experimental techniques (FCS and TCSPC)** The setup is equipped with two beam source (on being continues wave and the second being a pulsed laser). Both the lasers share same focal point at the objective as ensured by a single mode fiber for perfect spatial overlap. A high NA (1.2) 40× objective is at the heart of the optical setup. The sample stage is computer controlled piezo-stage and the fluorescence is filtered by a pinhole and a set of bandpass filters just before a pair of detectors.

2.3.1 Excitation arm with microscope and sample stage

Linearly polarized HeNe laser is used as an excitation source at 633 nm for all FCS experiments and a picosecond laser diode operating at 636 nm (Pico-Quant LDH-P-635, repetition rate 80 MHz) for fluorescence lifetime measurements. A single mode fiber

(Thorlabs P3-630A-FC-5) ensures spatial overlap between two different laser sources hence following same optical path for excitation same focal spot in objective focus for fluorescence spectroscopy and lifetime measurements. The excitation power is controlled by the half-wave plate just before the polarizing beam splitter. The beam is then focused onto the sample plane with a high 1.2 NA water-immersion objective from Zeiss (40×) customized with a three-axis piezoelectric stage.

2.3.2 Detection subsystem with correlator and TCSPC electronics

The emitted fluorescence is collected in epi-detection mode using a dichroic mirror (Omega Filters XF2072) designed to work at an incidence angle of 45^o reflecting excitation laser and transmitting only the fluorescence. A 30 μm pinhole in the detection path rejects the off-focal signal and sets the 0.5 fL confocal detection volume. The signal is then divided using a 50/50 beam-splitter, screened by 670 ± 20 nm bandpass filter and is finally fed into two avalanche photodiodes (PicoQuant MPD-5CTC: dead time of 50 ns and active surface of 50 μm). The temporal fluctuations of the fluorescence intensity are then analyzed with a hardware correlator (Flex02-12D/C, correlator.com, Bridgewater NJ) with 12.5 ns minimum channel width which computes the second order correlation. During the FCS experiments, both the fluorescence signal and the calculated correlation curve are displayed simultaneously on the computer screen, thereby facilitating adjustment and control of the experimental setup and conditions. The characteristic time and the number of molecules responsible for the fluctuation in the signal is derived by fitting the analytical expression represented in Equation 2.7. For fluorescence lifetime measurements, one of the photodiode output is sent to a fast time-correlated single photon counting module (PicoQuant PicoHarp 300). The characteristic fluorescence decay dynamics is then analyzed using the exponential decaying probability distribution as described in earlier section.

FCS experimental setup at ICFO, Barcelona

The FCS experiments on living cells (Chapter 6) were performed in ICFO, Barcelona with a commercial MicroTime 200 setup equipped with an inverted confocal microscope (Olympus 60×, 1.2 NA water-immersion objective). A three-axis piezoelectric stage (PhysikInstrumente, Germany) allows to select individual nanoantennas and linearly polarized light at 640 nm from picosecond laser diode (Pico-Quant LDH-D-C-640) in continuous wave mode is used as an excitation source. The emitted fluorescence signal is collected in epi-detection mode through a dichroic mirror and the signal is split into two avalanche photodiodes (PicoQuant MPD-50CT). An emission filter and a band

pass 650-690 nm filter just before each detector eliminate the scattered light by the excitation laser. A 30 μm pinhole in the detection arm yields 0.5 fL confocal detection volume at the sample plane. The fluorescence time traces are recorded on a fast time-correlated single photon counting module in the time-tagged time-resolved mode (PicoQuant MPD-50CT) and the correlation amplitudes are computed with the commercial software package SymPhoTime 64.

2.4 Nanophotonics enhanced fluorescence correlation spectroscopy

Considering the fact that the smallest possible volume attainable in any confocal system is set by the diffraction barrier to 0.2 fL at best, it limits the maximum concentration at which the technique can operate within nanomolar to few picomolar range. Use of nanometric apertures (or nanoantennas) squeezes excitation light in sub-diffraction limited volumes, making it possible to shine light only on a few (or even one) molecules at a time. In addition to the characteristic diffusion time and the mean number of molecules within the illumination volume, FCS can be used to compute fluorescence count rate per molecules (also called brightness per molecule).

As discussed in the earlier Chapter (Section 1.3), the enhancement factor (η_{F}) is defined as the ratio of the brightness per molecule in presence of a nanoantenna (or aperture) to the same in open solution in confocal illumination. Thus at a fixed excitation power, the fluorescence enhancement factor is computed as:

$$\text{fluorescence enhancement } (\eta_{\mathrm{F}}) = \frac{\text{brightness per molecule with nanoantenna } (Q^*)}{\text{brightness per molecule in open solution } (Q_{\mathrm{conf}})}$$

where Q (or Q*) = $\frac{(\langle \mathrm{F} \rangle - \langle \mathrm{B} \rangle)}{\mathrm{N}}$. The total fluorescence (F), background signal (B), are directly taken from experiment as measured by single-photon counting devices and the average number of molecules (N) is deduced from the correlation amplitude G(0) (at zero lag time) which is computed by numerically fitting the data to the model given by the Equation 2.7.

As FCS is a statistical technique, noise is an important limiting factor. Thus proper estimation of the signal-to-noise ratio helps largely in more accurate analysis of the data, and also enables optimization of the experimental design. Apart from the shot noise (resulting from the quantum nature of light), the stochastic nature of the signal fluctuation process also contributes to the noise in FCS. Following the work of Koppel

[77], it is shown that the SNR in FCS does not depend on the total fluorescence but on the brightness (also know as the count rate) per molecule (Q). This parameter is related with the total experiment acquisition time (T_{tot}) and the correlator's minimum channel width ($\Delta\tau$) and follows the relation [77, 78]:

$$\text{SNR} \propto Q\sqrt{T_{\text{tot}}\Delta\tau}$$

Considering the case when $N >> 1$ (large number of molecules in detection volume), small time delay ($\Delta\tau$), uniform excitation and negligible background, the signal-to-noise (SNR) for the first channel of the auto correlation function is given by:

$$\text{SNR}_{\tau\to 0} = Q\sqrt{T_{\text{tot}}\Delta\tau}$$

However without any prior assumption on the number of molecules the above equation takes the form of [78]:

$$\text{SNR}_{\tau\to 0} \approx \frac{Q\sqrt{T_{\text{tot}}\Delta\tau}}{(1+1/N)^2} \tag{2.9}$$

Further, keeping the detection electronics and correlator same, high SNR can be achieved by increasing the count rates per molecule (using nano apertures or nanoantennas). Even at relative low excitation power, and near physiological concentrations FCS with single-molecules resolution is possible. In addition, as the SNR scales with $Q\sqrt{T_{\text{tot}}}$, and hundred fold increase in counts per molecules can be achieved by using nanophotonics approach, it amounts to a significant 10^4-fold reduction in the total accusation time. It is important to note that this concept of Fast-FCS (with small acquisition time) is particularly important in experiment involving biomolecular interactions. Experiments involving emitters with low brightness require long acquisition time, to overcome the SNR issue, thereby limiting the access to the dynamics of single molecules at very short time scale. Fast-FCS helps to overcome this limitation eventually opening a new window to look at various dynamics events (such as: fast enzymatic reactions, protein-protein interactions at short time scales and ps rotational times of single molecules) which are otherwise restricted in conventional FCS [8, 78].

The photons emitted by the individual dye/molecules (termed as count rate or molecular brightness) is a deciding factor in FCS analysis. We will further discuss in detail the mechanism behind the enhancement in molecular brightness per molecule in the case of different nanoantennas (or apertures) whenever required in the following chapters.

Chapter 3

Double nanohole apertures for fluorescence enhancement

The double nanohole (DNH) structures milled into a metal film have recently attracted interest in single-particle trapping (from nanometric beads to single protein) as they offer new strategies for real time investigation of biochemical events at nanoscale dimensions [14, 79]. In this chapter, we introduce the use of double nanohole structure with 25 nm nominal gap and report enhanced single-molecule fluorescence detection in concentrated solutions exceeding 20 μM. The nanometer gap localizes the excitation light into an apex volume down to 70 zL (1 zL=10^{-21} L), 7000-fold below the diffraction-limited confocal volume. Using fluorescence correlation spectroscopy and time-correlated photon counting, we measure up to a 100-fold fluorescence enhancement, together with a 30-fold enhancement of the local density of optical states (LDOS).

This project was carried out in collaboration with Prof. Reuven Gordon from University of Victoria, Canada.

3.1 Double nanohole: Motivation and structure design

We start with a discussion on the distinctive advantages of double nanohole apertures (DNH) over various other antenna designs, the fabrication procedure of these innovative strategy for achieving nanoscale mode volume, before eventually demonstrating its application for enhancing the fluorescence of single-emitters. The DNH nanostructures have shown great promise in the field of enhanced spectroscopy, on-chip sensing [80],

The contents of this chapter have been published in:
Regmi, R., Al Balushi, A.A., Rigneault, H., Gordon, R. and Wenger, J., 2015. Nanoscale volume confinement and fluorescence enhancement with double nanohole aperture. *Scientific Reports*, 5.

and many biological studies involving optical trapping experiments [81]. The volume confinement and near field enhancement result from the sharp apex region in between two nearly spaced nanoholes enabling single molecule sensitivity. In particular the DNH structures have been successful in trapping single proteins [14] and monitoring single protein binding kinetics in a label free fashion [82, 83]. The variation in light transmission through these double nanohole aperture is used to detect and monitor these trapping (or binding) events [84]. In addition, the DNH structures have also been demonstrated for surface enhanced Raman Scattering [85] and second harmonic generation [86].

Thus the quantification of fluorescence enhancement factor in DNH is interesting for plasmon-enhanced luminescence applications and the measurement of the near field apex volume is important to understand the phenomenon leading to enhanced plasmonic trapping in DNH. In addition, prior to this PhD thesis, there has been no report of their use to enhance the fluorescence of single molecules.

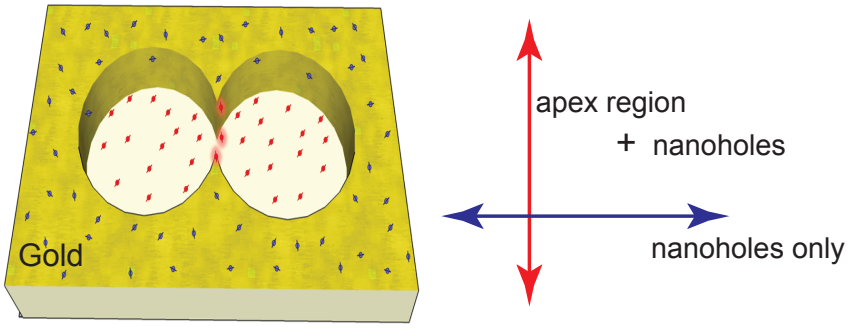

FIGURE 3.1: **Experimental strategy of DNH structure for fluorescence enhancement.** Sketch of double nanohole structure to enhance the fluorescence of single molecules diffusing within the apex region. The parallel excitation mode essentially results in the enhanced fluorescence signal from the molecules within in apex volume when compared to those diffusing in the nearby nanoholes.

The narrow gap between the two cusps of the double nanoholes leads to the concentration of light resulting in one single localized nearfield hot-spot and shows plasmonic resonance with respect to the polarization of the incoming light. As shown in Figure 3.1 the molecules diffusing along the apex region experience the concentrated near field and thereby significantly enhancing the fluorescence of these molecules when compared with those within the nearby nanoholes.

The key advantages of the DNH structure design can be summarized as following:

- the relatively simple structure design (compared to bowtie antenna [87, 88], bowtie aperture [89] or antenna-in-box [90]) makes the fabrication process much simpler,

- the apex between the two holes directly realizes sharp radii of curvature and nanometer gap sizes, providing high local intensity enhancement,
- the optically thick metal film efficiently screens out the background molecules around the structure, and
- the good thermal conductivity of the gold film helps avoiding the heating effects.

The nano structures are milled into a 100 nm thick gold film adhered to the glass substrate with 5 nm Ti adhesion layer using using focused ion beam (FEI Strata DB235). The FIB system tightly focuses a beam of gallium ions into the sample and can yield nanometer milling precision. The accelerating voltage and current of the gallium ion beam were respectively set to 30 kV and 10 pA. The DNH structure is achieved by milling two 190 nm diameter nanoholes connected by an apex region of 60 nm length and 25 nm gap width. Figure 3.2 shows the scanning electron microscope image of a 2×3 arrays(a), zoomed in image of a representative DNH with 25 nm nominal gap (b), and the same with 45^o sample tilt (c).

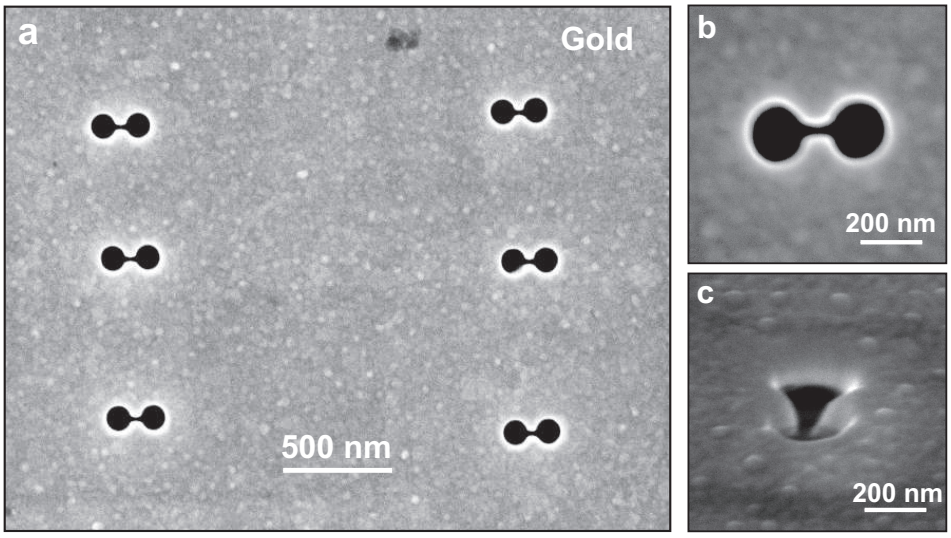

FIGURE 3.2: **Scanning electron microscope image of DNH structures using focused ion beam.** (a) DNH structure arrays milled in 100 nm thick gold film and imaged using a scanning electron microscope. (b) The zoom-in image of a single structure: two 190 nm diameter nanoholes connected by an apex region of 60 nm length and 25 nm gap width. (c) The same structure imaged with 45^o sample tilt.

3.2 Near field and transmission characteristics of DNH

The nanogap between the cusps of two nearby circular nano apertures results in a single hotspot located at the center of the structure. We compute finite-difference time-domain (FDTD) simulation using Rsoft Fullwave V6 software to investigate the strength

of the near field localization with respect to the polarization of the incoming light. We use a total-field scattered-field source and the 3D simulation region was enclosed with perfectly-matched-layer boundaries with a 2 nm mesh override (1 nm mesh for the intensity maps in Figure 3.3). The permittivity of gold is taken from Johnson and Christy [91] and the refractive indices for the glass substrate and water are respectively set to be 1.52 and 1.33.

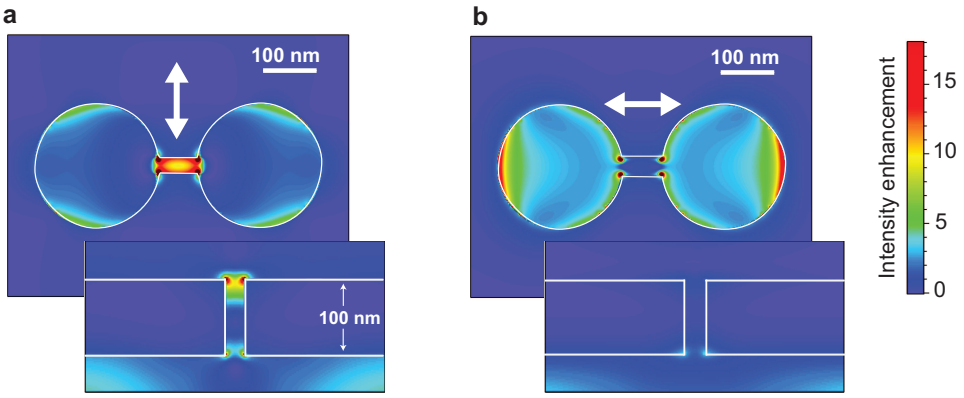

FIGURE 3.3: **Near field enhancement in the apex region of DNH.** Local intensity enhancement for a DNH of 25 nm gap and 190 nm diameter excited at 633 nm with a linear polarization parallel (a) and perpendicular (b) to the apex between the holes, taken in a plane 5 nm below the top metal surface. The inserts show the intensity enhancement along a vertical cut in the DNH center. All images share the same colorscale.

Figure 3.3 demonstrates the polarization dependence of the DNH with maximum field confinement with the incoming light polarization when oriented parallel to the apex between the nanoholes. The vertical profile further shows that the intensity is mainly localized inside the DNH and quickly vanishes within 10 nm above the metal surface (Figure 3.3a). However, a minimum intensity in the gap is observed when the incoming light polarization is oriented perpendicular to the apex (Figure 3.3b). This is essentially because the incident light is mainly concentrated in the two nearby circular nano apertures.

To further confirm this characteristic of the DNH, we record far-field transmission spectra using polarized illumination and is displayed in Figure 3.4a. Polarized white light is illuminated through the DNH and the transmission signal is sent to a spectrograph (Horiba iHR320) equipped with a Peltier-cooled CCD detector where the spectra is measured for each polarization with respect to the DNH apex. When the orientation is set parallel [79]. These findings are well reproduced by FDTD numerical simulations of the transmission spectra as shown in Figure 3.4b. Moreover, the recorded spectra shows that the DNH response covers well the 633 nm laser excitation wavelength and the 650-690 nm fluorescence emission band for the Alexa Fluor 647 dye.

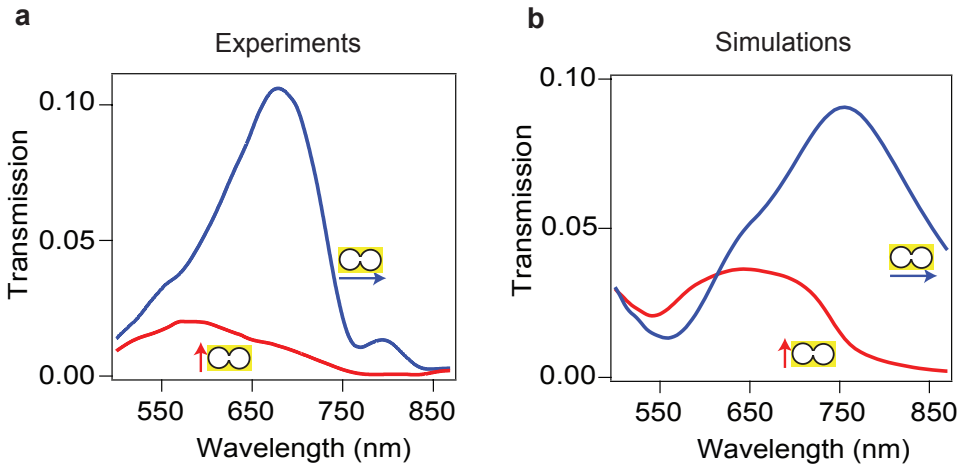

FIGURE 3.4: **Transmission characteristic of the DNH.** (a) Experimental and (b) simulated transmission spectra with normal illumination for two orthogonal linear polarizations along (red) and perpendicular (blue) to the apex. When the orientation is set parallel to the apex, a minimum of transmission is found as the electromagnetic intensity is concentrated in the gap, whereas a maximum transmission is obtained for a polarization oriented perpendicular to the apex.

3.3 Experiment and results: Single-molecules in solution

Materials and Experimental setup

Single-molecule experiments are performed with micromolar concentrations of Alexa 647 fluorophores (from Invitrogen, Carlsbad, CA) in a water based phosphate buffered saline (PBS) solution together with 200 mM or 80 mM methylviologen (1,1'-dimethyl-4,4'-bipyridiniumdichloride, Sigma-Aldrich) as the chemical quencher. The use of methylviologen changes the 30% initial quantum yield of the Alexa647 to 8% or 12% and thereby maximizes the fluorescence enhancement-factors (as discussed in Chapter 2). The DNH structure is first cleaned by UV-ozone treatment for 10 minutes to remove organic impurities and render the gold surface hydrophilic. Fluorescence experiments are then performed immediately afterward, with the sample being exposed to air for less than 2 minutes. The DNH structure is covered by the solution containing the Alexa Fluor 647 molecules at micromolar concentrations.

The fluorescence experiments are carried on a confocal inverted microscope (40×, 1.2 NA water-immersion objective) equipped with a three-axis piezoelectric stage for precise positioning of nanostructure in the focal plane. A linearly polarized He-Ne laser at 633 nm (with power 10-20 μW) is used as an excitation source. The emitted fluorescence signal is separated from the excitation light using a dichroic mirror and the out-of-focus fluorescence is rejected by a 30 μm pinhole conjugated to the sample plane. Finally, the fluorescence is recorded using two avalanche photodiodes with 670 $\pm$ 20 nm bandpass

filters. To quantify the hot spot detection volume and fluorescence enhancement, we analyze the fluorescence intensity temporal fluctuations $F(t)$ with a hardware correlator (Flex02-12D/C correlator.com, Bridgewater NJ, 12.5 ns minimum channel width) to perform fluorescence correlation spectroscopy (FCS).

3.3.1 FCS: Quantifying apex volume and fluorescence enhancement

In the DNH, the total fluorescence signal is the sum of the enhanced fluorescence from molecules within the nanoscale apex volume and the background fluorescence from the molecules present in each nanohole. Thus, it is necessary to carefully discriminate the contributions by each species in oder to have an accurate quantification of fluorescence-enhancement factors in the apex volumes alone. For this, we consider the raw fluorescence time trace as the sum of two molecular species with different number of molecules and brightness: N^* molecules within the apex region with brightness Q^*, and N_0 background molecules with brightness Q_0 diffusing away from the region of interest (essentially within the two nanoholes). An essential feature in FCS is that the molecules contribute to G in proportion to the square of their fluorescence brightness, so that the fluorescence from molecules in the apex region experiencing the maximum enhancement will have a major contribution in the FCS correlation amplitude. Following the Equation 2.6 derived in Chapter 2, the temporal correlation of the fluorescence intensity F can now be written as [43]:

$$\begin{aligned} G(\tau) &= \frac{\langle F(t)\, F(t+\tau)\rangle}{\langle F(t)\rangle^2} \\ &= 1 + \frac{N^* Q^{*2} G_d^*(\tau) + N_0 Q_0^2 G_{d0}(\tau)}{(N^* Q^* + N_0 Q_0)^2} \end{aligned} \tag{3.1}$$

where $G_d^*(\tau)$ and $G_{d0}(\tau)$ are the normalized correlation functions for each species taken individually based on a three dimensional Brownian diffusion model:

$$G_{di}(\tau) = \frac{1}{(1+\tau/\tau_{d,i})\sqrt{1+s_i^2\,\tau/\tau_{d,i}}}$$

$\tau_{d,i}$ stands for the mean residence time (set by translational diffusion) and s_i is the ratio of transverse to axial dimensions of the detection volume, whose value is set to $s = 0.2$.

To extract the number of molecules within the apex region (N^*) and the corresponding fluorescence brightness Q^* (for a given sample concentration), we use the asymptotic

value of the correlation function given by the Equation 3.1 towards zero lag time [90]:

$$G(0) = 1 + \frac{N_0 Q_0^2 + N^* Q^{*2}}{(N_0 Q_0 + N^* Q^*)^2} \tag{3.2}$$

The value of total fluorescence intensity F (*i.e.*, $N_0 Q_0 + N^* Q^*$) is known from the experimental measurement, thus replacing $N^* Q^* = F - N_0 Q_0$ into Equation (3.2), we obtain the fluorescence brightness and number of molecules within the apex region:

$$\begin{aligned} Q^* &= \frac{F^2(G(0)-1) - N_0 Q_0^2}{(F - N_0 Q_0)} \\ N^* &= \frac{(F - N_0 Q_0)^2}{F^2(G(0)-1) - N_0 Q_0^2} \end{aligned} \tag{3.3}$$

These expressions show that in addition to F and $G(0)$ (experimentally measured parameters), we need to estimate the number of molecules and brightness for the molecules diffusing away from the apex region (N_0, Q_0). At 20 μM concentration, we get $N_0 = 49$, and $Q_0 = 1.95$ counts/ms from the results obtained from control experiments with a double nanohole without any connecting gap region. These experimental findings are further supported from the earlier work on single nanometric apertures [92, 93].

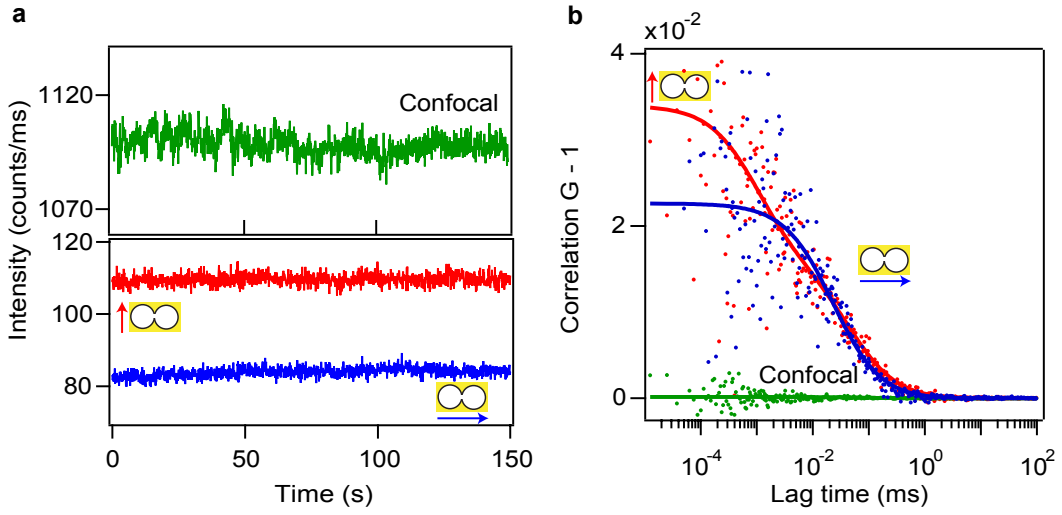

FIGURE 3.5: **FCS analysis to measure the near field apex volume.** (a) Fluorescence time trace with excitation light parallel (red) and perpendicular (blue) to the apex region. The time trace found for the confocal case (0.5 fL diffraction-limited volume) is shown in green for comparison. The binning time is 100 ms for all traces. (b) Correlation curves of the traces shown in (a). As expected, the stronger confinement of light with the polarization parallel to the apex yields a lower number of detected molecules. For all cases, 20 μM Alexa Fluor 647 concentration along with 200 mM of methylviologen at 10 μW excitation power is used. The binning time for the traces in (a) is 100 ms. The fit parameters are summarized in Table 3.1.

	Confocal	**Double nanohole**	
Excitation polarization	Linear	Parallel	Perpendicular
F (counts/ms)	1090	110	85
G(0)-1	0.16×10^{-3}	34×10^{-3}	22×10^{-3}
N	6200	0.9	46
τ_d (μs)	62	1.2	33
Q (counts/ms)	0.17	15.6	1.9
Detection volume (zL)	500×10^3	74	4×10^3
Fluorescence enhancement		92	11
Volume reduction		6900	140

TABLE 3.1: **Fitting parameter results for the FCS curves obtained on double nanohole (Figure 3.5b).** The polarization orientation with respective to the DNH apex shows high average fluorescence intensity, together with a higher correlation amplitude when compared with its perpendicular counterpart. For the DNH-parallel case, the FCS fit considers two species. The count rate per molecule ($Q^* = 15.6$ counts/ms) and the average number of molecules ($N^* = 0.9$) in the apex region are computed using the Equation 3.3. The number of molecules and diffusion time for the slowly diffusing species within the aperture region are respectively $N_0 = 49$ and $\tau_{d,0} = 33$ μs.

FCS results and discussions

Figure 3.5a shows the raw fluorescence intensity traces in a DNH with 20 μM Alexa Fluor 647 and 200 mM methylviologen. A higher fluorescence intensity is obtained when the excitation polarization is set parallel to the apex region between the double nanohole structure, in accordance with the higher localized excitation intensity expected from the simulations (Figure 3.3a). To characterize the apex detection volume and the fluorescence enhancement, we perform fluorescence correlation spectroscopy (FCS) analysis and compute the temporal correlation of the intensity traces displayed in the Figure 3.5a.

Figure 3.5b shows the FCS correlation curves for both the DNH and confocal mode. The FCS data supports the polarization dependency of the DNH as a high FCS correlation amplitude is found when the excitation is set parallel to the apex region. This relates to a reduced number of molecules within the nanoscale detection volume as the FCS amplitude scales inversely with the number of molecules withing the detection volume. The confocal measurement for the reference solution (without nanostructure) shows comparatively high average fluorescence intensity (green curve in Figure 3.5a) and very weak FCS correlation amplitude (Figure 3.5b). As expected, this corresponds to the situation that at 20 μM fluorophore concentrations there are about 6200 molecules in the 0.5 fL diffraction-limited confocal detection volume with a low average brightness per molecule. At 10 μW excitation power and in presence of chemical quencher, the brightness per molecules in the confocal setup is $Q_{sol} = 0.17$ counts/ms.

Following the FCS analysis procedure as explained in the earlier section, considering the two-species contribution in the total fluorescence intensity, we obtain an average

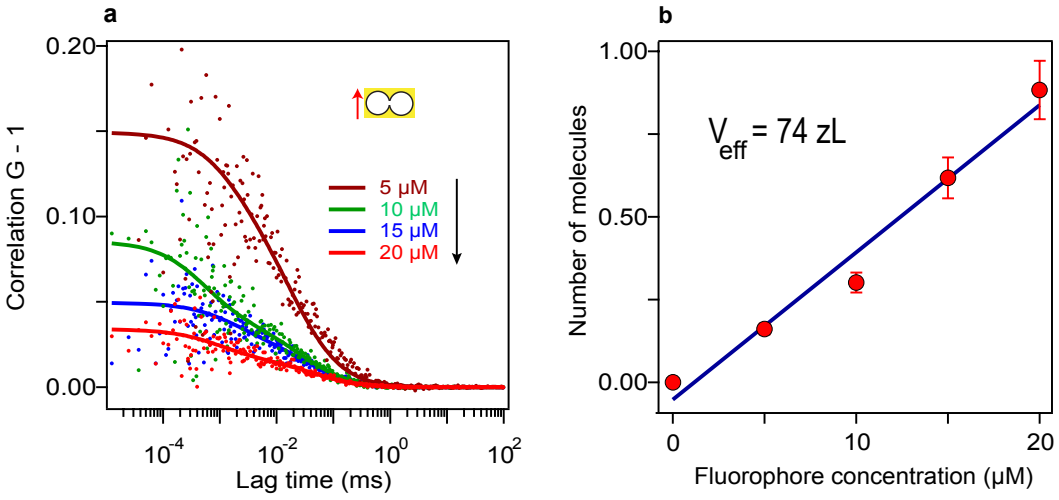

FIGURE 3.6: **FCS at varying fluorophore concentrations.** (a) FCS correlation functions for increasing concentrations of fluorescent dyes in a double nanohole with excitation polarization parallel to the apex. (b) Number of detected molecules in the apex region as function of the molecular concentration. The slope of the curve quantifies the apex near field volume V_{eff}.

number of $N^* = 0.9$ molecules in the hot spot with brightness $Q^* = 15.6$ counts/ms with excitation polarization parallel to the DNH apex. These values correspond to a fluorescence enhancement of $Q^*/Q_{conf} = 92$, and a hotspot volume of 74 zL (1 zL = 10^{-21} L), equivalent to a detection volume reduction of $N_{conf}/N^* = 6900$.

In addition to the fluorescence enhancement and nanoscale confinement of light, the FCS curves in DNH also show polarization-dependent microsecond residence time in the apex region. Two diffusion times are obtained from the fit for parallel excitation and these essentially correspond to the two populations: inside the DNH gap and within the two nearby nanoholes. The red curve in Figure 3.5b readily shows a fast component with correlation times in the μs range and in consistent with the 25 nm apex gap size. The diffusion time obtained from the FCS fit in Figure 3.5b is 1.2 μs and this value corresponds to the microsecond regime expected from the volume reduction. It is important to note that the long second time in the parallel configuration (33 μs) is indeed comparable to the time obtained from single-component fit for the perpendicular excitation configuration mode. This further confirms that the longer diffusion time in parallel excitation steams from the nanohole region and is independent of the excitation polarization. The fitting parameters for the FCS analysis (confocal and DNH case) are summarized in Table 3.1.

As compared to the first generation "antenna-in-box" platform [90], the DNH design has a comparatively lower detection volumes due to a better lateral and axial confinement. It is also significantly easier to fabricate using simple focused ion beam milling. The 25 nm

gap "antenna-in-box" design has been reported with 36 ± 6× fluorescence enhancement factors while using a simple double nanohole design we achieve a high 100× fluorescence enhancement values together with lower detection volumes. Further, the optical performance of the DNH is comparable with dimer gold antenna design. Towards the end of the next Chapter 4, we will discuss that using 20 nm gold dimer antennas we could reach on average 200-fold fluorescence enhancement factors with similar experimental conditions [22]. However, the efficient background screening in case of DNH design makes it more favorable for experiments at biologically relevant micromolar concentrations.

Effect of fluorophore concentration and quantum yield

After each FCS experiment, the coverslip containing DNH structures is rinsed with ethanol, dried with nitrogen and cleaned again under UV illumination for 10 minutes. Following this protocol, we are able to reuse the same sample several times without observing any major change in optical performance. To demonstrate the control and reproducibility of the experiments, we conduct a series of FCS measurements with increasing concentrations of fluorescent dye (Figure 3.6a). The increase in fluorophore concentration results in higher number of molecules within the detection volume and lower amplitude of the correlation curves. The linear relationship between the number of detected molecules (N^*) in the near field region with the fluorophore concentration further confirms the effective detection volume V_{eff} of 74 zL (Figure 3.6b). In addition, this volume corresponds very well to the geometrical dimensions of the apex region of $60 \times 25 \times 50$ nm^3 = 75 zL, considering a typical thickness of 50 nm for the intensity profile decaying evanescently inside the DNH obtained from numerical simulations as shown in insert of Figure 3.3a,b.

In Figure 3.7a we vary the excitation power and report the average fluorescence brightness per molecule for both polarization orientations with respect to the DNH apex region. With parallel orientation, count rates per molecule above 20 counts/ms are obtained, while for the confocal reference the fluorescence brightness saturates to values below 1 counts/ms in the presence of methylviologen. The experimental data points for increasing excitation power follows the general model of the fluorescence brightness $AI_{exc}/(1+I_{exc}/I_{sat})$, where I_{exc} is the excitation power, I_{sat} the saturation power, and A being a constant proportional to the molecular absorption cross-section, quantum yield and setup collection efficiency [92]. The fit results are summarized in Table 3.2.

Moreover the effect of the fluorophore's quantum yield is studied using different concentrations of methylviologen: 200 mM, 80 mM, and no methylviologen. Figure 3.7b

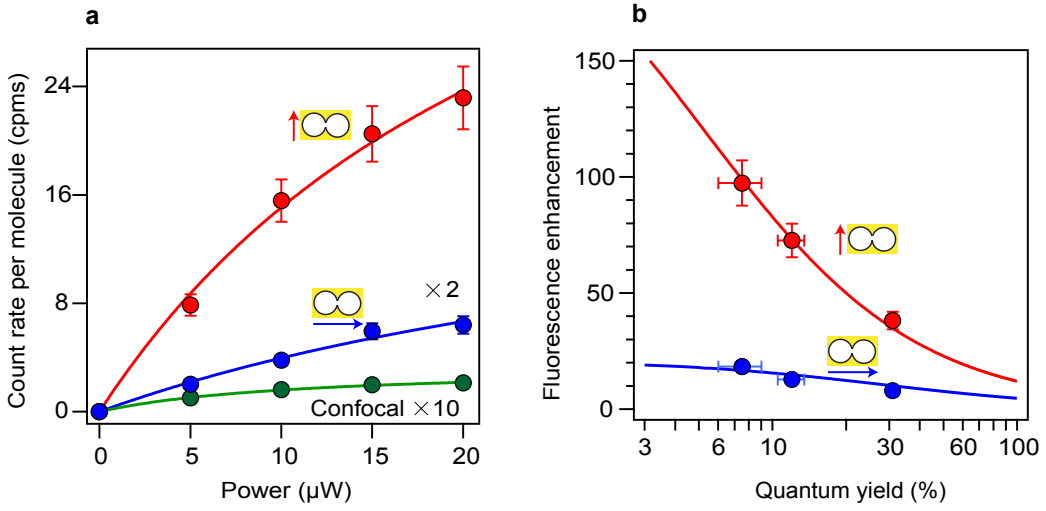

FIGURE 3.7: **Fluorescence brightness per molecule and influence of quantum yield.**(a) Fluorescence brightness per molecule versus the excitation power for Alexa Fluor 647 with 200 mM methylviologen (quantum yield $\sim 8\%$). The data for the double nanohole with perpendicular orientation respective to the apex (blue) and the reference confocal data (green) are multiplied respectively by $2\times$ and $10\times$. (b) Fluorescence enhancement factors with excitation polarization parallel (red) and perpendicular (blue) respective to the apex. For (b), the excitation power is 10 μW. Different concentrations of chemical quencher are used, corresponding to different values of quantum yield in solution: from left to right the data points correspond to methylviologen concentrations of 200 mM, 80 mM and 0. The solid lines (red for parallel and blue for perpendicular excitation polarization) are numerically obtained using the Equation 3.4.

Excitation	A (counts/ms/μW)	I_{sat} (μW)
Parallel	2.07 ± 0.21	26.7 ± 7.2
Perpendicular	0.49 ± 0.08	42.6 ± 26.1
Confocal	0.31 ± 0.01	11.1 ± 1.5

TABLE 3.2: **Fit results show fluorescence saturation at higher excitation powers with DNH.** The parallel excitation scheme shows fluorescence saturation occurring only at powers higher than 20 μW. All the FCS measurements with DNH are therefore recorded at 10 μW excitation powers.

summarizes the fluorescence enhancement results for both DNH polarization orientations for all three methylviologen cases. While Alexa Fluor 647 quantum yield is being quenched from 30% to 8%, the fluorescence enhancement factor increases significantly from 40 to 100×. This effect can be understood by describing the fluorescence enhancement factor η_F as function of the fluorophore's quantum yield in reference solution ϕ [93, 94]:

$$\eta_F = \frac{\eta_{exc}\,\eta_{em}}{(1-\phi)+\phi\zeta} \tag{3.4}$$

where η_{exc} is the excitation intensity enhancement, η_{em} is the radiative rate enhancement times the collection efficiency enhancement, and $\zeta = (\Gamma^*_{rad} + \Gamma^*_{loss})/\Gamma_{rad}$ is a parameter

describing the ratio of the radiative rate Γ^*_{rad} and the nonradiative rate to the metal Γ^*_{loss} due to ohmic losses relative to the dye's radiative rate Γ_{rad} in the confocal reference.

The value of ζ is actually equivalent to the enhancement of the local density of optical states (LDOS). The solid lines in the Figure 3.7b are numerically obtained using the Equation 3.4 and the value of ζ is set to the experimentally obtained LDOS enhancement from the fluorescence decay dynamics (as we will elaborate in next Section 3.3.2). Figure 3.7b shows an excellent agreement with the Equation (3.4) model and the experimental data for both polarization condition. Moreover, assuming that $\eta_{exc} \approx \eta_{em}$ and neglecting the gain in collection efficiency, the extrapolation of the data to $\phi \to 0$ indicates a local intensity enhancement of $\eta_{exc} \sim$14 for parallel and $\sim$4 for perpendicular orientation, in good agreement with the numerical simulations in Figure 3.3a,b.

3.3.2 Fluorescence photodynamics and LDOS enhancement

Fluorescence lifetime is the average time a fluorophore remains in the excited state following the excitation, and is defined as $\tau = \frac{1}{\Gamma_r + \sum \Gamma_{nr}}$, where Γ_{nr} denotes radiative process and $\sum \Gamma_{nr}$ indicates all possible non radiative pathways.

The lifetime and the quantum yield of a fluorophore are altered in the vicinity of nanoparticles as they open up many possible de-excitation routes for the excited molecule. In this section we elaborate all the decay rates with and without the DNH structures. Fluorescence lifetime experiments are performed by time-correlated single photon counting (TCSPC) technique. The experimental setup is as explained in the Chapter 2. In brief, the excitation source is switched to a picosecond pulsed laser diode operating at 636 nm (PicoQuant LDH-P-635, with 80 MHz repetition rate). A single mode optical fiber (from Thorlabs: P3-630A-FC-5) guarantees the same excitation spot in the sample plane for the FCS and TCSPC experiments.

As described for the FCS case, the TCSPC data analysis also needs additional care to accurately distinguish the decay dynamics between the molecules diffusing within the apex volume and in the nearby nanohole region. Therefore we use a bi-exponential model to the fluorescence decay traces obtained from the TCSPC measurements: first contribution from N^* molecules within the apex region with brightness Q^*, and second being from the N_0 background molecules with brightness Q_0 diffusing within the two nanoholes.

Figure 3.8 shows the amplitude-normalized fluorescence decay traces for the confocal reference and the DNH with excitation polarization parallel and perpendicular to the apex region (colored points being experimental data and black lines being the fits).

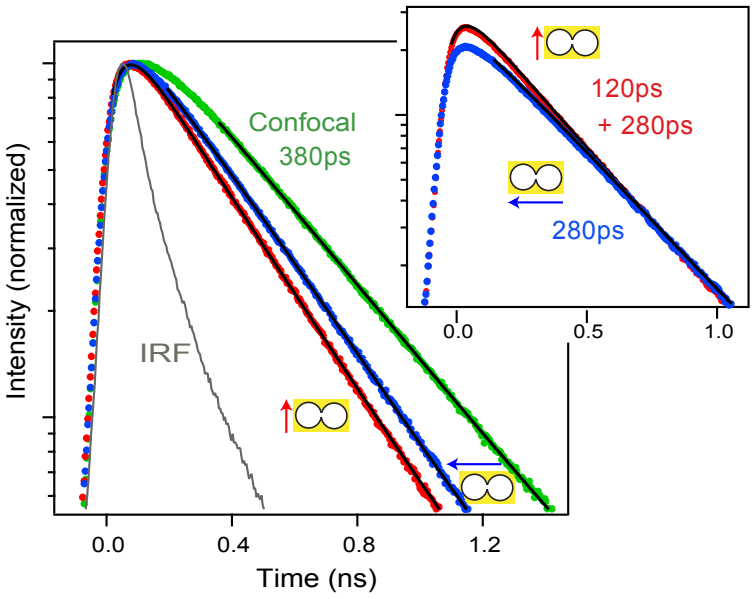

FIGURE 3.8: **Fluorescence decay dynamics at the DNH apex.** Typical fluorescence decay traces with excitation light parallel (red) and perpendicular (blue) to the apex region. The decay trace with the diffraction-limited volume (green) provides the reference for Alexa Fluor 647 with 200 mM methylviologen. Black lines are numerical fits used to determine the fluorescence lifetime indicated on the traces. IRF denotes the instrument response function. For a supplementary comparison between parallel and perpendicular cases, the inset displays the traces normalized so that the longer time decay component has a similar amplitude for both cases. The additional short lifetime contribution representative of the apex region clearly emerges when the polarization orientation is parallel to the apex.

The TCSPC data shows acceleration of the decay dynamics from confocal to DNH and from perpendicular to parallel orientation of the excitation light. For confocal case, the TCSPC data is fitted with a single exponential model and in the presence of 200 mM methylviologen, the Alexa Fluor 647 confocal fluorescence lifetime is 380 ps. For the DNH with parallel orientation, bi-exponential decays are observed (see insert in Figure 3.8): a fast 120 ps decay corresponding to the N^* molecules in the gap, and a longer 280 ps decay for the N_0 molecules outside the gap. For the DNH with perpendicular orientation, the presence of the nanoholes further reduce this lifetime to 280 ps (1.35× lifetime reduction), a value that is similar to the lifetime reduction obtained with single gold aperture as reported in our earlier works [92]. Mono-exponential decay dynamics seen in the case of perpendicular excitation behaves exactly similar to that of the longer time in parallel case. This further confirms that the background fluorescence mainly stems from the adjacent nanoholes. For each case, the model takes into account the temporal resolution of our apparatus by computing the de-convolution of the exponential decay with the instrument response function (IRF, full width at half maximum 120 ps) [92, 93].

With the use of methylviologen, the chemical quenching rate Γ_q represents a large fraction of the total decay rate Γ_{tot} (which is inverse of the fluorescence lifetime). Therefore in order to accurately estimate the local density of optical states (LDOS) enhancement with the DNH, the influence of the chemical quenching rate Γ_q must be taken into account prior to computing the ratio of decay rates.

Although the LDOS encompasses both radiative and non-radiative transitions set by the photonic environment (such as energy transfer to the free electrons in the metal), the LDOS is not proportional to the chemical quenching rate introduced by the presence of methylviologen [95, 96].

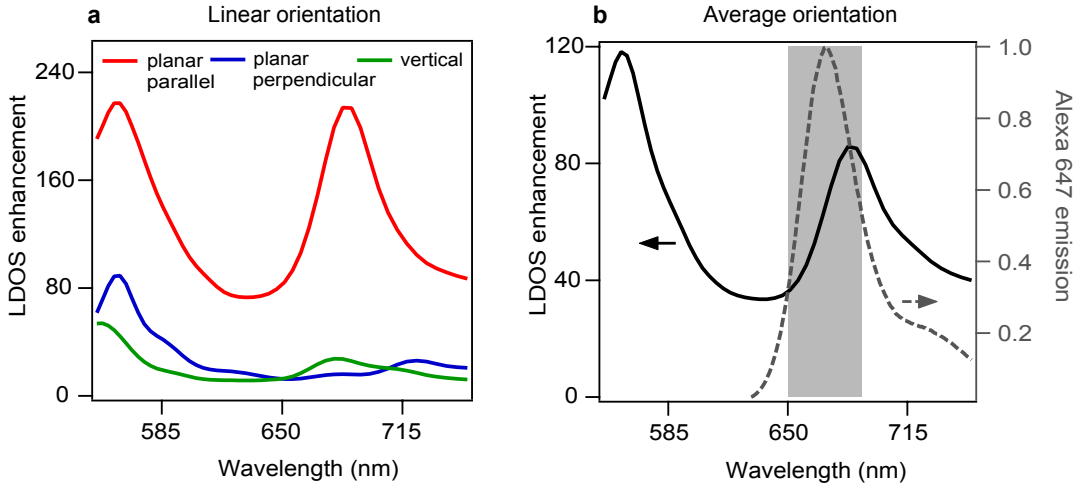

FIGURE 3.9: **Numerical simulations of LDOS enhancement for a dipolar emitter located in the center of the DNH gap.** In (a), three different dipole orientations are displayed, the case when the dipole is oriented parallel to the apex provides the highest LDOS enhancement. In (b), the orientation-averaged LDOS enhancement is plotted as function of the emission wavelength (solid line). The normalized Alexa Fluor 647 emission spectrum is shown in dashed gray line, and the 650-690 nm region used experimentally for fluorescence collection is indicated.

Thus to estimate the amount of decay rate that actually depend on the LDOS, we express the dye's total decay rate in the confocal case as $\Gamma_{tot} = \Gamma_{rad} + \Gamma_{nr} + \Gamma_q$, where Γ_{rad} denotes the radiative rate, and Γ_{nr} being the internal non-radiative decay rate. In the presence of the DNH, the decay rate now becomes $\Gamma^*_{tot} = \Gamma^*_{rad} + \Gamma_{nr} + \Gamma_q + \Gamma^*_{loss}$. The supplementary term Γ^*_{loss} is being added to account for non-radiative energy transfer to the metal, and we assume that the internal non-radiative decay rate Γ_{nr} and the methylviologen quenching rate Γ_q are independent of the presence of the DNH [95]. Finally, the LDOS enhancement is expressed as $(\Gamma^*_{rad} + \Gamma^*_{loss})/\Gamma_{rad}$, keeping only the rate influenced by the photonic environment, and taking into account non-radiative

transfer to the metal. This expression of the LDOS enhancement corresponds to the quantity ζ used in Equation 3.4.

	Γ_{rad}	Γ_{loss}	Γ_{nr}	Γ_q	Γ_{tot}	ϕ
Confocal	0.21	-	0.67	1.75	2.63	0.08
DNH perpendicular	0.84	0.31	0.67	1.75	3.57	0.24
DNH parallel	2.94	2.97	0.67	1.75	8.33	0.35

TABLE 3.3: **Fluorescence photokinetic rates inside the DNH.** Γ_{rad} radiative rate, Γ_{loss} non-radiative transitions to the metal, Γ_{nr} intramolecular non-radiative transitions, Γ_q methylviologen quenching rate, Γ_{tot} total decay rate (inverse of fluorescence lifetime), ϕ quantum yield. All rates are expressed in ns^{-1}, and the typical uncertainty is $\pm$ 0.05 ns^{-1}.

Next we estimate the internal non-radiative rate $\Gamma_{nr} = 0.67$ ns^{-1} and the quenching rate $\Gamma_q = 1.75$ ns^{-1} using the knowledge of the 30% quantum yield of Alexa Fluor 647 in pure water solution which is quenched to 8% by 200 mM methylviologen. A detailed Stern-Volmer analysis is presented in the supporting information of Ref. [90]. We can now subtract these values of Γ_{nr} and Γ_q from the total decay rate Γ^*_{tot} with the DNH so as to estimate the part depending on the LDOS.

For the DNH with perpendicular orientation, we get $\Gamma^*_{rad} + \Gamma^*_{loss} = 1.15$ ns^{-1} and a LDOS enhancement of 5.5× which is characteristic of nanoholes [92]. For the parallel orientation, the apex region further influences the decay rates so that $\Gamma^*_{rad} + \Gamma^*_{loss} = 5.9$ ns^{-1}. This corresponds to a LDOS enhancement of $5.9/0.21 = 28\times$, demonstrating the significant influence of the DNH apex on the LDOS. The influence of photonic environment over the emission properties of fluorescence dyes (in particular for enhancing FRET and LDOS) has been studied extensively in Ref. [97].

Table 3.3 provides a complete overview of the fluorescence photokinetics alteration in the DNH together with the different rates in the confocal case. For the enhancement of the radiative rate Γ_{rad}, we use the value of η_{em} deduced from Figure 3.7b. The analysis of Table 3.3 also reveals the increase of the non-radiative losses Γ_{loss} to the metal, which contribute to quench the fluorescence emission. Fortunately, this electromagnetic quenching is compensated by the simultaneous increase in radiative rate Γ_{rad} (Purcell effect), so that the effective quantum yield ϕ of the dye is actually increased by the presence of DNH structure.

To confirm the experimental results, we compute the LDOS enhancement as the relative increase in power released by a dipolar emitter located at the center between the DNH apex [94, 98]. Figure 3.9a shows the LDOS enhancement for a dipole with all three different orientations within the DNH. Clearly, the case of orientation parallel to the

Numerical simulations of the LDOS enhancement for the dipole with all three different orientations within the DNH were done by Ahmed A Al Balushi, University of Victoria, Canada.

DNH apex yields a maximum LDOS enhancement up to 210×. Further, we plot the orientation-averaged LDOS enhancement factors within the 650-690 nm range in Figure 3.9b, and obtain a mean 60× LDOS enhancement. This value is within a factor 2 of the experimental observation, which is satisfactory considering the 3D spatial averaging in the experiments, the limited temporal resolution of our apparatus, and possible minor nanofabrication deficiencies. In addition, the simulations result shows that the DNH design bears a resonance around 685 nm that covers well the Alexa Fluor 647 emission spectrum.

3.3.3 Stencil lithography for large scale nanoantenna fabrication

We further extend the DNH concept for single-molecule detection adopting a different fabrication procedure based on lithography and template stripping. This technique based on the use of nanoscale shadow mask achieves large scale antenna structures with reduced apex volumes. Figure 3.10a shows a typical SEM image of the structure with ∼20 nm nominal apex gap between two nearby nanoholes achieved by lithography fabrication. When compared to the FIB milled structures (Figure 3.2), the lithography based fabrication technique achieves sharp tips, and thus potentially a better candidate for enhanced single-molecule fluorescence detection. The fluorescence experiments are then carried out as explained in the earlier case of FIB milled structures, with solution containing Alexa647 fluorophore along with 200 mM methylviologen as chemical quencher.

	Confocal	**Double nanohole**	
Excitation	Linear	Parallel	Perpendicular
F (counts/ms)	1090	81	42
G(0)-1	0.16×10^{-3}	352.4×10^{-3}	94.4×10^{-3}
N	6200	0.8	11
τ_d (μs)	62	2	25
Q (counts/ms)	0.17	53	3.8
Detection volume (zL)	500×10^3	65	10^3
Fluorescence enhancement		312	22
Volume reduction		7700	500

TABLE 3.4: **Fitting parameter results for the FCS curves for DNH fabricated by lithography (Figure 3.10c).** The FCS experiment is performed with 20 μM concentration of Alexa Fluor 647 (along with 200 mM methylviologen) at 10 μW excitation power. Following the Equation (3.3) we use $N_0 = 11$ and $Q_0 = 3.8$ counts/ms as control parameters and compute $N^* = 0.8$ and $Q^* = 53$ counts/ms for DNH parallel excitation configuration.

The fluorescence time traces are then recorded with excitation light parallel and perpendicular to the apex of the DNH structure and are displayed in Figure 3.10b. The time

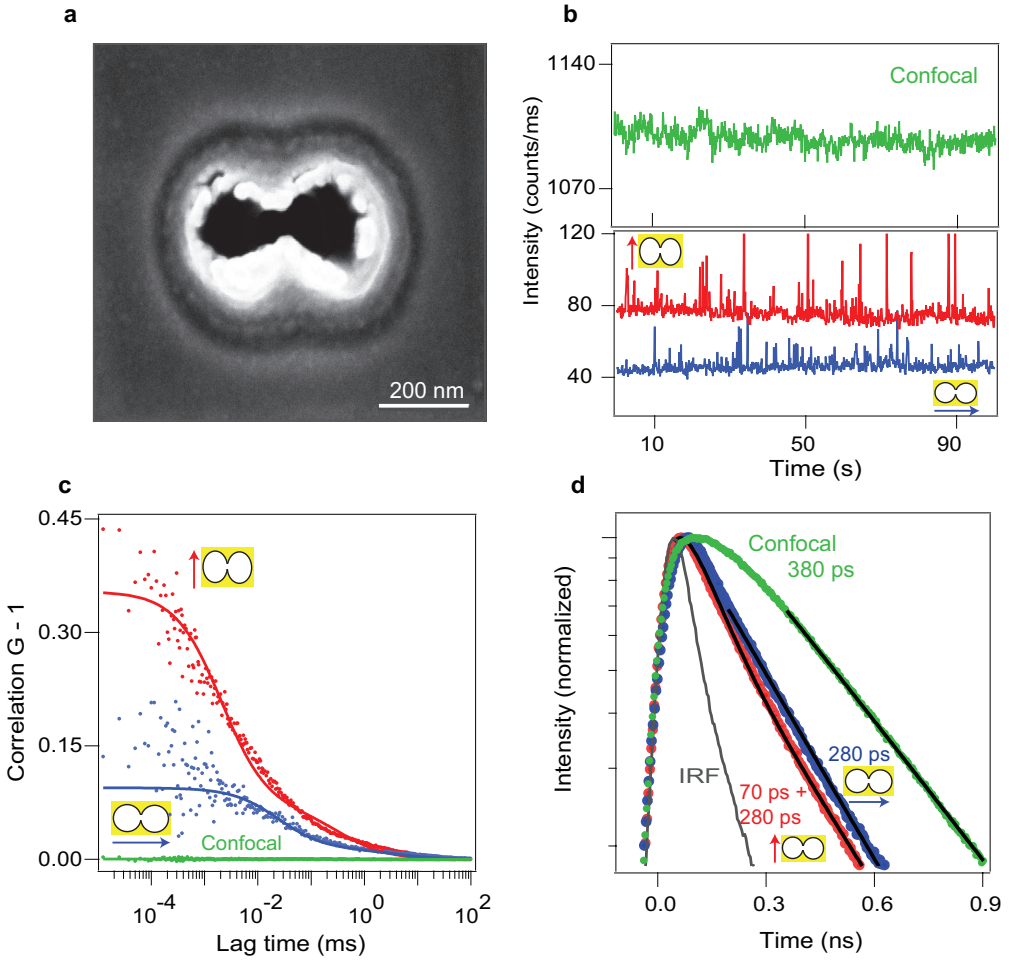

FIGURE 3.10: **FCS and TCSPC results obtained with DNH fabricated by lithography technique.** (a) Scanning electron microscope image of the structure fabricated by stencil lithography. (b) Fluorescence time trace with excitation light parallel (red) and perpendicular (blue) to the apex region. The time trace found for the confocal case is shown in green for comparison. FCS correlation function of the traces are shown in (c). For all cases, the Alexa Fluor 647 concentration 20 μM with 200 mM of methylviologen as chemical quencher, and the excitation power is 10 μW. Dots are experimental points, lines are numerical fits. The fit parameters are summarized in Table 3.4. (d) Amplitude-normalized fluorescence decay traces with excitation light parallel (red) and perpendicular (blue) to the apex region. The binning time for the traces in (b) is 100 ms.

	Γ_{rad}	Γ_{loss}	Γ_{nr}	Γ_q	Γ_{tot}	ϕ
Confocal	0.21	-	0.67	1.75	2.63	0.08
DNH perpendicular	0.84	0.31	0.67	1.75	3.57	0.24
DNH parallel	5.25	6.63	0.67	1.75	14.3	0.35

TABLE 3.5: **Fluorescence photokinetic rates inside DNH by lithography.** Γ_{rad} radiative rate, Γ_{loss} non-radiative transitions to the metal, Γ_{nr} intramolecular non-radiative transitions, Γ_q methylviologen quenching rate, Γ_{tot} total decay rate (inverse of fluorescence lifetime), ϕ quantum yield. All rates are expressed in ns^{-1}. For the parallel orientation, $\Gamma^*_{rad} + \Gamma^*_{loss} = 11.88$ ns^{-1}, and this corresponds to the LDOS enhancement of $11.88/0.21 = 57\times$.

trace with light parallel to the apex region (red) shows frequently occurring brighter fluorescence burst events when compared to the trace with perpendicular excitation (blue). This confirms the nanoscale near field localization in the apex volume with parallel excitation, and thereby the molecule experiencing enhanced fluorescence. These fluorescence time traces are further analyzed by fluorescence correlation spectroscopy to quantify the hot spot detection volume and fluorescence enhancement factor. Figure 3.10c shows the correlation curves for both the excitation case for the DNH along with confocal case (in green) and clearly shows the dependency on the polarization orientation respective to the apex volume. Unlike in confocal mode (without DNH) where the correlation amplitude is barely detectable at 0.16×10^{-3} (corresponding to about 6000 molecules in the 0.5 fL detection volume), the same with excitation parallel to the DNH apex yields remarkably higher correlation amplitude (352.4×10^{-3}) with high fluorescence brightness. Using the two-species model to analysis FCS correlation curves as introduced at the beginning of this chapter, we quantify an average number of $N^* = 0.8$ molecules with fluorescence brightness per molecule $Q^* = 53$ counts/ms, which corresponds to a fluorescence enhancement of $Q^*/Q_{conf} = 312\times$ together with a 8000-fold volume reduction to confocal scheme. The fitting results for all the correlation curves are summarized in Table 3.4.

Finally we compute the fluorescence lifetime analysis in these DNH made by stencil lithography by using time-correlated single photon counting technique, and compute the complete photokinetic rates as before. Figure 3.10d shows the normalized fluorescence decay traces for the DNH with excitation polarization parallel (red) and perpendicular (blue) together with the confocal reference (green). As the new energy decay routes are opened by the presence of DNH and thus the increased radiative emission rate for the dipole emitter withing the apex (together with non-radiative energy transfer to the metal) the TCSPC measurement shows significant reduction in fluorescence life-time with DNH (and parallel excitation) when compared to the confocal reference. As expected, the parallel excitation case shows bio-exponential decay dynamics: 70 ps originating from the sharp apex region and 280 ps essentially due to the fluorophores excited within the nearby nanoholes. TCSPC measurement with the perpendicular polarization (blue in Figure3.10d) which shows mono-exponential decay dynamics with decay time being 280 ps further supports the contribution of background fluorophores being excited within the nanoholes.

Further, taking into account the influence of the chemical quenching rate set by methylviologen, we compute LDOS enhancement of $11.88/0.21 = 57\times$ (as for the parallel orientation $\Gamma^*_{rad} + \Gamma^*_{loss} = 11.88$ ns^{-1}). As shown in Table 3.5, the LDOS enhancement for the perpendicular case remains comparable to that with the FIB milled structure (and

consistent with the influence of single nanometric apertures). However, in parallel excitation configuration and DNH with sharp tips and reduced apex gap we are able to see the influence in the decay dynamics as represented by a higher 60× LDOS enhancement.

3.4 Summary

We demonstrate the effectiveness of double nanohole structures to enhance single molecule fluorescence at micromolar concentrations by analyzing the fluorescence temporal dynamics from pico-to millisecond time scales. While DNH structures have been broadly applied for optical trapping of nano-objects, prior to this PhD project there has been no report of their use to enhance the fluorescence of single molecules. The polarization-dependent response of this design allows to selectively extract the relevant signal from the apex region to quantify the nanoscale DNH volumes.

Using fluorescence correlation spectroscopy, we measure the near field apex volume to $\lambda^3/3800$, realizing a volume reduction of 7000-fold as compared to diffraction-limited confocal setups. The high intensity confinement goes with fluorescence enhancement up to 100-fold, together with microsecond transit time, 30-fold LDOS enhancement and single molecule sensitivity at concentrations exceeding 20 μM. As compared to similar gap size 25 nm antenna-in-box platform, the DNH design shows comparatively lower detection volumes with high fluorescence enhancement factors. Although higher enhancement factor (up to 1000-fold) was reported with smaller 10 nm gap antenna-in-box platform, the same design could only yield 40× fluorescence enhancement for 25 nm gap size (as our DNH design) in similar experimental conditions. In addition, the DNH spectral resonance occurs in the range 550-700 nm enabling a better spectral overlap with the emission band of most common red fluorescent dyes.

Although the "antenna-in-box" provides a higher gap intensity due to the nanoantenna being disconnected from the metal film, the DNH partly compensates this feature by lower non-radiative losses and a better spectral overlap with the resonance. In addition, the DNH has a comparatively lower detection volume when compared to the FIB milled antenna-in-box design, due to a better lateral and axial confinement. The apex between the two holes directly realizes sharp radii of curvatures and nanometer gap sizes, and the optically thick metal film efficiently screens out the fluorescence form the background molecules, making DNH a attractive choice for single-molecule fluorescent detection in concentrated solutions.

We further discussed that should we aim for higher enhancements, there is plenty of room to achieve via optimization as shown by the lithography based DNH leading to

higher fluorescence enhancement of 300× and 57× LDOS enhancement. These findings are of interest to a broad scientific community working on optical nanoantennas for fluorescence enhancement, optical trapping, and single-molecule detection. The DNH provides an efficient design to reach nanometer confinement of light, with a comparatively much simpler nanofabrication as compared to other designs (such as antenna-in-box and bowtie antennas). The high optical performance and the robust design open promising perspectives to study complex biochemical dynamics at physiological concentrations.

However meeting the broad expectations of plasmonics requires nanogap antennas featuring sub-10 nm gap sizes, high fabrication throughput and planar surface topology. In addition, an alternative paradigm to compensate the losses induced my metallic structures are desired for experiments requiring either temperature control or high excitation powers. In the next chapter, we explore all-dielectric nanogap antennas and compare the optical performance with their plasmonic counterparts. Finally in Chapter 5 and Chapter 6, we address the planarity and reproducibility issues. Using planar nanoantennas with narrow gaps and sharp edges we demonstrate their relevance in single-molecules detection technique (Chapter 5) and for investigating membranes dynamics in living cells (Chapter 6).

Chapter 4

Dielectric nanogap antennas for single-molecule detection

Plasmonic metal nanostructures are at the heart of nanophotonics research, mainly because of their ability to localize electromagnetic energy into nanoscale spatial dimensions. However, energy transfer to the free electron gas in the metal generates losses, which leads to severe quenching of the fluorescence emission [15, 99] thereby limiting biologically-inspired applications. In this chapter, we demonstrate the effectiveness of an alternative approach using all-dielectric nanoantennas based on silicon dimers to enhance the fluorescence detection of single molecules. For a dimer geometry silicon nanoparticles with 20 nm gap, we achieve fluorescence enhancement factors above 200-fold and isolate detection volumes down to 140×10^{-21} L, equivalent to a 3600-fold reduction below the classical diffraction limited confocal volume. In addition, optical performance of gold nanoantennas with similar structure design will also be discussed.

This project was carried out in collaboration with the teams of Dr. Nicolas Bonod (Institut Fresnel, Marseille), Dr. Sébastien Bidault (Institut Langevin, Paris) and Dr. Mathieu Mivelle (Université Pierre et Marie Curie, Institut des NanoSciences de Paris).

The contents of this chapter have been published in:

Regmi, R., Berthelot, J., Winkler, P.M., Mivelle, M., Proust, J., Bedu, F., Ozerov, I., Begou, T., Lumeau, J., Rigneault, H., García-Parajo, M.F., Bidault, S., Wenger, J. and Bonod, N., 2016. All-dielectric silicon nanogap antennas to enhance the fluorescence of single molecules. *Nano Letters*, 16(8), pp.5143-5151.

Punj, D., **Regmi, R.**, Devilez, A., Plauchu, R., Moparthi, S.B., Stout, B., Bonod, N., Rigneault, H. and Wenger, J., 2015. Self-assembled nanoparticle dimer antennas for plasmonic-enhanced single-molecule fluorescence detection at micromolar concentrations. *ACS Photonics*, 2(8), pp.1099-1107.

4.1 All-dielectric platform: Experimental strategy

The resonant excitation of the surface plasmons in metallic nanoantennas (with various shapes and gap sizes) have been used to drastically enhance the interactions between a single emitter and its surrounding photonic environment [100], leading to giant luminescence enhancement [17, 20, 61, 90], ultrafast emission in the picosecond range [101], and directional emission control [93, 102]. All these features make optical nanoantennas ideal for the ultrasensitive biodetection of single molecules and enhanced spectroscopy. However, as the fluorescence emissions is quenched in the immediate vicinity of metallic structures, a compromise has to be made between the near field enhancement and the losses. Additionally, interband transitions in the metal induce absorption at the laser frequency and Joule heating of the nanoantenna and its environment [15, 103]. This brings further limitations in the applications which require either temperature control (such as biosensing) or high excitation powers (such as non-linear spectroscopy).

It is important to note that the plasmonic heating effects however have been used as a merit in the context of thermo plasmonics where metallic nanostructures are used as nano-sources of heat to selectively ablate tumors or to control the cell migration [104, 105]. Apart from the context where metal nanoparticles can been used as photothermal agents, applications involving fluorescence bio-sensing and monitoring dynamics of individual proteins and molecules require minimum perturbation in living systems. Mainly to circumvent the losses inherently present in metal nanoantennas, the use of dielectric nanoparticles has recently attracted significant research and industrial interest. Various dielectric materials such as silicon, germanium and gallium phosphide have been recently demonstrated as potential alternative contenders to metals [106, 107, 108].

As compared to gold and silver, these dielectric materials feature weaker absorption coefficients in the visible and the near infrared [109]. And most importantly, similar to their metal counterparts the sub-wavelength dielectric particles also support spectral resonances (commonly known as Mie resonances). Mie resonances are low order mode, typically dipolar which can easily be excited by increasing the optical contrast between the material and its surrounding. The postulation of the resonant electromagnetic interaction of small dielectric particles dates back to 1908 when G. Mie first derived the exact theoretical solutions of light scattering by small spherical dielectric particles (know as Mie theory) by solving the Maxwell equations [110]. As the sub-wavelength dielectric particles also resonantly interact with light, they too can efficiently enhance the local near-field intensity [111, 112, 113, 114, 115]. It is important to note that this approach is conceptually different from dielectric microcavities [116, 117] such as dielectric photonic crystal cavities [118, 119] or planar concentrators [120, 121] that feature high quality

Q-factors. Although sub wavelength-sized dielectric particles exhibit low Q-factor, this is however compensated by the small mode volumes [122].

In addition, unlike spherical metal nanoparticles which feature only electric modes, high refractive index dielectric nanoparticles have both electric and magnetic modes (characterized by peaks in the scattering coefficients) that can be of similar strengths [107, 108]. The presence of both electric and magnetic modes (feature popularly known as *magnetic light*) offers novel opportunities to tailor the light scattering or the chirality of light emission [123, 124, 125, 126]. Further, they have been demonstrated to enhance the radiative decay rate constants of nearby emitters [127, 128], improve the directivity of dielectric optical antennas [112, 129], and enhance the Raman scattering process [130, 131]. All these features open bright perspectives for all-dielectric optical nanoantennas for various single-molecule and biologically relevant experiments.

In particular, dielectric silicon microspheres have been used for strong three-dimensional sub-diffraction confinement of light [132] and to efficiently excite and increase the collection efficiency of single-molecule fluorescence [133]. Other higher refractive index material such as polystyrene spheres (dielectric constant 2.6) with 1-5 μm diameter deposited on a glass substrate were demonstrated for direct observation of 3-D photonic nanojets beams [134, 135]. These micron sized high index spheres have also been used to enhance the fluorescent detection of on-chip immunoassays [136] and for fast detection of single nanoparticles in flow [137]. Apart from the characteristic Mie resonance, dielectric microspheres are know to exhibit other higher order modes (such as Whispering gallery modes) [138, 139], which is beyond the scope of this thesis.

More recently, silicon dimer structures with nanometric gaps (silicon nanogap antennas) have been reported to enhance the fluorescence of a dense layer of dyes covering the nanostructures [113, 130]. However, issues related to photobleaching and surface coverage density challenge the estimation of the fluorescence enhancement factor. Measurements down to the single molecule level have never been reported so far on silicon nanoantennas. A clear quantification at the single molecule level is important to conclusively compare the experimental results to numerical simulations and discuss the physical origin of the fluorescence enhancement on all-dielectric nanoantennas.

Here we use silicon dimer antennas to enhance the fluorescence emission of single molecules diffusing in solutions of micromolar concentration. Fluorescence correlation spectroscopy (FCS) is implemented to analyze the fluctuations on the fluorescence signal and quantify the average fluorescence brightness per emitter and the size of the detection volume. The results are independently validated by fluorescence burst analysis technique, TCSPC measurements and numerical simulations. This project demonstrates well that all-silicon

nanoantennas are a valid alternative to plasmonic devices for enhanced single molecule fluorescence sensing, with a sensitivity down to the single-molecule level.

4.2 Silicon dimer nanoantenna fabrication

Silicon nanogap antennas are fabricated by creating a mask with electron beam lithography in a poly(methyl methacrylate) PMMA layer coated on a 60 nm thick silicon layer. Amorphous silicon layer is deposited on a 150 μm thick microscope glass coverslip by Plasma Assisted Reactive Magnetron Sputtering (Buhler, HELIOS) [140]. This results in an uniform 60 nm thick layer of silicon. The precise thickness control of the deposited layer is carried out using an in-situ optical monitoring system which measures the evolution of the monochromatic transmission during deposition. The monitoring wavelength is chosen to 1500 nm. At this wavelength the absorption of silicon layers is negligible and the real part of the refractive index is $\sim$3.695.

After deposition, the samples are cleaned in successive ultrasound baths in acetone and isopropyl alcohol (IPA, propan-2-ol), dried with nitrogen gas and exposed to oxygen plasma at 150^o C (Nanoplas, France) for 10 minutes. A 60-70 nm thick commercial PMMA positive e-beam resist (ARP-679, Allresist, Germany) diluted at 2% in ethyl lactate solvent is spin-coated at 4000 rpm onto the silicon surface and baked on a hotplate to remove the remaining solvent and harden the PMMA layer. A second conducting polymer layer (SX AR-PC 5000/90.1 from Allresist, Germany) of thickness of 30 nm is spin-coated on the first PMMA e-beam resist to reduce the sample charging and to increase the EBL resolution.

The samples are then exposed to electron beam using an EBL tool (Pioneer, Raith, Germany) equipped with field emission gun (FEG) electron source (acceleration voltage of 20 kV, apertures of 7.5 and 10 μm, beam current of 18 to 30 pA). We varied both the designed distances between the features and the exposure dose in order to finely tune the nanogap between the particles. After exposure, the conducting layer is removed in deionized water, and the PMMA is developed in a commercial solution (AR 600-55 from Allresist GmbH) for 60 seconds. A 15 nm thick metal nickel mask is then evaporated on the sample under vacuum (Auto 306 tool from Edwards, UK). After metallization, a lift-off process is performed in ethyl lactate using ultrasonic cleaning bath. During the lift-off, the remaining e-beam resist and the excess of nickel are removed. Finally, the sample is rinsed in deionized water and dried under nitrogen flow. The unprotected

Nanofabrication process was performed by Dr. Johann Berthelot (Institut Fresnel) in PLANETE CT PACA cleanroom facility, CINAM, Marseille (collaborators: Julien Proust, Frédéric Bedu, Igor Ozerov, Thomas Begou, Julien Lumeau).

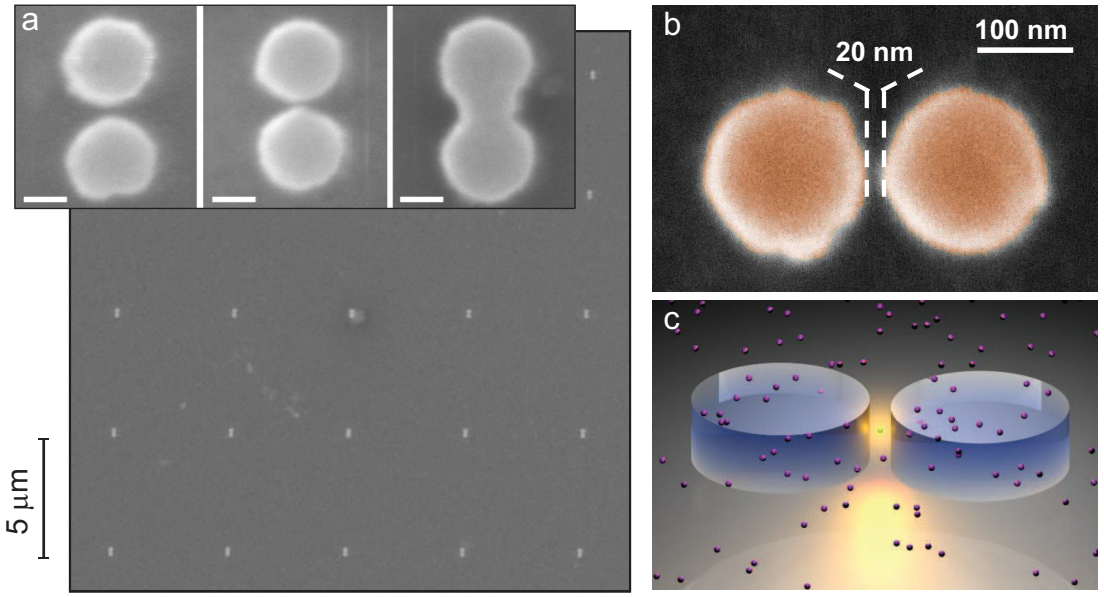

FIGURE 4.1: **SEM images of silicon nanogap antennas for enhanced single-molecule fluorescence.** (a) SEM image of an array of silicon dimer antennas with gaps measured ∼20 nm. The inset shows SEM images of silicon dimers as the function of e-beam exposure dose coefficient allowing to fabricate the 30 nm gap (dose 0.8×120 μC/cm^2) and the 20 nm gap antennas (dose 0.9×120 μC/cm^2). For higher doses, the antennas are bridged. The scale bar is 100 nm. (b) Scanning electron microscope image of a representative silicon dimer antenna with 20 nm nominal gap. The silicon thickness is 60 nm and each silicon disk is 170 nm in diameter. (c) Principle of the experiment: a silicon dimer antenna confines light in the nanoscale gap volume and enhances the fluorescence of single molecules diffusing in solution.

areas are etched in a RIE tool (MG-200, Plassys, France) by a gas mixture containing SF_6, O_2 and CHF_3 (respective fluxes 20, 8 and 5 sccm) for 10 seconds, alternated with a pure O_2 plasma for 5 seconds. Excited SF_6 is known to efficiently etch the silicon and the admixture of CHF_3 gas is used to passivate the vertical feature walls and to etch the silicon oxide on the very reactive silicon surfaces during the process. This process offers a very good etching anisotropy and nearly vertical walls of the structures. After RIE, the remaining nickel is removed chemically in the acid solution of HCl and $FeCl_3$. Finally, the samples are rinsed in deionized water and dried under nitrogen flow. Scanning electron microscopy images are performed on a FEI DB235 microscope with field emission gun and 5 kV acceleration voltage, providing about 4-5 nm spatial resolution.

Figure 4.1 shows an array of silicon dimer antennas with 5 μm pitch size (a) and a representative ∼20 nm nominal gap Si-dimer nanoantenna imaged with SEM (b). The inset in a shows image of silicon dimers as the function of e-beam exposure dose allowing to fabricate the 30 nm gap (dose 0.8×120 μC/cm^2) and the 20 nm gap antennas (dose 0.9×120 μC/cm^2). And for higher doses, the antennas are bridged. Figure 4.1c the

sketch depicting the principle of our experiment: a silicon dimer nanoantenna confining light in the nanoscale gap for enhanced single-molecule fluorescence detection.

4.3 Near field enhancement and nanoantenna resonance

We perform finite-difference time-domain (FDTD) modeling using RSoft Fullwave software-Version 6.0 and access the near field strength for silicon dimer geometry. We study the gap size influence and the distribution of near field with respect to the polarization of incoming excitation light. The model considers perfectly matched-layer boundary condition on all faces and the computation is done with 1 nm mesh size. The nanoantenna parameters are set to reproduce the fabricated devices: cylindrical shape with 170 nm diameter, 60 nm height and 20 or 30 nm gap separation. A glass substrate with refractive index 1.52 and water super-substrate are also considered. The excitation wavelength is 633 nm and the permittivity for amorphous silicon is taken from [109, 141].

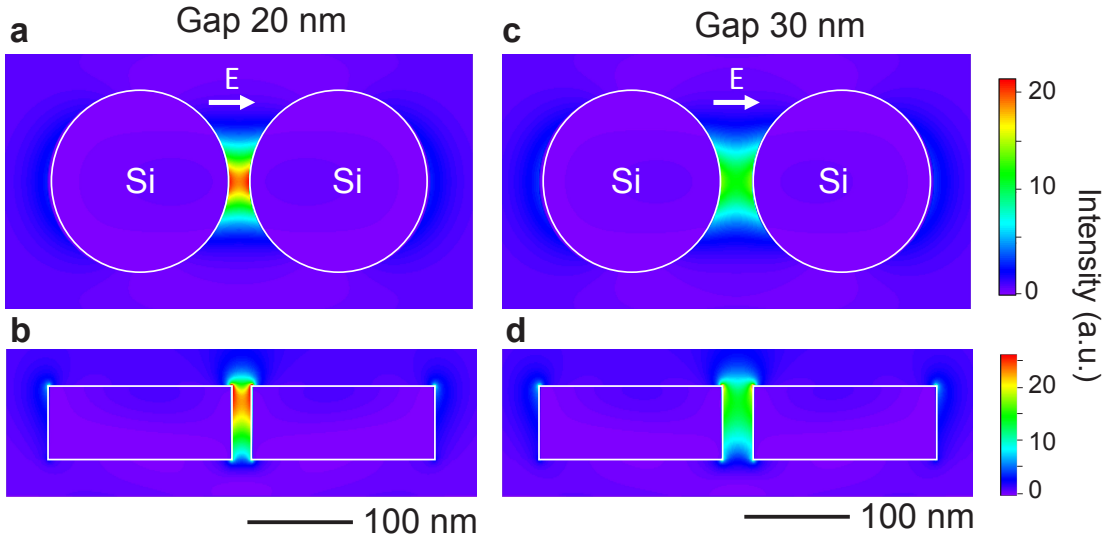

FIGURE 4.2: **Near field enhancement and gap size influence in silicon nanogap antenna.** FDTD simulations of the electric field intensity distributions around the silicon dimer of 170 nm diameter with 20 nm (a,b) and 30 nm (c,d) gap separations. The silicon antenna is illuminated at $\lambda = 633$ nm in normal incidence from the glass substrate with a linear electric field polarized parallel to the dimer axis. The images in (a,c) correspond to the horizontal plane crossing the center height of the dimer, while the images (b,d) are vertical cross-sections along the main dimer axis. The color scales are common for (a,c) and (b,d) to ease comparison between the gap sizes.

Figure 4.2 display the near field distributions for 20 nm (a,b) and 30 nm (c,d) gap silicon antenna with incident electric field polarized parallel to the dimer axis. An electric field intensity enhancement around 22× is achieved with the 20 nm gap antenna when the incident polarization is along the dimer axis. As the gap size is increased to 30 nm,

the intensity enhancement drops to 12×. This reveals the ability of amorphous silicon dimer antennas to confine the electric field energy in their nanogaps. Further, as seen in Figure 4.2a,c the spatial distribution of the near field is typical of an electric dipole resonance.

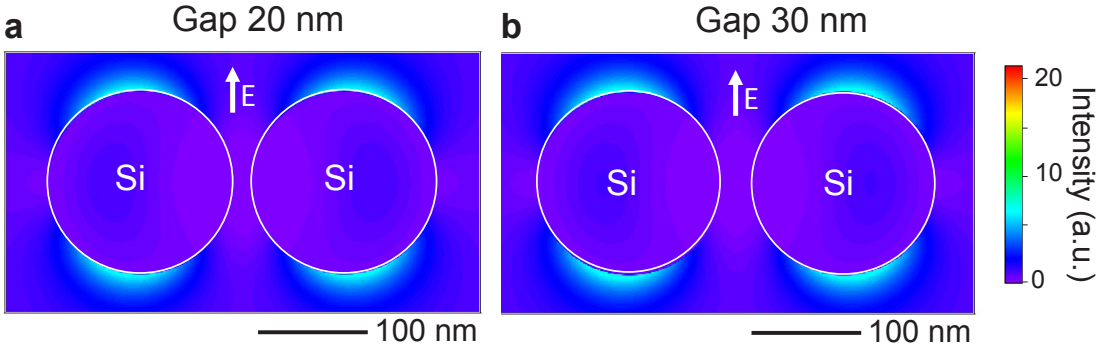

FIGURE 4.3: **Perpendicular excitation in silicon nanogap antenna shows no near field localization.** FDTD simulations of the electric field intensity distribution for excitation light perpendicular to dimers with 20 nm (a) and 30 nm (b) gap sizes. The simulation indicates no influence of the gap size in near field strength and thus no near field localization with this excitation polarization. The antenna is illuminated at λ=633 nm in normal incidence from the glass substrate with a linear electric field polarized perpendicular to the silicon antenna major axis.

Figure 4.3 shows the FDTD modeling for the transverse polarization yielding no significant near field enhancement in both 20 nm (a) and 30 nm (b) gap separations. This further highlights the strong influence of the incident polarization on the near field enhancement within the nanogap. To further emphasize polarization dependency and resonant feature of silicon dimer antennas, we carry optical spectroscopy on individual nanoantennas in transmission mode with a custom-build confocal microscope setup. A 250 W Quartz Tungsten Halogen lamp (Oriel QTH) is used as incident illumination source. The light is then polarized using a Glan-Thompson linear polarizer and focused from the top of the sample with a 10× objective (Olympus, NA 0.22). The light scattered by the nanostructure is collected by a 100× microscope objective with 10 mm long working distance (Mitutoyo, NA 0.7). The collected light is then focused with an optical fiber with a core diameter of 62.5 μm on the spectrometer (Isoplane, Princeton Instruments) equipped with a Peltier-cooled CCD detector.

Figure 4.4 shows experimental (a) and simulated (b) spectra of the scattering cross-section of the silicon dimer illuminated with an electric field polarized parallel (red line) or perpendicular (black line) to the dimer axis. The polarization contrast is more pronounced in the 550-750 nm range of the visible spectrum.

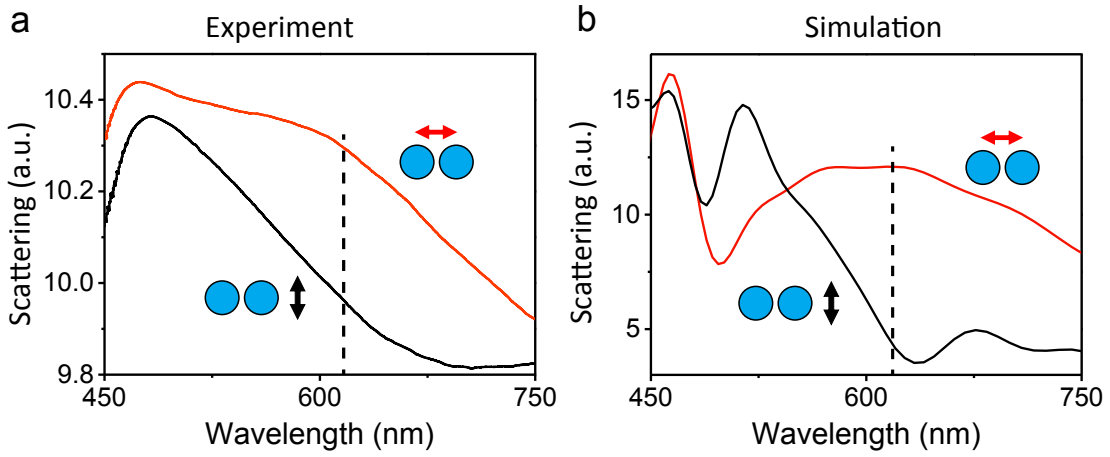

FIGURE 4.4: **Scattering property of silicon dimer nanoantenna.** Experimental (a) and simulated (b) spectra of the scattering cross-section of the silicon dimer illuminated with an electric field polarized parallel (red line) or perpendicular (black line) to the dimer major axis. The vertical dashed line represents the excitation laser wavelength used for florescence experiments.

As plasmonic nanoantennas (usually gold) are traditionally used to achieve high excitation intensity enhancement, we also carry FDTD simulations for the gold nanostructures with same gap sizes. In coming sections, we will compare the fluorescence performance of the silicon gap antennas with the one achieved with gold nanoantennas at similar experimental configuration. Figure 4.5 shows the electric field intensity distributions around the gold antenna of 80 nm diameter particles with gap sizes respectively 20 nm (a,b) and 30 nm (c,d). Although with 20 nm gap gold dimer nanoantenna we achieve nearly 160× fold near-field enhancement (compared to 22× for silicon dimers), the higher quenching losses in gold structures and also the volume averaging (as indicated in FDTD z-cuts) can spoil this effect, so that the net fluorescence gain with gold may eventually not be higher than the silicon nanostructures [113]. We now start the discussion about the fluorescence experiments with silicon nanoantennas and will present a detailed comparison with its gold counterpart in the sections to follow.

4.4 Experiment and results: Single-molecules in solution

Materials and Experimental setup

The optical setup for the fluorescence experiments is as discussed in Chapter 2. In brief, linearly polarized He-Ne laser at 633 nm (with 10-50 μW incident power) is used as an excitation source. The fluorescence correlation spectroscopy experiments are carried upon an inverted confocal microscope (with 40×, 1.2 NA water-immersion objective

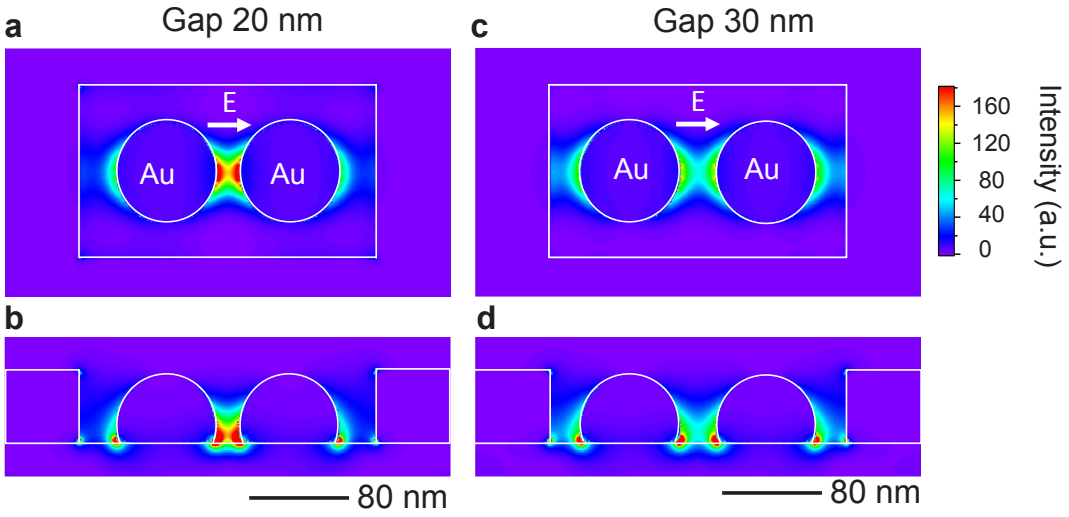

FIGURE 4.5: **Near field enhancement in gold nanogap antenna.** FDTD simulations of the electric field intensity distributions around the gold antenna of 80 nm diameter particles with 20 nm (a,b) and 30 nm (c,d) gap sizes. The gold antenna is illuminated at $\lambda = 633$ nm in normal incidence from the glass substrate with a linear electric field polarized parallel to the dimer axis. The images in (a,c) correspond to the horizontal plane located inside the antenna at 7 nm from the gold-glass interface, while the images (b,d) are vertical cross-sections along the main dimer axis. The color scales are common for all cases.

from Zeiss) customized with a three-axis piezoelectric stage. The emitted fluorescence is collected in epi-detection mode using a dichroic mirror, and set of two avalanche photodiodes. A 30 μm pinhole in the detection path rejects the off-focal signal and sets the 0.5 fL confocal detection volume. For lifetime measurements, the excitation source is a picosecond laser diode operating at 636 nm and one of the photodiode output is sent to a fast time-correlated single photon counting module. The change in source for FCS and TCSPC experiments is done with a set of two removable mirrors. A single mode optical fiber ensures a perfect spatial overlap between the cw-laser and the pulsed laser at same excitation spot in focal plane.

Fluorescence experiments with silicon nanogap antennas are carried out with two different fluorophores (i) Alexa Fluor 647 with 200 mM Methylviologen (8% quantum yield) and (ii) Crystal Violet molecules (2% quantum yield). Figure 4.6 shows the excitation and emission spectrum of Alexa 647 (a), and CV (b) fluorescent dyes. Both dyes have similar fluorescence spectrum and thus with minimum change in the existing setup we can directly compare results with earlier experiments carried out in similar conditions. For the experiments with CV molecules, we replace the 670 $\pm$ 20 nm bandpass filter in front of the photodetector in the detection arm with a longpass filter (cutoff $\lambda = 650$ nm). As the CV molecules has a rather boarder emission spectrum, the inclusion of longpass filter helps in maximizing the collection of the emitted photons by the CV molecules. In

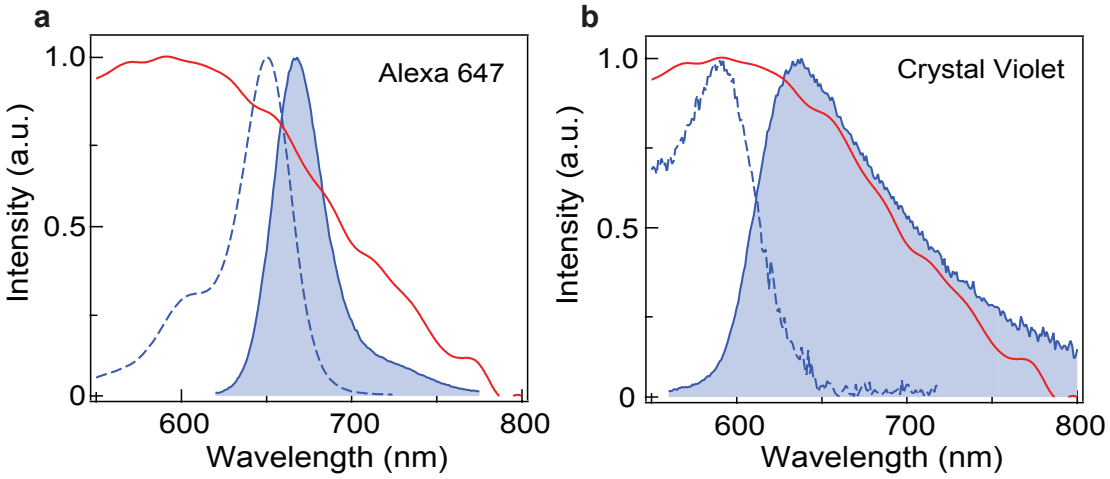

FIGURE 4.6: **Nanoantenna resonance and fluorescence absorption and emission spectra.** Spectral overlap between the scattering spectra for the silicon antenna with 20 nm gap (red line) and the excitation (dashed lines) and emission (solid shadowed lines) fluorescence spectra for Alexa Fluor 647 (a) and Crystal Violet molecules (b).

addition, Figure 4.6 also shows the nice spectral overlap between the scattering spectra (red lines) for the silicon nanogap antenna, especially in the 550-750 nm spectral range matching the emission of both the fluorescent dyes (Alexa Fluor 647 and Crystal Violet).

4.4.1 Burst analysis of Crystal Violet molecules

To assess the optical performance of the silicon nanogap dimer, the nanoantenna sample is covered by a solution containing 1 μM of CV molecules in a 1:1 water-glycerol solution. The use of glycerol slows down the diffusion of molecules passing through the hotspot making the single molecule events more prominent from a near constant background. Prior to this, the antennas are rinsed with ethanol and exposed to UV ozone treatment for 1 minute to remove any possible organic impurities. In addition to low excitation power (typically between 10-50 μW), as the fluorophores are constantly diffusing in and around the nanoantennas, problems related to photobleaching are avoided to a greater extent.

Figure 4.7a,c,e shows the fluorescence traces of the CV molecules recorded with silicon nanogap antennas with increasing gap size (a,b) and perpendicular excitation polarization (c). All the traces are recorded at 50 μW laser power (corresponding to $\sim$10 kW/cm^2 at the focus) and the events are collected in individual histogram (Figure 4.7b,d,f). At the 1 μM concentration, the confocal volume surrounding the antenna contains about 310 CV molecules creating a near constant fluorescence background. Fluorescence bursts

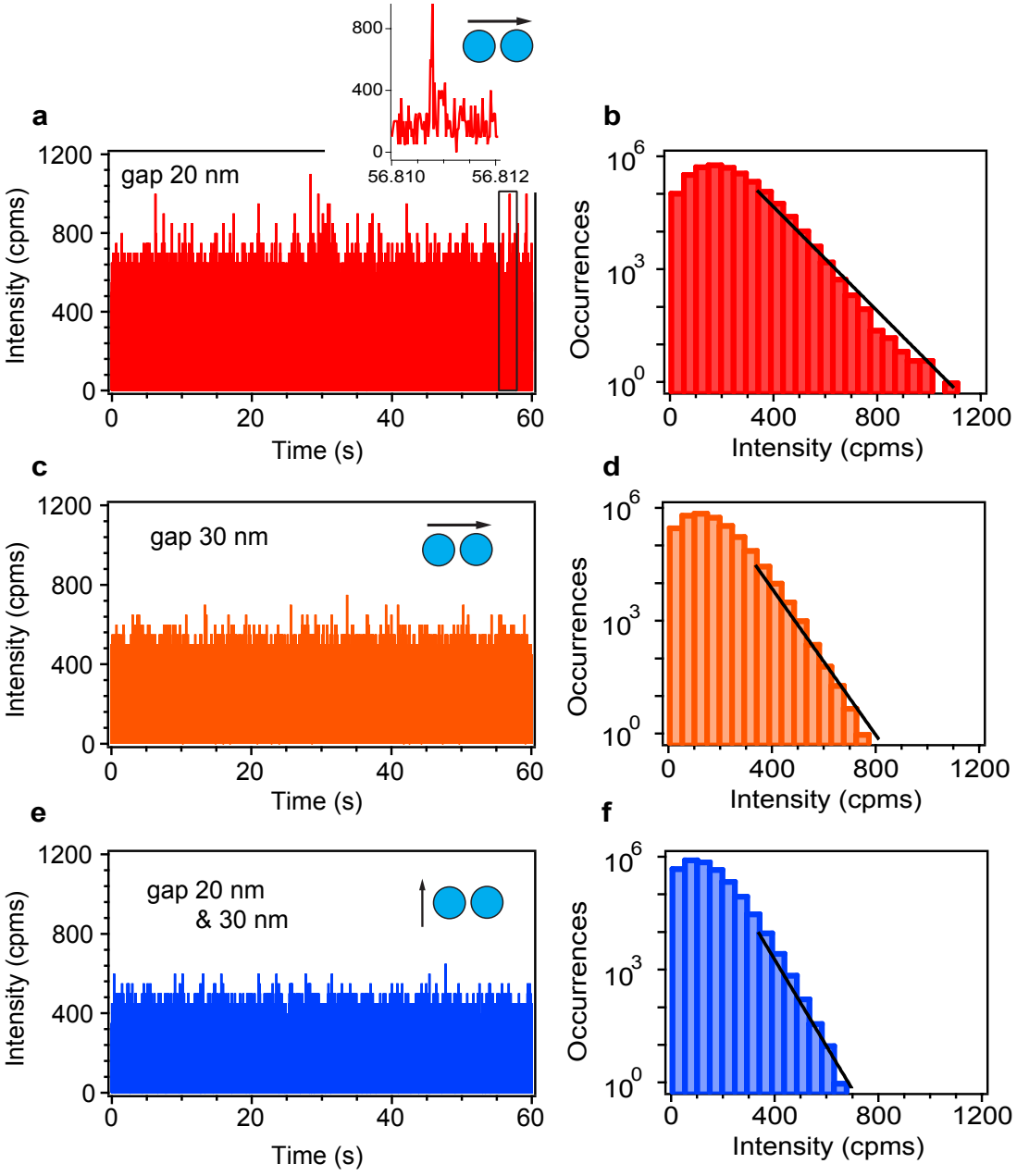

FIGURE 4.7: **Fluorescence bursts from single Crystal Violet molecules indicate fluorescence enhancement on silicon nanogap antennas.** (a,c,e) Fluorescence time traces and (b,d,f) corresponding photon count histograms recorded on individual silicon nanoantennas, with the excitation electric field polarization set parallel (a-d) or perpendicular (e,f) to the antenna main axis. The data for the perpendicular orientation (e,f) corresponds to a 20 nm gap antenna and similar results are obtained with 30 nm separation. The experiments are performed with 1 μM of Crystal Violet in water-glycerol 1:1 solution with 50 μW excitation power at 633 nm. The binning time for all the time fluorescence time traces is 20 μs and the count rates are back computed to counts per millisecond to ease comparison with Ref. [18]. The black lines in the histograms are fits by exponentially decaying probability distributions.

are seen on top of this background (see inset of Figure 4.7a), with intensities depending on the gap size (Figure 4.7a-d) and the excitation polarization (Figure 4.7e,f). This confirms that the intense fluorescence bursts recorded with parallel excitation (a-d) on the antenna originate from the fluorophore crossing the antenna gap region.

The fluorescence enhancement factors are derived from the photon count histograms in similar manner to the work from Orrit's Lab and done on gold nanorods [17, 18]. In the confocal reference condition using the same 50 μW excitation power at 633 nm, the peak fluorescence count per CV molecule is estimated to 1.5 counts/ms. The peak fluorescence intensity with the nanoantenna is determined using a subtraction method, that considers the difference between the maximum intensities for the parallel (Figure 4.7a,b) and perpendicular orientations (Figure 4.7e,f) to take into account the fluorescence background. This leads to a fluorescence intensity of 400 counts/ms for the 20 nm gap size, which is equivalent to a $400/1.5 = 270\times$ fluorescence enhancement. When the gap size is increased to 30 nm (Figure 4.7c,d), the fluorescence intensity and the enhancement factor decrease to 100 counts/ms and 70× respectively. From the fluorescence correlation spectroscopy analysis that we detail hereafter, we estimate that less than 0.08 CV molecules are present in the 20 nm gap region at a 1 μM concentration. This low number and the subtraction method to determine the peak intensity rule out the possibility that the estimated count rates originate from more than a single molecule diffusing in the nanogap.

4.4.2 FCS: Alexa Fluor 647 at micromolar concentrations

We now switch to Alexa Fluor 647 molecules with 8% quantum yield and test the performance of the silicon nanogap antennas at 6 μM fluorophore concentration. We study the temporal fluctuations of the fluorescence intensity F(t) to perform fluorescence correlation spectroscopy (FCS) using the hardware correlator (Flex02-12D/C correlator.com, Bridgewater NJ) with 12.5 ns minimum channel. FCS computes the temporal correlation of the time-dependent fluorescence signal, which is used to determine the average number of detected molecules, their mean diffusion time to cross the hot spot volume and the fluorescence brightness per emitter.

A major difficulty of experiments operating at high fluorophore concentrations is that the enhanced fluorescence signal from the dimer hotspot is hidden by the fluorescence background from the large number of non-enhanced molecules within the diffraction-limited confocal volume. At the working concentration of 6 μM, typically 1800 molecules are present in the 0.5 fL diffraction-limited confocal volume around the silicon dimer antenna, whose collective contribution can easily overwhelm the enhanced single-molecules

fluorescence from the nanogap region. Hence as in the case of DNH, we use the two-species model in the total fluorescence signal for the silicon dimer experiments as well and quantify the average number of molecules and their fluorescence brightness in the hotspot alone.

Thus the total fluorescence intensity measured experimentally (F) is the sum of two molecular species with different number of molecules and brightness: N^* molecules within the dimer gap region with brightness Q^*, and N_0 background molecules with brightness Q_0 diffusing away from the region of interest but still within the diffraction-limited confocal detection volume. However, as the molecules contribute to G in proportion to the square of their fluorescence brightness, the fluorescence from molecules in the nanogap region experiencing the maximum enhancement will have a major contribution in the FCS correlation. And using the values of background molecules and their brightness from control experiment, we can easily quantify the average number of molecules in the nanogap and their brightness per molecule. This will eventually give an independent validation and direct comparison to the enhancement factors derived from the fluorescence burst analysis technique.

The temporal correlation of the fluorescence intensity F can be written as:

$$\begin{aligned} G(\tau) &= \frac{\langle F(t)\, F(t+\tau)\rangle}{\langle F(t)\rangle^2} \\ &= 1 + \frac{N^* Q^{*2} G_d^*(\tau) + N_0 Q_0^2 G_{d0}(\tau)}{(N^* Q^* + N_0 Q_0)^2} \end{aligned}$$

where $G_d^*(\tau)$ and $G_{d0}(\tau)$ are the normalized correlation functions for each species taken individually based on a classical three dimensional model:

$$G_{di}(\tau) = \frac{1}{(1+\tau/\tau_{d,i})\sqrt{1+s_i^2\,\tau/\tau_{d,i}}}$$

$\tau_{d,i}$ stands for the mean residence time (set by translational diffusion) and s_i is the ratio of transversal to axial dimensions of the analysis volume, whose value is set to $s = 0.2$ as it has negligible influence on the estimates of the number of molecules and brightness within the gap (N^*, Q^*). To extract the number of molecules within the gap (N^*) and their corresponding fluorescence brightness (Q^*), we use the asymptotic value of the correlation function towards zero lag time [65]:

$$G(0) = 1 + \frac{N_0 Q_0^2 + N^* Q^{*2}}{(N_0 Q_0 + N^* Q^*)^2} \tag{4.1}$$

As the sum $N_0 Q_0 + N^* Q^*$ amounts to the value of total fluorescence intensity (F) measured experimentally, we can safely replace $N^* Q^*$ in Equation (4.1) with $F - N_0 Q_0$

to obtain the fluorescence brightness and number of molecules within the nanogap region as:

$$\begin{aligned} Q^* &= \frac{F^2(G(0)-1) - N_0 Q_0^2}{(F - N_0 Q_0)} \\ N^* &= \frac{(F - N_0 Q_0)^2}{F^2(G(0)-1) - N_0 Q_0^2} \end{aligned} \tag{4.2}$$

For background molecules contribution: the fluorescence brightness Q_0 is set according to the value found for the confocal reference Q_{conf}. In addition, the number of background molecules N_0 is deduced from the fluorescence intensity when the excitation polarization is set perpendicular to the dimer axis. As total fluorescence intensity F and $G(0)$ are experimentally measured with excitation parallel to the dimer axis, we can now use the set of expression in Equation 4.2 to get Q^* and N^*.

	Excitation	
Silicon nanogap antenna	Perpendicular	Parallel
F (counts/ms)	165 ± 1	183 ± 1
N^*	–	0.5 ± 0.1
N_0	970 ± 50	970 ± 50
τ_d (μs)	50 ± 5	0.2 ± 0.1
Q^* (counts/ms)	–	36 ± 5
Q_0 (counts/ms)	0.17 ± 0.02	0.17 ± 0.02
Detection volume (zL)	$2.7 \pm 0.2 \times 10^5$	140 ± 30
Fluorescence enhancement	–	210 ± 40
Volume reduction	–	3600 ± 700

TABLE 4.1: **Fitting parameter for the FCS curves on silicon nanoantennas and displayed in Figure 4.8b,c.** Using two-species analysis we quantify average number of molecule $N^* = 0.5$ with brightness $Q^* = 36$ counts/ms for those diffusing within the nanoagap of the silicon dimer antenna.

Figure 4.8 displays the raw fluorescence intensity time traces (a) and the FCS correlation functions with excitation polarization parallel (b) and perpendicular (c) to the silicon dimer major axis. As demonstrated in FDTD simulations (Figure 4.2), the high localization of near field with incident light parallel to the dimer axis, results in larger fluorescence intensities and higher correlation amplitudes. This experimentally confirms the coupling between the two silicon particles and the generation of an electromagnetic hotspot in the gap region separating the nanoparticles.

Using the two-species model as described above, FCS analysis quantifies the average number of fluorescent molecules N^* in the antenna hotspot and the brightness per emitter Q^*. From the data in Figure 4.8a with parallel excitation and a 20 nm gap size, we find $N^* = 0.5$ molecule with brightness $Q^* = 36$ counts/ms. These values should be compared to the confocal reference of N_{conf}=1800 molecules with brightness $Q_{conf} = 0.17$ counts/ms. The increase in fluorescence brightness per emitter in the

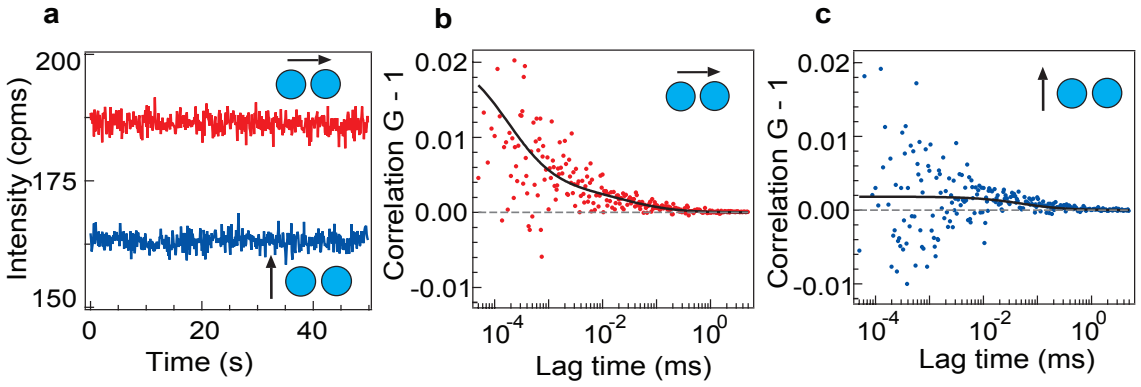

FIGURE 4.8: **Fluorescence correlation spectroscopy in silicon nanogap antenna shows polarization contrast.** (a) Fluorescence time traces with excitation electric field parallel (red) and perpendicular (blue) to the dimer antenna with 20 nm gap. The binning time is 100 ms. (b,c) FCS correlation functions corresponding to the traces shown in (a). Dots are experimental data and black lines are numerical fits, whose parameters are summarized in Table 4.1. The experiments are performed with 6 μM concentration of Alexa Fluor 647 and 200 mM methylviologen at 10 μW excitation power.

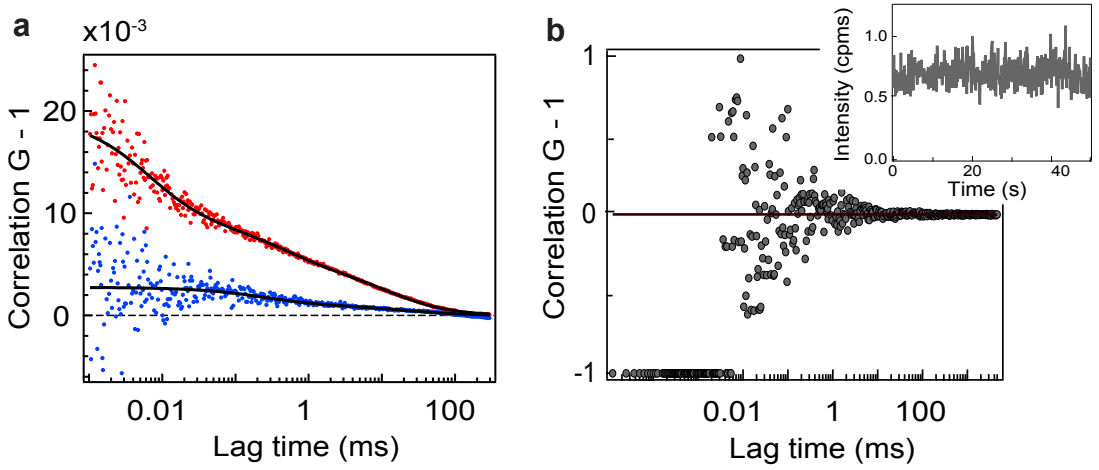

FIGURE 4.9: **FCS with CV molecules and luminescence background when no fluorescent dye is present.** FCS correlation function for the fluorescence trace recorded with Crystal Violet on 20 nm silicon nanogap antenna with the excitation polarization parallel (red) and perpendicular (blue) to the antenna main axis (the raw intensity traces are shown in Figure 4.7a,e). The long correlation times in the millisecond range show that the fluorescence fluctuations for Crystal Violet are not limited by translational diffusion and indicate adsorption on the silicon surface. (b) Correlation function (inset: intensity time trace) for a silicon antenna with 20 nm gap size with no fluorescent molecules to record the level of luminescence background. The 10 μW excitation power at 633 nm is similar to the conditions used in Figure 4.8a-c. No correlation is seen for lag times > 10 μs as the curve is symmetrical around zero. For lag times < 10 μs, the extremely low detection rate does not enable to construct any correlation function, so the correlator output remains at the -1 level.

nanogap quantifies the antenna fluorescence enhancement as $Q^*/Q_{conf} = 210\times$. The FCS data also shows that the volume in the silicon nanogap is $N_{conf}/N^* = 3600\times$ lower than the diffraction-limited confocal volume. Additionally, the calibrated 6 μM Alexa 647 concentration allows us to express the number of molecules N^* as the nanoantenna detection volume of 140 zL (1 zL = 10^{-21}L), which is equivalent to $\lambda^3/1800$. This volume measured by FCS corresponds well to the $25\times90\times60$ nm^3 = 135 zL value expected from the numerical simulations (Figure 4.2a,b). In contrast, the perpendicular excitation leads to a nearly flat correlation curve (Figure 4.8c), with N=970 molecules and brightness Q = 0.17 counts/ms. This supports the fact that no volume confinement is achieved with an excitation polarization perpendicular to the dimer axis, and confirms the nanogap origin of the signal for a parallel polarization. The FCS fitting results are summarized in Table 4.1.

In addition, we also computed correlation functions for the CV fluorescence time traces shown in Figure 4.7) (in the earlier section 4.4.1: Burst analysis with CV molecules). Figure 4.9a shows the correlation curves for CV molecules diffusing within 20 nm silicon nanoantenna. This further validates the polarization sensitivity as the parallel excitation (red) shows higher correlation amplitudes (indicating fewer molecules probed due to localized excitation hotspot) when compared to the perpendicular excitation case (blue). We also checked that no bursts are detected in the absence of fluorescent molecules (inset of Figure 4.9b), indicating a negligible luminescence background from the silicon antenna itself. No correlation is seen for the same trace recorded without any fluorophore. For lag times >10 μs the curve is symmetrical around zero, and for lag times <10 μs, the extremely low detection rate does not enable to construct any correlation function, thereby correlator output remaining at the -1 level.

Effect of excitation power and saturation regime

We perform a series of FCS experiments for varying excitation power and for both gap sizes with Alexa Fluor 647 in presence of methylviologen as the chemical quencher. Figure 4.10 plots the fluorescence count rate per molecules as measured by FCS and as the function of excitation power for 20 nm and 30 nm gap sizes. The confocal case (without nanoantenna in the sample plane) is also shown in green for direct comparison. The experimental data points for increasing excitation power follows the general model of the fluorescence brightness $AI_{exc}/(1 + I_{exc}/I_{sat})$, where I_{exc} is the excitation power, I_{sat} the saturation power, and A being a constant proportional to the molecular absorption cross-section, quantum yield and setup collection efficiency [92]. The fit results are summarized in Table 4.2. Moreover, brightness per molecule above 40,000 counts/s can be readily obtained with the silicon nanoantenna, while the fluorescence brightness

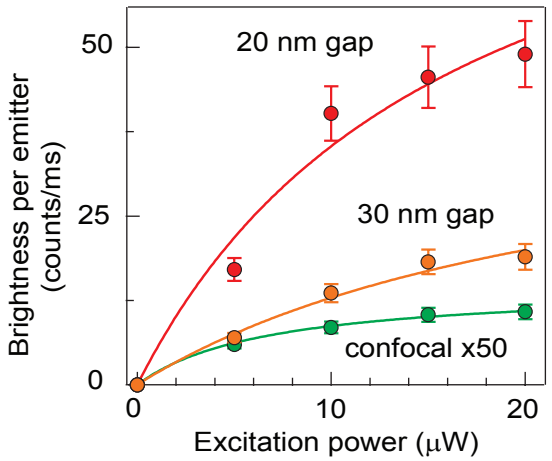

FIGURE 4.10: **Effect of excitation power and saturation regime.** Fluorescence brightness per emitter as a function of the excitation power to show fluorescence saturation occurring at powers higher than 15 μW. For the silicon antennas, the electric field excitation is set parallel to the dimer axis. For the confocal reference, the data is multiplied by 50× to ease display on the same graph.

saturates to values below 1,000 counts/s for the confocal reference in the presence of methylviologen.

For the silicon nanoantennas, the electric field excitation is set parallel to the dimer axis and shows fluorescence saturation occurring only at powers higher than 15 μW. All our FCS measurements involving methylviologen (Figure 4.8) are therefore recorded at 10 μW excitation powers. The dependency of the brightness per emitter with the excitation power and the saturation trend is typical in fluorescence and confirm that our data is not affected by laser leakage on the detection channel or other spurious effects.

Gap size	A (counts/ms/μW)	I_{sat} (μW))
20 nm	5.7 ± 1.6	16.4 ± 9.3
30 nm	1.8 ± 0.4	24.3 ± 13.3
Confocal	2.2 ± 0.2	6.8 ± 0.8

TABLE 4.2: **Fit results show fluorescence saturation at higher excitation powers.** The parallel excitation scheme shows fluorescence saturation occurring only at powers higher than 15 μW. All our FCS measurements involving methylviologen (Figure 4.8) are therefore recorded at 10 μW excitation power.

4.4.3 Photokinetic rate enhancement in silicon nanogap antennas

The presence of a nanogap antenna affects the fluorescence signal mainly *via*: (i) local enhancement of the excitation intensity, (ii) accelerated decay rates (Purcell effect) in the nanogaps, (iii) enhancement in the quantum yield of the emitter. We start this

section with the discussion on the influence of the antenna on the radiative rate Γ^*_{rad}, the non-radiative rate Γ^*_{loss} and the total decay rate $\Gamma^*_{tot} = \Gamma^*_{rad} + \Gamma^*_{loss}$. Figure 4.11 shows the numerical simulations of the decay rate constants as a function of the emission wavelength for a perfect dipole emitter with parallel orientation located in the dimer center of a silicon antennas with 20 (a) and 30 nm (b) gap separations. All rates are normalized to the dipole's radiative rate in free space and the simulations take into account the complex permittivity of amorphous silicon [109, 141]. In agreement with the reciprocity theorem [142], the computed radiative rate enhancement $\Gamma^*_{rad}/\Gamma_{rad}$ appears very close to the excitation intensity enhancement I^*_{exc}/I_{exc}, and increases as the gap size is reduced. The fluorescence enhancement mechanism in silicon nanogap antennas can be thoroughly explained by a combination of excitation intensity enhancement and radiative rate enhancement with near similar strengths. However, our calculations reveal a non-negligible contribution of the non-radiative losses, which decrease the antenna's radiative efficiency (ratio of radiative rate to the total decay rate displayed in Figure 4.11c) in the visible region. While amorphous silicon has almost real permittivity in the near infrared minimizing the optical losses [113], the remaining absorption in the visible range is a phenomenon that must be taken into account.

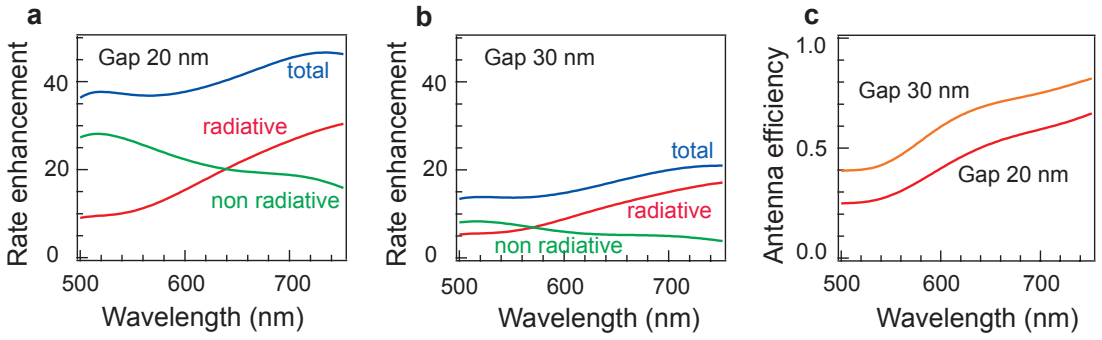

FIGURE 4.11: **Decay rate constants as function of the emission wavelength for silicon nanogap antennas.** (a-b) Numerical simulations of the decay rate constants as a function of the emission wavelength for a perfect dipole emitter with parallel orientation located in the dimer center with increasing gap sizes. All rates are normalized to the dipole's radiative rate in free space. (c) Antenna radiative efficiency (ratio of radiative rate to total decay rate) for a perfect dipole emitter with parallel orientation located in the dimer center with 20 nm (red) and 30 nm (orange) gap size.

Further, reducing the emitters intrinsic quantum yield (8% for Alexa647 to 2% for CV molecules), we benefit from higher enhancement factors. As with the CV molecules, we clearly observe enhancements of several hundreds and even higher values can be foreseen for further reduced gap sizes. Figure 4.12 displays simulation results for quantum yield enhancement computed for a dipole source oriented parallel to the silicon antenna

Numerical simulations of the decay rate constants and the quantum yield enhancements were done by Dr. Mathieu Mivelle, Université Pierre et Marie Curie, Institut des NanoSciences de Paris.

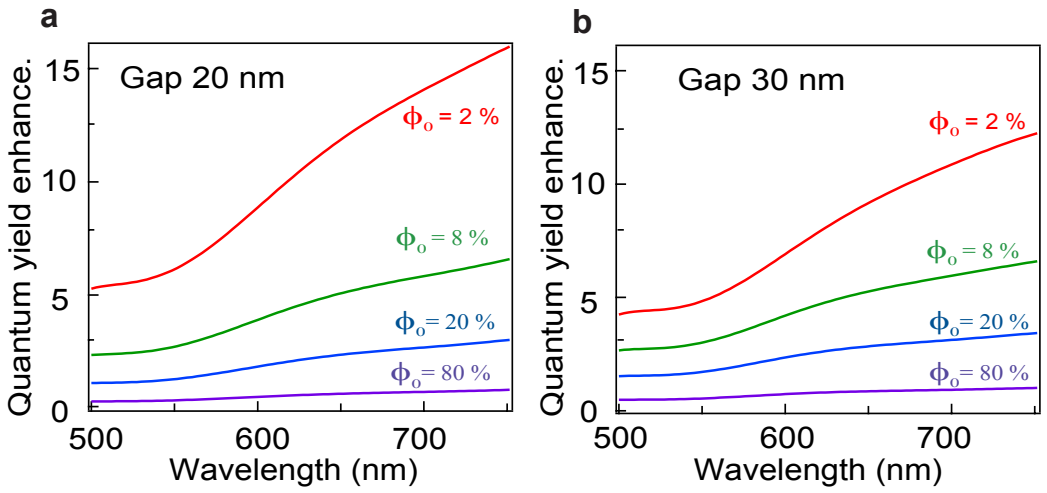

FIGURE 4.12: **Quantum yield enhancement in silicon nanogap antenna.** Quantum yield enhancement computed for a dipolar source oriented parallel to the silicon antenna main axis. The different values ϕ_0 indicate the initial (intrinsic) quantum yield of the source. While no quantum yield enhancement is seen with a high efficiency emitter ($\phi_0 > 80\%$), using emitters with low intrinsic quantum yields maximizes the quantum yield enhancement.

main axis for both 20 nm (a) and 30 nm (b) gap sizes. In addition to the excitation intensity enhancement, decreasing the gap size indeed maximizes the contributions of the radiative rate in the silicon nanogap. Thus using emitter with low intrinsic quantum yield with narrow gap antennas helps maximizing the quantum yield enhancement to achieve higher fluorescent enhancement factors. It is important to note here that, as displayed in Figure 4.12, for low quantum yield emitters ($\phi_0 < 20\%$) the Purcell enhancement of the radiative rate can compensate the quenching effect of the ohmic losses, leading to a net enhancement of the apparent quantum yield.

As de-excitation of the molecules to the ground state is expected to be mainly governed by the increased radiative emission, we now study this phenomenon with TCSPC measurements. We study the decay rate enhancement in the nanogap between silicon dimers by recording the fluorescence decay kinetics upon picosecond pulsed excitation. Figure 4.13a displays typical decay traces for Alexa Fluor 647 with 200 mM methylviologen on a 20 nm gap silicon antenna. While the decay kinetics are similar for the confocal reference (green) and the antenna with perpendicular orientation (blue in Figure 4.13b), turning the excitation polarization to parallel (red) induces a clear acceleration of the decay dynamics. While a single exponential model with 350 ± 15 ps lifetime accounts well for the observed decay dynamics in the case of the antenna with the excitation in perpendicular orientation, we find that a bi-exponential model is needed to describe the decay in the case of the excitation parallel to the silicon antenna dimer. This bi-exponential model accounts for the respective contributions of the N^* molecules in the

gap region (that we assign to the newly appearing short lifetime contribution) and the N_0 molecules in the confocal volume (away from the nanoantenna, which have a 350 ps lifetime independent of the excitation polarization). Taking into account the convolution with the instrument response function (IRF), our data indicate a fluorescence lifetime of 150 ± 20 ps in the gap region. This lifetime reduction may seem weak as compared to the 40× decay acceleration computed in Figure 4.11a. As discussed in Chapter 2 and Chapter 3, a significant contribution in the experimentally observed decay dynamics comes from the internal non-radiative rate $\Gamma_{nr} = 0.67$ ns^{-1} of Alexa Fluor 647 and the quenching rate $\Gamma_q = 1.9$ ns^{-1} set by methylviologen [65]. Thus these contributions must be subtracted to the observed total decay rate to recover only the contribution from the local density of optical states (LDOS which encompasses both radiative Γ^*_{rad} and non-radiative Γ^*_{loss} transitions set by the photonic environment). This provides a decay rate of 0.28 ns^{-1} for the confocal reference and 4.1 ns^{-1} for the 20 nm gap silicon antenna with parallel excitation, leading to an LDOS enhancement of 14.1/0.28 = 15× which clearly indicates the significant influence of the silicon antenna on the LDOS. The discrepancy with the predicted values from the numerical simulations (40×) stems mainly from the spatial and orientation averaging within the gap region that affects the experimental data, as well as local defects on the fabricated nanodiscs [143].

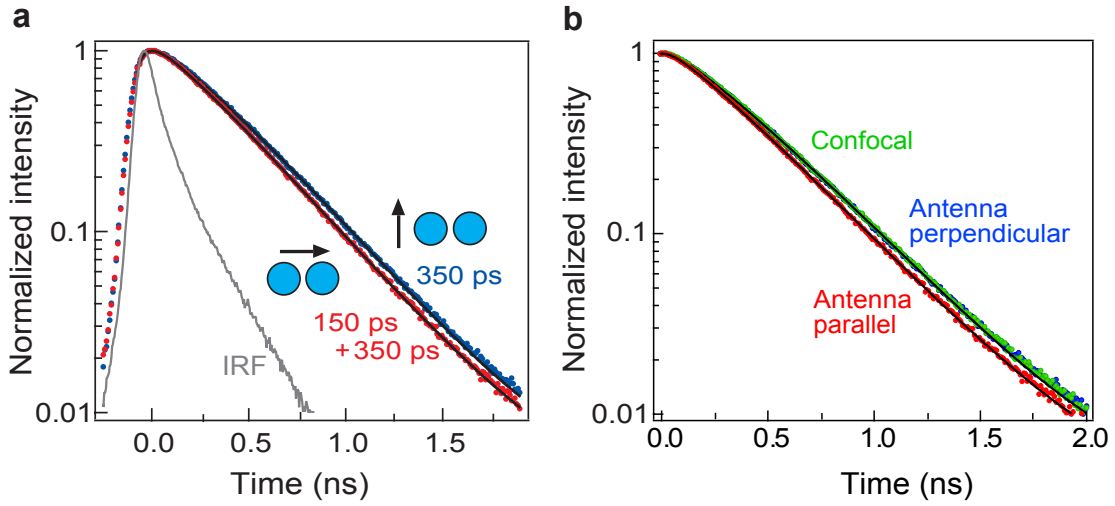

FIGURE 4.13: **Photokinetic rate enhancement in silicon nanogap antennas measured by TCSPC.** (a) Normalized fluorescence decay traces of Alexa Fluor 647 with 200 mM methylviologen obtained on a 20 nm gap silicon antenna with excitation light parallel (red) and perpendicular (blue) to the dimer axis. (b) The fluorescence decay traces of Alexa Fluor 647 are further compared with confocal reference (green). A single exponential decay with 350 ps lifetime is used to model the decay kinetics for the confocal reference and the nanoantenna with perpendicular orientation. Black lines are numerical fits convoluted by the instrument response function (IRF).

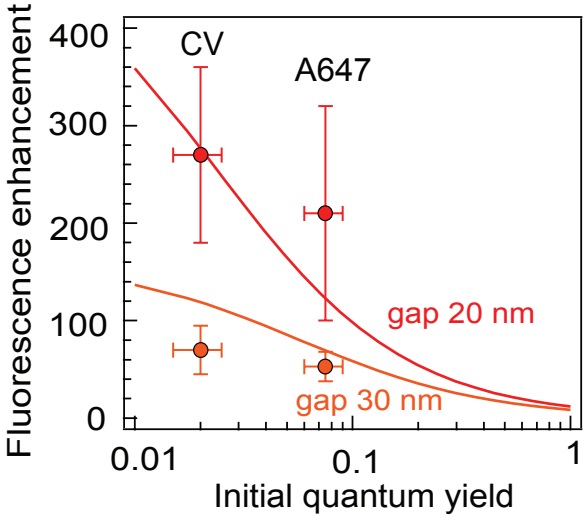

FIGURE 4.14: **Fluorescence enhancement factors: Numerical simulation and experimental data.** Numerical simulations of the fluorescence enhancement factor η_F using Equation 4.3 as a function of the initial quantum yield of the emitter (in homogeneous environment without the antenna) for silicon antennas with 20 nm (red line) and 30 nm (orange line) gap sizes. The lines represent the evolution predicted using only the numerical simulations results. They are not a fit to the experimental data, there is no free parameter. The excitation wavelength is 633 nm and the emission is averaged over the 650-690 nm region for a dipole with parallel orientation to the dimer main axis. The dots represent the experimental data, CV stands for the experiments on Crystal Violet and A647 for the measurements on Alexa Fluor 647 with 200 mM methylviologen. The vertical error bars represent the extreme values found in the set of experiments, the horizontal error bars indicate a 20% uncertainty on the fluorescence quantum yield.

As the fluorescence enhancement is mainly due to: higher local excitation intensity leading to increased excitation rate and increased radiative emission rate for the dipole emitter inside the gap. The fluorescence enhancement factor η_F can be expressed as [94]:

$$\eta_F = \frac{I^*_{exc}}{I_{exc}} \frac{\Gamma^*_{rad}}{\Gamma_{rad}} \frac{1}{1-\phi_0 \; + \; \phi_0 \, (\Gamma^*_{rad} + \Gamma^*_{loss})/\Gamma_{rad}} \tag{4.3}$$

where I^*_{exc}/I_{exc} is the excitation intensity enhancement in the nanogap, $\Gamma^*_{rad}/\Gamma_{rad}$ is the enhancement of the radiative decay rate constants, $\phi_0 = \Gamma_{rad}/(\Gamma_{rad} + \Gamma_{nr})$ is the intrinsic quantum yield of the fluorescent molecule in homogeneous solution and Γ^*_{loss} is an additional decay rate constant describing the non-radiative energy transfer to the antenna's material induced by ohmic losses.

Figure 4.14 summarizes all the fluorescence enhancement results (dots represent the experimental data and lines being numerical simulations) for Alexa Fluor 647 with 200 mM methylviologen and CV molecules. The lines are predicted by solely using the numerical simulation of the fluorescence enhancement factor η_F is obtained by using Equation 4.3

as a function of the initial quantum yield (ϕ_0) of the emitter in homogeneous environment without the antenna. The excitation rate enhancement $\frac{I^*_{exc}}{I_{exc}} = 22$ (for 20 nm gap); 12 (for 30 nm) and the radiative rate enhancement $\frac{\Gamma^*_{rad}}{\Gamma_{rad}} = 40$ (for 20 nm gap); 18 (for 30 nm) are taken from the simulations displayed in Figure 4.2 and Figure 4.11. The excitation wavelength is 633 nm and the emission is averaged over the 650-690 nm region for a dipole with parallel orientation with 20 nm (red line) and 30 nm (orange line) gap silicon dimer antennas. These solid lines represent the evolution predicted using only the numerical simulations results. They are not a fit to the experimental data, there is no free parameter. The good agreement with the experimental observations for Crystal Violet and Alexa Fluor 647 and for both gap sizes further supports our approach of using all-dielectric platform for enhanced single-molecule fluorescence detection.

4.5 Performance comparison with gold nanoantenna

As we already showed with FDTD simulations, plasmonic nanoantennas have higher near field localization factors when compared to their dielectric counterparts. However, the ohmic losses and joule heating induced in metallic structures can severely limit the achievable fluorescence enhancements. In this section, we compare the optical performance of all-dielectric nanogap antennas with those acheived with plasmonic structures in similar experimental conditions.

In Figure 4.15 we compare our results of silicon dimers with the ones achieved with the gold dimer antennas of similar gap sizes featuring 80 nm diameter gold particles to have a resonance near the 633 nm excitation and 650-690 nm emission for Alexa 647 [90]. For both silicon and gold case, clear increase on the fluorescence enhancement (a) and volume reduction (b) is observed as the gap size is reduced. This is consistent with the electric field confinement in the gap region as we discussed computing the near field strength using FDTD (Figure 4.2 for silicon and Figure 4.5 for gold). As the experimental conditions are identical between the experiments (for Si and Au), the fluorescence enhancement factors and detection volumes can be readily compared. Remarkably, the silicon antennas have fluorescence enhancement and optical confinement properties that are very similar to the gold antennas of similar gap sizes. This is a very positive indication for the field of all-dielectric nanophotonics and a further motivation to reach sub-10 nm gaps by improving the challenging lithography and etching of silicon.

As the local intensity enhancement with the nanoantennas critically depends on the gap size, we performed similar FCS experiments with gold dimer and trimer nanoantennas at similar experimental configurations and following similar FCS analysis procedure as

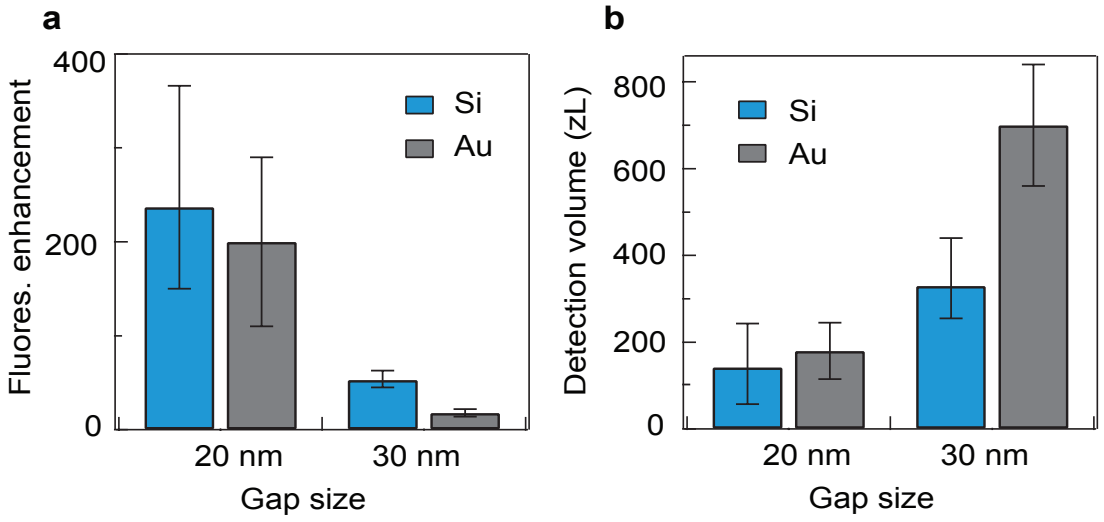

FIGURE 4.15: **Fluorescence enhancement and detection volume in silicon nanogap antennas analyzed by fluorescence correlation spectrocopy**. Comparison of the fluorescence enhancement (a) and detection volume (b) measured in the nanogap of silicon nanoantennas and gold nanoantennas of similar gap sizes, for which the excitation electric field polarization set parallel to the dimer axis. The data for gold nanoantennas is taken from Ref. [90] which uses the same experimental conditions with Alexa Fluor 647 and 200 mM methylviologen. The gold nanoantennas have a diameter of 80 nm, a gap size of 20 or 30 nm, a thickness of 50 nm, and are surrounded by a 280×140 nm^2 box aperture in a gold film to further suppress the fluorescence background. The error bars are deduced from the extreme values found in a set of different nanoantennas of similar design parameters (8 and 11 antennas respectively for 20 and 30 nm gap sizes).

adopted for silicon dimers. Gold nanoparticles with 80 nm diameter (commercially available from BBI Solutions) are diluted in pure water and dispersed on a glass coverslip as in Ref.[16]. We then cover the sample with 15 μM Alexa 647 with 200 mM methylviologen and perform FCS as before at 10 μW excitation power. Figure 4.16a represents the schematic of the experimental configuration for the gold dimer nanoantennas. The polarization sensitivity in the dimer configuration allows to selectively probe dimer antennas, which are further confirmed by SEM imaging. Figure 4.16b shows the SEM images of dimer, trimer, monomor, and the aggregate of self-assembled gold nanoparticles. Using numerical modeling and experimentally obtained scattering spectra from the individual nanoantenna, we estimate nominal dimer antenna gap size as 6 nm [22]. Additionally, in order to study the gap size influence with gold nanoantenna we use Poly(ethylene glycol) methyl ether thiol (PEG) as capping agent to the gold nanoparticles. PEG is know to replace the citrate cover on the gold nanoparticles with thiol agent to bind on the surface of gold nanoparticles, and eventually provides an additional surface on gold nanoparticles. As the length of spacer arm of PEG in our case in 6 nm we achieve gold dimer antenna with 12 nm gap size with PEG treatment. The gap sizes are further

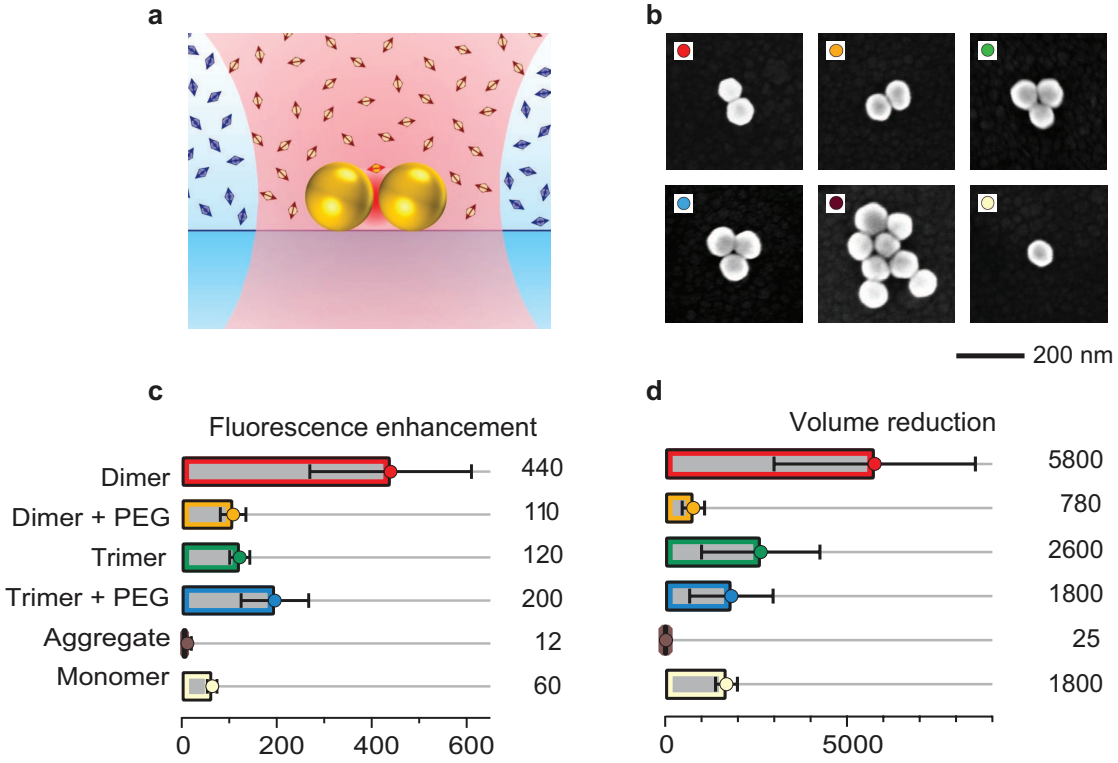

FIGURE 4.16: **Fluorescence enhancement and volume reduction with self-assembled gold nanoantennas.** (a) Schematic of a dimer antenna illuminated by a diffraction-limited focused laser beam. A solution of fluorescent molecules at micromolar concentration covers the antenna, only a few molecules randomly diffuse in the hot spot inside the nanoparticles gap, while thousands of molecules are in the diffraction-limited confocal volume. (b) Representative SEM images (along with the markers) of the different gold nanoantennas tested. Their color is associated to different configurations and to the presence of an additional PEG layer around the nanoparticles. (c,d) Average fluorescence enhancement and volume reduction for the different antenna configurations. Error bars indicate the standard deviation, numerical values at the right of the graphs indicate the average value over the different samples.

validated by an experimentally observed blue shift in the scattering spectra as compared to the dimers where no PEG is used [22].

Figure 4.16c,d summarizes the fluorescence experiments achieved for all possible cases: dimers (no PEG), dimers (with PEG), trimers (no PEG), trimers (with PEG), aggregates and monomors of gold nanoparticles. As expected with 6 nm gap dimers (without PEG) we get on average 440× fluorescence enhancement together with nearly 6000× volume reduction when compared to all other cases of trimer, aggregate or monomer. With the use of PEG spacer the gap separation is nearly 12 nm, and this directly influences the optical performance of the nanoantennas: with observed 100-fold fluorescence enhancement and 780-fold volume reduction when compared to confocal configuration. The result obtained for 12 nm gap gold nanoantenna is interesting because it gives a

sense of how efficient the all-silicon nanogap antennas can be for fluorescence experiment. As we demonstrated with slightly larger gap (20 nm), we are still able to achieve a higher fluorescence enhancement up to 270× together with 3600× volume reduction. Altogether, these results establish that all-silicon platform is an attractive choice to enhance the emission from single molecules diffusing across the nanoscale gap region.

4.6 Summary

We demonstrate the first proof-of-principal experiment with all-dielectric nanoantennas for enhanced single-molecule fluorescence detection and nanoscale volume localization. Using burst analysis and FCS, we provide clear quantification of enhanced fluorescence and compare the results with simulations. With 20 nm nominal gap silicon nanoantennas, we report fluorescence enhancement factors up to 270× with single molecule sensitivity at micromolar concentrations. The excitation polarization dependence, the gap size influence, the microsecond transit time and the excellent agreement with numerical simulations confirm that the fluorescence signal stems from the electromagnetic hotspot of the silicon dimer geometry. The low Q-factor of the resonance is compensated by the ultralow mode volume of $\lambda^3/1800$ to enhance simultaneously both the excitation intensity and the radiative decay rate by about 20×. In addition, the scattering spectra of silicon dimer antenna accommodates the full emission spectrum of the fluorescent dye at room temperature, avoiding the narrow spectral range of operation and the cryogenic temperatures (usually the case with high Q-factor microcavities). Additionally it should be noted that these nanogap antennas indicate better optical performance in near IR region (see scattering spectra in Figure 4.6) and thus room for further improvements. We further compared the optical performance (both the fluorescence enhancement factors and the hotspot detection volume) with gold dimers at similar experimental conditions. Our results show that amorphous silicon is an attractive alternative to plasmonic materials to design optical antennas and use them for single molecule fluorescence experiments. Compared to gold antennas, the silicon antenna design circumvents the major limitations of nonradiative quenching and heat losses in the metal.

In contrast to most structures supporting Mie resonances, which have the maximum field enhancement inside the particles [108, 144], the gap antenna design proposed here, sets the the maximum field enhancement in the gap region between the silicon nanoparticles, and thus being attractive for biosensing applications. Further, silicon is very abundant in nature and thus is cost-effective. Being compatible with CMOS processing, the field of optically resonant dielectric particles has huge potential technological impact. The

demonstration that silicon nanogap antennas as efficient platforms to probe single fluorescent molecules constitutes an important step forward for the implementation of molecular sensors with on-chip CMOS-compatible nanophotonic devices.

However, although the all-dielectric platform appears an attractive choice for various CMOS compatible applications, in absence of a screening layer surrounding the dimer antennas, it is tricky to quantitatively analyze the hotspot fluorescence from the background molecules while working at higher molecular concentration. Together with fabrication challenge (currently limited to 20 nm nominal gap), our fluorescence experiments are thereby limited within the concentration range of 1-6 μM. In addition, this design is limited to experiments with fluorophore freely diffusing in solution droplets. Extending antenna enhanced fluorescence experiments for live cell research (to study single molecule dynamics in plasma membranes) will need further improvement in this antenna design. In next Chapter 5, we will address this issue and demonstrate large scale gold dimer nanoantenna with surface hotspot and planar surface topology optimized for single-molecule experiments at concentrations exceeding 20 μM. We will further discuss the applicability of these planar nanoantenna design with giant fluorescence enhancement-factors in the context of (i) single-molecules diffusing in solution, (ii) model lipid bilayers and (iii) plasma membranes in living cells.

Chapter 5

Surface nanogaps for giant fluorescence enhancement

The use of nanoantennas for biological applications, such as dynamic sensing and molecular spectroscopy in plasma membranes of cells require large-scale availability of narrow accessible gaps. Not only should the nanogaps with sub 20 nm dimensions be reproducibly fabricated, but also the gap region (electromagnetic hotspot) must remain accessible to the target molecules. In this chapter, we introduce the concept of surface nanogaps achieved with a new nanofabrication technique that applies planarization, etch back and template stripping to expose the excitation hotspot at the top surface of the nanostructure. We will then discuss the optical performance of these "planar nanoantennas" for enhanced single-molecule fluorescence detection and demonstrate their superior performance over conventional electron beam lithography methods.

This project was carried out in collaboration with the teams of Prof. Jürgen Brugger (EFPL, Switzerland) and Prof. Niek F. van Hulst (Molecular Nanophotonics, ICFO, Barcelona).

5.1 Nanoantennas with surface nanogaps: Motivation

Optical nanoantenna can efficiently confine light energy into nanoscale dimensions breaching the classical diffraction limit. This leads to enhanced light-matter interactions at

The contents of this chapter have been published in:

Flauraud, V., **Regmi, R.**, Winkler, P.M., Alexander, D.T., Rigneault, H., van Hulst, N.F., García-Parajo, M.F., Wenger, J. and Brugger, J., 2017. In-plane plasmonic antenna arrays with surface nanogaps for giant fluorescence enhancement. *Nano Letters*, 17(3), pp.1703-1710.

the nanoscale, and thus making nanoantenna a powerful tool for investigating single-molecule dynamics that requires both high spatial and temporal resolution [10, 11]. However, in most nanoantenna designs, the region of maximum field localization and enhancement (*i.e.*, electromagnetic hotspot) is not readily accessible to the sample since it is buried in the nanostructure. For example, solution based single-molecule measurements at biologically-relevant high micromolar concentrations and investigation nanoscale membrane architecture in plasma membranes of living cells, requires large availability of narrow gaps with the smallest gap region (hotspot) at the top of the nanostructure. Exposing the narrowest region of the gap towards the sample proximity ensures that probe molecules experience only the "brighter side" of the nanoantenna while simultaneously providing a near flat substrate favored for live-cell research. Despite impressive recent progress using electron beam [145], focused ion beam [146] or stencil lithographies [147, 148], the challenges of reliable narrow gap fabrication and hotspot accessibility remain major hurdles limiting the impact and performance of optical nanoantennas.

As the current large-scale fabrication techniques lack reproducible geometrical control below 20 nm, limiting the applicability of these efficient platforms for bio-inspired applications, we propose a new nanofabrication technique that applies planarization, etch back and template stripping resulting a large scale production of surface nanogaps (normally at the bottom, now at the top of the structure). We demonstrate large scale arrays of planar nanoantennas (fabricated at EPFL, Switzerland), featuring gaps as small as 10 nm with sharp edges and full surface accessibility of the confined hotspot region for enhanced single-molecule fluorescence detection. The novel fabrication approach drastically improves the optical performance of plasmonic nanoantennas to yield giant fluorescence enhancement factors, together with zeptoliter range detection volumes. This fabrication method achieves excellent geometric control in the nanometer range over large areas, and is fully adaptable to different antenna designs providing direct access to the enhanced field at the gap region. As we will demonstrate, this fabrication approach will significantly improve the effectiveness of plasmonic antennas for various applications, including ultra-sensitive biosensing and live cell research.

In the next section, we will detail on how the current limitations in fabrication accuracy (specially for gaps smaller then 20 nm) and scalability can be addressed using planarization, etch back and template stripping. The burst analysis, FCS and TCSPC measurements will be then discussed in detail to demonstrate the superior performance over conventional electron beam lithography methods. After the discussions on the optical performance of these in-plane nanoantennas at very high fluorophore concentrations

for enhanced single-molecule fluorescence detection, in the next Chapter 6, we will exploit the extreme planarity of these structure to investigate the dynamics of membrane lipids in living cells.

5.2 Large scale in-plane nanoantennas: Fabrication

The antenna design is based on the "antenna-in-box" platform featuring a nanogap dimer antenna inside a rectangular box aperture. The central nanogap antenna between two 80 nm gold half-spheres creates the hotspot for fluorescence experiments and the cladding 300 $\times$ 140 nm^2 box, essentially screens the background signal by preventing direct excitation of molecules diffusing away from the hotspot [90, 149]. This design is tailored for optimal enhanced single molecule analysis in solutions at high μM concentrations.

Figure 5.1 summarizes the different steps of the nanofabrication procedure. The nanoantenna fabrication is performed on a 100 nm-thick silicon nitride deposited over silicon wafers (100 mm diameter, prime grade). Negative tone hydrogen-silsesquioxane (HSQ) resist is spun at 1500 rpm for 240 seconds yielding an approximately 100 nm-thick coating. The samples are then exposed by electron-beam lithography using a 1 nm grid and a 2 nA beam (5 nm FWHM) (a). After exposure, the samples are developed at room temperature in 25% tetramethylammonium hydroxide for 2 minutes, rinsed in deionized water and isopropanol prior to drying in order to avoid any possible collapse of the narrowest features induced by capillary force. A 50 nm-thick gold film is then evaporated (10 $\mathring{A}/s$) by electron beam heating at a pressure of 8×10^{-7} mBar on static substrates (b). The stage temperature is maintained at -50^o C to reduce the gold grain size by approximately a factor of two as compared to room temperature evaporation, allowing for low edge roughness and improved shape accuracy.

Planarization is then carried out by spinning flowable oxide (Dow Corning FOX-16) at 1000 rpm for 240 seconds (c). This yields 1 μm thick film with a residual topography above the structures of interest below 10 nm. Broad argon ion beam milling (Veeco Nexus IBE350) is then performed at -45^o sample tilt to etch back the flowable oxide until the top gold caps were fully removed (d). End point detection is performed by monitoring the signal from gold on a secondary ion mass spectrometer. A 30 seconds etching with hydrofluoric acid diluted 1:10 in deionized water is then carried out to clear out the residual HSQ in the antenna apertures (e). The 100 mm silicon wafer is then cleaved into individual dies each of which contains nanoantennas with various gap sizes.

Nanofabrication procedure was performed by Dr. Valentin Flauraud (EPFL, Switzerland) at the Center of Micro/ Nanotechnology (CMI) of EPFL, Switzerland.

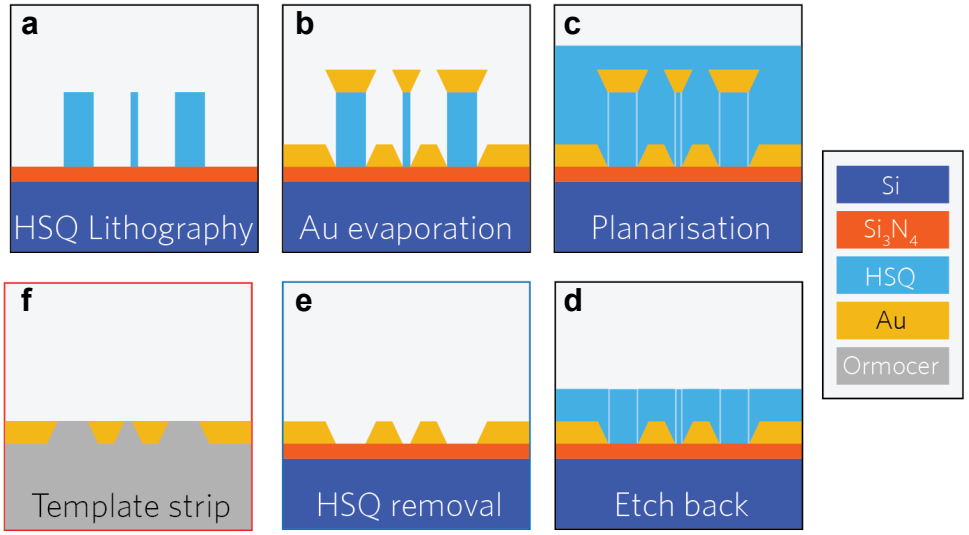

FIGURE 5.1: **Fabrication of planar nanoantenna arrays.** The nanoantenna fabrication process flow is performed over a silicon nitride layer deposited in silicon thin-film. The HSQ resist is patterned by electron-beam lithography (a) followed by a 50 nm thick gold layer evaporation (b). Flowable oxide is then spun for planarization (c) which is then etched back by Ar ion beam (d) to remove the top metal capping. Wet etching of the remaining HSQ (e) clears out the antenna geometry and then finally template stripping is done using UV curable adhesive (f).

As sketched in Figure 5.1e, the gold sidewalls bear a tapering angle due to metal diffusion during the evaporation. Therefore the narrowest gap region lies at the bottom of the structure close to the substrate interface. This hotspot position is impractical for biosensing and fluorescence enhancement applications, where the narrowest gap position should be on the top surface of the structure in order to maximize the contact with the probe solution. Thus the template stripping approach is implemented by using UV curable adhesive (f) in which the gold structures are transferred, and flipped over, onto a microscope coverslip to facilitate access to the narrowest and brightest region of the nanogap.

For template stripping procedure, a 150 μm thick microscope coverslip (30 mm diameter) is cleaned in piranha solution and then surface activated by oxygen plasma treatment (Tepla Gigabtach 1000 W, 500 SCCM O_2). The plasma exposed surface of the coverslip is then brought in contact with the gold substrates in silicon wafer dice with a drop of UV curable OrmoComp (microresist technology GMBH) and is cross-linked under UV and light pressure (ESCO EUN-4200 375 nm, 2.5 mW/cm^2) for 3 minutes followed by separation of the glass from the silicon with a razor blade. It is important to note that the last template stripping step can be performed just before the final fluorescence measurements, so the antenna hotspot is protected from surface contaminants during long term storage.

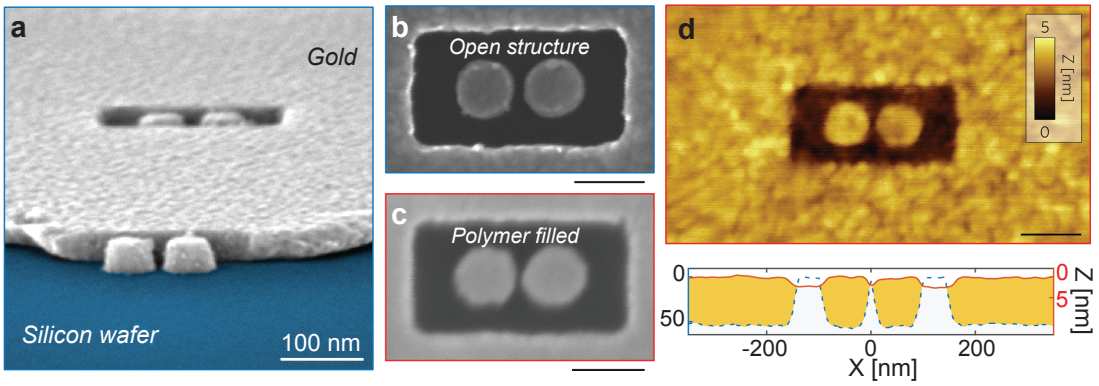

FIGURE 5.2: **SEM and AFM images of planar "antenna-in-box" devices.** (a) Tilted SEM view of an opened "antenna-in-box" before template stripping. The smallest part of the gap (∼12 nm in this case) lies at the surface level. A similar structure is imaged from the top before (b) and after (c) template striping. Dimensions are preserved and the space surrounding the antenna is filled by the UV curable polymer as seen in the AFM image (d) and shows less than 5 nm residual topography. Lower panel in d shows two AFM profiles averaged over 20 line scans before (dashed blue) and after (red) template stripping of the 50 nm-thick gold structure. All scale bars are 100 nm.

Figure 5.2a shows the tilted SEM view of an open "antenna-in-box" before template stripping (as sketched in Figure 5.1e). The smallest part of the gap, here 12 nm, lies at the surface level, closer to the silicon wafer interface. A similar structure is imaged from the top before (b) and after (c) template striping. This comparison before and after template stripping, clearly shows that the narrowest gap region emerges on a flat top surface enabling maximum fluorescence enhancement in a minimal near-field probe volume. Figure 5.2d is a representative AFM image of the template-stripped nanoantenna showing less than 5 nm residual topography. These AFM analysis further confirm that the dimensions are preserved after template stripping procedure and the space surrounding the nanoantenna is filled by the UV curable polymer (see lower panel in Figure 5.2d). As all these fabrication processes are performed on conductive silicon substrates, the final structures can be easily transferred to microscope coverslips, avoiding the need for a supplementary adhesion layer that can damp the plasmonic performance [150].

Moreover, we use transmission electron microscopy (TEM) to accurately quantify the dispersion in the nanoantenna dimensions and to test the accuracy of the production process. The same fabrication process, excluding template stripping, is carried out on a 30 nm thick silicon nitride membranes for accurate TEM metrology on prototypical arrays of nanoantennas. Figure 5.3a shows a representative image of a 5×5 antenna array with 10 nm nominal gap width used for metrology purposes with no template stripping performed. Various gap separations (from 10 nm to 45 nm) are achieved with narrow dispersion and the results are summarized in Figure 5.3b,c. It should be noted that

although the resist HSQ is patterned at dimensions in the range of 5 nm for the central nanogap region, the effective gap separation of the gold dimer appears systematically larger. This effect is due to a combination of metal diffusion and aperture clogging during evaporation, as well as metal wetting and diffusion onto the substrate.

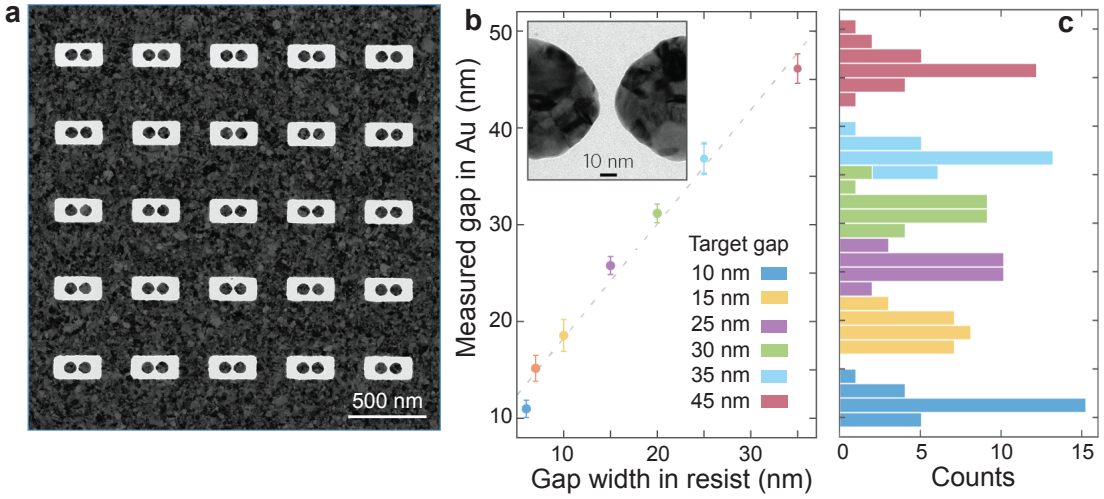

FIGURE 5.3: **TEM metrology and nominal gap size.** (a) TEM image of a 5 × 5 antenna array with a 10 nm nominal gap width used for metrology purposes with no template stripping performed. The scale bar is 500 nm. The rectangular apertures have 300 × 140 nm^2 dimensions with each nanosphere being 80 nm in diameter. (b) Measured gap width of the Au dimers as a function of HSQ structure design width. Average gap width and associated standard deviation error bars are displayed. (c) Corresponding distribution histogram with 1.5 nm bin width. The gap size variations are due to the finite grain size in the Au film.

5.3 Near field enhancement and nanoantenna resonance

We perform numerical modeling based on FDTD method using Rsoft Fullwave 6.0 software for nanoantenna with 10 nm (Figure 5.4a-c) and 30 nm (Figure 5.4d-f) gap sizes and access excitation intensity enhancement at 633 nm with polarization along the dimer axis. The computation considers the mesh size of 0.5 nm for 10 nm gap antenna and 1 nm for 30 nm gap antenna and uses 214 temporal steps of 8.1×10^{-19} s. The permittivity of gold is modeled according to the data in Ref. [151].

The intensity recorded at the antenna surface for 10 nm gap (a) shows excitation intensity enhancement up to 600×, while a 30 nm gap antenna yields nearly 160× near field enhancement (d). We perform a series of such modeling to study the evolution of the peak intensity enhancement as a function of the antenna nanogap separation (g), and then estimate the detection volume for each case (h). The estimation of the detection

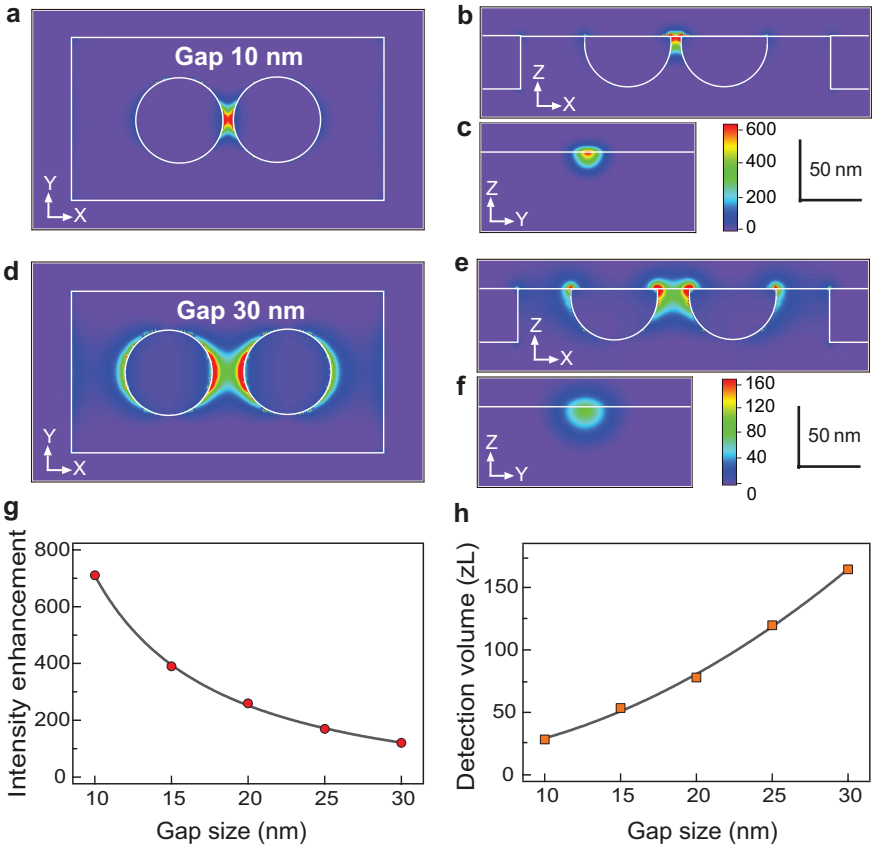

FIGURE 5.4: **Numerical simulations of excitation intensity enhancement and estimation of detection volume.** Excitation intensity enhancement at 633 nm are computed using finite-difference time-domain method for a nanoantenna of 10 nm gap size (a-c) and 30 nm gap (d-f). FDTD modeling is performed using mesh size 0.5 nm for (a-c) and 1 nm for (d-f). The intensity is recorded at the antenna surface for (a,d) and along planes crossing the antenna's center for (b,c) and (e,f). (g) Evolution of the peak intensity enhancement at 633 nm computed in the gap region as a function of the antenna gap size. (h) Evolution of the detection volume as a function of the nanoantenna gap size.

volumes, considers the product of the typical decay distances along X, Y and Z axis obtained from the intensity maps. To accurately model the experimental data, for the X axis we take the gap size plus the nanoparticle radius, while for the Y axis, we take the full width at $1/e^2$. For the Z axis, we take the decay length at $1/e^2$, taking only into account the zone accessible to the solution sample. As we will discuss later in the upcoming Section 5.5.1 (FCS to quantify near field detection volume), these empirical estimation of the detection volumes stand in excellent agreement with those acquired from fluorescence experimental data.

Figure 5.5 shows the experimental dark-field scattering spectra measured for 10 nm (a) and 35 nm (b) gap sizes and both polarization configurations of the illumination light. The polarization sensitivity, and gap size influence is further confirmed by these dark-field spectra. Figure 5.5c,d displays the fluorescence spectra of both the dyes (Alexa Fluor

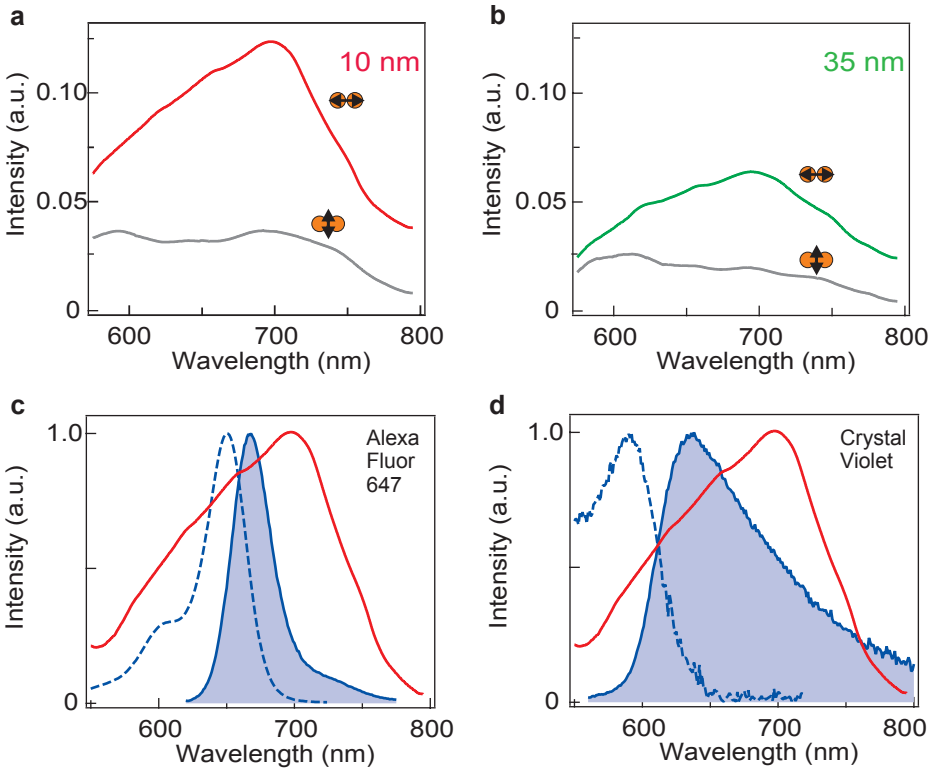

FIGURE 5.5: **Nanoantenna resonance and overlap with the fluorescence spectra.** (a,b) Dark-field scattering spectra for 10 nm (a) and 35 nm (b) gap sizes and two orientations of the illumination polarization. (c,d) Spectral overlap of the 10 nm antenna's response (red lines) with parallel orientation compared to the fluorescence spectra for Alexa Fluor 647 (c) and Crystal Violet (d). Excitation spectra are shown with dashed lines, emission spectra with solid shaded lines.

647 and Crystal Violet) indicating the excellent overlap with the spectral response of 10 nm antenna (red lines) excited in parallel configuration. The dashed lines represent the excitation spectra, while the solid shaded lines being the emission spectra of the fluorophores.

5.4 Experiment and results: Burst analysis of single-diffusing fluorophores

The fluorescence experiment setup is based on an inverted confocal microscope with a high NA water-immersion objective and is the same as used in earlier experiments (double nanohole and silicon dimers). The details on each optical component is presented in Chapter 2. Fluorescence burst analysis with these planar "antennna-in-box" devices are performed using two different dyes: Alexa 647 molecules with 200 mM methylviologen (8% quantum yield) and Crystal Violet molecules (2% quantum yield), both of which have similar excitation spectra.

Fluorescence experiments are performed by covering the nanoantenna substrate with a solution containing 1 μM Alexa Fluor 647 with 200 mM methylviologen in water-glycerol solution (1:1 ratio). Use of glycerol essentially slows down the diffusion of molecules through the confined nanoantenna hotspot eventually making the single-molecule events stand out more prominently on top of a near constant background. The experiments are carried out for different gap separations (10, 25 and 35 nm gaps), the fluorescence enhancement factors are then quantified in each case.

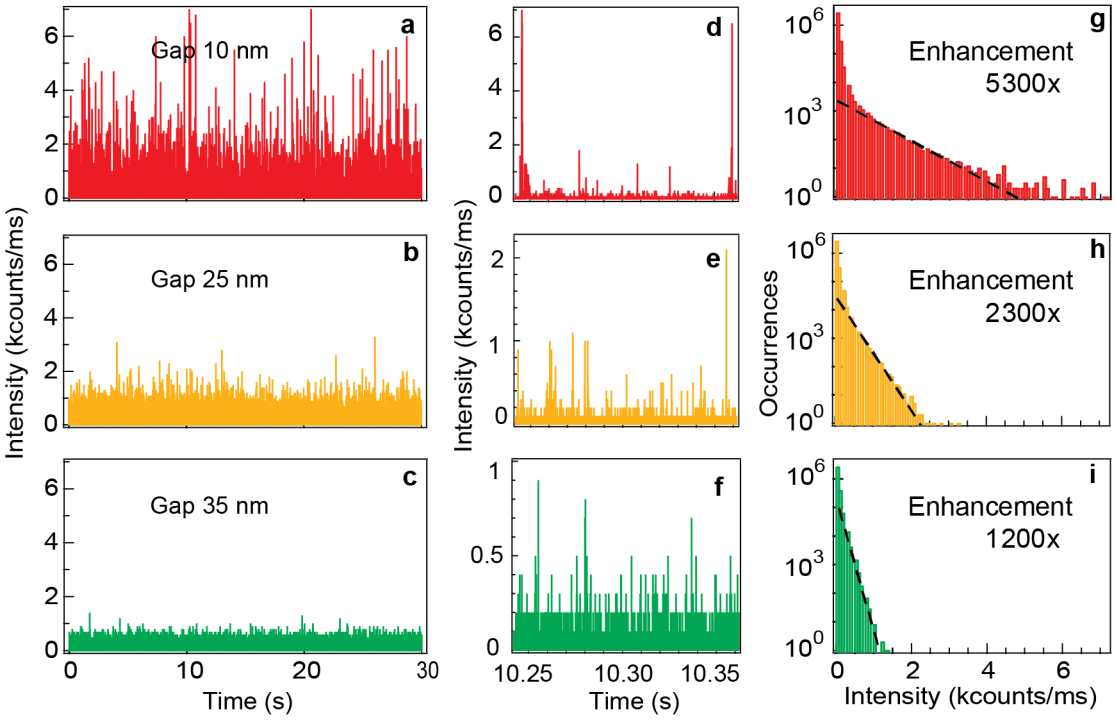

FIGURE 5.6: **Fluorescence bursts analysis on Alexa Fluor 647 molecules.** Fluorescence bursts analysis to determine the enhancement factors for Alexa Fluor 647 molecules with 200 mM methylviologen. (a-c) Fluorescence time traces recorded on nanoantennas with increasing gap sizes using 1 μM Alexa Fluor 647 in water-glycerol 1:1 solution with 2.3 kW/cm^2 excitation intensity at 633 nm. The binning time is 10 μs. (d-f) Enlarged temporal windows showing discrete bursts that correspond to individual molecules crossing the antenna detection volume. (g-i) Photon count rate histograms deduced from the traces in (a-c). The dashed lines are fits by exponentially decaying probability distributions. A reference of 0.85 counts/ms for Alexa Fluor 647 (with 200 mM methylviologen as chemical quencher) is used to compute the fluorescence enhancement factors.

Figure 5.6a-c shows the single molecule fluorescence time trace for Alexa Fluor 647 probed with planar "antenna-in-box" devices with increasing gap sizes: 10 nm (a), 25 nm (b) and 35 nm (c). Enlarged temporal windows (d-f) display discrete bursts that correspond to individual molecules crossing the nanoantenna detection volume. Intense fluorescence bursts are clearly detected on the fluorescence time traces, with their amplitude decreasing as the gap size is enlarged. This feature confirms that the fluorescence

bursts stem from the confined nanoantenna gap region (hotspot). All the time traces are recorded with 2.3 kW/cm^2 excitation intensity at 633 nm, binned at 10 μs and finally collected in the photon count histograms (g-i). These histograms are then fitted using exponentially decaying probability distributions represented by the dashed lines. The recorded maximum peak amplitude is then used to calculate the fluorescence enhancement factors for each gap size.

For a 10 nm gap antenna, we record a peak amplitude with intensity 4.5 kcounts/ms. Using the reference of 0.85 counts/ms for Alexa Fluor 647 (with 200 mM methylviologen as chemical quencher), we derived 4.5k/0.85 = 5300× fluorescence enhancement for a nanoantenna with 10 nm nominal gap. The calculation of 0.85 counts/ms brightness per molecules in the case of confocal reference is summarized in Figure 5.7. Alexa Fluor 647 molecules fluorescence bursts events recorded with confocal configuration (without nanoantenna) with very diluted ∼ 10 pM fluorophore concentration. This low fluorophore concentrations ensures that the fluorescence bursts (a,b) stem from individual molecules crossing the 0.5 fL confocal detection volume. No methylviologen is used to reach ∼30% quantum yield and the excitation intensity is increased by 4× to reach 9.2 kW/cm^2. Thus to compute the reference count rate per molecule for the experiments in Figure 5.6, we take the highest intensity in the confocal photon count rate histogram (Figure 5.7c), correct for the 4× lower excitation intensity and 4× lower quantum yield in the presence of methylviologen, to reach a value of 13/(4*4) = 0.85 counts/ms.

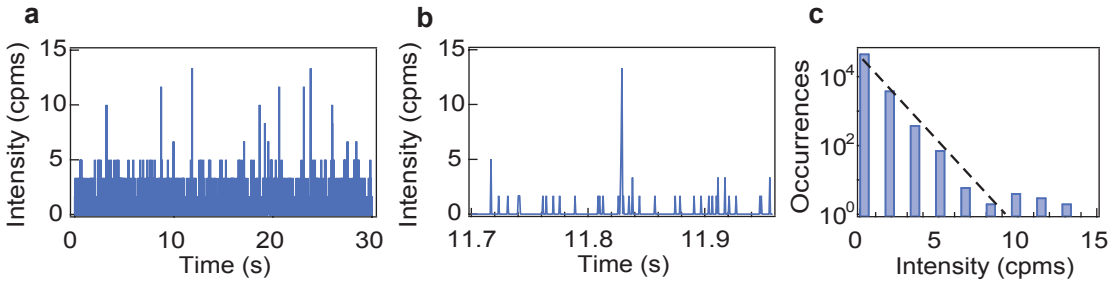

FIGURE 5.7: **Reference fluorescence bursts analysis for Alexa Fluor 647.** (a) Fluorescence time trace for Alexa Fluor 647 in confocal setup (detection volume 0.5 fL). A concentration of 10 pM ensures that the fluorescence bursts stem from individual molecules (b). No methylviologen is used to reach a quantum yield ∼30%. The excitation intensity is increased here by 4× to reach 9.2 kW/cm^2. The binning time is 0.6 ms to optimize the signal-to-noise ratio. (c) Photon count rate histogram deduced from the trace in (a). The dashed line is a fit by an exponentially decaying probability distribution. To compute the reference count rate per molecule for the experiments in Figure 5.6, we take the highest intensity, correct for the 4× lower excitation intensity and 4× lower quantum yield in the presence of methylviologen, to reach a value of 13/(4*4) = 0.85 counts/ms.

Emitters with low quantum yields allow reaching higher fluorescence enhancement factors, as the nanoantenna benefits from a larger increase in the emission quantum yield of the dye [152, 153]. To experimentally demonstrate this effect, we perform similar fluorescence burst analysis measurements with Crystal Violet molecules which have a weaker 2% quantum yield as compared to 8% in case of Alexa647 with 200 mM methylviologen. As in the case of Alexa 647, Crystal Violet fluorophore is set to a concentration of 1 μM in a water-glycerol 1:1 solution to slow down the diffusion of fluorophore crossing the nanoantenna hotspot, and thereby allowing direct analysis of the fluorescence bursts for individual molecules.

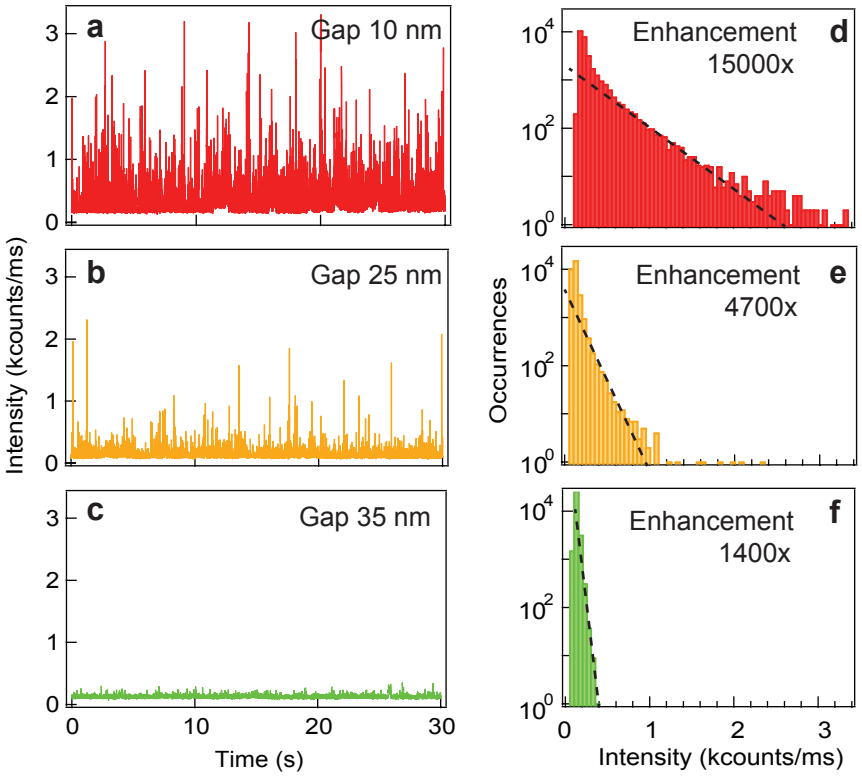

FIGURE 5.8: **Fluorescence enhancement on Crystal Violet molecules measured with fluorescence bursts analysis.** (a-c) Fluorescence time traces recorded on nanoantennas with increasing gap sizes using 1 μM of Crystal Violet in water-glycerol 1:1 solution with 2.3 kW/cm^2 excitation intensity at 633 nm. The binning time is 1 ms. (d-f) Photon count rate histograms deduced from the traces in (a-c). The dashed lines are fits by exponentially decaying probability distributions.

Figure 5.8 summarizes the fluorescence burst analysis for Crystal Violet molecules as probed by the planar antenna-in-box platforms with increasing gap separations. Intense fluorescence bursts are detected on the fluorescence time traces (a-c), with their amplitude decreasing as the gap size is enlarged from 10 nm to 35 nm. This feature is consistent with the burst analysis for Alexa647 molecules and confirms that the fluorescence bursts stem from the confined nanoantenna hotspot region. To measure the fluorescence

enhancement factors for the case of diffusing CV molecules, we fit the photon count histograms in Figure 5.8d-f with exponentially decaying probability distributions and record the maximum peak amplitude in the fitted distribution. The estimation of the peak fluorescence count per CV molecule for confocal reference is shown in Figure 5.9. As the CV molecules have a very low ∼2% quantum yield, detecting individual burst and estimating their count rates for confocal reference need extra care. We perform burst analysis at ∼pM concentration with higher excitation powers followed by a confocal FCS analysis (at ∼nM concentration) to accurately estimate the confocal count rates for CV molecules.

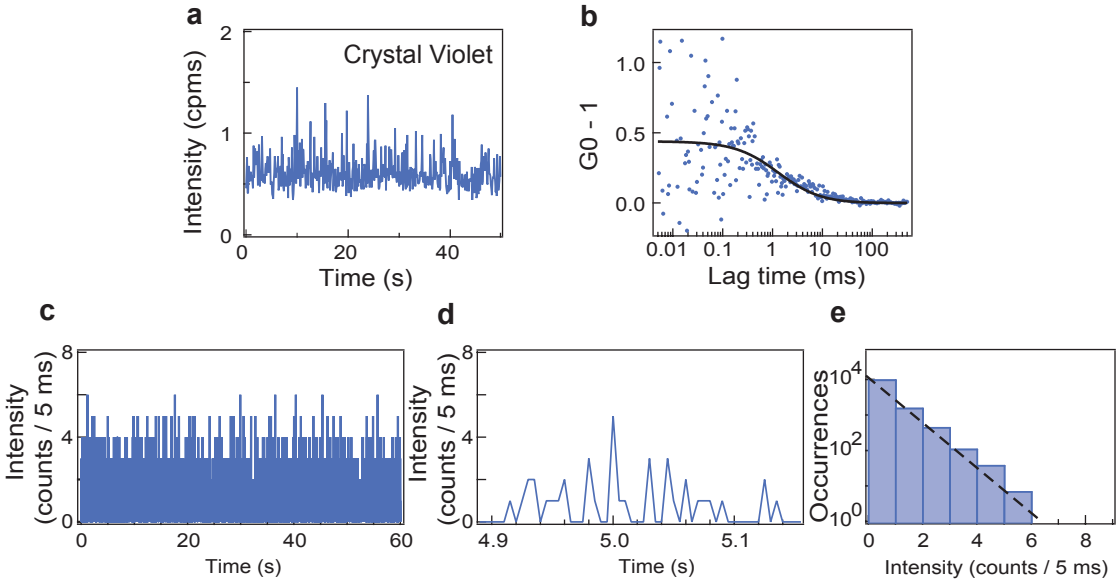

FIGURE 5.9: **Confocal reference data for Crystal Violet molecules.** (a) Intensity time trace and (b) correlation curve for Crystal Violet molecules diffusing in confocal volume. The excitation intensity at 633 nm is raised to 6× to 13.8 kW/cm^2 to provide enough signal to noise ratio. For the FCS analysis on this experiment, we take into account the 0.15 counts/ms dark count noise of our APDs to quantify an average number of 1.3 molecules with 0.36 counts/ms as brightness per molecule. The concentration is further diluted by 5× to to ensure that the fluorescence bursts stem from individual molecules (c,d), and the photon count rate histogram deduced from the time trace in (c) is displayed in (e). The dashed line is a fit by an exponentially decaying probability distribution. The excitation intensity is 13.8 kW/cm^2, and is 6× higher that the intensity used for the antenna experiments of Figure 5.8. The binning time is 5 ms. To compute the reference count rate per molecule for the experiments in Figure 5.8, we take the highest intensity above the noise level, correct for the 6× lower excitation intensity and 5 ms binning time to reach a value of 5.5/(6*5) = 0.18 counts/ms.

Figure 5.9 shows the fluorescence time trace (a) of the diluted Crystal Violet molecules diffusing through the confocal volume and recorded at a higher excitation powers 6× to 13.8 kW/cm^2 to provide enough signal to noise ratio, and the corresponding correlation curve (b). For FCS analysis on this experiment, we take into account the 0.15 counts/ms dark count noise of our APDs to quantify an average number of 1.3

molecules with brightness per emitter being 0.36 counts/ms. Now we further dilute the solution by 5× to visualize single diffusing fluorophore in confocal volume (c,d). Photon count rate histogram is then deduced from the confocal time trace and is displayed in (e). The excitation intensity is 13.8 kW/cm^2 and is 6× higher than the intensity used for the nanoantenna experiments of Figure 5.8. The dashed line is a fit by an exponentially decaying probability distribution indicating a peak intensity amplitude being 5.5 counts/bin time. Thus using this peak intensity value above the noise level, correcting for the 6× lower excitation intensity and 5 ms binning time, we reach the value of 5.5/(6*5) = 0.18 counts/ms. This value of confocal reference is then used to estimate the fluorescence enhancement factors for time traces acquired with antenna-in-box devices. The confocal reference fluorescence counts per CV molecule estimated at 0.18 counts/ms at 2.30 kW/cm^2 excitation power is in agreement with values reported independently in Refs. [17, 18].

From the photon counts histogram for 10 nm gap antenna (Figure 5.8a), the maximum count is 2750 counts/ms with a background of 100 counts/ms set by the fluorescence from the CV molecules diffusing away from the hotspot region and the residual photoluminescence from the metal. This quantifies to an impressive fluorescence enhancement of 2750/0.18 = 15,000× for CV molecules diffusing through the nanogaps. The same procedure for 25 nm and 35 nm gap separations yields fluorescence enhancement of 4700× and 1400× respectively. It is worth recalling that the same procedure performed on Alexa Fluor 647 with 200 mM methylviologen (8% quantum yield) indicated a fluorescence enhancement of 5300× for a 10 nm gap antenna. The relative change in the enhancement factors results from the differences in the quantum yield between CV (2%) and Alexa 647 with 200 mM methylviologen (8%) and further confirms that our measurements are not influenced by artifacts.

5.5 Optical performance at high molecular concentration

After discussion on the fluorescence burst analysis (experiments performed at 1 μM concentration), we now elaborate the optical performance of these nanoantennas with FCS experiments at very high 26 μM concentrations of Alexa 647 molecules along with 200 mM methylviologen as the chemical quencher.

5.5.1 FCS: Planar nanoantennas at 26 μM Alexa Fluor concentration

FCS determines the average number of detected molecules from which the fluorescence brightness per emitter and the detection volume can be deduced. This gives an alternative validation to the fluorescence enhancement factors from burst analysis and also provides an estimation on the antenna's near field detection volume. Figure 5.10a,b displays the raw fluorescence intensity time traces and corresponding correlation curves with excitation polarization parallel (colored dots) and perpendicular (gray dots) to the antenna dimer axis for two different 10 nm and 35 nm gap separations. Larger fluctuations in fluorescence time trace and higher correlation amplitudes are clearly observed when the incident electric field is parallel to the dimer axis and when the gap size is reduced. This directly evidences the presence of an electromagnetic hotspot in the nanoantenna gap region. In contrast to the parallel excitation, all the relevant observables, nanoscale volume confinement and fluorescence enhancement disappear when the laser polarization is oriented perpendicular to the main antenna axis or when the gap size is increased to 35 nm gap. We performed control experiments with an extra 8 nm thick silica layer deposited on top of the nanoantennas to prevent the molecules from accessing the hotspot region. In this case, the FCS signal is lost (see Figure 5.10c,d) confirming the crucial role of the few nanometer region surrounding the antenna gap.

All the FCS experiments are performed at 26 μM concentration of Alexa Fluor 647, corresponding to about 7630 molecules in the 0.5 fL confocal detection volume. Figure 5.11 shows the confocal FCS analysis for Alexa 647 with 200 mM methylviologen with experimental condition exactly similar to those for Nanoantenna-FCS measurements displayed in Figure 5.10. The correlation amplitude scales as the inverse of the number of fluorescent molecules in the detection volume, so for the confocal reference without the nanoantenna, the FCS amplitude is barely detectable at $1.31e^{-4}$, which amount to 7630 molecules in the 0.5 fL confocal volume. The average fluorescence brightness per molecule is then derived as 1800/7630 = 0.24 counts/ms.

However the correlation amplitudes of 3.9 are detected with the nanoantennas of 10 nm gap size, representing 0.26 number of molecules on average diffusing through the hotspot region. This corresponds to $N_{conf}/N_{antenna} = 30{,}000\times$ volume reduction than the diffraction limited confocal volume. Using the known 26 μM fluorophore concentration and the 0.5 fL confocal volume, the antenna detection volume is then quantified to be 17 zL (1 zL $= 10^{-21}$ L $= 1000\ \mu\text{m}^3$). This represents the smallest antenna detection volume reported so far for FCS applications on nanoantennas. The reduction of the detection volume is further confirmed by the shortening of the diffusion time, from 64 μs in the diffraction-limited confocal volume to 0.9 μs in the nanoantenna case.

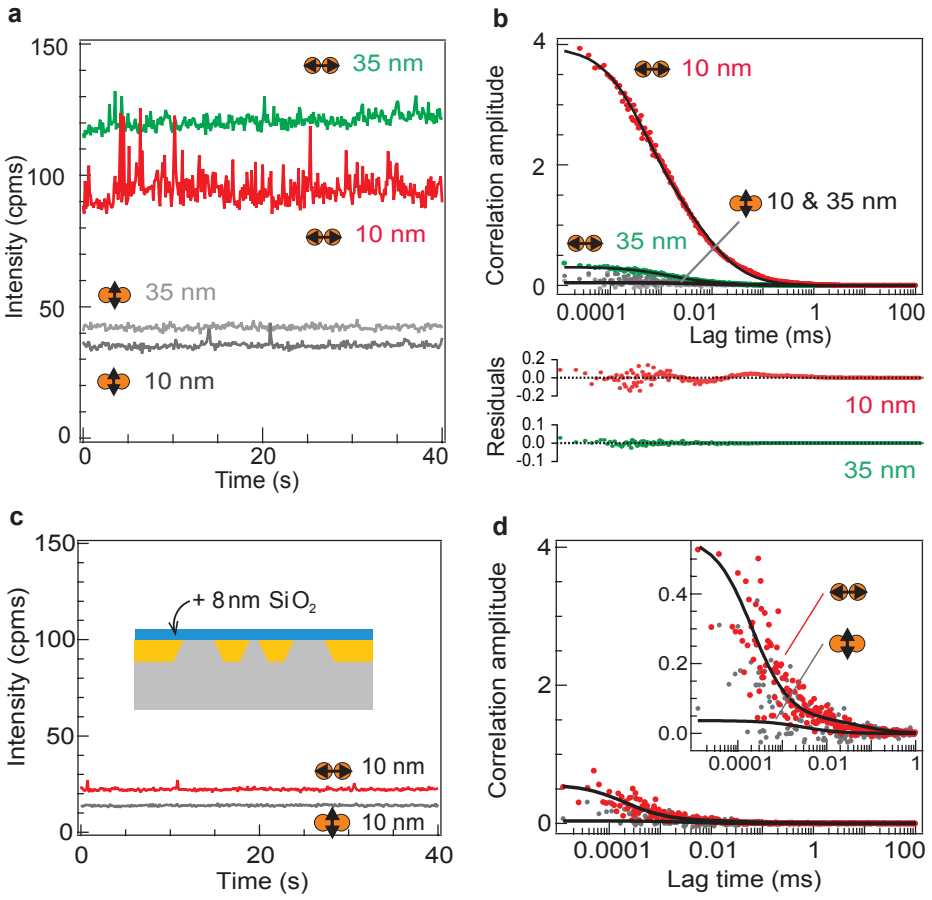

FIGURE 5.10: **Nanoantennas enhance the fluorescence detection of Alexa Fluor 647 molecules in solution.** (a) Fluorescence time traces and (b) corresponding FCS correlation functions (dots, raw data; lines, numerical fits) for nanoantennas with 10 and 35 nm gap sizes with the excitation polarization set parallel or perpendicular to the antenna's main axis. The experimental conditions correspond to 26 μM of Alexa Fluor 647 with 200 mM of methylviologen as chemical quencher under 2.3 kW/cm^2 excitation intensity at 633 nm wavelength. The bottom panel shows the residuals of the fits for 10 nm and 35 nm gap nanoantennas. (c) Control experiment with 8 nm SiO_2 deposited on top of the nanoantenna. Adding an extra 8 nm layer of silica on top of the nanoantenna blocks most of the fluorescence by preventing the molecules from accessing the hot spot region. To enable a direct comparison, the experimental conditions and figure scales in c, d are identical to the ones used in a, b, and confirm that the nanoscale detection volume is located at the antenna surface.

For our earlier experiments (double nanoholes and silicon dimer antennas), the background fluorescence from molecules diffusing away from the hotspot had a significant contribution in the total fluorescence signal, thereby complicating the FCS analysis. In our earlier chapters, we used a two-species model (incorporating hotspot and background contribution) for FCS analysis to estimate count rate per molecule only from the hotspot region. However, in the case of planar antenna-in-box devices, we find that the signal from the hotspot always largely dominates the background, so that the previously used corrections are no longer needed. The number of detected molecules is simply the inverse of the correlation amplitude at zero lag time, and the fluorescence brightness

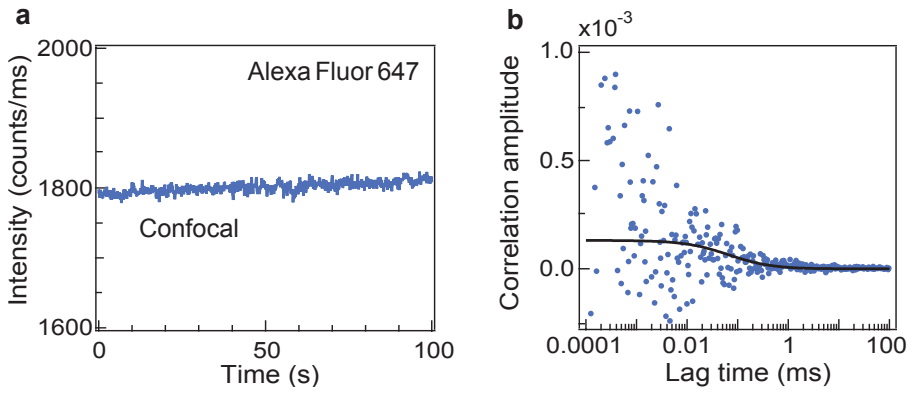

FIGURE 5.11: **Confocal reference for FCS experiments on Alexa Fluor 647.** (a) Intensity trace and (b) FCS correlation function. The experimental conditions are identical to the measurements on nanoantennas: the concentration of Alexa Fluor 647 is 26 μM, with 200 mM of methylviologen as chemical quencher. The excitation intensity is 2.3 kW/cm^2 at 633 nm wavelength. The FCS correlation amplitude is $1.31e^{-4}$, which amount to 7630 molecules in the 0.5 fL confocal detection volume. The average fluorescence brightness per molecule is 1800/7630 = 0.24 counts/ms.

per emitter can be computed by normalizing the average fluorescence intensity by this number of detected molecules. For the antenna with 10 nm gap size, we find a brightness of 370 counts/ms. This value is 1600× higher than the 0.24 counts/ms estimated for the dye in the confocal reference. The polarization sensitive correlation curves with amplitudes confirms the occurrence of large fluorescence enhancement in the nanogaps.

It should be noted that the fluorescence enhancement factors for Alexa 647 estimated from the burst peak intensity (5300× for 10 nm gap antenna as shown in Figure 5.6) is about 3× higher than the one measured with FCS (1600× for same gap separation as shown in Figure 5.14). This is expected as the burst analysis favors the best event where the emitter's position and orientation lead to the highest fluorescence intensity.

We carried out similar FCS experiments with 10 nm gap nanoantenna (excitation parallel to the dimer axis) to study the excitation power dependence on the optical performance. Figure 5.12 shows the raw fluorescence trace of 26 μM Alexa647 with 200 mM of methylviologen as chemical quencher (a), the evolution of the average fluorescence intensity as the function of excitation intensity (b) and the corresponding normalized correlation curves (c). The average fluorescence intensity count rate shows limited saturation for excitation intensity exceeding 3.4 kW/cm^2. As all of our fluorescence experiments are carried out at 2.3 kW/cm^2 excitation intensity, our results are not affected by any photophysical artifacts. Moreover, as the shapes of the correlation curves at short lag times appear similar with different excitation powers, the influence of triplet blinking is avoided in the FCS analysis. As a final control experiment, in Figure 5.13 we show that in the absence of fluorescent molecules, the residual background luminescence from the

gold nanoantenna (a) remains negligible and thereby exhibiting no temporal correlation (b).

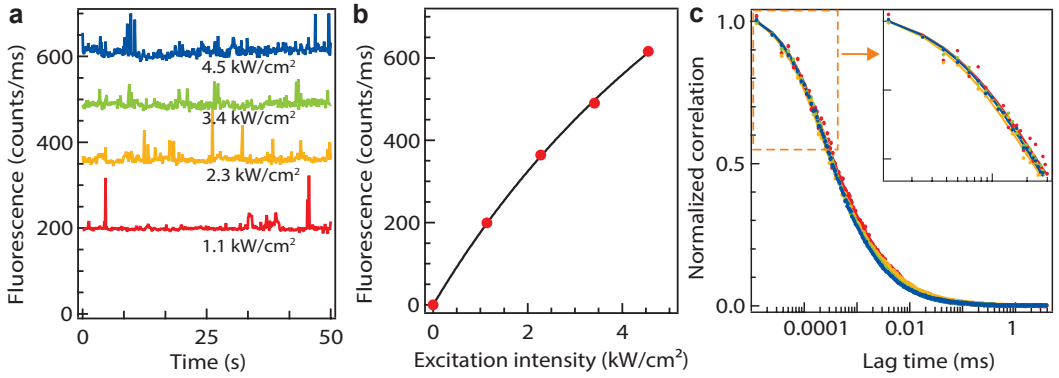

FIGURE 5.12: **Power dependence study shows limited saturation and no triplet blinking effects.** (a) Fluorescence time trace recorded on a 10 nm gap antenna with increasing illumination intensities. (b) Evolution of the average fluorescence intensity as function of the excitation intensity showing that the 2.3 kW/cm^2 used in this study is well within the linear fluorescence regime. (c) Normalized FCS correlation functions of the traces in (a) with same color code. The similar shapes at short lag times reveal a negligible influence of triplet state blinking in the FCS data.

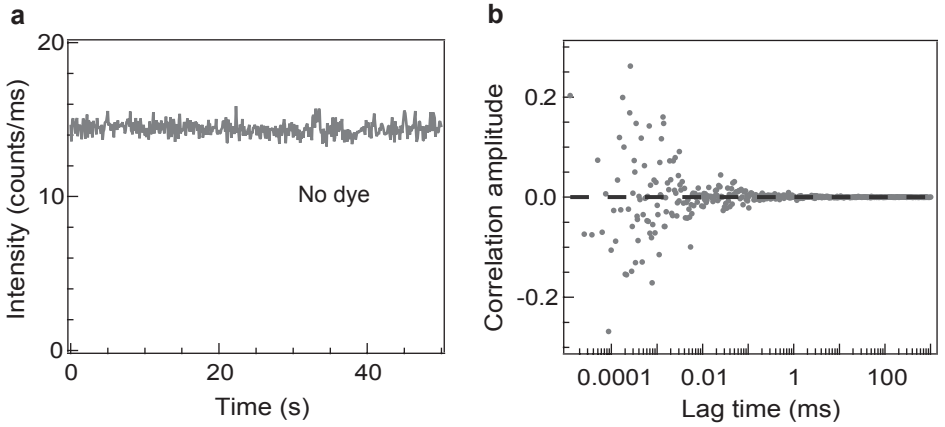

FIGURE 5.13: **Nanoantenna luminescence background in the presence of 200 mM methylviologen and no fluorescent dye.** (a) Intensity trace and (b) FCS correlation function on a 10 nm gap antenna. The 2.3 kW/cm^2 excitation intensity at 633 nm is similar to all experiments.

For bio-inspired applications of nanoantennas, it is desired to have arrays of structures having sharp edges with reproducible optical performances. As shown in TEM metrology (see Figure 5.3), using the described procedure, mass fabrication of sub 20 nm gap antenna is possible. To assess the statistical reproducibility of the antenna performance, we repeat the FCS experiments on a set of more than 80 different antennas and measure for each antenna its fluorescence enhancement and the near field detection volume. Scatter plot displayed in Figure 5.14a, clearly indicates a correlation between the fluorescence enhancement and the detection volume following an empirical power law with

-2/3 exponent: the volume scales as cube power of the typical near field size, while the fluorescence enhancement is dominated by the gain in local excitation intensity which scales as the square of the typical near-field size.

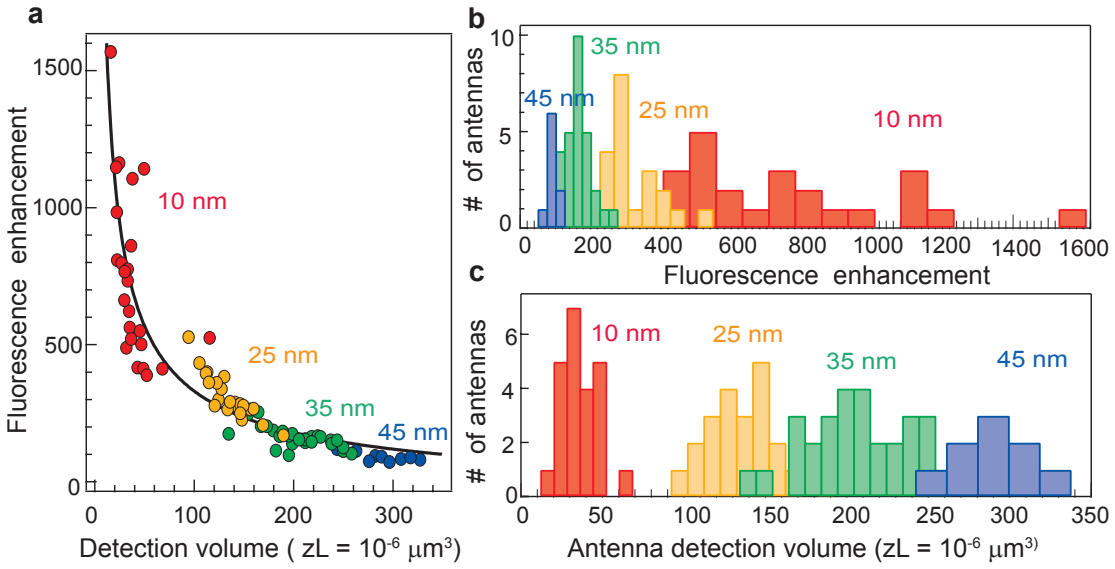

FIGURE 5.14: **Statistical reproducibility of the nanoantennas measured by FCS.** (a) Scatter plot of the fluorescence enhancement versus the nanoantenna's detection volume as deduced from FCS analysis on 83 different nanoantennas. The black line fit follows a power law dependence with a fixed -2/3 exponent. (b) Distribution of fluorescence enhancement factors deduced from the data in (a) for different gap sizes. (c) Distribution of the nanoantenna detection volume.

Figure 5.14 shows the histograms of the fluorescence enhancement (b) and detection volume (c) illustrating the statistical dispersion of the data around the average for each value of the desired nominal gap size. The variability of the gap sizes as characterized by TEM (see Figure 5.3), influences this dispersion. This is more prominent for the smaller gaps where a nanometeric variation in the gap size can have a large influence on the antenna's performance and the measured enhancement factor.

We now compare the performance of these planar nanoantennas with the FCS results achieved previously using focused ion beam milling [90]. Figure 5.15 compares the average values of fluorescence enhancement (a) and detection volume (b) obtained for nanoantennas fabricated with conventional FIB milling and template-stripped E-beam lithography. The nanoantennas are tested under similar conditions for FCS experiments to ensure a consistent benchmarking. As demonstrated in Figure 5.15, template-stripped E-beam lithography provides higher fluorescence enhancement factors in smaller detection volumes. The improvement over FIB milling is especially significant for gap sizes above 25 nm, where the new fabrication technique can lead to a 10× increase for the fluorescence enhancement factor together with a 5× reduction for the detection volume.

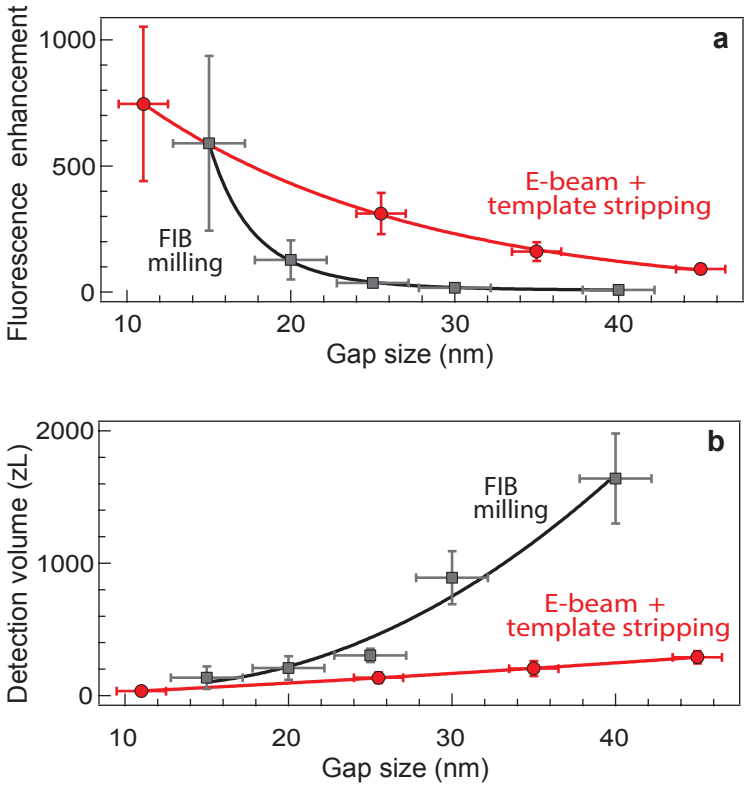

FIGURE 5.15: **Improved nanoantenna's performance with template-stripped electron beam lithography as compared to focused ion beam milling (FIB).** Average values of fluorescence enhancement (a) and detection volume (b) as a function of the gap size. The data for focused ion beam (FIB) milling is taken from Ref. [90]. The experimental conditions are similar for both fabrication methods (Alexa 647 fluorophores with 200 mM methylviologen). Error bars correspond to one standard deviation. The performance of these new optical nanoantennas significantly outperforms the values achieved previously using focused ion beam lithography providing higher fluorescence enhancement factors in smaller detection volumes.

5.5.2 Fluorescence lifetime reduction and LDOS enhancement

The presence of a nanoantenna in the vicinity of the fluorophore accelerates the decay rates as compared to the free space de-exciation. We now study this increased LDOS (Purcell effect) in case of planar "antenna-in-box" platforms and discuss different rates and the evolution with gap sizes. The experimental setup is the same as used in earlier projects (double nanohole and silicon dimers), and the description of the optical setup is already presented in Chapter 2.

The TCSPC experiment for planar "antenna-in-box" is carried out with Alexa647 fluorophore with 200 mM methylviologen. The experimental conditions are similar to those used for FCS (Figure 5.10), with only difference being the pulsed excitation. Figure 5.16a shows the normalized time-resolved decay traces for three cases: confocal (blue dots),

35 nm gap (green dots) and 10 nm (red) gap separation for antenna in box with parallel excitation. The inset summarizes the fluorescence lifetime for all gap separations together with confocal and box-only configuration. As expected, the decay kinetics are comparable for the confocal reference and the box-only geometry. In contrast, excitation along the gap induces a clear acceleration of the decay dynamics for all gap separations: fast acceleration with smallest gap size. The fluorescence lifetime is significantly reduced from 380 ± 15 ps in confocal illumination to 45 ± 10 ps for the 10 nm gap antenna.

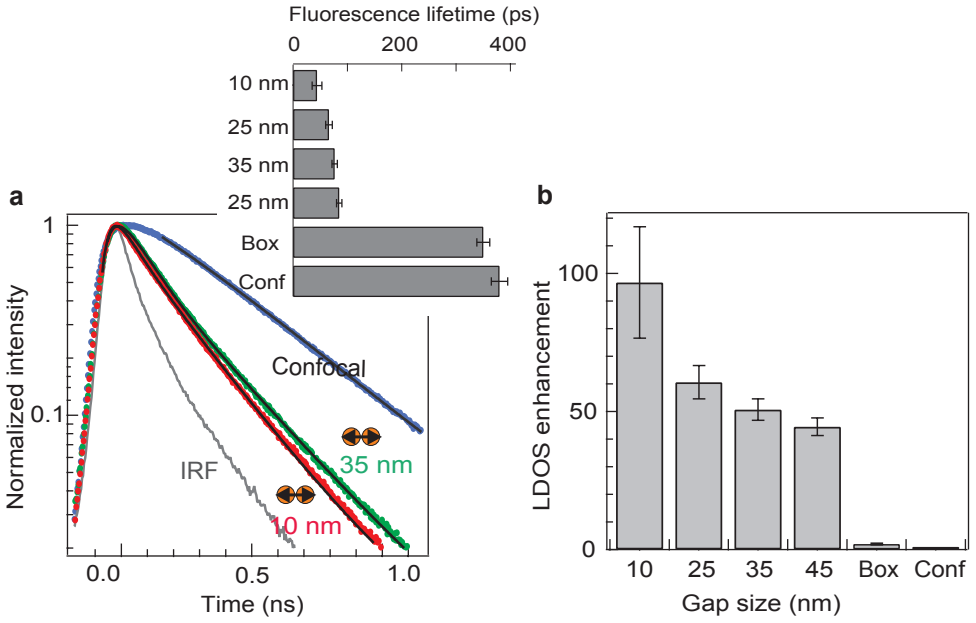

FIGURE 5.16: **Fluorescence lifetime reduction and LDOS enhancement.** (a) Normalized time-resolved decay traces show Alexa Fluor 647 fluorescence lifetime reduction as the gap size is reduced. Black lines are numerical fits convoluted by the instrument response function (IRF). The inset shows the fluorescence lifetime of Alexa Fluor 647 in presence of 200 mM of methylviologen as function of the nanoantenna gap size. (b) Local density of optical states (LDOS) enhancement deduced from the lifetimes in (a), after correction of the methylviologen quenching rate and Alexa Fluor 647 natural non-radiative decay rate, following the procedure in Chapter 3 and 4.

Figure 5.16b summarizes the evolution of the local density of optical states (LDOS) enhancement as the function of nanoantenna gap size. LDOS is computed by removing the internal non-radiative rate contribution $\Gamma_{nr} = 0.67$ ns^{-1} of Alexa Fluor 647 and the quenching rate $\Gamma_q = 1.9$ ns^{-1} contribution set by methylviologen from the lifetime data measured from TCSPC experiments (see inset of Figure 5.16a).

The total decay rate (inverse of fluorescence lifetime) for 10 nm antenna, Γ_{tot} is 22.22 ns^{-1}. The contribution set only by the photonic environment is estimated to be $\Gamma^*_{rad} + \Gamma^*_{loss}$ = Γ_{tot} - Γ_{nr} - Γ_q = 19.7 ns^{-1}. The LDOS enhancement is then computed as $(\Gamma^*_{rad} + \Gamma^*_{loss})/\Gamma_{rad}$ = 19.7/0.21 = 100× keeping only the rate influenced by the photonic environment. This correction procedure is consistently used throughout the thesis, as the

internal non-radiative rate of Alexa and the quenching rate from the methylviologen are not influence by the presence of nanoantenna.

Finally the measured fluorescence enhancement factors is modeled using the equation [94]:

$$\eta_F = \frac{I^*_{exc}}{I_{exc}} \; \frac{\Gamma^*_{rad}}{\Gamma_{rad}} \; \frac{1}{1-\phi_0 \; + \; \phi_0 \, (\Gamma^*_{rad} + \Gamma^*_{loss})/\Gamma_{rad}} \tag{5.1}$$

This equation follows that the fluorescence enhancement η_F is the consequence of the excitation intensity enhancement I^*_{exc}/I_{exc}, enhancement of the radiative decay rates $\Gamma^*_{rad}/\Gamma_{rad}$, and together with the influence of initial quantum yield ϕ_0 of the fluorescent molecule modified within the nanogap. The third term in the above Equation 5.1 incorporates an additional decay rate Γ^*_{loss} describing the non-radiative energy transfer to the antenna's material induced by ohmic losses. For the smallest 10 nm gap and a dipole emitter located in the gap center, the FDTD simulations estimate the different contributions to be $I^*_{exc}/I_{exc} = 600$, $\Gamma^*_{rad}/\Gamma_{rad} = 700$ and $(\Gamma^*_{rad}+\Gamma^*_{loss})/\Gamma_{rad} = 1100$ (see near field simulations in Figure 5.4). Neglecting the collection efficiency improvement brought by the nanoantenna, the fluorescence enhancement values can be predicted to be 18,000× for Crystal Violet and 4700 for Alexa 647, which come in excellent agreement with the experimental results. The 1000-fold LDOS enhancement used in numerical estimation should be compared with the 100-fold LDOS enhancement observed experimentally by the lifetime measurements. This mismatch can partially be explained because of the spatial and orientation averaging during the experiments, and also due to the limited resolution of the TCSPC electronics.

Figure of merit

Using FCS and fluorescence burst analysis, we demonstrated the superior optical performance of these planar "antenna-in-box" devices reaching giant fluorescence enhancement factors up to 10^4-10^5 times, together with nanoscale detection volumes in the 20 zL range. Fluorescence enhancement factors displayed strong dependence in the initial quantum yield of the dye (2% for Crystal Violet and 8% for Alexa 647 with 200 mM methylviologen). To avoid this dependence of the fluorescence enhancement on the intrinsic quantum yield of the fluorescent reporter, the fluorescence enhancement figure of merit is defined as the product of the enhancement factor by the reference quantum yield of the emitter in homogeneous medium [61]. Thus, for Crystal Violet and Alexa Fluor 647, the fluorescence enhancement figures of merit amount to 300 and 420 respectively, and are among the highest reported values to date [17, 18, 19, 61, 90].

5.6 Polymer stability and nanoantenna durability

As described in the fabrication procedure, the semi-spheres gold dimers are embedded into an optically transparent polymer (ormocer) during the template-stripping step. This is important in order to bring the narrowest gap region at the top of the structure making it efficiently accessible to the probe sample. We demonstrated that these new class of optical antennas hold great interest for ultrasensitive fluorescence bio-sensing, especially for detecting single molecules at biologically-relevant micromolar concentrations. During the course of experimental measurements, the microscope coverslip containing these planar "antenna-in-box" structures is first rinsed with water-ethanol mixture and then cleaned with UV-Ozone treatment for 2 minutes to remove organic impurities. This optimized cleaning procedure is carried out once before and after every fluorescence experiment in order to increase the durability of these antennas. However, exposing the antenna to the UV-ozone atmosphere for a repeatedly long time can potentially damage the polymer thereby influencing the dimer position and the desired gap sizes.

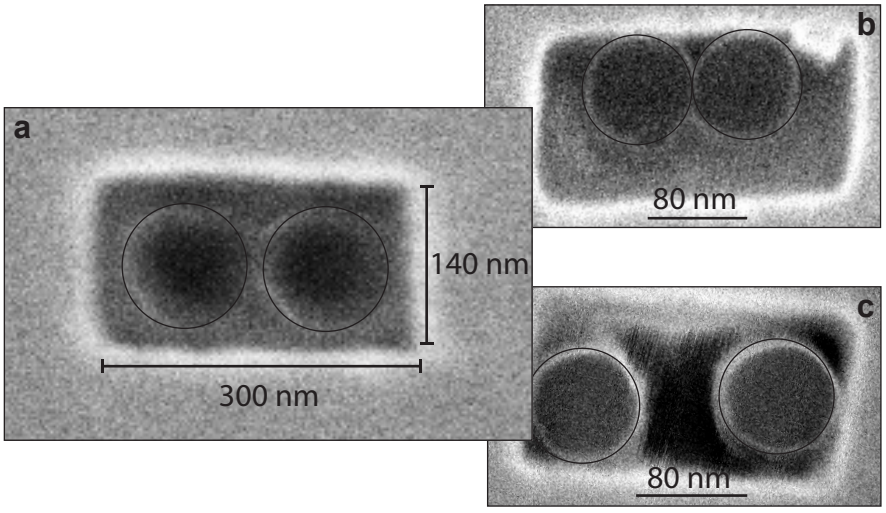

FIGURE 5.17: **Affect of UV-Ozone cleaning on the durability of nanoantennas.** Scanning electron microscope images of a representative structure imaged after 5× cleaning procedure each of them involving 5 minutes of UV exposure followed by water-ethanol rinsing (a). The same sample with addition 10× cleaning procedure shows significant damage in the polymer leading to displacement of the dimers within the box and eventually changing the desire gap dimensions (b,c). The SEM images are acquired at at 1 kV to prevent further damage to the polymer and thereby the low SNR in the acquired images.

We repeatedly carried out out this cleaning procedure involving UV-Ozone treatment and performed successive SEM image analysis to study the effect of the UV-Ozone treatment on the polymer stability. Figure 5.17a shows a representative structure imaged after 5× cleaning procedure (each of them involving 5 mins of UV exposure followed by water-ethanol rinsing). As seen in the SEM image (a), the 5× cleaning procedure indicates no

major troubles and the dimers are placed at the center of the box aperture. However the same coverslip when exposed to 10× cleaning procedure shows significant displacement of the dimers (Figure 5.17b,c). Although the UV-Ozone treatment is important just before the experiments to renders the gold surface hydrophilic and to remove any residual dyes after each fluorescence experiment, one should be aware that an excessive UV-Ozone treatment may eventually lead to significant damage to the polymer in which the dimers are embedded after template stripping. This etching rate (1-2 nm/min of UV-exposure), if not paid proper care will lead to displacement of the dimers within the box changing the desire gap dimensions and thereby misleading observations of the optical performance.

5.7 Summary

We have described the combination of electron beam lithography and template stripping as a reliable method to fabricate nanoantennas with direct accessibility of the hotspot region, large-scale availability, and gap sizes as small as 10 nm with sharp edges. Fluorescence burst analysis on single diffusing fluorophore resulted on impressive 15,000-fold fluorescence enhancement with micro second transit time in 10 nm gap antennas. Moreover we demonstrated the potential of these devices for single-molecule detection at very high 26 μM concentrations and realized a 30,000-fold volume reduction (20 zL) as compared to 0.5 μm^3 diffraction-limited confocal volume. Moreover using TCSPC experiments, we measured a 100-fold LDOS enhancement for fluorophores diffusing within these nanometric gaps.

Several additional test experiments confirmed the near-field origin of the fluorescence signal. First, all the relevant observables, fluorescence enhancement, nanoscale volume confinement and lifetime reduction disappeared when the excitation laser was oriented perpendicular to the antenna's dimer axis or when the gap size was increased. Experiments with an extra 8 nm thick silica layer deposited on top of the antennas showed neither enhancement in the fluorescence signal and nor any correlation in FCS analysis. This confirmed that the near field volume is confined within a few-nm and with an addition layer on top, prevents the diffusing molecules from accessing the hotspot region.

Finally, we compared template-stripped electron beam lithography based nanoantenna's performance with FIB milled structures. Using fluorescence burst anlaysis, FCS and TCSPC measurements we demonstrated that the template-stripped E-beam lithography provides higher fluorescence enhancement factors in smaller detection volumes. The fabrication method is fully scalable and adaptable to a broad wide range of antenna designs. We foresee broad applications of these in-plane antenna geometries ranging from

large-scale ultra-sensitive sensor chips, to microfluidics and live cell membrane investigations. In next chapter, we will exploit the surface planarity of these devices to investigate the diffusion dynamics of membranes lipids in living cells.

Chapter 6

Planar optical antenna for nanospectroscopy in living cells

In this chapter, we investigate the nanoscopic organization of the plasma membrane of living cells combining FCS with resonant optical nanoantennas. Using planar "antenna-in-box" devices with gap separation down to 10 nm, we investigate the diffusion dynamics of phosphoethanolamine (PE) and sphingomyelin (SM) on the membranes of living Chinese hamster ovary (CHO) cells. Together with cholesterol depletion experiments, we provide compelling evidence of cholesterol-induced nanodomain partitioning in plasma membranes and discuss the impact of these results in the context of *lipid rafts*.

This project was carried out in collaboration with the team of Prof. Jürgen Brugger (EFPL, Switzerland).

6.1 Plasma membrane structure and FCS diffusion laws

The plasma membrane plays a major role in cell physiology and is thus of fundamental importance to living systems. The spatial organization and diffusion dynamics of its constituents (lipids and proteins) occurring at the nanoscale largely influence cellular processes: from transmembrane signaling, intracellular trafficking to the cell adhesion

The contents of this chapter have been published in:

Regmi, R., Winkler, P.M., Flauraud, V., Borgman, K.J.E., Manzo, C., Brugger, J., Rigneault, H., Wenger, J. and García-Parajo, M.F., 2017. Planar optical nanoantennas resolve cholesterol-dependent nanoscale heterogeneities in the plasma membrane of living cells. *Nano Letters*, 17 (10), pp.6295-6302.

Winkler, P.M., **Regmi, R.**, Flauraud, V., Brugger, J., Rigneault, H., Wenger, J. and García-Parajo, M.F., 2017. Transient nanoscopic phase separation in biological lipid membranes resolved by planar plasmonic antennas. *ACS Nano*, 11(7), pp.7241-7250.

[154, 155]. Recent advances in cell biology have shown that the plasma membrane is much more complex than just a continuous fluidic system [156, 157, 158]. It has been postulated that sphingolipids, cholesterol and certain types of proteins can be enriched into dynamic nanoscale assemblies or nanodomains, also termed *lipid rafts* [159, 160]. Lipid rafts have been defined as highly dynamic and fluctuating nanoscale assemblies of cholesterol and sphingolipids that in the presence of lipid- or protein-mediated activation events become stabilized to compartmentalize cellular processes [161]. However, the true nature of these nanodomains remains debated with many conflicting evidences and predicated domain sizes in the broad range of 10-200 nm [162, 163, 164, 165, 166, 167]. This can be understood as the direct observation of these transient and nanoscopic features are restricted by the diffraction limit in the convectional optical microscopy techniques.

Early investigations on membrane organization were mostly based on fluorescence recovery after photobleaching (FRAP) [168] and single particle tracking (SPT) [156, 169]. Both techniques are limited either in space (with μm^2 probe area in FRAP) or in time (with millisecond temporal resolution in SPT). In addition, the conventional FCS measurements on the plasma membranes were limited to ∼300 nm spatial resolution set by the diffraction limit [163, 164, 170]. FCS is a widely adopted alternative for studying dynamics and biomolecular interactions [171] because of its high temporal resolution and a rather straightforward data analysis procedure [172, 173].

Various illumination strategies combined with FCS have been implemented over the past decade to achieve high spatial and temporal resolution, but membrane studies have so far remained above a ∼40 nm detection size. Stimulated emission depletion microscopy (STED) constrains the excitation spot down to ∼40 nm [174] and has been combined with FCS to explore the nanoscale dynamics occurring in lipid membranes on living cells [175, 176, 177, 178]. An alternative strategy takes advantage of nanophotonic structures to engineer the light intensity distribution at the nanoscale [8]. As summarized in Chapter 1, other notable designs include zero-mode waveguides [52, 53, 179, 180, 181, 182], bowtie structures [32, 148, 183], gold nanorods [56] and sub-wavelength tip based NSOM probes [10, 30]. These various approaches allow to confine the illumination light in the range of 50 to 100 nm. In recent years, resonant optical nanogap antennas have shown great potential to further constrain the laser light on a sub-20 nm scale [11] and greatly enhance the light-matter interactions [19, 61, 90]. However, so far the applications of such resonant nanogap antennas have been mostly employed to probe fluorescent molecules in solutions at high micromolar concentration.

In this project, we take advantage of recent advances in the nanofabrication to produce arrays of nanoantennas with controlled gap sizes, sharp edges and planar hotspots facing the upper surface of the sample (as introduced in earlier Chapter 5). We carried out

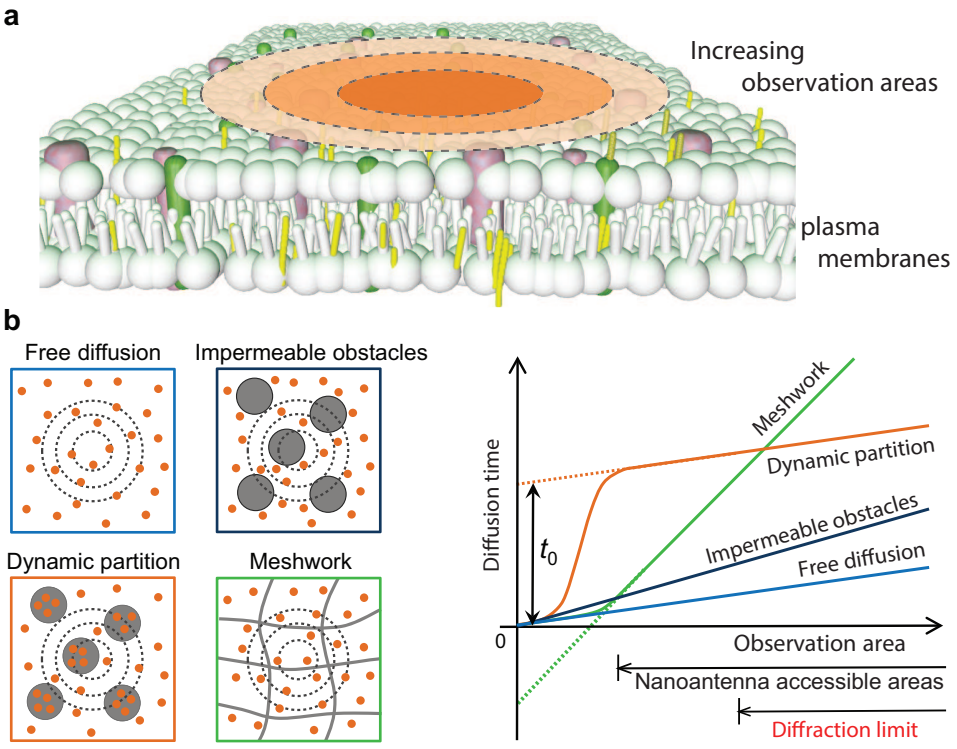

FIGURE 6.1: **Principles of FCS diffusion laws.** (a) FCS diffusion laws are constructed by measuring the average diffusion time across the increasing observation areas on a membrane. (b) Different diffusion models depending on the membrane organization lead to noticeable changes in the extrapolation of the curves through the y-axis intercept t_0, revealing the nature of the diffusion process. Free diffusion and impermeable obstacles are characterized by $t_0 = 0$, while a positive t_0 intercept indicates the presence of nanodomains transiently trapping the molecular probe. A negative t_0 intercept relates to a mesh-work of barriers separating adjacent domains.

FCS experiments on nanantennas with different gap sizes (see Figure 6.1a) to record the evolution of the diffusion time as a function of the illumination probe area. This essentially allows us to assess the nanoscale heterogeneities in the plasma membranes that would hinder the diffusion dynamics of the dye.

First introduced by Lenne *et al* [163, 170], this so called "FCS diffusion law" approach, allows to determine the nature of the diffusion process and the underlying membrane organization at scales smaller than the accessible experimental observation areas (see Figure 6.1b). The slope of the diffusion plot *vs* probe area essentially represents the effective diffusion coefficient describing the long-range mobility of the molecule, while the y-intercept t_0 on the time axis indicates the underlying membrane organization principle at small scales. Mathematically, the overall diffusion time (t) for a molecule passing through the focal spot can be expressed as [170, 184]:

$$t = t_0 + \frac{\omega^2}{4\mathrm{D}_{\mathrm{eff}}}$$

where t_0 is the offset derived from the FCS diffusion laws, ω being the FCS beam waist that essentially defines the probe area, and D_{eff} being the effective mobility diffusion constant that depends on the probability of crossing the barriers, and the microscopic diffusion coefficients. This mobility constant also depends upon the density of domains in the case of isolated microdomains.

Free diffusion is characterized by a near zero y-intercept (*i.e.*, $t_0 = 0$) for vanishing probe area as the curve crosses the origin. The presence of impermeable obstacles hinders the effective diffusion of the molecules and thus increases the transit time to cross through a given probe area. The slope of the FCS diffusion curve in such a case is higher, but still crossing through the origin. In contrast, the dynamic partitioning into nanodomains is characterized by a deviation of the y-intercept on the time axis from the origin (*i.e.*, $t_0 > 0$), while a trapping into in a molecular mesh-work is revealed by a negative y-intercept (*i.e.*, $t_0 < 0$) [173]. Using this approach, spot variation FCS (sv-FCS) have been demonstrated to study the transient confinement times of mobile tracers in the plasma membrane with minimum attainable spot size being the diffraction limit of the excitation light [184].

In this Chapter, we taking advantage of the nanoscale spatial resolution achieved by the nanogap antenna to establish the FCS diffusion laws with spatial resolution being as small as 10 nm. Combining FCS with resonant planar nanoantennas, we investigate the diffusion dynamics of phosphoethanolamine (PE) and sphingomyelin (SM) on the membranes of living Chinese hamster ovary (CHO) cells. The nanoantenna approach is straightforward to implement on any confocal microscope equipped with FCS as contrarily to STED, it does not require adding any supplementary illumination beam. Moreover, the need for high power density laser beams in order to push the minimum resolution achievable in STED makes it prone to photophysical damage and interfering with the dynamic biochemical processes in living cells. Using the extreme near field localization and superior optical performance achieved for fluorescence experiments, we now exploit the planar "antenna-in-box" devices for investigating plasma membrane organization in living cells.

Prior to the experiments with living cells, we discuss the FCS calibration experiments for planar nanoantenna by using a free dye Alexa647 using a 3D model. Nanoantenna calibration with model lipid bilayers (2D-diffusion) is also discussed, validating the use of the planar "antenna-in-box" devices for biological systems [63].

6.2 Diffusion time analysis: Free dye Alexa647 on planar "antenna-in-box"

In this section, we discuss the FCS calibration experiments with planar "antenna-in-box" devices by using the Alexa647 molecules with a known diffusion constant. As we will demonstrate, using a physically relevant model supported by the FDTD simulations, it is possible to describe the diffusion properties of Alexa647 molecules in the nanogap and retrieve the diffusion coefficient.

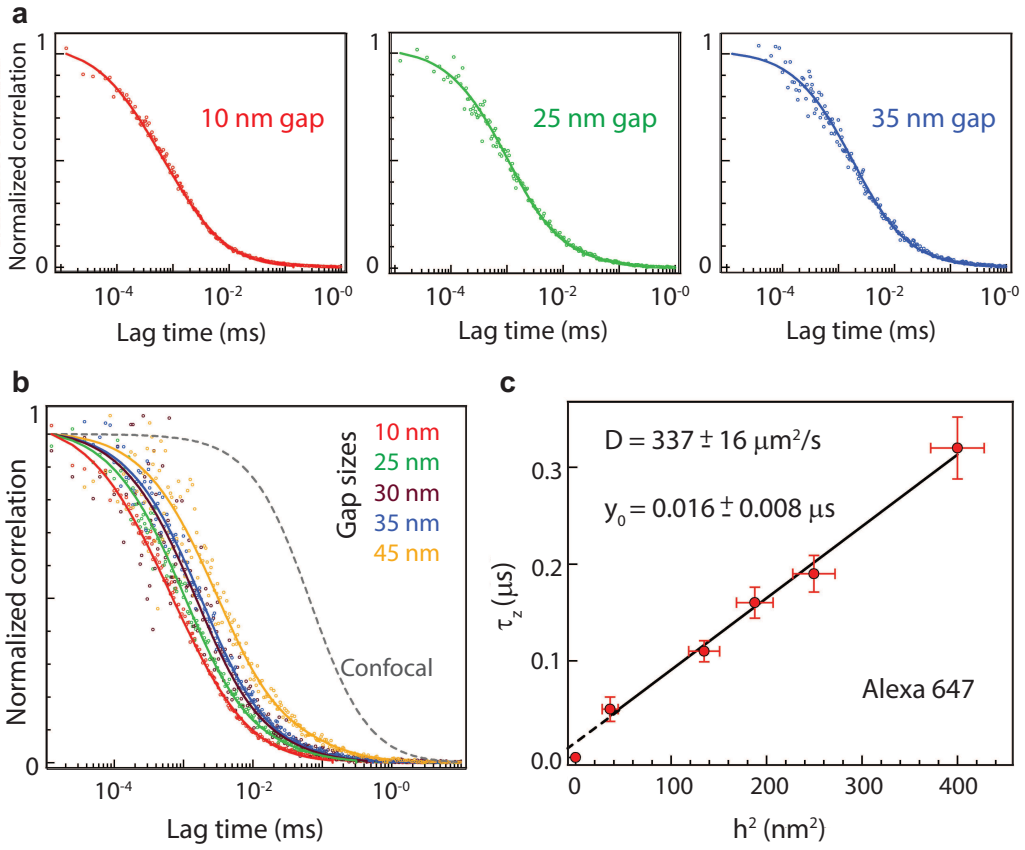

FIGURE 6.2: **FCS calibration diffusion time *vs* probe area for 3D diffusion of Alexa647.** (a) FCS correlation functions for three representative gap sizes(from left: 10 nm, 25 nm and 35 nm gap separation). Dots are the experimental data and lines being the two-component fit modeled by the Equation 6.1. (b) Normalized ACF's showing the evolution in diffusion time scales for Alexa647 molecules with increasing gap separations. The confocal diffusion (in gray dotted line) is also shown for direct comparison. (c) FCS diffusion law for Alexa647 molecules shows negligible y-intercept at the origin, in agreement with unhindered Brownian diffusion. The linear fit retrieves the confocal diffusion constant D = 337 ± 16 $\mu m^2/s$ with linear correlation coefficient of 0.99649 very close to unity. The uncertainty on h^2 considers a 0.7 nm uncertainty in the determination of the decay length (the mesh size is 1 nm for gaps 25-45 nm and 0.5 nm for gap 10 nm gap antenna)

Correlation curves from the FCS experiments presented in earlier Chapter 5, are further analyzed to study the evolution of the diffusion time with different gap antennas. In

brief, 26 μM concentration of Alexa647 along with 200 mM methyl viologen in PBS solution are probed with excitation light along the dimer axis. Figure 6.2a shows raw (dots) and the fit (solid lines) for three different gap sizes (from left: 10 nm, 25 nm and 35 nm gap separations). The ACFs fitting involves a two-species model to take into account the tail component appearing at lag times > 10 μs:

$$G(\tau) = A \times G_{\mathrm{TIRF}}(\tau) + (1 - A) \times G_{\mathrm{3D}}(\tau) \tag{6.1}$$

where A is the amplitude of the main component, G_{TIRF} is the TIRF-FCS model and G_{3D} is the model for Brownian 3D free diffusion. We use the G_{TIRF} model as it accounts for the contribution from the nanogap with exponentially decaying intensity profile. The second G_{3D} component takes into account the residual fluorescence contribution from the surrounding box region.

G_{TIRF} considers exponential decaying illumination profile along the z axis and lateral detection volume confinement with a confocal pinhole. Following the works by Starr [185] and Hassler [34, 186], $G_{\mathrm{TIRF}}(\tau)$ is derived as:

$$= \frac{1}{1 + (\tau / {S_{\mathrm{z}}}^2\ \tau_{\mathrm{z}})} \times \left[(1 - \tau/2\tau_{\mathrm{z}}) \times \exp(\tau/4\tau_{\mathrm{z}}) \times \mathrm{erfc}\sqrt{\tau/4\tau_{\mathrm{z}}} + \sqrt{\tau/\pi\tau_{\mathrm{z}}}\right] \tag{6.2}$$

where $\tau/S_{\mathrm{z}} = h^2/4D$ is the vertical diffusion time and $S_{\mathrm{z}} = d_{\mathrm{xy}}/h$ is the shape parameter. h indicates decay length at 1/e of the illumination intensity profile, D is the diffusion constant and d_{xy} is the lateral half-width at $1/e^2$ of the illumination intensity profile. $G_{\mathrm{3D}}(\tau)$ is the regular model for Brownian free diffusion:

$$G_{\mathrm{3D}}(\tau) = \frac{1}{1 + \tau/\tau_{\mathrm{d}}} \times \frac{1}{\sqrt{1 + {S_{\mathrm{xy}}}^2\ \tau/\tau_{\mathrm{d}}}}$$

where $\tau_{\mathrm{d}} = {W_{\mathrm{xy}}}^2/4D$ is the lateral diffusion time, $S_{\mathrm{xy}} = {W_{\mathrm{xy}}}^2/W_{\mathrm{z}}$ is the shape parameter. D is the diffusion coefficient and the waist W_{xy} is half-width at $1/e^2$ of the Gaussian detection volume.

During the ACF fitting procedure as modeled by the Equation 6.1, A is fixed to 0.9. This means that the amplitude of the 3D component (second component in the same equation) is at maximum only 10%. The shape parameter S_{z} for TIRF is fixed to S_{z} = 6 except for the smallest gap (10 nm nominal) which requires $S_{\mathrm{z}} = 10$. These values derived after empirical optimization of the fits are in correct agreement with the FDTD profiles (discussed in Chapter 5). The shape parameter for 3D diffusion is kept to the standard value for confocal $S_{\mathrm{xy}} = 0.2$ and has negligible influence on the fit result for

the TIRF component which is the main interest. Hence the remaining free parameters for optimization are τ_z for G_{TIRF} and τ_d for G_{3D}.

Figure 6.2b displays the raw correlation data (dots) and their corresponding fits (solid lines) for various gap size nanoantennas. Using the fit model that incorporates the TIRF component as the dominating factor in the diffusion of Alexa647 molecules in solution shows a very good fit to the experimental data. The detail fit results for all five different gap size nanoantennas is summarized in Table 6.1.

Gap size	τ_z	S_z	τ_{xy}	S_{xy}	A	h
10 nm	0.05 μs	10	10 μs	0.2	0.9	6 nm
25 nm	0.11 μs	6	26 μs	0.2	0.9	11.6 nm
30 nm	0.16 μs	6	32 μs	0.2	0.9	13.7 nm
35 nm	0.19 μs	6	31 μs	0.2	0.9	15.8 nm
45 nm	0.32 μs	6	90 μs	0.2	0.9	20 nm

TABLE 6.1: **FCS calibration results with Alexa647 diffusing in solution probed with increasing nanoantenna gap size.** Fitting of the ACF curves displayed in Figure 6.2 using Equation 6.1 with Alexa647 molecules probed with increasing gap sizes. τ_z for the G_{TIRF} component and τ_{xy} for the G_{3D} component are the only free parameters.

Finally from the results of the fit, we derive the "FCS diffusion law" representing τ_z as a function of the decay length at $1/e$ of the illumination intensity profile h. This represents the main contribution from the nanogap region (TIRF model). It is important to note that with $S_z = 6$ (or 10), the contribution from the lateral diffusion along x and y (term $\frac{1}{1+(\tau/{S_z}^2\ \tau_z)}$, the first term in Equation 6.2 for G_{TIRF} has a rather weak contribution, exemplified by its lateral diffusion time ${S_z}^2\ \tau_z$ which is $6^2 = 36\times$ (or $100\times$) longer than the τ_z.

Figure 6.2c summarizes the calibration results on Alexa647 using this TIRF model. τ_z (in y-axis) and probe area (h^2 in x-axis) follow linearity with linear correlation coefficient being very close to unity (r = 0.99649). The diffusion coefficient D is then determined from the slope of this "FCS diffusion law" using $\tau_z = h^2/4D$, with decay length (h) at 1/e (and not at $1/e^2$) of the illumination intensity profile [34, 185, 186]. h is deduced from the FDTD simulations, it's not a free parameter. The derived diffusion coefficient D = 337 $\pm$ 16 $\mu m^2/s$ is in excellent agreement with the calibrated value for Alexa647 [187]. The linearity and near-zero intercept y_0 confirm the nanoantenna is not introducing artifacts in the diffusion dynamics of the Alexa647 molecules.

It should be noted that for the smallest gap (desired 10 nm gap), the FDTD calculations are taken with 12 nm gap separations (instead of 10 nm) as this provides a better match and is consistent with the TEM characterization. In every analysis hereafter (experiments

with model lipid bilayers and living cells), the area for the smallest gap nanoantennas will be thereby fixed at 300 nm^2 (as we will further validate with model membranes).

6.3 Nanoantennas calibration with model lipid membrane

In addition to the experimental calibration of the probe areas by means of individual Alexa647 dyes diffusing in solution (3D-model), we now study the evolution in the diffusion time scales with increasing probe areas on pure model lipid bilayers (2D-model). This will independently validate the probe area calibration before the live cell experiments with full biological complexity.

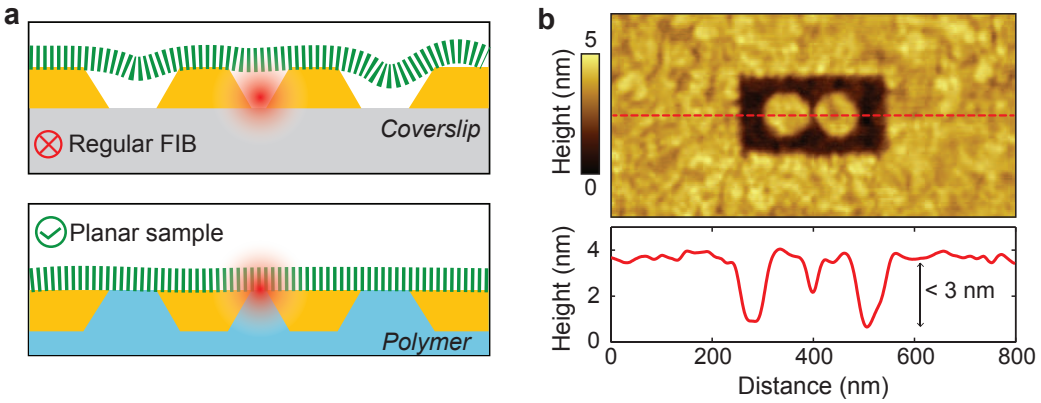

FIGURE 6.3: **Planar nanoantennas for membrane investigations.** (a) Schematic representations of the antenna geometry and cell membrane interface depicted without (as in conventional FIB) and with template stripping. The planar geometry allows easier access to the narrow and bright hotspot region and minimizes unwanted membrane curvature and distortion. (b) Detailed AFM image of a representative planar "antenna-in-box" with 10 nm nominal gap width and line profile showing a 3 nm total residual topography.

The fluorescence experiments with model lipid bilayer labeled deposited on top of the planar nanoantennas are depicted in Figure 6.3a. A highly confined nanometric illumination hotspot is created on the top surface of the nanogap region, which is in direct contact with the membrane region. Importantly, the planarization strategy avoids possible curvature induced effects on the cell membrane providing an ideal platform for live cell membrane research when compared to those structures obtained *via* FIB milling [180, 181]. Further, the AFM image in Figure 6.3b indicates a planarity better than 3 nm for the top surface of the nanoantennas.

Lipid bilayers are prepared by mixing unsaturated phospholipid 1,2-dioleoyl-sn-glycerol-3-phosphocholine (DOPC) dissolved at 1 mg/mL in chloroform:methanol (9:1) together with 0.01 mol% of the fluorescent dye DiD. The mixture of DOPC and fluorescence

dye is stored in small glass tubes at 4^o C and is deposited on the clean nanoantenna substrates only prior to the fluorescence experiments. The fluorescently labeled DOPC is then allowed to dry for an hour in presence of a weak nitrogen flow which is then stored in vacuum for another additional hour. The samples are finally hydrated in PBS (pH 7.4), carefully rinsed to remove excess lipids and then immediately probed by FCS at room temperature. Nanoantennas are excited by focusing the excitation laser light ($\lambda = 640$ nm, $\sim$2 kW/cm^2) into individual antennas using a water-immersion objective (NA = 1.2). Excitation along the dimer axis is used to achieve maximum field enhancement and ultra confined electromagnetic hotspot.

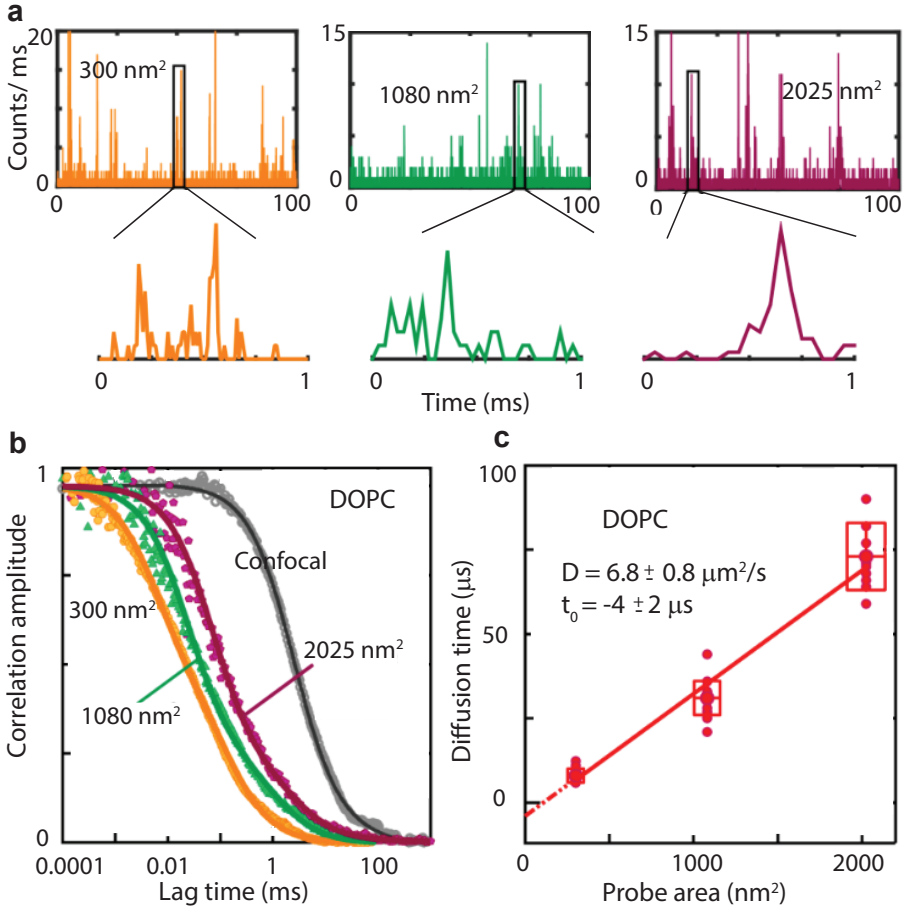

FIGURE 6.4: **Planar nanoantennas probe model lipid bilayers.** (a) Representative fluorescence intensity time traces of DiD embedded in a pure DOPC bilayer for three different antenna gap areas together with enlarged views of representative bursts. (b) Normalized ACF curves as obtained with different nanoantenna probe areas and with confocal excitation. (c) Diffusion times as extracted from the ACF fitting as a function of the antenna gap area. Each dot corresponds to an individual ACF measurement in a single antenna. Number of measurements: 13, 8 and 12 for 300 nm^2, 1080 nm^2 and 2025 nm^2 antenna probe areas respectively.

Figure 6.4 shows the representative fluorescent intensity time traces (a) and the corresponding normalized ACFs (b) of DiD diffusion in a pure DOPC membrane over three

	1st component		**2nd component**	
probe area	time (t_1)	amplitude (ρ_1 in %)	time (t_2)	amplitude (ρ_2 in %)
300 nm^2	6 ± 1 μs	67 ± 3	170 ± 150 μs	33 ± 8
1080 nm^2	25 ± 3 μs	79 ± 8	1.4 ± 0.2 ms	21 ± 7
2025 nm^2	71 ± 25 μs	75 ± 9	1.6 ± 0.3 ms	25 ± 10

TABLE 6.2: **Fitting of the ACF curves on DOPC bilayers for different antenna gap areas.** Fitting of the ACF curves on DOPC bilayers for different antenna gap areas. The shortest times (t_1) correspond to the diffusion times of DiD through the antenna hotspot regions while t_2 corresponds to residual excitation of the dye inside the box-aperture.

different antenna probe areas. The probe areas are estimated by using the product of the gap size (as measured with TEM characterization) by the full width at half maximum for the intensity profile along the direction perpendicular to the nanoantenna major axis. Thus, the nanoantennas with 10, 30 and 45 nm nominal gap sizes correspond to the illumination areas of 300 ± 50 nm^2, 1080 ± 80 nm^2 and 2025 ± 110 nm^2. The estimated probe areas were also validated by using a free dye Alexa647 molecules.

As shown in Figure 6.4a, the fluorescence burst duration increases with gap area, confirming that the detected signal arises from the excitation of the dye diffusing at the nanometric gap regions. The normalized ACFs in Figure 6.4b shows the evolution of the diffusion timescale for different gap nanoantennas (colored lines) and compares with the confocal case (in gray). The characteristic diffusion times for nanoantenna experiments are derived by fitting the ACF curves following the equation [63]:

$$G(\tau) = \sum_{i=1}^{n_{\text{diff}}} \frac{\rho(i)}{1 + \left[\frac{\tau}{\tau_{\text{diff}}(i)}\right]} \tag{6.3}$$

where $\tau_{\text{diff}}(i)$ the average residence time of the i^{th} diffusing modality, $\rho(i)$ denotes the respective amplitude contribution. As the diffusion in lipid bilayers is 2D, we do not need to follow the same procedure as used for 3D diffusion of Alexa647 molecules in solution. The complete derivation of the correlation function for both 3D and 2D diffusion cases are already discussed in Chapter 2.

Consistence with our earlier experiments with nanoantennas, we adopt two-component 2D Brownian fittings to account for both, direct excitation from the gap region and residual excitation of DiD diffusing through the box-aperture. Using Equation 6.3, the main component of the fitted curves displayed in Figure 6.4b, render diffusion time scale of 6 ± 1 μs, 25 ± 3 μs and 71 ± 25 μs respectively for 300, 1080 and 2025 nm^2 and should be compared with the 3.5 ms diffusion time for confocal excitation (gray circles). The

detailed results of the fitting procedure and relative contributions of each component (from the gap and box-aperture excitation) are listed in Table 6.2.

Figure 6.4c shows the diffusion times obtained from multiple measurements on individual nanoantenna as a function of the probe area. The diffusion times versus probe areas is well-fitted to a straight line with an intercept close to the zero-origin point, indicating that τ_{DOPC} scales linearly with the probe area, consistent with free Brownian diffusion of the dye in the pure DOPC membrane. It also confirms that the DOPC bilayers are homogenous down to the nanoscale and the slope of the fitting rendered a diffusion coefficient of 6.8 $\pm$ 0.5 $\mu\mathrm{m}^2/\mathrm{s}$ compares well to our confocal measurements and values reported elsewhere [188]. These results on pure DOPC validate the application of planar plasmonic nanoantennas to record the diffusion of individual molecules in lipid bilayers with microsecond time resolution.

6.4 Atto647N-labeling and experimental strategy on living cells

After the calibration experiments with freely diffusing Alexa647 molecules (3D model) and the validation with a mimetic system (DOPC bilayers as a 2D model), we now perform live cell experiments with Chinese hamster ovary (CHO) cells. CHO cells are seeded on a coverslip containing arrays of nanoantennas with two different gaps: 10 nm and 35 nm (see Figure 6.5). As the experiments on living cells membranes are very time consuming (for both data recording and subsequent time trace analysis), we decide to focus our attention on two specific gap sizes and record many different antennas and cells. All the live cell experiments are complete within the first 30 minutes from the time of incorporation of fluorescent lipid analogs into the plasma membranes to avoid artifacts arising from dye internalization in living cells.

Lipid conjugates are separately prepared by labeling 1,2-dipalmitoyl-sn-glycero-3-phosphoethanolamine (PE) and sphingomyelin (SM) with the organic dye Atto647N (from Invitrogen) following the protocol described in Ref. [175]. The fluorescence spectrum of Atto647N is displayed in Figure 6.6 along with the nanoantenna resonance measured by dark field spectroscopy. The excellent spectral overlap is desired to achieve maximize fluorescence enhancement. The cells are incubated on the nanoantenna substrates at 37^o C in a controlled atmosphere with 5% of CO_2 for nearly 48 hours prior to the experiments to allow them to freely grow and adhere onto the antenna platform (see Figure 6.7). The planar antenna platform contains multiple gold nanoantenna arrays with nominal gap sizes of 10 nm and 35 nm on which a circular cell culture well is

mounted for live CHO cell culturing. Figure 6.7a depicts the strategy chosen for the fluorescence live cell experiment conducted on the nanoantenna platform.

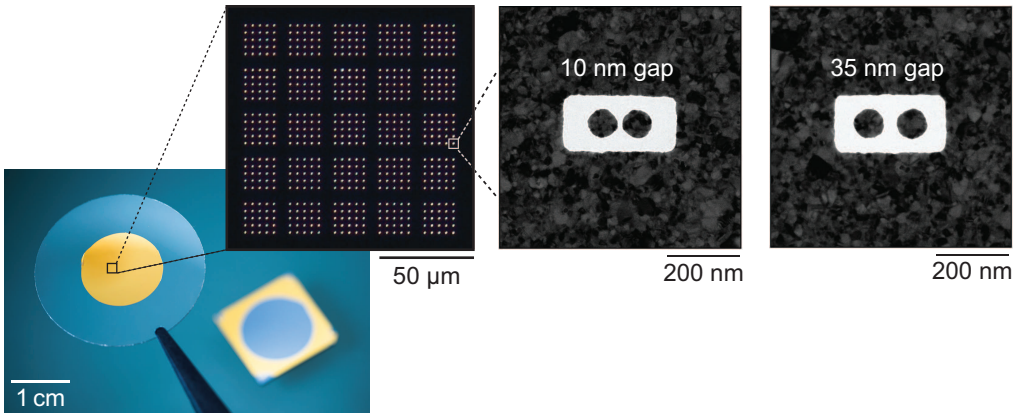

FIGURE 6.5: **Large-scale antenna arrays and TEM images.** From left to right: macro-photograph of a coverslip with a stripped Au film with large-scale planar antenna arrays; dark field optical micrograph of a small portion of the antenna arrays showing here 625 antennas with 10 nm nominal gap size; transmission electron microscope (TEM) images of antennas with 10 and 35 nm gap size.

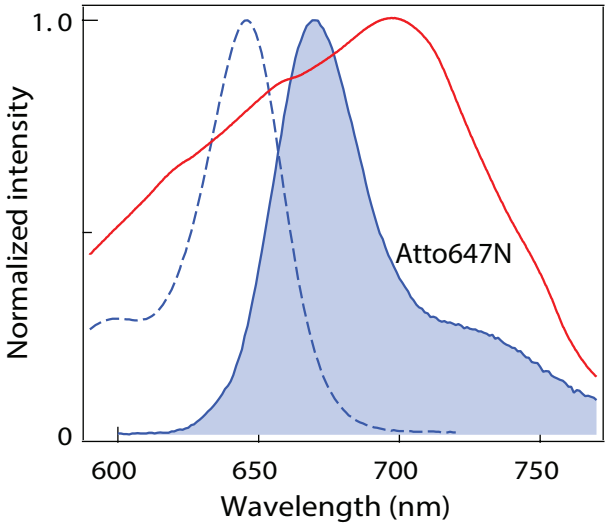

FIGURE 6.6: **Overlap between antenna's resonance and Atto647N fluorescence spectra.** Overlap of the dark-field scattering spectrum recorded for a 10 nm gap antenna (red line, illumination polarization along the nanoantenna dimer major axis) with the fluorescence spectra for Atto647N (blue lines). The excitation spectrum is displayed in with a dashed line and the solid shaded line represents the emission spectrum.

Prior to the fluorescence experiments, separately prepared lipid analogues (either PE or SM with the organic dye Atto647N are incorporated in the cell membrane during a 3 minute incubation period at room temperature, dissolved in the corresponding medium for CHO cells (Ham's F12 nutrient mixture). Stained cell cultures are rinsed to remove

residual dye molecules before placing the sample coverslip on the piezo-stage of an inverted microscope to carry out the measurements as in the case of model lipid membranes. All fluorescence staining are performed at a ∼300 nM concentration of Atto647N and the measurements being completed within 30 minutes after the incorporation of the fluorescent analogs into the plasma membranes. Due to the incorporation within the limited 3 minutes time and subsequent washing step, the concentration of fluorescent lipids in the cell membrane is significantly less. From the number of detected fluorescence bursts and the FCS amplitude (as we will show in next section), we estimate that the density of fluorescent lipids for the nanoantenna experiments is on the order of 20 - 80 probes per μm^2. Figure 6.7b shows a representative confocal image of the morphology of the CHO cells adhered on a glass coverslip taken after the incorporation of the fluorescent lipid analogs.

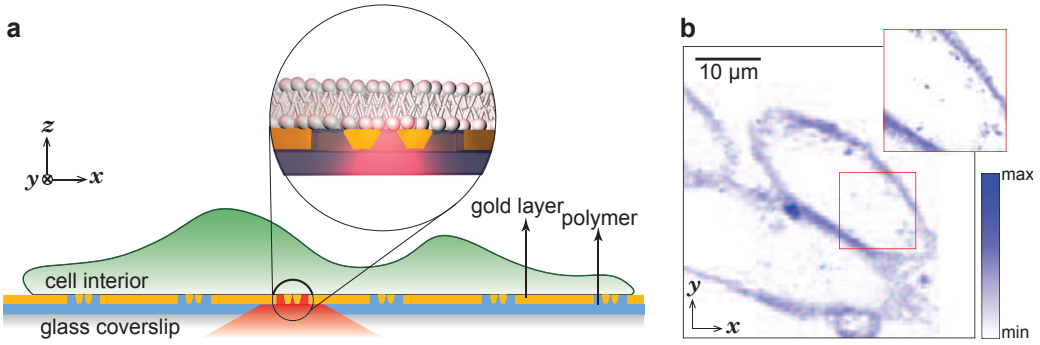

FIGURE 6.7: **Planar nanoantennas for investigationg membrane dynamics in living cells.** (a) CHO cells are seeded onto a microscope coverslip containing multiple planar nanoantennas with 10 and 35 nm gap sizes. The inset shows the cross section of the "antenna-in-box" stripped and embedded into a polymer, bringing the region of maximum electromagnetic field intensity onto the surface in direct contact with the plasma membrane of living cells. (b) Confocal image of CHO cells showing the morphology after incorporating the fluorescent SM lipid analog labeled with Atto647N.

6.5 Experiment and results: Membrane dynamics in living cells

The fluorescence experiments are performed with a commercial MicroTime 200 setup equipped with an inverted confocal microscope (Olympus 60×, 1.2 NA water-immersion objective) and a three-axis piezoelectric stage (PhysikInstrumente, Germany) allowing to select individual nanoantennas. A linearly polarized 640 nm picosecond laser diode (Pico-Quant LDH-D-C-640) in continuous wave mode is used to resonantly excite individual nanoantennas. The emitted fluorescence signal is collected in epi-detection mode through a dichroic mirror and the signal is finally split into two avalanche photodiodes

(PicoQuant MPD-50CT). An emission filter and a band pass 650-690 nm filter just before each detectors eliminate the scattered light by the excitation laser. A 30 μm pinhole in the detection arm yields a 0.5 fL confocal detection volume at the sample plane. The fluorescence time traces are recorded on a fast time-correlated single photon counting module in the time-tagged time-resolved mode (PicoQuant MPD-50CT). All the fluorescence measurements are performed by illuminating the sample at an excitation power density of ∼2-3 kW/cm^2. The measurements are acquired for a typical run time of 50 s and the correlation amplitudes computed for ∼20 s windows with the commercial software package SymPhoTime 64. The detailed optical setup for the FCS experiments with cells (performed at ICFO, Barcelona) is described in Chapter 2.

6.5.1 Burst analysis of PE and SM on living cells

Single-molecule fluorescence time traces are acquired in the Tagged Time-Resolved (TTTR) mode (recording each event at its arrival time) with 4 ps temporal resolution. Figure 6.8 shows representative single-molecule fluorescence time traces for PE and SM in the confocal (a,b) and in the nanoantenna configuration (c,d). The spatial resolution set by the diffraction limited spot in the confocal scheme (usually 300 nm) does not allow to resolve heterogeneities that may occur at the nanometric spatial scale. Hence we observe the indistinguishable time traces for both PE and SM. In contrast, the highly confined surface hotspot originating from the 10 nm gap antenna clearly reveals the difference in the characteristic diffusion dynamics of PE and SM (c,d). As shown in Figure 6.8c, PE displays sharp peaks in the fluorescence time trace as a result of the sub-diffraction excitation hotspot created by the planar nanogap antenna. Unlike PE, the signature of SM is discernibly different at the nanoscale: the short bursts (hallmark of free diffusion in ultra-small detection areas) are accompanied by high intensity bursts of significantly longer durations. This is a direct indication that the nanoscopic diffusion of SM on the plasma membrane is deviating from free Brownian diffusion as compared to larger macroscopic scales.

To provide more quantitative information about the fluorescence time traces, we perform fluorescence burst analysis to represent the distributions of burst duration versus burst intensity. Fluorescence bursts analysis is carried out with a likelihood-based algorithm to test the null hypothesis (no burst, recording compatible with background noise) against the hypothesis that a single-molecule burst arises as a consequence of a molecule crossing the excitation area. The background threshold is set to 20-30 counts/ms following an empirical optimization [148, 189].

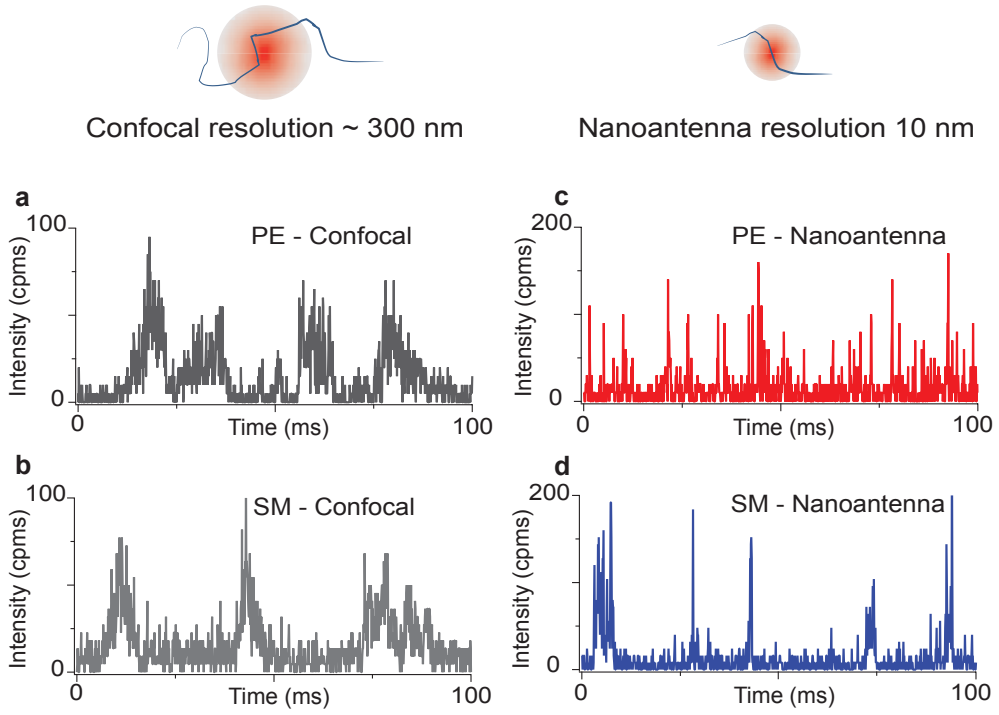

FIGURE 6.8: **Single-molecule fluorescence time traces in living CHO cells.** Fluorescence time traces for phosphoethanolamine (PE: a,c) and sphingomyelin (SM: b,d) labeled with Atto647N recorded with confocal (left) and with a 10 nm gap planar nanoantenna (right). The binning time is 0.1 ms for all traces. The diffraction-limited spot in the confocal configuration cannot resolve the nanoscopic and heterogeneous membrane organization, this results in indistinguishable fluorescence time traces for both PE and SM (a,b). In contrast, the confined nanoantenna hotspot reveals clear differences in the diffusion dynamics of PE and SM (c,d).

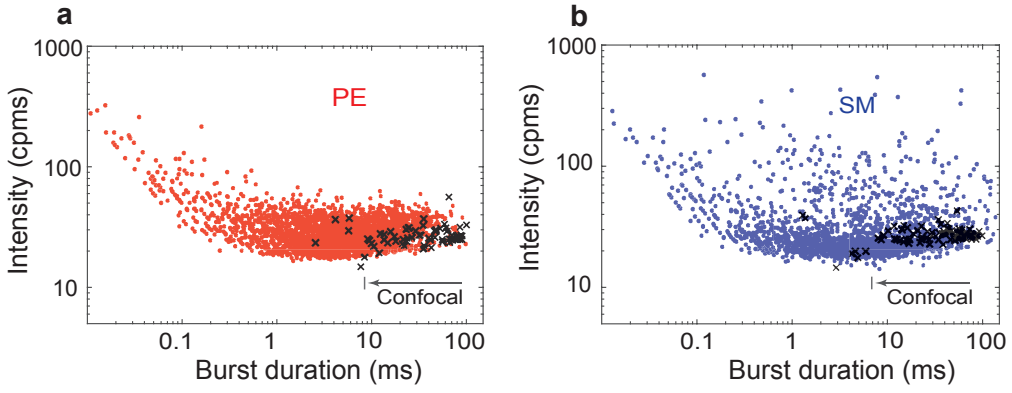

FIGURE 6.9: **Single-molecule burst analysis for PE and SM.** The fluorescence time traces are analyzed to produce scatter plots showing the distribution of fluorescence burst intensity versus burst duration. Single-molecule events (PE in a and SM in b) in sub-ms time scales are observed with nanoantennas (color dots) as the confined electromagnetic hotspots allow to probe the dynamics occurring beyond the diffraction limit. Single-molecule events obtained with confocal illumination are displayed for comparison (black dots).

Figure 6.9 shows the results for both PE (a) and SM (b) for the 10 nm nanogap antenna (colored dots) compared to the confocal configuration (black cross). The scatter plots for PE and SM in the confocal configuration show no visible differences with burst durations in the range 5-100 ms and intensities around 20-30 counts/ms. However, in stark contrast, the distributions obtained on the nanoantennas show clear differences between PE and SM. Diffusion events in sub-ms time scales are notably observed with the nanoantennas exhibiting burst durations as short as 10 μs. Such short events are more than two orders of magnitude faster than in the confocal reference. Regarding the diffusion dynamics for PE (red dots) probed with the nanogap antennas a general trend can be deduced, namely, brighter events arise at shorter timescales. These can be understood as the detection of a "best burst event" directly resulting as a consequence of an individual molecule diffusing through the hotspot in the optimal position and orientation for maximum enhancement. The tighter the excitation beam confinement, the higher is the local intensity which leads to high fluorescence counts with short burst duration. We thus relate the events with burst durations < 1 ms to the trajectories occurring within the nanogap region [148]. In the case of PE, the bursts with durations above 1 ms feature a lower intensity in the range of 20-70 counts/ms, which is only slightly increased as compared to the confocal case (black cross). We assign these longer burst duration events to the residual excitation of diffusing molecules within the larger 300 $\times$ 140 nm^2 box aperture region where the electromagnetic field intensity enhancement is negligible and is thus comparable to the confocal reference.

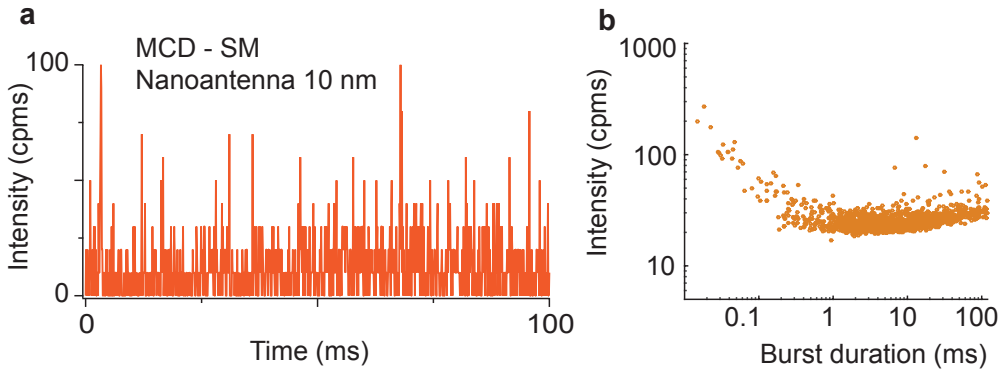

FIGURE 6.10: **Representative time trace of SM after cholesterol depletion.** (a) Representative single-molecule time trace of Atto647N for SM after cholesterol depletion with 10 nm gap planar "antenna-in-box" platform (binning time 0.1 ms). (b) The scatter plots showing the distribution of representative bursts (#1587) recorded for the same is shown alongside. Cholesterol induced hindrance in diffusion of SM molecules is avoided with incorporation of the MCD in the plasma membranes.

In contrast to PE, SM probed with the nanoantenna arrays shows a significantly broader

distribution of burst lengths against peak burst intensities (Figure 6.8d). High intensities are also observed for burst durations above 1 ms. Since these events are not observed for PE, we relate their occurrence to nanoscopic heterogeneities such as transient molecular complexes on the cell membrane hindering the diffusion of SM. To support this conclusion, next we perturb the cholesterol composition in the cell membrane with methyl-β-cyclodextrin (MCD) as cholesterol is expected to play a significant role in the formation and stability of the lipid nanodomains. For cholesterol depletion, the CHO cells are incubated in serum free buffer with 10 mM methyl-β-cyclodextrin (MCD) for 30 minutes at 37^{o}C, and the fluorescent labeling is then carried out as described previously. The result of the burst analysis for SM after MCD treatment (Figure 6.10) recovers a distribution which closely resembles the one for PE (see Figure 6.9a). In other words, the intense bursts of duration between 0.1 and 10 ms disappear after cholesterol depletion, consistent with the loss of nanodomains. Altogether, the results from the fluorescence burst analysis demonstrate the benefits of planar nanogap antennas to explore the nanoscopic organization of lipids in live cell membranes. Clear differences between PE and SM diffusion dynamics are unveiled that otherwise would remain hidden in the confocal measurements.

6.5.2 FCS in ultra confined illumination hotspots

To further support the burst analysis results, we performed fluorescence correlation spectroscopy analysis. We use two different gap sizes (10 and 35 nm) to quantify the lipid dynamics for increasing detection areas in the plasma membranes of living CHO cells. The mobility of molecules shows strong dependence on the local environment and thus in living systems the concept of ideal Brownian diffusion may not always hold true. Considering possible anomalous diffusion in living cells, the temporal correlation of the fluorescence intensity F can be written as [172]:

$$G(\tau) = \sum_{i=1}^{n_{\text{diff}}} \frac{\rho(i)}{1 + \left[\frac{\tau}{\tau_{\text{diff}}(i)}\right]^{\alpha(i)}} \tag{6.4}$$

where $\tau_{\text{diff}}(i)$ the average residence time of the i^{th} diffusing modality, $\rho(i)$ denotes the respective amplitude contribution and $\alpha(i)$ being the anomaly parameter of the same. We find that the FCS curves recorded with nanoscopic illumination can only be fitted with a model assuming two different diffusion modalities (*i.e.,* $n_{\text{diff}} = 2$). Two-species model is important to fit the FCS data in order to account for the fluorescence contributions stemming from the nanogap and from the residual excitation stemming from the surrounding box-aperture. A key feature in FCS is that the molecules contribute to the correlation amplitude in proportion to the square of their fluorescence brightness, hence

the signal from molecules in the nanogap experiencing maximum enhancement will have a dominating contribution in the FCS curves [152].

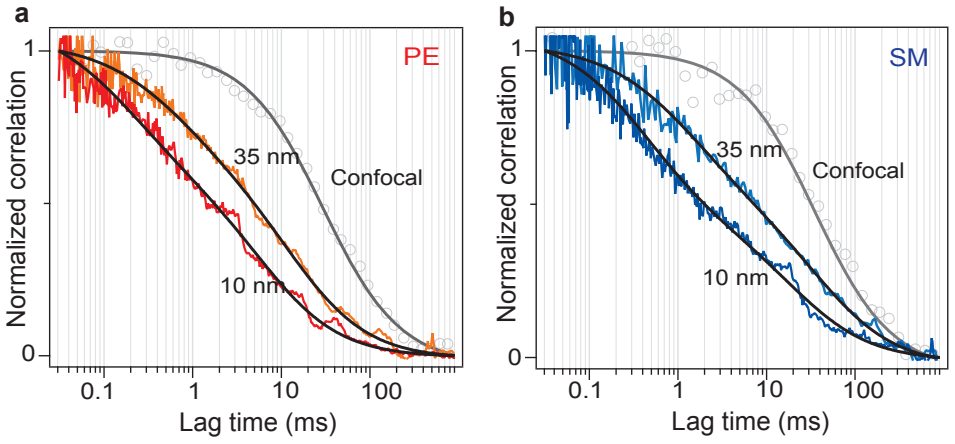

FIGURE 6.11: **Nanoantenna FCS with varying gap sizes on living cell membranes.** Normalized fluorescence correlation curves for Atto647N labeled PE (a) and SM (b) lipid analogs probed with nanoantennas of varying gap size. The color lines are experimental data and the black curves are numerical fits. The diffraction-limited confocal measurements are shown in gray for direct comparison.

	PE - 10 nm		**PE - 35 nm**	
component	1^{st}	2^{nd}	1^{st}	2^{nd}
time (t)	0.25 ± 0.06 ms	8 ms	0.75 ± 0.15 ms	16 ms
anomaly (α)	0.85	1	0.8	1
amplitude (ρ in %)	53 ± 4	47 ± 5	50 ± 3	50 ± 5

TABLE 6.3: **Fitting parameter results for PE in Figure 6.11a for two different gap sizes.**

	SM - 10 nm		**SM - 35 nm**	
component	1^{st}	2^{nd}	1^{st}	2^{nd}
time (t)	0.35 ± 0.04 ms	17 ms	1.4 ± 0.2 ms	45 ms
anomaly (α)	0.65	1	0.85	1
amplitude (ρ in %)	80 ± 2	20 ± 1	55 ± 5	45 ± 6

TABLE 6.4: **Fitting parameter results for SM in Figure 6.11b for two different gap sizes.**

Figure 6.11 shows the normalized correlation curves for PE (a) and SM (b) in case of the nanoantennas and the confocal reference. Similar to the burst analysis, we find no significant differences between the FCS curves for PE and SM for the confocal reference, yielding comparable diffusion times of 25 ± 4 ms (PE) and 30 ± 4 ms (SM), respectively. In the case of the nanoantennas, we observe that decreasing the gap size leads to a faster diffusion, confirming that the fluorescence signal stems from the nanogap region.

The differences between PE and SM diffusion dynamics are highlighted in Figure 6.12a where a direct comparison of the FCS data for the 10 nm gap antenna is shown for

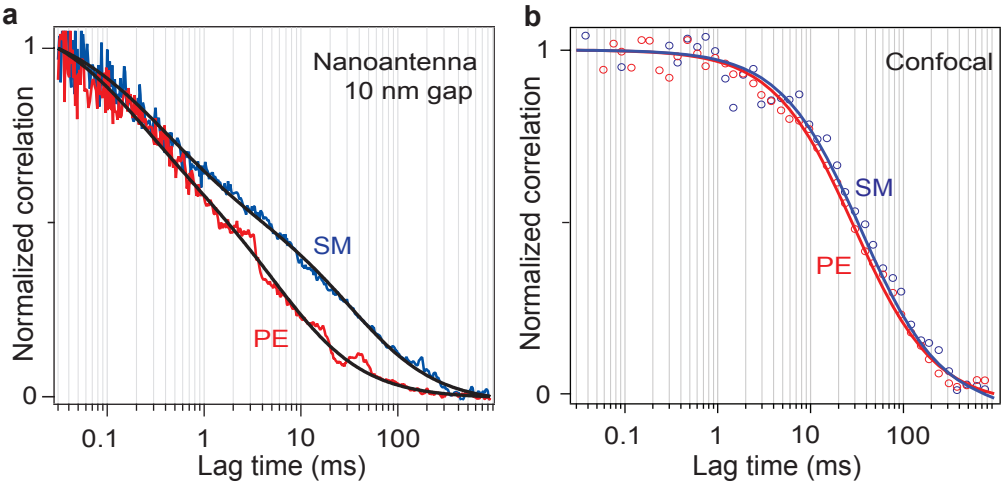

FIGURE 6.12: **Hindered diffusion in SM as revealed by the nanoantenna-FCS.** (a) Comparison of FCS curves for PE and SM for a 10 nm gap antenna reveals clear differences between the dynamics of PE and SM at the nanoscale. (b) The confocal reference however shows no significant differences between the FCS curves for PE and SM yielding comparable diffusion times of 25 ± 4 ms (PE) and 30 ± 4 ms (SM), respectively. The color circles are experimental data and the lines are numerical fits described with single species Brownian diffusion.

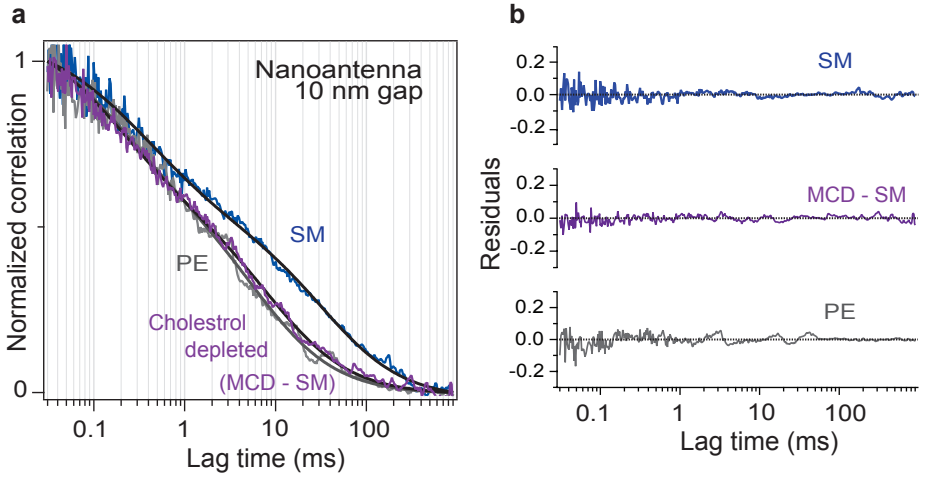

FIGURE 6.13: **Cholesterol depleted SM indicates loss of nanodomains.** (a) Normalized fluorescence correlation curves for Atto647N labeled SM (blue) and cholesterol depleted SM (Purple) for a 10 nm gap antenna. After cholesterol depletion, the SM diffusion dynamics are significantly faster and resemble the PE case (overlay in gray). (b) The residuals of the fits for each case is displayed alongside.

10 nm	**1^{st} component**			**2^{nd} component**		
	time (t)	anomaly (α)	amplitude (ρ in %)	time (t)	anomaly (α)	amplitude (ρ in %)
PE	0.25 ± 0.06 ms	0.85	53 ± 4	8 ms	1	47 ± 5
SM	0.35 ± 0.04 ms	0.7	59 ± 4	38 ms	1	41 ± 5
MCD-SM	0.19 ± 0.03 ms	0.85	53 ± 4	10 ms	1	47 ± 4

TABLE 6.5: **Fitting results for PE, SM and MCD-SM with 10 nm gap antenna displayed in Figure 6.13**

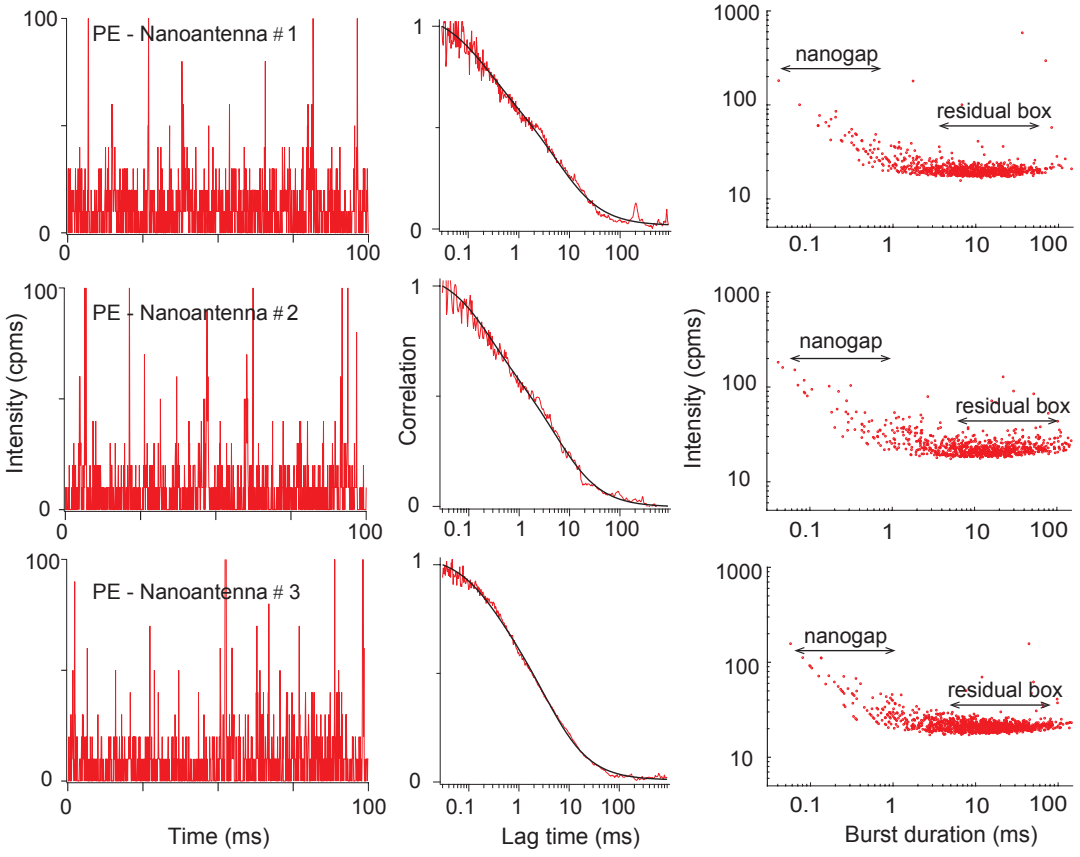

FIGURE 6.14: **Examples of PE-nanoantenna showing excellent reproducibility.** The representative time traces (binning time 0.1 ms), correlation curves and the scatter plots for three different 10 nm gap antenna is shown. In all cases Atto647N with PE is recorded with excitation light along the dimer axis. The correlation curves shows sub-ms diffusion dynamics and the scatter plots (#866 for Nanoantenna-1, #834 for Nanoantenna-2, #1364 for Nanoantenna-3) further indicate no hindrance.

both the fluorescent lipid analogs. Contrary to the confocal case (see Figure 6.12b), the difference in diffusion times between the two lipids becomes more prominent at the nanoscale, with PE exhibiting diffusion times of 0.25 ± 0.06 ms and SM of 0.35 ± 0.04 ms. The complete results and values for the FCS fits are detailed in Table 6.3 and Table 6.4. Moreover, after MCD treatment, the diffusion dynamics for cholesterol-depleted SM closely resembles that of PE with a diffusion time of 0.19 ± 0.03 ms (Figure 6.13, and see Table 6.5). These FCS results confirm the presence of cholesterol-enriched nanodomains hindering the diffusion of SM, in agreement with the results found for the fluorescence burst analysis.

In addition, the anomaly parameter (α in Equation 6.4) retrieved for SM depends on the probe area, deviating from unity as the illumination area reduced, from a $\sim$0.85 (for the 35 nm gap) to a $\sim$0.65 (for the 10 nm gap), which is again consistent with hindered diffusion (see Tables 6.3, 6.4, and 6.5). In contrast, the α values are large and close to unity for both the PE and cholesterol depleted SM cases ($\alpha = 0.85$), display no dependency with the probe areas, as one would expect for unhindered diffusion scenario.

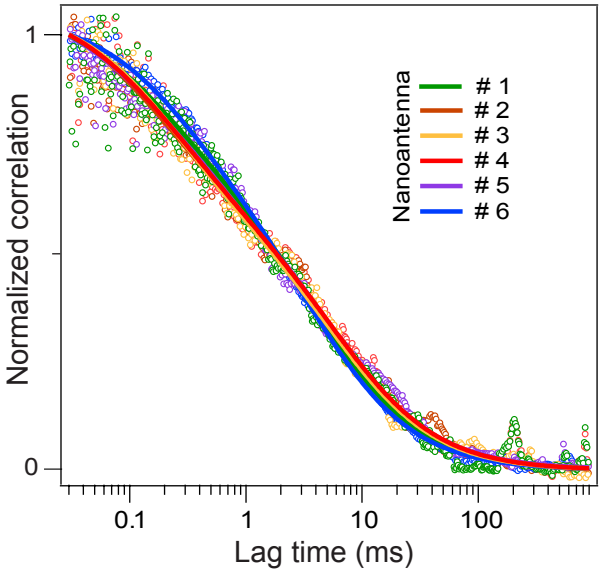

FIGURE 6.15: **Correlation curves recorded for PE-nanoantenna on different cells.** The FCS correlation curves for six different 10 nm gap antenna and different cells is shown. In all cases Atto647N with PE are recorded with excitation light along the dimer axis and the correlation curves indicate sub-ms diffusion dynamics.

Moreover, these planar nanoantennas show excellent excellent reproducibility in terms of optical performance. Figure 6.14 shows some additional fluorescent time traces, burst analysis and the corresponding correlation curves for PE case when probed with 10 nm gap planar "antenna-in-box" devices. Moreover, Figure 6.15 displays the FCS curves recorded for PE and overlayed for six different nanoantennas and different cells confirming sub-ms temporal resolution achieved with 10 nm gap antennas.

6.5.3 Extending FCS diffusion laws at the nanoscale

To further analyze and exploit the FCS data we take advantage of the large number of planar nanoantennas with controlled gaps to carry out a FCS analysis over many different antennas and cells. As discussed earlier for Alexa647 molecules (3D) and DOPC bilayers (2D), this approach follows the so-called FCS diffusion law, which is a representation of the diffusion time versus the detection area [53, 170]. Extrapolation of the experimental curve to the intercept with the time axis provides information on the type of diffusion exhibited by the molecule, *i.e.*, free diffusion is characterized by a linear curve crossing the origin (0,0), while hindered diffusion due to the occurrence of nanodomains leads to a positive intercept on the time axis [53, 170].

Figure 6.16 summarizes the characteristic diffusion times for PE, SM and SM after cholesterol depletion for two antenna probe areas. From these graphs we derive the following three values plot in Figure 6.17: the diffusion coefficient (from the slope), the time axis intercept (by extrapolating the linear fit for vanishing probe area) and the normalized spread in the data points (defined as the width of upper and lower quartiles divided by the median value). As the diffusion time proportionally scales with the detection area, the diffusion coefficient D is retrieved from the slope of the linear fit matching the measured transient diffusion times obtained from the FCS curves versus the effective detection areas according to the relation D = probe area/4 $\times$ τ_{diff} [172].

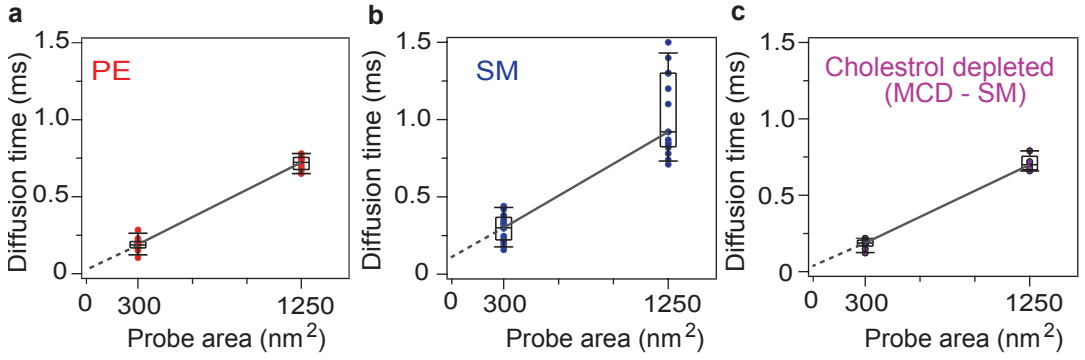

FIGURE 6.16: **Characteristic diffusion dynamics of membrane lipids probed with ultra-confined nanoantenna hotspots.** The diffusion time measured by FCS (for 60 different nanoantennas) is plotted as a function of the probe area for PE (a), SM (b), and SM after MCD treatment(c). The solid lines are linear fits through the median values. In the case of free diffusion, the origin $(0, 0)$ is aligned with the expected line, while a positive intercept at the y-axis denotes hindered diffusion due to nanodomains.

The diffusion coefficients derived from nanoantenna measurements are $D_{PE} = 0.44 \pm 0.07$ $\mu m^2/s$, $D_{SM} = 0.38 \pm 0.19$ $\mu m^2/s$ and $D_{MCD\text{-}SM} = 0.46 \pm 0.07$ $\mu m^2/s$ (Figure 6.17a) and they are consistent with the confocal measurements and values reported independently using STED-FCS [175]. It should be noted that these diffusion coefficients represent

the diffusion time in the lipidic region between the nanodomains, with an additional contribution from diffusion within the nanodomains. In addition, diffusion of the nanodomains and the contributions for the membrane height fluctuations might also have some contribution in the measured time-scales.

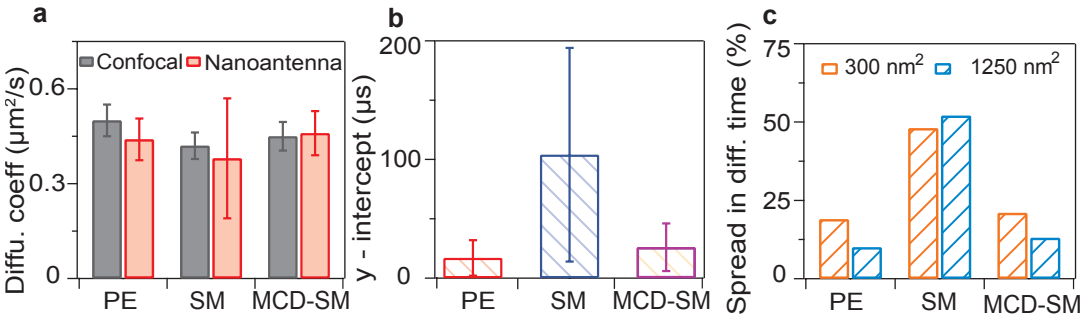

FIGURE 6.17: **Diffusion laws discussion at the nanoscale.** (a) The diffusion coefficients computed from the slopes in Figure 6.16 are compared with confocal results. (b) y-axis intercept deduced from the linear fits in the Figure 6.16a-c. PE and MCD-treated SM show near-zero y-intercept consistent with free diffusion, while the significant y-intercept for SM indicates that the diffusion is constrained by nanodomains. (c) Normalized spread in diffusion time (width of upper and lower quartiles / median) in each case. The large dispersion observed is SM is another indication that sphingolipids are preferentially recruited into transient nanoscopic domains.

Extrapolating the fits in Figure 6.16a-c towards diminishing probe area leads to the intercepts with the time axis as summarized in Figure 6.17b. The almost zero intercept hitting the origin observed for PE confirms the expected free Brownian motion diffusion mode. In contrast, SM features a positive y-intercept of about 100 μs, which highlights a significant deviation from free Brownian diffusion and the occurrence of nanoscopic domains hindering SM diffusion. Depletion of cholesterol results in SM diffusion with a close-to-zero time intercept, demonstrating the crucial role of cholesterol establishing the nanodomains and hindering SM diffusion. Such small nanoscale heterogeneities have never been detected so far with confocal microscopy, although STED-FCS down to 1000 nm^2 detection area could indicate clues about their occurrence. Our results are fully aligned with these previous findings and importantly, we further reduce the detection areas down to 300 nm^2 .

Lastly, we take a closer look at the degree of statistical dispersion of the obtained transient trapping times scattered around the median value for each probe area (Figure 6.17c). The spread in diffusion times for PE and SM after MCD treatment remains well under 25% and can be partially explained by variations of the gap size stemming from the nanofabrication process [63]. However, we observe for SM diffusion a significantly higher dispersion of the data (around 50%) which is specific to this lipid analog. These results are fully consistent with the presence of transient cholesterol-enriched

nanodomains affecting SM diffusion. To further support these conclusions, we take advantage of the confocal data to represent a third point (see Figure 6.18) and show nice alignment with the nanoantenna data.

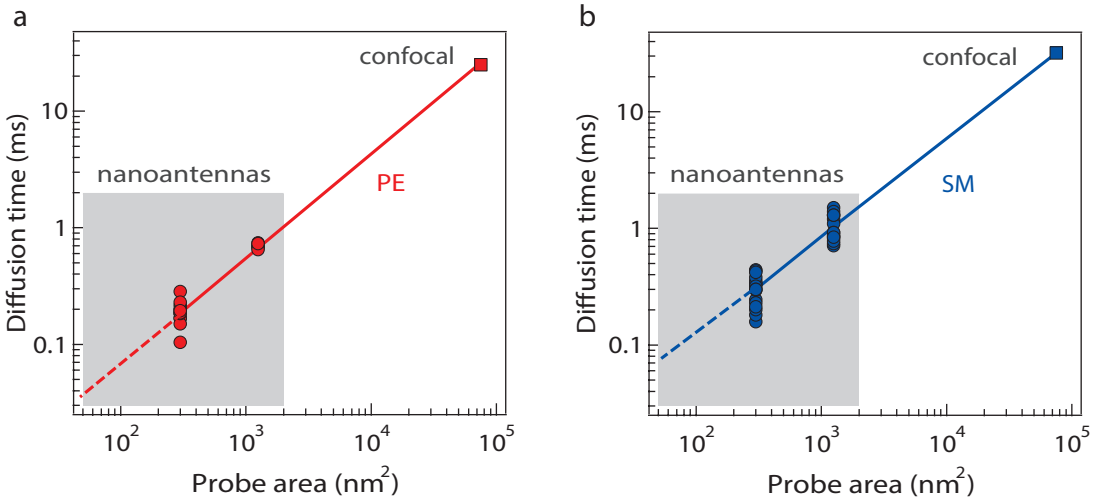

FIGURE 6.18: **FCS diffusion laws with confocal data.** FCS diffusion laws extended to include the confocal data for PE (a) and SM (b). The nanoantenna data is identical to Figure 6.16.

Altogether, our results provide compelling evidence for the existence of highly transient and fluctuating nanoscale assemblies of sterol and sphingolipids in living cell membranes. These experimental observations stand in excellent agreement with the notion that without stabilizing proteins, lipid rafts can be viewed as intrinsic nanoscale membrane heterogeneities that are small and highly transient [155, 159, 160, 162]. We estimate the characteristic residence time of the fluorescent SM lipid analogs in the nanodomain from the y-intercept in Figure 6.16b and Figure 6.17b, and find a value $\sim$100 μs . The typical size of the nanodomains could in principle also be deduced from the FCS diffusion laws which should feature a characteristic transition from confined to normal diffusion [53, 170]. As we do not observe this characteristic transition in our data, we conclude that the typical size of the nanodomain is smaller than the nominal gap size of our nanoantenna, that is 10 nm. Both the typical nanodomain size about 10 nm and the transient time about 100 μs stand in good agreement with the predictions from stochastic models [190], and from the earlier experiments with STED-FCS [175, 176, 177] and recent high-speed interferometric scattering (iSCAT) measurements on mimetic lipid bilayers containing cholesterol [165, 191, 192].

6.6 Summary

We demonstrate the promising approach of exploiting planar optical nanoantennas with accessible surface nanogaps to investigate the nanoscale architecture of live cell membranes. The key strengths of our approach rely on the 10 nm spatial resolution combined with a microsecond time resolution on a (nearly) perfectly flat substrate compatible with live cell culturing. The single-molecule data on nanoantennas reveal striking differences between PE and SM diffusion dynamics that remain hidden in confocal measurements. Fluorescence burst and correlation spectroscopy analysis for PE are consistent with a free Brownian diffusion model. In contrast, the diffusion dynamics of SM at the nanoscale show heterogeneities in both time and space which are cholesterol dependent. Further, removal of cholesterol leads to a recovery of free Brownian diffusion for SM, consistent with the loss of nanodomains. Our results show the existence of dynamic nanodomains on the plasma membranes of living cells of $\sim$10 nm diameter which is comparable to our measurement gap size. The corresponding transient trapping times are short of about $\sim$100 μs. We believe that the combination of optical nanoantennas with fluorescence microscopy is a powerfool tool to investigate the dynamics and interactions of raft associated proteins and their recruitment into molecular complexes on the plasma membrane of living cells. The proposed technique is fully bio-compatible and thus provides ample opportunities for biophysics and live cell research with single-molecule sensitivity at nanometric and (sub)microsecond spatiotemporal resolution, far beyond the diffraction limit of light.

Conclusion and Perspective

In this thesis, we explored various nanoantenna designs to achieve optimum optical performance with single-molecule sensitivity at molecular concentrations exceeding 20 μM. The enhanced near field intensity, increased quantum yield of the emitter in the vicinity of the nanoantenna together with high Purcell effects collectively result in giant fluorescence enhancements within very small mode volumes (up to 30k-fold below the diffraction-limited confocal scheme). The near field confinement of the excitation intensity together with the polarization sensitivity of these nanostructures were then demonstrated for (i) detecting single-molecules diffusing in solution and (ii) investigating nanoscale membrane architecture of the plasma membrane in the living cells.

As the fluorescence strongly depends upon the local environment to which an single emitter is exposed, the emission can be tailored by varying the shapes, dimensions or even the composition of the nanostructures. In Chapter 3, we explored double nanoholes antenna design for enhanced single-molecule fluorescence detection. Using fluorescence correlation spectroscopy, we measured a 70 zL near field apex volume, realizing a volume reduction of 7000-fold as compared to the diffraction-limited confocal configuration. The high intensity confinement goes with fluorescence enhancement up to 100-fold, together with microsecond transit time, 30-fold LDOS enhancement and single molecule sensitivity at concentrations exceeding 20 μM. The DNH provides an efficient design to reach nanometeric confinement of light, with a much simpler nanofabrication as compared to other designs such as "antenna-in-box" or bowtie structures. The DNH spectral resonance occurs in the range 550-700 nm therefore enables a better spectral overlap with the emission band of most common red fluorescent dyes. We also point out that much room remains for a thorough optimization of the DNH design. In this regard, we further demonstrated higher enhancement factors above 300-fold achieved with DNH bearing sharp apex tips fabricated *via* stencil lithography. Reaching sub-10 nm apex sizes with modern fabrication tools (such as He ion source FIB), mass fabrication of DNH structures with sharp apex tips will significantly upgrade the caliber of DNH structures with single-molecule sensitivity at much higher molecular concentrations.

Single molecule fluorescence sensors based on plasmonic nanostructures are currently limited by the nonradiative energy transfer (between emitters and free electron gas), and by the Joule heating caused by the excitation laser beam. Silicon based all-dielectric nanoantennas overcome these limitations, and thus are potential cost effective alternative for realizing molecular sensors with on-chip and CMOS compatibility. In Chapter 4, we

demonstrated the first proof-of-principle all-dielectric nanoantennas with single-molecule sensitivity and explained the fluorescence enhancement mechanism by a combination of excitation intensity enhancement and radiative rate enhancement with near similar strengths. For an all-silicon dimer nanoantenna with 20 nm nominal gap fabricated on glass substrates, we quantify fluorescence enhancement factors above 200-fold, together with 3600-fold volume reduction as compared to the diffraction-limited confocal schemes. At present, the maximum fluorophore concentration to reach single-molecule sensitivity is limited to around 10 μM, which can be further improved either by reducing the dimer gap separations, or *via* introducing a surrounding box-aperture to keep-out the fluorescence light originating from the background molecules (similar to the "antenna-in-box" geometry). Since all-dielectric nanoantenna has negligible losses, sub-nm gaps can be conceived for single-molecule experiments. Moreover, as the scattering spectrum of the silicon nanoantenna shows higher efficiency in the near-IR, optimized experimental strategy (with proper dye selection and reduced gap sizes) could significantly improve the detection of individual molecules at higher molecular concentrations using dielectric materials only.

Further, meeting the broad expectations of biologically-inspired experiments require nanoantennas featuring narrow gap sizes, full accessibility to the electromagnetic hotspot and high fabrication throughput. Our planar "antenna-in-box" design (Chapter 5, 6) address this concerns with an innovative fabrication approach combining e-beam lithography with planarization, etch back and template stripping. We present large sets of fully flat gold nanoantennas arrays featuring 10 nm nominal gaps with sharp edges and direct surface accessibility of the hotspots. We demonstrate the superior performance of these in-plane nanoantennas by probing single fluorescent molecules, and reach fluorescence enhancement factors up to 15,000-fold, outperforming any previous plasmonic realizations. In excellent agreement with numerical simulations, we relate this performance increase to the optimized position of the plasmonic hotspot which are accessible and exposed directly at the surface. The fabrication approach is scalable with excellent reproducibility, and can be applied to any nanoantenna designs. This provides a highly efficient platform for biochemical assays analysis with single molecule sensitivity at physiological conditions. The "antenna-in-box" shows spectral resonance occurring in the near-infrared regime, thus optimizing the nanoantenna geometry for the excitation wavelength, can further boost the fluorescence enhancement factors and the nanoantenna efficiency.

In Chapter 6, we explored planar nanoantennas to investigate the cholesterol-dependent nanoscale heterogeneities in the plasma membrane of living cells. Combining FCS with resonant planar nanoantenna with different gap sizes we could assess the dynamic nanoscale organization of phosphoethanolamine (PE) and sphingomyelin (SM) in the

living plasma membranes. Our approach takes advantage of the highly confined excitation light provided by dimer nanoantennas together with their outstanding planarity to investigate membrane regions as small as 10 nm in size with sub-ms temporal resolution. Fluorescence correlation spectroscopy and burst analysis show free 2D Brownian diffusion for PE (with both confocal and nanoantenna). However the diffusion dynamics of SM at the nanoscale indicates extremely heterogeneous behavior which were otherwise hidden in the ensemble averaging. Together with cholesterol depletion experiments, we demonstrate the existence of dynamic nanodomains (diameter less than 10 nm) with characteristic trapping times as short as 100 μs. These findings are crucial to understand the spatiotemporal and heterogeneous organization of live cell membranes at the nanoscale. This planar nanoantenna design with full access of the hotspot opens up the possibility of exploiting the physical properties of plasmonic antennas for a broad range of applications, such as biosensing in nano/microfluidic channels, light harvesting, photocatalysis *etc.* As an immediate extension, one could possibly think of investigating the raft-associated GPI anchored protein and their co-localization with SM (and cholesterol) in the plasma membranes. This could possibly provide complementary insights into the local organization of the plasma membrane in living cells. The proposed technique is bio-compatible and thus provides ample opportunities in biophysics and live cell experiments. To further increase the flexibility of these planar nanoantenna platforms, designing hybrid nanoantenna for broadband excitation, and time-gated detection for further reduction in spatial resolution remain as some of the immediate experimental strategies.

Altogether, using FCS, TCSPC, FDTD modeling and numerical simulations, this thesis provides a thorough investigation on different optical nanoantenna designs (double nanohole, nanogap dimer antennas and planar "antenna-in-box") along with the discussion on their respective merits. Probing emitters with different intrinsic quantum yields (Alexa Fluor 647, CV and Atto647N) we discussed the origin of fluorescence in the nanoantenna mediated single-molecule experiments. The high optical performance achieved with the robust designs open up promising perspectives to study complex biochemical dynamics at physiological expression levels. In addition, the nanoantenna approach is quite straightforward to implement on any confocal setup, as it does not require supplementary illumination beam (or optics). For now, the race for the higher enhancement factors should be only secondary to the potential applications of these nanoantennas in biophysics and live cell research.

Publications based on the Thesis

Regmi, R., Winkler, P.M., Flauraud, V., Borgman, K.J.E., Manzo, C., Brugger, J., Rigneault, H., Wenger, J. and García-Parajo, M.F., 2017. Planar optical nanoantennas resolve cholesterol-dependent nanoscale heterogeneities in the plasma membrane of living cells. *Nano Letters*, 17 (10), pp.6295-6302.

Winkler, P.M., **Regmi, R.**, Flauraud, V., Brugger, J., Rigneault, H., Wenger, J. and García-Parajo, M.F., 2017. Transient nanoscopic phase separation in biological lipid membranes resolved by planar plasmonic antennas. *ACS Nano*, 11(7), pp.7241-7250.

Flauraud, V., **Regmi, R.**, Winkler, P.M., Alexander, D.T., Rigneault, H., van Hulst, N.F., García-Parajo, M.F., Wenger, J. and Brugger, J., 2017. In-plane plasmonic antenna arrays with surface nanogaps for giant fluorescence enhancement. *Nano Letters*, 17(3), pp.1703-1710.

Regmi, R., Berthelot, J., Winkler, P.M., Mivelle, M., Proust, J., Bedu, F., Ozerov, I., Begou, T., Lumeau, J., Rigneault, H., García-Parajo, M.F., Bidault, S., Wenger, J. and Bonod, N., 2016. All-dielectric silicon nanogap antennas to enhance the fluorescence of single molecules. *Nano Letters*, 16(8), pp.5143-5151.

Wenger, J., **Regmi, R.**, and Rigneault, H., 2016. Plasmonic-enhanced fluorescence detection of single molecules at high concentrations, in Roadmap article edited by E. Di Fabrizio, *Journal of Optics*, 18(6), p.063003.

Regmi, R., Al Balushi, A.A., Rigneault, H., Gordon, R. and Wenger, J., 2015. Nanoscale volume confinement and fluorescence enhancement with double nanohole aperture. *Scientific Reports*, 5.

Punj, D., **Regmi, R.**, Devilez, A., Plauchu, R., Moparthi, S.B., Stout, B., Bonod, N., Rigneault, H. and Wenger, J., 2015. Self-assembled nanoparticle dimer antennas for plasmonic-enhanced single-molecule fluorescence detection at micromolar concentrations. *ACS Photonics*, 2(8), pp.1099-1107.

Acknowledgements

I would like to take this opportunity to thank everyone who has always been the source of inspiration throughout my life: all my wonderful friends, colleagues, inspirational teachers, and my family. This thesis was developed during my doctoral research within the Institut Fresnel, CNRS, Marseille (France) and ICFO - Institute of Photonic Sciences, Barcelona (Spain). I sincerely thank my thesis advisor Dr. Jérôme Wenger (Marseille) for his remarkable generosity and great support in my academic and personal issues. I feel proud to have you as my mentor early in my research career, and will proudly carry the character I built while growing under your supervision. Thanks, Jérôme!

I am equally grateful to thesis co-advisor Prof. María García-Parajo (Barcelona) for her kind support and guidance. Thanks, María! It was a great learning experience while being around you, and I will always remain thankful for all the inspiration and motivation. I feel very fortunate to have had this opportunity to be a part of these two esteem institutes in France and Spain. And, I extend my kind regards to Dr. Sophie Brasselet, Dr. Hugues Giovannini and entire EuroPhotonics Consortium for the doctoral fellowship, without which this would still have stayed a distance dream.

I thank all my thesis committee members: Prof. Didier Marguet (CIML, Marseille), Prof. Niek F. van Hulst (ICFO, Barcelona), Dr. Peter Zijlstra (TU Eindhoven, The Netherlands), and Dr. Guillermo Acuna (TU Braunschweig, Germany) for their valuable comments and encouragement during my thesis review/defense process. I have had the pleasure to collaborate with the teams of Prof. J. Brugger (EPFL, Switzerland), Prof. R. Gordon (University of Victoria, Canada) and Dr. Sébastien Bidault (Institut Langevin, Paris). Special thanks to Valentin Flauraud (EPFL, Switzerland) regarding his help with the nano-fabrication procedure of the planar nanoantennas (all champion antennas!). I am extremely thankful to Dr. Nicolas Bonod (Marseille) with whom I explored the dielectric nanoantenna project. In addition, sincere regards to Prof. Hervé Rigneault for providing the fantastic research atmosphere within the spirited Mosaic team.

I have had the pleasure of working alongside Juan de Torres, Deep Punj, Satish Moparthi, Petru Ghenuche, and Stéphanie Vial. Special thanks to Juan with whom, I also shared the same dining table during my stay in Marseille. Many thanks to Naveen and Sid for being such an unbelievable support to me for all these years. I feel fortunate to get to know and grow around you, precious you both! Special thanks to Johann for his kindness and support; both on and off-campus. Merci beaucoup, Johann!

Sincere thanks to all my amazing friends in Marseille: Matthias, Caio, Victor, Susmita, Swaroop, Soundarya, Valentina, Barbara for all the moments of fun and celebrations. In addition, many thanks to my awesome office-mates: Xavier, Camille, Paulina, Arthuro, Rafael, and Faris. Special thanks to Luisa for her continuous motivation and for all the wonderful memories. I acknowledge the support from my friends back home: Kamal Sigdel, Pashupati Shrestha, Janak Ghimire, Kshitiz Lamichhanne, Narayan Bastola. Durga Datta Kandel, Jyoti Sapkota, Rachana Poudel, Chetana D., Veronica Errasti for their love and care in every endeavor of my life. Special thanks to Shilpa for her continuous encouragement, and support in every aspect of my life. Many thanks, Shilpa for your love and care. And thanks a lot, Laurine, for everything, for being there, and for not letting me be alone.

My stay in Barcelona was a wonderful experience too. Thanks to Maria Sanz Paz, Jonas Fischer for being kind to let me share the same roof. In the office, I am grateful to Pamina Winkler for sharing her setup and showing me how biology works. Sincere gratitude to Merche Rivas, Kyra Borgman, Carlo Manzo and Mathieu Mivelle for the help with cell sample preparation and the computation support. Thanks to Felix and Eric for the stimulating discussion and technical support during my stay at ICFO. Many thanks to Claude, Nitin and Anshuman for their care during my installation at Barcelona. I am grateful to all the administrative staffs: Nelly Bardet, Aurore Piazzoli, Evelyne Santacroce, Claire Guene in Marseille, and Anne Gstöttner, Mery Gil, ICFO travel unit in Barcelona. I will forever remain indebted to every one of you.

Finally, my family: mom, dad, Kiran, and Raju Adhikari for all those lessons of perseverance and for having faith in me regardless of what I take up in life. My three princes Milan, Hridaya, and Aarambha for their love that inspires me to live a life of purpose. I owe you everything.

Regmi, Raju
30^{th} November, 2017
Marseille, France

Bibliography

[1] Betzig, E., Hell, S.W. and Moerner, W.E., 2015. The Nobel Prize in Chemistry 2014. *Nobelprize.org/nobel_prizes/chemistry/laureates/2014/* (Accessed September 13, 2017)

[2] Moerner, W.E., 2015. Nobel Lecture: Single-molecule spectroscopy, imaging, and photocontrol: Foundations for super-resolution microscopy. *Reviews of Modern Physics*, 87, pp.1183-1212.

[3] Moerner, W.E. and Kador, L., 1989. Optical detection and spectroscopy of single molecules in a solid. *Physical Review Letters*, 62(21), p.2535.

[4] Orrit, M. and Bernard, J., 1990. Single pentacene molecules detected by fluorescence excitation in a p-terphenyl crystal. *Physical Review Letters*, 65(21), p.2716.

[5] Moerner, W.E. and Orrit, M., 1999. Illuminating single molecules in condensed matter. *Science*, 283(5408), pp.1670-1676.

[6] Abbe, E., 1873. Beiträge zur Theorie des Mikroskops und der mikroskopischen Wahrnehmung. *Archiv für mikroskopische Anatomie*, 9(1), pp.413-418.

[7] Di Fabrizio, E., Schlücker, S., Wenger, J., Regmi, R., Rigneault, H., Calafiore, G., West, M., Cabrini, S., Fleischer, M., Van Hulst, N.F. and García-Parajo, M.F., 2016. Roadmap on biosensing and photonics with advanced nano-optical methods. *Journal of Optics*, 18(6), p.063003.

[8] Punj, D., Ghenuche, P., Moparthi, S.B., de Torres, J., Grigoriev, V., Rigneault, H. and Wenger, J., 2014. Plasmonic antennas and zeromode waveguides to enhance single molecule fluorescence detection and fluorescence correlation spectroscopy toward physiological concentrations. *Wiley Interdisciplinary Reviews: Nanomedicine and Nanobiotechnology*, 6(3), pp.268-282.

[9] Wenger, J. and Rigneault, H., 2010. Photonic methods to enhance fluorescence correlation spectroscopy and single molecule fluorescence detection. *International Journal of Molecular Sciences*, 11(1), pp.206-221.

[10] García-Parajo, M.F., 2008. Optical antennas focus in on biology. *Nature Photonics*, 2(4), pp.201-203.

[11] Novotny, L. and Van Hulst, N., 2011. Antennas for light. *Nature Photonics*, 5(2), pp.83-90.

[12] Wenger, J., 2017. Fluorescence spectroscopy enhancement on photonic nanoantennas. arXiv preprint arXiv:1709.06749.

[13] Wientjes, E., Renger, J., Curto, A.G., Cogdell, R. and Van Hulst, N.F., 2014. Strong antenna-enhanced fluorescence of a single light-harvesting complex shows photon antibunching. *Nature Communications*, 5.

[14] Pang, Y. and Gordon, R., 2011. Optical trapping of a single protein. *Nano Letters*, 12(1), pp.402-406.

[15] Anger, P., Bharadwaj, P. and Novotny, L., 2006. Enhancement and quenching of single-molecule fluorescence. *Physical Review Letters*, 96(11), p.113002.

[16] Punj, D., de Torres, J., Rigneault, H. and Wenger, J., 2013. Gold nanoparticles for enhanced single molecule fluorescence analysis at micromolar concentration. *Optics Express*, 21(22), pp.27338-27343.

[17] Yuan, H., Khatua, S., Zijlstra, P., Yorulmaz, M. and Orrit, M., 2013. Thousand-fold enhancement of single-molecule fluorescence near a single gold nanorod. *Angewandte Chemie International Edition*, 52(4), pp.1217-1221.

[18] Khatua, S., Paulo, P.M., Yuan, H., Gupta, A., Zijlstra, P. and Orrit, M., 2014. Resonant plasmonic enhancement of single-molecule fluorescence by individual gold nanorods. *ACS Nano*, 8(5), pp.4440-4449.

[19] Kinkhabwala, A., Yu, Z., Fan, S., Avlasevich, Y., Müllen, K. and Moerner, W.E., 2009. Large single-molecule fluorescence enhancements produced by a bowtie nanoantenna. *Nature Photonics*, 3(11), pp.654-657.

[20] Acuna, G.P., Möller, F.M., Holzmeister, P., Beater, S., Lalkens, B. and Tinnefeld, P., 2012. Fluorescence enhancement at docking sites of DNA-directed self-assembled nanoantennas. *Science*, 338(6106), pp.506-510.

[21] Ureña, E.B., Kreuzer, M.P., Itzhakov, S., Rigneault, H., Quidant, R., Oron, D. and Wenger, J., 2012. Excitation enhancement of a quantum dot coupled to a plasmonic antenna. *Advanced Materials*, 24(44).

[22] Punj, D., Regmi, R., Devilez, A., Plauchu, R., Moparthi, S.B., Stout, B., Bonod, N., Rigneault, H. and Wenger, J., 2015. Self-assembled nanoparticle dimer antennas for plasmonic-enhanced single-molecule fluorescence detection at micromolar concentrations. *ACS Photonics*, 2(8), pp.1099-1107.

[23] Holzmeister, P., Acuna, G.P., Grohmann, D. and Tinnefeld, P., 2014. Breaking the concentration limit of optical single-molecule detection. *Chemical Society Reviews*, 43(4), pp.1014-1028.

[24] Hell, S.W., 2007. Far-field optical nanoscopy. *Science*, 316(5828), pp.1153-1158.

[25] Eid, J., Fehr, A., Gray, J., Luong, K., Lyle, J., Otto, G., Peluso, P., Rank, D., Baybayan, P., Bettman, B. and Bibillo, A., 2009. Real-time DNA sequencing from single polymerase molecules. *Science*, 323(5910), pp.133-138.

[26] Lee, S.A., Ponjavic, A., Siv, C., Lee, S.F. and Biteen, J.S., 2016. Nanoscopic cellular imaging: confinement broadens understanding. *ACS Nano*, 10(9), pp.8143-8153.

[27] Punj, D., 2014. *Optical antennas for single molecule fluorescence detection at physiological concentration* (Doctoral dissertation, Aix Marseille université).

[28] Betzig, E. and Trautman, J.K., 1991. Breaking the diffraction barrier: optical microscopy on a nanometric scale. *Science*, 251(5000), p.1468.

[29] Trautman, J.K., Macklin, J.J., Brus, L.E. and Betzig, E., 1994. Near-field spectroscopy of single molecules at room temperature. *Nature*, 369(6475), pp.40-42.

[30] Manzo, C., van Zanten, T.S. and García-Parajo, M.F., 2011. Nanoscale fluorescence correlation spectroscopy on intact living cell membranes with NSOM probes. *Biophysical Journal*, 100(2), pp.L8-L10.

[31] Ruiter, A.G.T., Veerman, J.A., García-Parajo, M.F. and Van Hulst, N.F., 1997. Single molecule rotational and translational diffusion observed by near-field scanning optical microscopy. *The Journal of Physical Chemistry A*, 101(40), pp.7318-7323.

[32] Mivelle, M., van Zanten, T.S., Neumann, L., van Hulst, N.F. and García-Parajo, M.F., 2012. Ultrabright bowtie nanoaperture antenna probes studied by single molecule fluorescence. *Nano Letters*, 12(11), pp.5972-5978.

[33] Fish, K.N., 2009. Total internal reflection fluorescence (TIRF) microscopy. *Current Protocols in Cytometry*, pp.12-18.

[34] Hassler, K., Leutenegger, M., Rigler, P., Rao, R., Rigler, R., Gösch, M. and Lasser, T., 2005. Total internal reflection fluorescence correlation spectroscopy (TIR-FCS)

with low background and high count-rate per molecule. *Optics Express*, 13(19), pp.7415-7423.

[35] Hell, S.W. and Wichmann, J., 1994. Breaking the diffraction resolution limit by stimulated emission: stimulated-emission-depletion fluorescence microscopy. *Optics Letters*, 19(11), pp.780-782.

[36] Klar, T.A., Jakobs, S., Dyba, M., Egner, A. and Hell, S.W., 2000. Fluorescence microscopy with diffraction resolution barrier broken by stimulated emission. *Proceedings of the National Academy of Sciences*, 97(15), pp.8206-8210.

[37] Ahrens, M.B., Orger, M.B., Robson, D.N., Li, J.M. and Keller, P.J., 2013. Whole-brain functional imaging at cellular resolution using light-sheet microscopy. *Nature Methods*, 10(5), pp.413-420.

[38] Singh, A.P., Krieger, J.W., Buchholz, J., Charbon, E., Langowski, J. and Wohland, T., 2013. The performance of 2D array detectors for light sheet based fluorescence correlation spectroscopy. *Optics express*, 21(7), pp.8652-8668.

[39] Krieger, J.W., Singh, A.P., Garbe, C.S., Wohland, T. and Langowski, J., 2014. Dual-color fluorescence cross-correlation spectroscopy on a single plane illumination microscope (SPIM-FCCS). *Optics Express*, 22(3), pp.2358-2375.

[40] Giannini, V., Sánchez-Gil, J.A., Muskens, O.L. and Rivas, J.G., 2009. Electrodynamic calculations of spontaneous emission coupled to metal nanostructures of arbitrary shape: nanoantenna-enhanced fluorescence. *JOSA B*, 26(8), pp.1569-1577.

[41] Berman, P.R., 1994. Cavity quantum electrodynamics.

[42] Giannini, V., FernándezDomínguez, A.I., Sonnefraud, Y., Roschuk, T., FernándezGarcía, R. and Maier, S.A., 2010. Controlling light localization and light-matter interactions with nanoplasmonics. *Small*, 6(22), pp.2498-2507.

[43] Zander, C., Enderlein, J. and Keller, R. A., 2002. *Single-Molecule Detection in Solution - Methods and Applications.* VCH-Wiley, Berlin/New York.

[44] Taylor, A. and Zijlstra, P., 2017. Single-molecule plasmon sensing: current status and future prospects. *ACS Sensors*.

[45] Park, J.E., Kim, J. and Nam, J.M., 2017. Emerging plasmonic nanostructures for controlling and enhancing photoluminescence. *Chemical Science*, 8(7), pp.4696-4704.

[46] Gérard, D., Wenger, J., Bonod, N., Popov, E., Rigneault, H., Mahdavi, F., Blair, S., Dintinger, J. and Ebbesen, T.W., 2008. Nanoaperture-enhanced fluorescence: Towards higher detection rates with plasmonic metals. *Physical Review B*, 77(4), p.045413.

[47] Levene, M.J., Korlach, J., Turner, S.W., Foquet, M., Craighead, H.G. and Webb, W.W., 2003. Zero-mode waveguides for single-molecule analysis at high concentrations. *Science*, 299(5607), pp.682-686.

[48] Aouani, H., Itzhakov, S., Gachet, D., Devaux, E., Ebbesen, T.W., Rigneault, H., Oron, D. and Wenger, J., 2010. Colloidal quantum dots as probes of excitation field enhancement in photonic antennas. *ACS Nano*, 4(8), pp.4571-4578.

[49] Aouani, H., Mahboub, O., Devaux, E., Rigneault, H., Ebbesen, T.W. and Wenger, J., 2011. Large molecular fluorescence enhancement by a nanoaperture with plasmonic corrugations. *Optics Express*, 19(14), pp.13056-13062.

[50] Rigneault, H., Capoulade, J., Dintinger, J., Wenger, J., Bonod, N., Popov, E., Ebbesen, T.W. and Lenne, P.F., 2005. Enhancement of single-molecule fluorescence detection in subwavelength apertures. *Physical Review Letters*, 95(11), p.117401.

[51] Popov, E., Nevière, M., Wenger, J., Lenne, P.F., Rigneault, H., Chaumet, P., Bonod, N., Dintinger, J. and Ebbesen, T., 2006. Field enhancement in single subwavelength apertures. *JOSA A*, 23(9), pp.2342-2348.

[52] Moran-Mirabal, J.M., Torres, A.J., Samiee, K.T., Baird, B.A. and Craighead, H.G., 2007. Cell investigation of nanostructures: zero-mode waveguides for plasma membrane studies with single molecule resolution. *Nanotechnology*, 18(19), p.195101.

[53] Wenger, J., Conchonaud, F., Dintinger, J., Wawrezinieck, L., Ebbesen, T.W., Rigneault, H., Marguet, D. and Lenne, P.F., 2007. Diffusion analysis within single nanometric apertures reveals the ultrafine cell membrane organization. *Biophysical Journal*, 92(3), pp.913-919.

[54] Wenger J, Rigneault H, Dintinger J, Marguet D, Lenne PF. Single-fluorophore diffusion in a lipid membrane over a subwavelength aperture. *Journal of Biological Physics*. 2006 Jan 8;32(1):SN1-4.

[55] Wenger, J., Cluzel, B., Dintinger, J., Bonod, N., Fehrembach, A.L., Popov, E., Lenne, P.F., Ebbesen, T.W. and Rigneault, H., 2007. Radiative and nonradiative photokinetics alteration inside a single metallic nanometric aperture. *The Journal of Physical Chemistry C*, 111(30), pp.11469-11474.

[56] Pradhan, B., Khatua, S., Gupta, A., Aartsma, T., Canters, G. and Orrit, M., 2016. Gold-nanorod-enhanced fluorescence correlation spectroscopy of fluorophores with high quantum yield in lipid bilayers. *The Journal of Physical Chemistry C*, 120(45), pp.25996-26003.

[57] Zijlstra, P., Paulo, P.M. and Orrit, M., 2012. Optical detection of single non-absorbing molecules using the surface plasmon resonance of a gold nanorod. *Nature Nanotechnology*, 7(6), pp.379-382.

[58] Akselrod, G.M., Argyropoulos, C., Hoang, T.B., Ciracì, C., Fang, C., Huang, J., Smith, D.R. and Mikkelsen, M.H., 2014. Probing the mechanisms of large Purcell enhancement in plasmonic nanoantennas. *Nature Photonics*, 8(11), pp.835-840.

[59] Rose, A., Hoang, T.B., McGuire, F., Mock, J.J., Ciracì, C., Smith, D.R. and Mikkelsen, M.H., 2014. Control of radiative processes using tunable plasmonic nanopatch antennas. *Nano Letters*, 14(8), pp.4797-4802.

[60] Yi, M., Zhang, D., Wang, P., Jiao, X., Blair, S., Wen, X., Fu, Q., Lu, Y. and Ming, H., 2011. Plasmonic interaction between silver nano-cubes and a silver ground plane studied by surface-enhanced Raman scattering. *Plasmonics*, 6(3), pp.515-519.

[61] Puchkova, A., Vietz, C., Pibiri, E., Wünsch, B., Sanz Paz, M., Acuna, G.P. and Tinnefeld, P., 2015. DNA origami nanoantennas with over 5000-fold fluorescence enhancement and single-molecule detection at 25 μM. *Nano Letters*, 15(12), pp.8354-8359.

[62] Flauraud, V., Regmi, R., Winkler, P.M., Alexander, D.T., Rigneault, H., Van Hulst, N.F., García-Parajo, M.F., Wenger, J. and Brugger, J., 2017. In-plane plasmonic antenna arrays with surface nanogaps for giant fluorescence enhancement. *Nano Letters*, 17(3), pp.1703-1710.

[63] Winkler, P.M., Regmi, R., Flauraud, V., Brugger, J., Rigneault, H., Wenger, J. and García-Parajo, M.F., 2017. Transient nanoscopic phase separation in biological lipid membranes resolved by planar plasmonic antennas. *ACS Nano*, 11(7), pp.7241-7250.

[64] Regmi, R., Winkler, P.M., Flauraud, V., Borgman, K.J.E., Manzo, C., Brugger, J., Rigneault, H., Wenger, J. and García-Parajo, M.F., 2017. Planar optical nanoantennas resolve cholesterol-dependent nanoscale heterogeneities in the plasma membrane of living cells. *Nano Letters*, 17(10), pp.6295-6302.

[65] Regmi, R., Al Balushi, A.A., Rigneault, H., Gordon, R. and Wenger, J., 2015. Nanoscale volume confinement and fluorescence enhancement with double nanohole aperture. *Scientific Reports*, 5.

[66] Wenger, J., Lenne, P.F., Popov, E., Rigneault, H., Dintinger, J. and Ebbesen, T.W., 2005. Single molecule fluorescence in rectangular nano-apertures. *Optics Express*, 13(18), pp.7035-7044.

[67] Acuna, G., Grohmann, D. and Tinnefeld, P., 2014. Enhancing singlemolecule fluorescence with nanophotonics. *FEBS Letters*, 588(19), pp.3547-3552.

[68] Regmi, R., Berthelot, J., Winkler, P.M., Mivelle, M., Proust, J., Bedu, F., Ozerov, I., Begou, T., Lumeau, J., Rigneault, H., García-Parajo, M.F., Wenger, J., and Bonod, N., 2016. All-dielectric silicon nanogap antennas to enhance the fluorescence of single molecules. *Nano Letters*, 16(8), pp.5143-5151.

[69] Maiti, S., Haupts, U. and Webb, W.W., 1997. Fluorescence correlation spectroscopy: diagnostics for sparse molecules. *Proceedings of the National Academy of Sciences*, 94(22), pp.11753-11757.

[70] Magde, D., Elson, E. and Webb, W.W., 1972. Thermodynamic fluctuations in a reacting system-measurement by fluorescence correlation spectroscopy. *Physical Review Letters*, 29(11), p.705.

[71] Wenger, J., Gérard, D., Lenne, P.F., Rigneault, H., Dintinger, J., Ebbesen, T.W., Boned, A., Conchonaud, F. and Marguet, D., 2006. Dual-color fluorescence cross-correlation spectroscopy in a single nanoaperture: towards rapid multicomponent screening at high concentrations. *Optics Express*, 14(25), pp.12206-12216.

[72] Haustein, E. and Schwille, P., 2004. Fluorescence correlation spectroscopy: an introduction to its concepts and applications. *Biophysics Textbook Online*.

[73] Rigler, R. and Elson, E.S. eds., 2001. *Fluorescence correlation spectroscopy: theory and applications* (Vol. 65). Springer Science & Business Media.

[74] Wahl, M., 2002. Time-Correlated Photon Counting Tech Note TCSPC1. 2. *PicoQuant GmbH*.

[75] Grecco, H.E. and Verveer, P.J., 2011. FRET in cell biology: Still shining in the age of super-resolution?. *ChemPhysChem*, 12(3), pp.484-490.

[76] Elson, D., Requejo-Isidro, J., Munro, I., Reavell, F., Siegel, J., Suhling, K., Tadrous, P., Benninger, R., Lanigan, P., McGinty, J. and Talbot, C., 2004. Time-domain fluorescence lifetime imaging applied to biological tissue. *Photochemical & Photobiological Sciences*, 3(8), pp.795-801.

[77] Koppel, D.E., 1974. Statistical accuracy in fluorescence correlation spectroscopy. *Physical Review A*, 10(6), p.1938.

[78] Wenger, J., Gerard, D., Aouani, H., Rigneault, H., Lowder, B., Blair, S., Devaux, E. and Ebbesen, T.W., 2008. Nanoaperture-enhanced signal-to-noise ratio in fluorescence correlation spectroscopy. *Analytical Chemistry*, 81(2), pp.834-839.

[79] Pang, Y. and Gordon, R., 2011. Optical trapping of 12 nm dielectric spheres using double-nanoholes in a gold film. *Nano Letters*, 11(9), pp.3763-3767.

[80] Kotnala, A., DePaoli, D. and Gordon, R., 2013. Sensing nanoparticles using a double nanohole optical trap. *Lab on a Chip*, 13(20), pp.4142-4146.

[81] Gelfand, R.M., Wheaton, S. and Gordon, R., 2014. Cleaved fiber optic double nanohole optical tweezers for trapping nanoparticles. *Optics Letters*, 39(22), pp.6415-6417.

[82] Al Balushi, A.A., Zehtabi-Oskuie, A. and Gordon, R., 2013. Observing single protein binding by optical transmission through a double nanohole aperture in a metal film. *Biomedical Optics Express*, 4(9), pp.1504-1511.

[83] Al Balushi, A.A. and Gordon, R., 2014. A label-free untethered approach to single-molecule protein binding kinetics. *Nano Letters*, 14(10), pp.5787-5791.

[84] Al Balushi, A.A. and Gordon, R., 2014. Label-free free-solution single-molecule proteinsmall molecule interaction observed by double-nanohole plasmonic trapping. *ACS Photonics*, 1(5), pp.389-393.

[85] Lesuffleur, A., Kumar, L.K.S., Brolo, A.G., Kavanagh, K.L. and Gordon, R., 2007. Apex-enhanced Raman spectroscopy using double-hole arrays in a gold film. *The Journal of Physical Chemistry C*, 111(6), pp.2347-2350.

[86] Lesuffleur, A., Kumar, L.K.S. and Gordon, R., 2007. Apex-enhanced second-harmonic generation by using double-hole arrays in a gold film. *Physical Review B*, 75(4), p.045423.

[87] Fromm, D.P., Sundaramurthy, A., Schuck, P.J., Kino, G. and Moerner, W.E., 2004. Gap-dependent optical coupling of single "bowtie" nanoantennas resonant in the visible. *Nano Letters*, 4(5), pp.957-961.

[88] Lu, G., Li, W., Zhang, T., Yue, S., Liu, J., Hou, L., Li, Z. and Gong, Q., 2012. Plasmonic-enhanced molecular fluorescence within isolated bowtie nano-apertures. *Acs Nano*, 6(2), pp.1438-1448.

[89] Berthelot, J., Aćimović, S.S., Juan, M.L., Kreuzer, M.P., Renger, J. and Quidant, R., 2014. Three-dimensional manipulation with scanning near-field optical nanotweezers. *Nature Nanotechnology*, 9(4), pp.295-299.

[90] Punj, D., Mivelle, M., Moparthi, S.B., Van Zanten, T.S., Rigneault, H., Van Hulst, N.F., García-Parajo, M.F. and Wenger, J., 2013. A plasmonic "antenna-in-box" platform for enhanced single-molecule analysis at micromolar concentrations. *Nature Nanotechnology*, 8(7), pp.512-516.

[91] Johnson, P.B. and Christy, R.W., 1972. Optical constants of the noble metals. *Physical Review B*, 6(12), p.4370.

[92] Wenger, J., Gérard, D., Dintinger, J., Mahboub, O., Bonod, N., Popov, E., Ebbesen, T.W. and Rigneault, H., 2008. Emission and excitation contributions to enhanced single molecule fluorescence by gold nanometric apertures. *Optics Express*, 16(5), pp.3008-3020.

[93] Aouani, H., Mahboub, O., Bonod, N., Devaux, E., Popov, E., Rigneault, H., Ebbesen, T.W. and Wenger, J., 2011. Bright unidirectional fluorescence emission of molecules in a nanoaperture with plasmonic corrugations. *Nano Letters*, 11(2), pp.637-644.

[94] Bharadwaj, P. and Novotny, L., 2007. Spectral dependence of single molecule fluorescence enhancement. *Optics Express*, 15(21), pp.14266-14274.

[95] Ghenuche, P., de Torres, J., Moparthi, S.B., Grigoriev, V. and Wenger, J., 2014. Nanophotonic enhancement of the Förster resonance energy-transfer rate with single nanoapertures. *Nano Letters*, 14(8), pp.4707-4714.

[96] Novotny, L., Hecht, B., 2006. *Principles of Nano-Optics.* Cambridge University press.

[97] De Torres, J., 2016. *Nanophotonic control of Förster Resonance Energy Transfer* (Doctoral dissertation, Aix Marseille université).

[98] Chowdhury, M.H., Pond, J., Gray, S.K. and Lakowicz, J.R., 2008. Systematic computational study of the effect of silver nanoparticle dimers on the coupled emission from nearby fluorophores. *The Journal of Physical Chemistry C*, 112(30), pp.11236-11249.

[99] Lakowicz, J.R. and Fu, Y., 2009. Modification of single molecule fluorescence near metallic nanostructures. *Laser & Photonics Reviews*, 3(12), pp.221-232.

[100] Biagioni, P., Huang, J.S. and Hecht, B., 2012. Nanoantennas for visible and infrared radiation. *Reports on Progress in Physics*, 75(2), p.024402.

[101] Bidault, S., Devilez, A., Maillard, V., Lermusiaux, L., Guigner, J.M., Bonod, N. and Wenger, J., 2016. Picosecond lifetimes with high quantum yields from single-photon-emitting colloidal nanostructures at room temperature. *ACS Nano*, 10(4), pp.4806-4815.

[102] Curto, A.G., Volpe, G., Taminiau, T.H., Kreuzer, M.P., Quidant, R. and van Hulst, N.F., 2010. Unidirectional emission of a quantum dot coupled to a nanoantenna. *Science*, 329(5994), pp.930-933.

[103] Baffou, G. and Quidant, R., 2013. Thermo-plasmonics: using metallic nanostructures as nanosources of heat. *Laser & Photonics Reviews*, 7(2), pp.171-187.

[104] Abadeer, N.S. and Murphy, C.J., 2016. Recent progress in cancer thermal therapy using gold nanoparticles. *The Journal of Physical Chemistry C*, 120(9), pp.4691-4716.

[105] Zhu, M., Baffou, G., Meyerbröker, N. and Polleux, J., 2012. Micropatterning thermoplasmonic gold nanoarrays to manipulate cell adhesion. *ACS nano*, 6(8), pp.7227-7233.

[106] García-Etxarri, A., Gómez-Medina, R., Froufe-Prez, L.S., López, C., Chantada, L., Scheffold, F., Aizpurua, J., Nieto-Vesperinas, M. and Senz, J.J., 2011. Strong magnetic response of submicron silicon particles in the infrared. *Optics express*, 19(6), pp.4815-4826.

[107] Evlyukhin, A.B., Novikov, S.M., Zywietz, U., Eriksen, R.L., Reinhardt, C., Bozhevolnyi, S.I. and Chichkov, B.N., 2012. Demonstration of magnetic dipole resonances of dielectric nanospheres in the visible region. *Nano Letters*, 12(7), pp.3749-3755.

[108] Kuznetsov, A.I., Miroshnichenko, A.E., Fu, Y.H., Zhang, J. and Luk'yanchuk, B., 2012. Magnetic light. *Scientific Reports*, 2, p.srep00492.

[109] $http://refractiveindex.info/$(accessed July 12, 2016)

[110] Mie, G., 1908. Beiträge zur Optik trüber Medien, speziell kolloidaler Metallösungen. *Annalen der Physik*, 330(3), pp.377-445.

[111] Sigalas, M.M., Fattal, D.A., Williams, R.S., Wang, S.Y. and Beausoleil, R.G., 2007. Electric field enhancement between two Si microdisks. *Optics Express*, 15(22), pp.14711-14716.

[112] Rolly, B., Bebey, B., Bidault, S., Stout, B. and Bonod, N., 2012. Promoting magnetic dipolar transition in trivalent lanthanide ions with lossless Mie resonances. *Physical Review B*, 85(24), p.245432.

[113] Albella, P., Poyli, M.A., Schmidt, M.K., Maier, S.A., Moreno, F., Saenz, J.J. and Aizpurua, J., 2013. Low-loss electric and magnetic field-enhanced spectroscopy with subwavelength silicon dimers. *The Journal of Physical Chemistry C*, 117(26), pp.13573-13584.

[114] Boudarham, G., Abdeddaim, R. and Bonod, N., 2014. Enhancing the magnetic field intensity with a dielectric gap antenna. *Applied Physics Letters*, 104(2), p.021117.

[115] Bakker, R.M., Permyakov, D., Yu, Y.F., Markovich, D., Paniagua-Domnguez, R., Gonzaga, L., Samusev, A., Kivshar, Y., Luk'yanchuk, B. and Kuznetsov, A.I., 2015. Magnetic and electric hotspots with silicon nanodimers. *Nano Letters*, 15(3), pp.2137-2142.

[116] Vahala, K.J., 2003. Optical microcavities. *Nature* 424(6950), p.839.

[117] Lodahl, P., Mahmoodian, S. and Stobbe, S., 2015. Interfacing single photons and single quantum dots with photonic nanostructures. *Reviews of Modern Physics*, 87(2), p.347.

[118] Armani, D.K., Kippenberg, T.J., Spillane, S.M. and Vahala, K.J., 2003. Ultra-high-Q toroid microcavity on a chip. *Nature*, 421(6926), p.925.

[119] Armani, A.M., Kulkarni, R.P., Fraser, S.E., Flagan, R.C. and Vahala, K.J., 2007. Label-free, single-molecule detection with optical microcavities. *Science*, 317(5839), pp.783-787.

[120] Lee, K.G., Chen, X.W., Eghlidi, H., Kukura, P., Lettow, R., Renn, A., Sandoghdar, V. and Götzinger, S., 2011. A planar dielectric antenna for directional single-photon emission and near-unity collection efficiency. *Nature Photonics*, 5(3), pp.166-169.

[121] Chu, X.L., Brenner, T.J., Chen, X.W., Ghosh, Y., Hollingsworth, J.A., Sandoghdar, V. and Götzinger, S., 2014. Experimental realization of an optical antenna designed for collecting 99% of photons from a quantum emitter. *Optica*, 1(4), pp.203-208.

[122] Zambrana-Puyalto, X. and Bonod, N., 2015. Purcell factor of spherical Mie resonators. *Physical Review B*, 91(19), p.195422.

[123] Zywietz, U., Evlyukhin, A.B., Reinhardt, C. and Chichkov, B.N., 2014. Laser printing of silicon nanoparticles with resonant optical electric and magnetic responses. *Nature Communications*, 5, p.3402.

[124] Andres-Arroyo, A., Gupta, B., Wang, F., Gooding, J.J. and Reece, P.J., 2016. Optical manipulation and spectroscopy of silicon nanoparticles exhibiting dielectric resonances. *Nano Letters*, 16(3), pp.1903-1910.

[125] van de Groep, J., Coenen, T., Mann, S.A. and Polman, A., 2016. Direct imaging of hybridized eigenmodes in coupled silicon nanoparticles. *Optica*, 3(1), pp.93-99.

[126] Zambrana-Puyalto, X. and Bonod, N., 2016. Tailoring the chirality of light emission with spherical Si-based antennas. *Nanoscale*, 8(19), pp.10441-10452.

[127] Dodson, C.M. and Zia, R., 2012. Magnetic dipole and electric quadrupole transitions in the trivalent lanthanide series: Calculated emission rates and oscillator strengths. *Physical Review B*, 86(12), p.125102.

[128] Schmidt, M.K., Esteban, R., Senz, J., Surez-Lacalle, I., Mackowski, S. and Aizpurua, J., 2012. Dielectric antennas-a suitable platform for controlling magnetic dipolar emission. *Optics Express*, 20(13), pp.13636-13650.

[129] Devilez, A., Stout, B. and Bonod, N., 2010. Compact metallo-dielectric optical antenna for ultra directional and enhanced radiative emission. *ACS Nano*, 4(6), pp.3390-3396.

[130] Caldarola, M., Albella, P., Cortés, E., Rahmani, M., Roschuk, T., Grinblat, G., Oulton, R.F., Bragas, A.V. and Maier, S.A., 2015. Non-plasmonic nanoantennas for surface enhanced spectroscopies with ultra-low heat conversion. *Nature Communications*, 6.

[131] Dmitriev, P.A., Baranov, D.G., Milichko, V.A., Makarov, S.V., Mukhin, I.S., Samusev, A.K., Krasnok, A.E., Belov, P.A. and Kivshar, Y.S., 2016. Resonant Raman scattering from silicon nanoparticles enhanced by magnetic response. *Nanoscale*, 8(18), pp.9721-9726.

[132] Devilez, A., Bonod, N., Wenger, J., Gérard, D., Stout, B., Rigneault, H. and Popov, E., 2009. Three-dimensional subwavelength confinement of light with dielectric microspheres. *Optics Express*, 17(4), pp.2089-2094.

[133] Gérard, D., Devilez, A., Aouani, H., Stout, B., Bonod, N., Wenger, J., Popov, E. and Rigneault, H., 2009. Efficient excitation and collection of single-molecule fluorescence close to a dielectric microsphere. *JOSA B*, 26(7), pp.1473-1478.

[134] Ferrand, P., Wenger, J., Devilez, A., Pianta, M., Stout, B., Bonod, N., Popov, E. and Rigneault, H., 2008. Direct imaging of photonic nanojets. *Optics Express*, 16(10), pp.6930-6940.

[135] Ghenuche, P., Rigneault, H. and Wenger, J., 2012. Photonic nanojet focusing for hollow-core photonic crystal fiber probes. *Applied Optics*, 51(36), pp.8637-8640.

[136] Yang, H. and Gijs, M.A., 2013. Microtextured substrates and microparticles used as in situ lenses for on-chip immunofluorescence amplification. *Analytical Chemistry*, 85(4), pp.2064-2071.

[137] Yang, H., Cornaglia, M. and Gijs, M.A., 2015. Photonic nanojet array for fast detection of single nanoparticles in a flow. *Nano Letters*, 15(3), pp.1730-1735.

[138] Nobis, T., Kaidashev, E.M., Rahm, A., Lorenz, M. and Grundmann, M., 2004. Whispering gallery modes in nanosized dielectric resonators with hexagonal cross section. *Physical Review Letters*, 93(10), p.103903.

[139] Teraoka, I. and Arnold, S., 2006. Enhancing the sensitivity of a whispering-gallery mode microsphere sensor by a high-refractive-index surface layer. *JOSA B*, 23(7), pp.1434-1441.

[140] Scherer, M., Pistner, J. and Lehnert, W., 2010, June. UV-and VIS filter coatings by plasma assisted reactive magnetron sputtering (PARMS). In Optical Interference Coatings (p. MA7). *Optical Society of America*.

[141] Pierce, D.T. and Spicer, W.E., 1972. Electronic structure of amorphous Si from photoemission and optical studies. *Physical Review B*, 5(8), p.3017.

[142] Cao, D., Cazé, A., Calabrese, M., Pierrat, R., Bardou, N., Collin, S., Carminati, R., Krachmalnicoff, V. and De Wilde, Y., 2015. Mapping the radiative and the apparent nonradiative local density of states in the near field of a metallic nanoantenna. *ACS Photonics*, 2(2), pp.189-193.

[143] Oubre, C. and Nordlander, P., 2004. Optical properties of metallodielectric nanostructures calculated using the finite difference time domain method. *The Journal of Physical Chemistry B*, 108(46), pp.17740-17747.

[144] Devilez, A., Zambrana-Puyalto, X., Stout, B. and Bonod, N., 2015. Mimicking localized surface plasmons with dielectric particles. *Physical Review B*, 92(24), p.241412.

[145] Duan, H., Hu, H., Kumar, K., Shen, Z. and Yang, J.K., 2011. Direct and reliable patterning of plasmonic nanostructures with sub-10-nm gaps. *ACS Nano*, 5(9), pp.7593-7600.

[146] Kollmann, H., Piao, X., Esmann, M., Becker, S.F., Hou, D., Huynh, C., Kautschor, L.O., Bösker, G., Vieker, H., Beyer, A. and Gölzhäuser, A., 2014. Toward plasmonics with nanometer precision: nonlinear optics of helium-ion milled gold nanoantennas. *Nano Letters*, 14(8), pp.4778-4784.

[147] Wang, Y.M., Lu, L., Srinivasan, B.M., Asbahi, M., Zhang, Y.W. and Yang, J.K., 2015. High aspect ratio 10-nm-scale nanoaperture arrays with template-guided metal dewetting. *Scientific Reports*, 5, p.9654.

[148] Flauraud, V., van Zanten, T.S., Mivelle, M., Manzo, C., García-Parajo, M.F. and Brugger, J., 2015. Large-scale arrays of bowtie nanoaperture antennas for nanoscale dynamics in living cell membranes. *Nano Letters*, 15(6), pp.4176-4182.

[149] De Torres, J., Mivelle, M., Moparthi, S.B., Rigneault, H., Van Hulst, N.F., García-Parajo, M.F., Margeat, E. and Wenger, J., 2016. Plasmonic Nanoantennas Enable Forbidden Förster DipoleDipole Energy Transfer and Enhance the FRET Efficiency. *Nano Letters*, 16(10), pp.6222-6230.

[150] Aouani, H., Wenger, J., Gérard, D., Rigneault, H., Devaux, E., Ebbesen, T.W., Mahdavi, F., Xu, T. and Blair, S., 2009. Crucial role of the adhesion layer on the plasmonic fluorescence enhancement. *ACS Nano*, 3(7), pp.2043-2048.

[151] McPeak, K.M., Jayanti, S.V., Kress, S.J., Meyer, S., Iotti, S., Rossinelli, A. and Norris, D.J., 2015. Plasmonic films can easily be better: Rules and recipes. *ACS Photonics*, 2(3), pp.326-333.

[152] Langguth, L. and Koenderink, A.F., 2014. Simple model for plasmon enhanced fluorescence correlation spectroscopy. *Optics Express*, 22(13), pp.15397-15409.

[153] Kinkhabwala, A.A., Yu, Z., Fan, S. and Moerner, W.E., 2012. Fluorescence correlation spectroscopy at high concentrations using gold bowtie nanoantennas. *Chemical Physics*, 406, pp.3-8.

[154] Brown, D.A. and London, E., 2000. Structure and function of sphingolipid- and cholesterol-rich membrane rafts. *Journal of Biological Chemistry*, 275(23), pp.17221-17224.

[155] Lingwood, D. and Simons, K., 2010. Lipid rafts as a membrane-organizing principle. *Science*, 327(5961), pp.46-50.

[156] Kusumi, A., Nakada, C., Ritchie, K., Murase, K., Suzuki, K., Murakoshi, H., Kasai, R.S., Kondo, J. and Fujiwara, T., 2005. Paradigm shift of the plasma membrane concept from the two-dimensional continuum fluid to the partitioned fluid:

high-speed single-molecule tracking of membrane molecules. *Annu. Rev. Biophys. Biomol. Struct.*, 34, pp.351-378.

[157] Gowrishankar, K., Ghosh, S., Saha, S., Rumamol, C., Mayor, S. and Rao, M., 2012. Active remodeling of cortical actin regulates spatiotemporal organization of cell surface molecules. *Cell*, 149(6), pp.1353-1367.

[158] Sezgin, E., Levental, I., Mayor, S. and Eggeling, C., 2017. The mystery of membrane organization: composition, regulation and roles of lipid rafts. *Nat. Rev. Mol. Cell Biol.*, 18, pp.361-374.

[159] Mayor, S. and Rao, M., 2004. Rafts: scaledependent, active lipid organization at the cell surface. *Traffic*, 5(4), pp.231-240.

[160] Simons, K. and Gerl, M.J., 2010. Revitalizing membrane rafts: new tools and insights. *Nat. Rev. Mol. Cell Biol.*, 11(10), pp.688-699.

[161] Pike, L.J., 2006. Rafts defined: a report on the keystone symposium on lipid rafts and cell function. *Journal of Lipid Research*, 47(7), pp.1597-1598.

[162] Hancock, J.F., 2006. Lipid rafts: contentious only from simplistic standpoints. *Nature reviews. Molecular cell biology*, 7(6), p.456.

[163] Lenne, P.F., Wawrezinieck, L., Conchonaud, F., Wurtz, O., Boned, A., Guo, X.J., Rigneault, H., He, H.T. and Marguet, D., 2006. Dynamic molecular confinement in the plasma membrane by microdomains and the cytoskeleton meshwork. *The EMBO Journal*, 25(14), pp.3245-3256.

[164] Marguet, D., Lenne, P.F., Rigneault, H. and He, H.T., 2006. Dynamics in the plasma membrane: how to combine fluidity and order. *The EMBO journal*, 25(15), pp.3446-3457.

[165] Wu, H.M., Lin, Y.H., Yen, T.C. and Hsieh, C.L., 2016. Nanoscopic substructures of raft-mimetic liquid-ordered membrane domains revealed by high-speed single-particle tracking. *Scientific Reports*, 6, p.20542.

[166] van Zanten, T.S., Cambi, A., Koopman, M., Joosten, B., Figdor, C.G. and García-Parajo, M.F., 2009. Hotspots of GPI-anchored proteins and integrin nanoclusters function as nucleation sites for cell adhesion. *Proceedings of the National Academy of Sciences*, 106(44), pp.18557-18562.

[167] van Zanten, T.S., Gómez, J., Manzo, C., Cambi, A., Buceta, J., Reigada, R. and García-Parajo, M.F., 2010. Direct mapping of nanoscale compositional connectivity on intact cell membranes. *Proceedings of the National Academy of Sciences*, 107(35), pp.15437-15442.

[168] Meder, D., Moreno, M.J., Verkade, P., Vaz, W.L. and Simons, K., 2006. Phase coexistence and connectivity in the apical membrane of polarized epithelial cells. *Proceedings of the National Academy of Sciences of the United States of America*, 103(2), pp.329-334.

[169] Dietrich, C., Yang, B., Fujiwara, T., Kusumi, A. and Jacobson, K., 2002. Relationship of lipid rafts to transient confinement zones detected by single particle tracking. *Biophysical Journal*, 82(1), pp.274-284.

[170] Wawrezinieck, L., Rigneault, H., Marguet, D. and Lenne, P.F., 2005. Fluorescence correlation spectroscopy diffusion laws to probe the submicron cell membrane organization. *Biophysical Journal*, 89(6), pp.4029-4042.

[171] Maiti, S., Haupts, U. and Webb, W.W., 1997. Fluorescence correlation spectroscopy: diagnostics for sparse molecules. *Proceedings of the National Academy of Sciences*, 94(22), pp.11753-11757.

[172] Bacia, K., Kim, S.A. and Schwille, P., 2006. Fluorescence cross-correlation spectroscopy in living cells. *Nature Methods*, 3(2), p.83.

[173] He, H.T. and Marguet, D., 2011. Detecting nanodomains in living cell membrane by fluorescence correlation spectroscopy. *Annual Review of Physical Chemistry*, 62, pp.417-436.

[174] Kastrup, L., Blom, H., Eggeling, C. and Hell, S.W., 2005. Fluorescence fluctuation spectroscopy in subdiffraction focal volumes. *Physical Review Letters*, 94(17), p.178104.

[175] Eggeling, C., Ringemann, C., Medda, R., Schwarzmann, G., Sandhoff, K., Polyakova, S., Belov, V.N., Hein, B., von Middendorff, C., Schönle, A. and Hell, S.W., 2009. Direct observation of the nanoscale dynamics of membrane lipids in a living cell. *Nature*, 457(7233), p.1159.

[176] Mueller, V., Ringemann, C., Honigmann, A., Schwarzmann, G., Medda, R., Leutenegger, M., Polyakova, S., Belov, V.N., Hell, S.W. and Eggeling, C., 2011. STED nanoscopy reveals molecular details of cholesterol-and cytoskeleton-modulated lipid interactions in living cells. *Biophysical Journal*, 101(7), pp.1651-1660.

[177] Honigmann, A., Mueller, V., Ta, H., Schoenle, A., Sezgin, E., Hell, S.W. and Eggeling, C., 2014. Scanning STED-FCS reveals spatiotemporal heterogeneity of lipid interaction in the plasma membrane of living cells. *Nature communications*, 5, p.5412.

[178] Vicidomini, G., Ta, H., Honigmann, A., Mueller, V., Clausen, M.P., Waithe, D., Galiani, S., Sezgin, E., Diaspro, A., Hell, S.W. and Eggeling, C., 2015. STED-FLCS: an advanced tool to reveal spatiotemporal heterogeneity of molecular membrane dynamics. *Nano Letters*, 15(9), pp.5912-5918.

[179] Edel, J.B., Wu, M., Baird, B. and Craighead, H.G., 2005. High spatial resolution observation of single-molecule dynamics in living cell membranes. *Biophysical Journal*, 88(6), pp.L43-L45.

[180] Kelly, C.V., Baird, B.A. and Craighead, H.G., 2011. An array of planar apertures for near-field fluorescence correlation spectroscopy. *Biophysical Journal*, 100(7), pp.L34-L36.

[181] Kelly, C.V., Wakefield, D.L., Holowka, D.A., Craighead, H.G. and Baird, B.A., 2014. Near-field fluorescence cross-correlation spectroscopy on planar membranes. *ACS Nano*, 8(7), pp.7392-7404.

[182] Richards, C.I., Luong, K., Srinivasan, R., Turner, S.W., Dougherty, D.A., Korlach, J. and Lester, H.A., 2012. Live-cell imaging of single receptor composition using zero-mode waveguide nanostructures. *Nano Letters*, 12(7), pp.3690-3694.

[183] Lohmüller, T., Iversen, L., Schmidt, M., Rhodes, C., Tu, H.L., Lin, W.C. and Groves, J.T., 2012. Single molecule tracking on supported membranes with arrays of optical nanoantennas. *Nano Letters*, 12(3), pp.1717-1721.

[184] Ruprecht, V., Wieser, S., Marguet, D. and Schütz, G.J., 2011. Spot variation fluorescence correlation spectroscopy allows for superresolution chronoscopy of confinement times in membranes. *Biophysical Journal*, 100(11), pp.2839-2845.

[185] Starr, T.E. and Thompson, N.L., 2001. Total internal reflection with fluorescence correlation spectroscopy: combined surface reaction and solution diffusion. *Biophysical Journal*, 80(3), pp.1575-1584.

[186] Hassler, K., Anhut, T., Rigler, R., Gösch, M. and Lasser, T., 2005. High count rates with total internal reflection fluorescence correlation spectroscopy. *Biophysical Journal*, 88(1), pp.L01-L03.

[187] Kapusta, P., 2010. Absolute diffusion coefficients: compilation of reference data for FCS calibration. *Application note*.

[188] Kahya, N., Scherfeld, D., Bacia, K., Poolman, B. and Schwille, P., 2003. Probing lipid mobility of raft-exhibiting model membranes by fluorescence correlation spectroscopy. *Journal of Biological Chemistry*, 278(30), pp.28109-28115.

[189] Zhang, K. and Yang, H., 2005. Photon-by-photon determination of emission bursts from diffusing single chromophores. *The Journal of Physical Chemistry B*, 109(46), pp.21930-21937.

[190] Nicolau, D.V., Burrage, K., Parton, R.G. and Hancock, J.F., 2006. Identifying optimal lipid raft characteristics required to promote nanoscale protein-protein interactions on the plasma membrane. *Molecular and Cellular Biology*, 26(1), pp.313-323.

[191] Spillane, K.M., Ortega-Arroyo, J., de Wit, G., Eggeling, C., Ewers, H., Wallace, M.I. and Kukura, P., 2014. High-speed single-particle tracking of GM1 in model membranes reveals anomalous diffusion due to interleaflet coupling and molecular pinning. *Nano Letters*, 14(9), pp.5390-5397.

[192] Spindler, S., Ehrig, J., König, K., Nowak, T., Piliarik, M., Stein, H.E., Taylor, R.W., Garanger, E., Lecommandoux, S., Alves, I.D. and Sandoghdar, V., 2016. Visualization of lipids and proteins at high spatial and temporal resolution *via* interferometric scattering (iSCAT) microscopy. *Journal of Physics D: Applied Physics*, 49, p.274002.